JSCSEN 87(10)1109–1235(2022)

ISSN 1820-7421(Online)

Journal of the Serbian Chemical Society

Electronic version

Serbian Chemical Society 125 ANNIVERSARY

Available on line at

www.shd.org.rs/JSCS/

VOLUME 87

No 10

BELGRADE 2022

The full search of JSCS is available through

DOAJ DIRECTORY OF OPEN ACCESS JOURNALS

www.doaj.org

The **Journal of the Serbian Chemical Society** (formerly Glasnik Hemijskog društva Beograd), one volume (12 issues) per year, publishes articles from the fields of chemistry. The **Journal** is financially supported by the **Ministry of Education, Science and Technological Development of the Republic of Serbia.**

Articles published in the **Journal** are indexed in **Clarivate Analytics products: Science Citation Index-Expanded™** – accessed *via* **Web of Science®** and **Journal Citation Reports®**.

Impact Factor announced 2022: **1.100; 5-year Impact Factor**: **1.175**.

Articles appearing in the **Journal** are also abstracted by: **Scopus, Chemical Abstracts Plus (CAplus℠), Directory of Open Access Journals, Referativnii Zhurnal (VINITI), RSC Analytical Abstracts, EuroPub, Pro Quest** and **Asian Digital Library.**

Publisher:	**Serbian Chemical Society**, Karnegijeva 4/III, P. O. Box 36, 1120 Belgrade 35, Serbia tel./fax: +381–11–3370–467, E-mails: **Society** – shd@shd.org.rs; **Journal** – jscs@shd.org.rs Home Pages: **Society** – http://www.shd.org.rs/, **Journal** – http://www.shd.org.rs/JSCS/
Internet Service:	Contents, Abstracts and full papers (from Vol 64, No. 1, 1999) are available in the electronic form at the Web Site of the **Journal** (http://www.shd.org.rs/JSCS/).
Former Editors:	**Nikola A. Pušin** (1930–1947), **Aleksandar M. Leko** (1948–1954), **Panta S. Tutundžić** (1955–1961), **Miloš K. Mladenović** (1962–1964), **Đorđe M. Dimitrijević** (1965–1969), **Aleksandar R. Despić** (1969–1975), **Slobodan V. Ribnikar** (1975–1985), **Dragutin M. Dražić** (1986–2006).
Editor-in-Chief:	BRANISLAV Ž. **NIKOLIĆ**, Serbian Chemical Society (E-mail: jscs-ed@shd.org.rs)
Deputy Editor:	DUŠAN **SLADIĆ**, Faculty of Chemistry, University of Belgrade
Sub editors:	
Organic Chemistry	DEJAN **OPSENICA**, Institute of Chemistry, Technology and Metallurgy, University of Belgrade JÁNOS **CSANÁDI**, Faculty of Science, University of Novi Sad
Biochemistry and Biotechnology	OLGICA **NEDIĆ**, INEP – Institute for the Application of Nuclear Energy, University of Belgrade
Inorganic Chemistry	MILOŠ **ĐURAN**, Serbian Chemical Society
Theoretical Chemistry	IVAN **JURANIĆ**, Serbian Chemical Society
Physical Chemistry	LJILJANA **DAMJANOVIĆ-VASILIĆ**, Faculty of Physical Chemistry, University of Belgrade
Electrochemistry	SNEŽANA **GOJKOVIĆ**, Faculty of Technology and Metallurgy, University of Belgrade
Analytical Chemistry	SLAVICA **RAŽIĆ**, Faculty of Pharmacy, University of Belgrade
Polymers	BRANKO **DUNJIĆ**, Faculty of Technology and Metallurgy, University of Belgrade
Thermodynamics	MIRJANA **KIJEVČANIN**, Faculty of Technology and Metallurgy, University of Belgrade
Chemical Engineering	TATJANA **KALUĐEROVIĆ RADOIČIĆ**, Faculty of Technology and Metallurgy, University of Belgrade
Materials	RADA **PETROVIĆ**, Faculty of Technology and Metallurgy, University of Belgrade
Metallic Materials and Metallurgy	ANA **KOSTOV**, Mining and Metallurgy Institute Bor, University of Belgrade
Environmental and Geochemistry	VESNA **ANTIĆ**, Faculty of Agriculture, University of Belgrade
History of and Education in Chemistry	DRAGICA **TRIVIĆ**, Faculty of Chemistry, University of Belgrade
English Language Editors:	LYNNE **KATSIKAS**, Serbian Chemical Society VLATKA **VAJS**, Serbian Chemical Society JASMINA **NIKOLIĆ**, Faculty of Technology and Metallurgy, University of Belgrade
Technical Editors:	VLADIMIR **PANIĆ**, ALEKSANDAR **DEKANSKI**, VUK **FILIPOVIĆ**, Institute of Chemistry, Technology and Metallurgy, University of Belgrade
Journal Manager & Web Master:	ALEKSANDAR **DEKANSKI,** Institute of Chemistry, Technology and Metallurgy, University of Belgrade
Office:	VERA **ĆUŠIĆ**, Serbian Chemical Society

Editorial Board

From abroad: **R. Adžić**, Brookhaven National Laboratory (USA); **A. Casini**, University of Groningen (The Netherlands); **G. Cobb**, Baylor University (USA); **D. Douglas**, University of British Columbia (Canada); **G. Inzelt**, Etvos Lorand University (Hungary); **J. Kenny**, University of Perugia (Italy); **Ya. I. Korenman**, Voronezh Academy of Technology (Russian Federation); **M. D. Lechner**, University of Osnabrueck (Germany); **S. Macura**, Mayo Clinic (USA); **M. Spiteller**, INFU, Technical University Dortmund (Germany); **M. Stratakis**, University of Crete (Grecce); **M. Swart**, University de Girona (Cataluna, Spain); **G. Vunjak-Novaković**, Columbia University (USA); **P. Worsfold**, University of Plymouth (UK); **J. Zagal**, Universidad de Santiago de Chile (Chile).

From Serbia: **B. Abramović**, **V. Antić**, **V. Beškoski**, **J. Csanadi**, **Lj. Damjanović-Vasilić**, **A. Dekanski**, **V. Dondur**, **B. Dunjić**, **M. Đuran, S. Gojković**, **I. Gutman**, **B. Jovančićević**, **I. Juranić**, **T. Kaluđerović Radioičić**, **L. Katsikas**, **M. Kijevčanin**, **A. Kostov**, **V. Leovac**, **S. Milonjić**, **V.B. Mišković-Stanković**, **O. Nedić**, **B. Nikolić**, **J. Nikolić**, **D. Opsenica**, **V. Panić**, **M. Petkovska**, **R. Petrović**, **I. Popović**, **B. Radak**, **S. Ražić**, **D. Sladić**, **S. Sovilj**, **S. Šerbanović**, **B. Šolaja**, **Ž. Tešić**, **D. Trivić**, **V. Vajs**.

Subscription: The annual subscription rate is **150.00 €** including postage (surface mail) and handling. For Society members from abroad rate is **50.00 €**. For the proforma invoice with the instruction for bank payment contact the Society Office (E-mail: shd@shd.org.rs) or see JSCS Web Site: http://www.shd.org.rs/JSCS/, option Subscription.

Godišnja pretplata: Za članove SHD: **2.500,00 RSD**, za penzionere i studente: **1000,00 RSD**, a za ostale: **3.500,00 RSD**:za organizacije i ustanove: **16.000,00 RSD**. Uplate se vrše na tekući račun Društva: **205-13815-62**, poziv na broj **320**, sa naznakom "pretplata za JSCS".

Nota: Radovi čiji su svi autori članovi SHD prioritetno se publikuju.

Odlukom Odbora za hemiju Republičkog fonda za nauku Srbije, br. 66788/1 od 22.11.1990. godine, koja je kasnije potvrđena odlukom Saveta Fonda, časopis je uvršten u kategoriju međunarodnih časopisa (**M-23**). Takođe, aktom Ministarstva za nauku i tehnologiju Republike Srbije, 413-00-247/2000-01 od 15.06.2000. godine, ovaj časopis je proglašen za publikaciju od posebnog interesa za nauku. **Impact Factor** časopisa objavljen 2022. godini iznosi **1,100**, a petogodišnji **Impact Factor 1,175**.

INSTRUCTIONS FOR AUTHORS (2021)

GENERAL

The *Journal of the Serbian Chemical Society* (the *Journal* in further text) is an international journal publishing papers from all fields of chemistry and related disciplines. Twelve issues are published annually. The Editorial Board expects the editors, reviewers, and authors to respect the well-known standard of professional ethics.

Types of Contributions

Original scientific papers	(up to 15 typewritten pages, including Figures, Tables and References) report original research which must not have been previously published.
Short communications	(up to 8 pages) report unpublished preliminary results of sufficient importance to merit rapid publication.
Notes	(up to 5 pages) report unpublished results of short, but complete, original research
Authors' reviews	(up to 40 pages) present an overview of the author's current research with comparison to data of other scientists working in the field
Reviews[a]	(up to 40 pages) present a concise and critical survey of a specific research area. Generally, these are prepared at the invitation of the Editor
Surveys	(about 25 pages) communicate a short review of a specific research area.
Book and Web site reviews	(1 - 2 pages)
Extended abstracts	(about 4 pages) of Lectures given at meetings of the Serbian Chemical Society Divisions
Letters to the Editor	report miscellaneous topics directed directly to the Editor

[a]Generally, Authors' reviews, Reviews and Surveys are prepared at the invitation of the Editor.

Submission of manuscripts

Manuscripts should be submitted using the **OnLine Submission Form**, available on the JSCS Web Site (**http://www.shd-pub.org.rs/index.php/JSCS**). The manuscript must be uploaded as a Word.doc or .rtf file, with tables and figures (including the corresponding captions – above Tables and below Figures), placed within the text to follow the paragraph in which they were mentioned for the first time.

Please note that **Full Names (**First Name, Last Name), **Full Affiliation** and **Country** (from drop down menu) of **ALL OF AUTHORS** (written in accordance with English spelling rules - the first letter capitalized) must be entered in the manuscript Submission Form (Step 3). Manuscript Title, authors' names and affiliations, as well as the Abstract, **WILL APPEAR** in the article listing, as well as in **BIBLIOGRAPHIC DATABASES (WoS, SCOPUS...)**, in the form and in the order entered in the author details

Graphical abstract

Graphical abstract is a one-image file containing the main depiction of the authors work and/or conclusion and must be supplied along with the manuscript. It must enable readers to quickly gain the main message of the paper and to encourage browsing, help readers identify which papers are most relevant to their research interests. Authors must provide an image that clearly represents the research described in the paper. The most relevant figure from the work, which summarizes the content, can also be submitted. The image should be submitted as a separate file in **Online Submission Form - Step 2**.

Specifications: The graphical abstract should have a clear start and end, reading from top to bottom or left to right. Please omit unnecessary distractions as much as possible.

- **Image size:** minimum of 500×800 pixels (W×H) and a minimum resolution of 300 dpi. If a larger image is sent, then please use the same ratio: 16 wide × 9 high. Please note that your image will be scaled proportionally to fit in the available window in TOC; a 150x240 pixel rectangle. Please be sure that the quality of an image cannot be increased by changing the resolution from lower to higher, but only by rescanning or exporting the image with a higher resolution, which can be set in usual "settings" option.
- **Font:** Please use Calibri and Symbol font with a large enough font size, so it is readable even from the image of a smaller size (150 × 240 px) in TOC.
- **File type:** JPG and PNG only.

No additional text, outline or synopsis should be included. Please do not use white space or any heading within the image.

Cover Letter

Manuscripts must be accompanied by a cover letter (strictly uploaded in **Online Submission Step 2**) in which the type of the submitted manuscript and a warranty as given below are given. The Author(s) has(have) to warranty that the manuscript submitted to the *Journal* for review is original, has been written by the stated author(s) and has not been published elsewhere; is currently not being considered for publication by any other journal and will not be submitted for such a review while under review by the *Journal*; the manuscript contains no libellous or other unlawful statements and does not contain any materials that violate any personal or proprietary rights of any other person or entity. All manuscripts will be acknowledged on receipt (by e-mail).

Illustrations

Illustrations (Figs, schemes, photos…) in TIF or EPS format (JPG format is acceptable for colour and greyscale photos, only), must be additionally uploaded (Online Submission Step 2) as a separate file or one archived (.zip, .rar or .arj) file. Figures and/or Schemes should be prepared according to the **Artwork Instructions -** http://www.shd.org.rs/JSCS/jscs-pdf/Artwork_Instructions.pdf!

For any difficulties and questions related to **OnLine Submission Form -** https://www.shd-pub.org.rs/index.php/JSCS/submission/wizard, please refer to **User Guide -** https://openjournal-systems.com/ojs-3-user-guide/ , Chapter **Submitting an Article -** https://openjournalsystems.com/ojs-3-user-guide/submitting-an-article/. If difficulties still persist, please contact JSCS Editorial Office at **JSCS@shd.org.rs**

A manuscript not prepared according to these instructions will be returned for resubmission without being assigned a reference number.

Conflict-of-Interest Statement*: Public trust in the peer review process and the credibility of published articles depend in part on how well a conflict of interest is handled during writing, peer review, and editorial decision making. A conflict of interest exists when an author (or the author's institution), reviewer, or editor has financial or personal relationships that inappropriately influence (bias) his or her actions (such relationships are also known as dual commitments, competing interests, or competing loyalties). These relationships vary from those with negligible potential to those with great potential to influence judgment, and not all relationships represent true conflict of interest. The potential for a conflict of interest can exist whether or not an individual believes that the relationship affects his or her scientific judgment. Financial relationships (such as employment, consultancies, stock ownership, honoraria, paid expert testimony) are the most easily identifiable conflicts of interest and the most likely to undermine the credibility of the journal, the authors, and of science itself. However, conflicts can occur for other reasons, such as personal relationships, academic competition, and intellectual passion.

Informed Consent Statement*: Patients have a right to privacy that should not be infringed without informed consent. Identifying information, including patients' names, initials, or hospital numbers, should not be published in written descriptions, photographs, and pedigrees unless the information is essential for scientific purposes and the patient (or parent or guardian) gives written informed consent for publication. Informed consent for this purpose requires that a patient who is identifiable be shown the manuscript to be published. Authors should identify Individuals who provide writing assistance and disclose the funding source for this assistance. Identifying details should be omitted if they are not essential. Complete anonymity is difficult to achieve, however, and informed consent should be obtained if there is any doubt. For example, masking the eye region in photographs of patients is inadequate protection of anonymity. If identifying characteristics are altered to protect anonymity, such as in genetic pedigrees, authors should provide assurance that alterations do not distort scientific meaning and editors should so note. The requirement for informed consent should be included in the journal's instructions for authors. When informed consent has been obtained it should be indicated in the published article.

Human and Animal Rights Statement* When reporting experiments on human subjects, authors should indicate whether the procedures followed were in accordance with the ethical standards of the responsible committee on human experimentation (institutional and national) and with the Helsinki Declaration of 1975, as revised in 2000 (5). If doubt exists whether the research was conducted in accordance with the Helsinki Declaration, the authors must explain the rationale for their approach, and demonstrate that the institutional review body explicitly approved the doubtful aspects of the study. When reporting experiments on animals, authors should be asked to indicate whether the institutional and national guide for the care and use of laboratory animals was followed.

---

*International Committee of Medical Journal Editors ("Uniform Requirements for Manuscripts Submitted to Biomedical Journals"), February 2006

PROCEDURE

All contributions will be peer reviewed and only those deemed worthy and suitable will be accepted for publication. The Editor has the final decision. To facilitate the reviewing process, authors are encouraged to suggest up to three persons competent to review their manuscript. Such suggestions will be taken into consideration but not always accepted. If authors would prefer a specific person not be a reviewer, this should be announced. The Cover Letter must be accompanied by these suggestions. Manuscripts requiring revision should be returned according to the requirement of the Editor, within 60 days upon reception of the reviewing comments by e-mail.

The *Journal* maintains its policy and takes the liberty of correcting the English as well as false content of manuscripts **provisionally accepted** for publication in the first stage of reviewing process. In this second stage of manuscript preparation by JSCS Editorial Office, the author(s) may be required to supply some **additional clarifications and corrections**. This procedure will be executed during copyediting actions, with a demand to author(s) to perform corrections of unclear parts before the manuscript would be published OnLine as **finally accepted manuscript (OLF Section of the JSCS website)**. Please note that the manuscript can receive the status of **final rejection** if the author's corrections would not be satisfactory.

When finally accepted manuscript is ready for printing, the corresponding author will receive a request for proof reading, which should be performed within 2 days. Failure to do so will be taken as the authors agree with any alteration which may have occurred during the preparation of the manuscript for printing.

Accepted manuscripts of active members of the Serbian Chemical Society (all authors) have publishing priority.

MANUSCRIPT PRESENTATION

Manuscripts should be typed in English (either standard British or American English, but consistent throughout) with 1.5 spacing (12 points Times New Roman; Greek letters in the character font Symbol) in A4 format leaving 2.5 cm for margins. For Regional specific, non-standard characters that may appear in the text, save documents with Embed fonts Word option: *Save as -> (Tools) -> Save Options… -> Embed fonts in the text.*

The authors are requested to seek the assistance of competent English language expert, if necessary, to ensure their English is of a reasonable standard. The Serbian Chemical Society can provide this service in advance of submission of the manuscript. If this service is required, please contact the office of the Society by e-mail (jscs-info@shd.org.rs).

Tables, figures and/or schemes must be embedded in the main text of the manuscript and should follow the paragraph in which they are mentioned for the first time. **Tables** must be prepared with the aid of the **WORD table function**, without vertical lines. The minimum size of the font in the tables should be **10 pt**. Table columns must not be formatted using multiple spaces. Table rows must not be formatted using any returns (enter key; ↵ key) and are **limited to 12 cm width**. Tables should not be incorporated as graphical objects. **Footnotes to Tables** should follow them and are to be indicated consequently (in a single line) in superscript letters and separated by semi-column.

Table caption must be placed above corresponding Table, while **Captions of the Illustrations** (Figs. Schemes...) must follow the corresponding item. **The captions, either for Tables or Illustrations**, should make the items comprehensible without reading of the main text (but clearly referenced in), must follow numerical order (Roman for Tables, Arabic for Illustrations), and should not be provided on separate sheets or as separate files.

High resolution Illustrations (named as Fig. 1, Fig. 2… and/or Scheme 1, Scheme 2…) in **TIF or EPS format** (JPG format is acceptable for photos, only) **must be additionally uploaded as a separate files or one archived (.zip, .rar) file.**

Illustrations should be prepared according to the ARTWORK INSTRUCTIONS - http://www.shd.org.rs/JSCS/jscs-pdf/Artwork_Instructions.pdf. **!**

All pages of the manuscript must be numbered continuously.

DESIGNATION OF PHYSICAL QUANTITIES AND UNITS

IUPAC recommendations for the naming of compounds should be followed. SI units, or other permissible units, should be employed. The designation of physical quantities must be in italic throughout the text (including figures, tables and equations), whereas the units and indexes (except for indexes having the meaning of physical quantities) are in upright letters. They should be in Times New Roman font. In graphs and tables, a slash should be used to separate the designation of a physical quantity from the unit

(example: p / kPa, j / mA cm^{-2}, t / °C, T_0 / K, τ / h, ln (j / mA cm^{-2})…). Designations such as: p (kPa), t [min]…, are not acceptable. However, if the full name of a physical quantity is unavoidable, it should be given in upright letters and separated from the unit by a comma (example: Pressure, kPa; Temperature, K; Current density, mA cm^{-2}…). Please do not use the axes of graphs for additional explanations; these should be mentioned in the figure captions and/or the manuscript (example: "pressure at the inlet of the system, kPa" should be avoided). The axis name should follow the direction of the axis (the name of y-axis should be rotated by 90°). Top and right axes should be avoided in diagrams, unless they are absolutely necessary.

Latin words, as well as the names of species, should be in *italic*, as for example: *i.e.*, *e.g.*, *in vivo*, *ibid*, *Calendula officinalis* L., *etc*. The branching of organic compound should also be indicated in *italic*, for example, *n*-butanol, *tert*-butanol, *etc*.

Decimal numbers must have decimal points and not commas in the text (except in the Serbian abstract), tables and axis labels in graphical presentations of results. Thousands are separated, if at all, by a comma and not a point.

Mathematical and chemical equations should be given in separate lines and must be numbered, Arabic numbers, consecutively in parenthesis at the end of the line. All equations should be embedded in the text Complex equations (fractions, integrals, matrix…) should be prepared with the aid of the **Microsoft Equation 3.0** (or higher) or **MathType** (Do not use them to create simple equations and labels). **Using the Insert -> Equation option, integrated in MS Office 2010 and MS Office 2013, as well as insertion of equation objects within paragraph text IS NOT ALLOWED.**

ARTICLE STRUCTURE

- TITLE PAGE;
- MAIN TEXT – including Tables and Illustrations with corresponding captions;
- SUPPLEMENTARY MATERIAL (optional**)**

Title page

- **Title** in bold letters, should be clear and concise, preferably 12 words or less. The use of non-standard abbreviations, symbols and formulae is discouraged.
- AUTHORS' NAMES in capital letters with the full first name, initials of further names separated by a space and surname. Commas should separate the author's names except for the last two names when 'and' is to be used. In multi-affiliation manuscripts, the author's affiliation should be indicated by an Arabic number placed in superscript after the name and before the affiliation. Use * to denote the corresponding author(s).
- *Affiliations* should be written in italic. The e-mail address of the corresponding author should be given after the affiliation(s).
- *Abstract:* A one-paragraph abstract written of 150 – 200 words in an impersonal form indicating the aims of the work, the main results and conclusions should be given and clearly set off from the text. Domestic authors should also submit, on a separate page, an Abstract - Izvod, the author's name(s) and affiliation(s) in Serbian (Cyrillic letters). (Домаћи аутори морају доставити Извод (укључујући имена аутора и афилијацију) на српском језику, исписане ћирилицом, иза Захвалнице, а пре списка референци.) For authors outside Serbia, the Editorial Board will provide a Serbian translation of their English abstract.
- *Keywords:* Up to 6 keywords should be given. Do not use words appearing in the manuscript title
- RUNNING TITLE: A one line (maximum five words) short title in capital letters should be provided.

Main text – should have the form:

- **INTRODUCTION,**
- **EXPERIMENTAL (RESULTS AND DISCUSSION),**
- **RESULTS AND DISCUSSION (EXPERIMENTAL),**
- **CONCLUSIONS,**
- **NOMENCLATURE (optional) and**
- ***Acknowledgements*: If any.**
- REFERENCES (Citation of recent papers published in chemistry journals that highlight the significance of work to the general readership is encouraged.)

The sections should be arranged in a sequence generally accepted for publication in the respective fields. They subtitles should be in capital letters, centred and NOT numbered.

- The INTRODUCTION should include the aim of the research and a concise description of background information and related studies directly connected to the paper.
- The EXPERIMENTAL section should give the purity and source of all employed materials, as well as details of the instruments used. The employed methods should be described in sufficient detail to enable experienced persons to repeat them. Standard procedures should be referenced and only modifications described in detail. On no account should results be included in the experimental section.

Chemistry

Detailed information about instruments and general experimental techniques should be given in all necessary details. If special treatment for solvents or chemical purification were applied that must be emphasized.

Example: Melting points were determined on a Boetius PMHK or a Mel-Temp apparatus and were not corrected. Optical rotations were measured on a Rudolph Research Analytical automatic polarimeter, Autopol IV in dichloromethane (DCM) or methanol (MeOH) as solvent. IR spectra were recorded on a Perkin-Elmer spectrophotometer FT-IR 1725X. ^{1}H and ^{13}C NMR spectra were recorded on a Varian Gemini-200 spectrometer (at 200 and 50 MHz, respectively), and on a Bruker Ultrashield Advance III spectrometer (at 500 and 125 MHz, respectively) employing indicated solvents (*vide infra*) using TMS as the internal standard. Chemical shifts are expressed in ppm (δ / ppm) values and coupling constants in Hz (J / Hz). ESI-MS spectra were recorded on Agilent Technologies 6210 Time-Of-Flight LC-MS instrument in positive ion mode with CH_3CN/H_2O 1/1 with 0.2 % HCOOH as the carrying solvent solution. Samples were dissolved in CH_3CN or MeOH (HPLC grade purity). The selected values were as follows: capillary voltage = 4 kV, gas temperature = 350 °C, drying gas flow 12 L min^{-1}, nebulizer pressure = 310 kPa, fragmentator voltage = 70 V.The elemental analysis was performed on the Vario EL III- C,H,N,S/O Elemental Analyzer (Elementar Analysensysteme GmbH, Hanau-Germany). Thin-layer chromatography (TLC) was performed on precoated Merck silica gel 60 F254 and RP-18 F254 plates. Column chromatography was performed on Lobar LichroPrep Si 60 (40-63 μm), RP-18 (40-63 μm) columns coupled to a Waters RI 401 detector, and on Biotage SP1 system with UV detector and FLASH 12+, FLASH 25+ or FLASH 40+ columns pre packed with KP-SIL [40-63 μm, pore diameter 6 nm (60 Å)], KP-C18-HS (40-63 μm, pore diameter 9 nm (90 Å) or KP-NH [40-63 μm, pore diameter 10 nm (100 Å)] as adsorbent. Compounds were analyzed for purity (HPLC) using a Waters 1525 HPLC dual pump system equipped with an Alltech, Select degasser system, and dual λ 2487 UV-VIS detector. For data processing, Empower software was used (methods A and B). Methods C and D: Agylent Technologies 1260 Liquid Chromatograph equipped with Quat Pump (G1311B), Injector (G1329B) 1260 ALS, TCC 1260 (G1316A) and Detector 1260 DAD VL+ (G1315C). For data processing, LC OpenLab CDS ChemStation software was used. For details, see Supporting Information.

1. Synthesis experiments

Each paragraph describing a synthesis experiment should begin with the name of the product and any structure number assigned to the compound in the Results and Discussions section. Thereafter, the compound should be identified by its structure number. Use of standard abbreviations or unambiguous molecular formulas for reagents and solvents, and of structure numbers rather than chemical names to identify starting materials and intermediates, is encouraged.

When a new or improved synthetic method is described, the yields reported in key experimental examples, and yields used for comparison with existing methods, should represent amounts of isolated and purified products, rather than chromategraphically or spectroscopically determined yields. Reactant quantities should be reported in weight and molar units and for product yields should be reported in weight units; percentage yields should only be reported for materials of demonstrated purity. When chromatography is used for product purification, both the support and solvent should be identified.

2. Microwave experiments

Reports of syntheses conducted in microwave reactors must clearly indicate whether sealed or open reaction vessels were used and must document the manufacturer and model of the reactor, the method of monitoring the reaction mixture temperature, and the temperature-time profile. Reporting a wattage rating or power setting is not an acceptable alternative to providing temperature data. Manuscripts describing work done with domestic (kitchen) microwave ovens will not be accepted except for studies where the unit is used for heating reaction mixtures at atmospheric pressure.

3. Compound characterization

The Journal upholds a high standard for compound characterization to ensure that substances being added to the chemical literature have been correctly identified and can be synthesized in known yield and purity by the reported preparation and isolation methods. For **all new** compounds, evidence adequate to establish both **identity** and **degree of purity** (homogeneity) must be provided.

Identity *- Melting point.* All homogeneous solid products (*e.g.* not mixtures of isomers) should be characterized by melting or decomposition points. The colors and morphologies of the products should also be noted.

Specific rotations. Specific rotations based on the equation $[\alpha]^t; D = (100\ \alpha) / (l\ c)$ should be reported as unitless numbers as in the following example: $[\alpha]^{20}$; D = -25.4 (c 1.93, $CHCl_3$), where c / g mL^{-1} is concentration and l / dm is path length. The units of the specific rotation, (deg mL) / (g dm), are implicit and are not included with the reported value.

Spectra/*Spectral Data.* Important IR adsorptions should be given.

For all new diamagnetic substances, NMR data should be reported (^1H, ^{13}C, and relevant heteronuclei). ^1H NMR chemical shifts should be given with two digits after the decimal point. Include the number of protons represented by the signal, signal multiplicity, and coupling constants as needed (*J* italicized, reported with up to one digit after the decimal). The number of bonds through which the coupling is operative, ^xJ, may be specified by the author if known with a high degree of certainty. ^{13}C NMR signal shifts should be rounded to the nearest 0.01 ppm unless greater precision is needed to distinguish closely spaced signals. Field strength should be noted for each spectrum, not as a comment in the general experimental section. Hydrogen multiplicity (C, CH, CH_2, CH_3) information obtained from routine DEPT spectra should be included. If detailed signal assignments are made, the type of NOESY or COSY methods used to establish atom connectivity and spatial relationships should be identified in the Supporting Information. Copies of spectra should also be included where structure assignments of complex molecules depend heavily on NMR interpretation. Numbering system used for assignments of signals should be given in the Supporting Information with corresponding general structural formula of named derivative.

HPLC/LCMS can be substituted for biochemistry papers where the main focus is not on compound synthesis.

HRMS/*elemental analysis.* To support the molecular formula assignment, HRMS data accurate within 5 ppm, or combustion elemental analysis [carbon and hydrogen (and nitrogen, if present)] data accurate within 0.5 %, should be reported for new compounds. HRMS data should be given in format as is usually given for combustion analysis: calculated mass for given formula following with observed mass: (+)ESI-HRMS *m*/*z*: [molecular formula + H]$^+$ calculated mass, observed mass. Example: (+)ESI-HRMS *m*/*z*: calculated for [$C_{13}H_8BrCl_2N + H^+$] 327.92899, observed 327.92792.

NOTE: in certain cases, a crystal structure may be an acceptable substitute for HRMS/elemental analysis.

Biomacromolecules. The structures of biomacromolecules may be established by providing evidence about sequence and mass. Sequences may be inferred from the experimental order of amino acid, saccharide, or nucleotide coupling, from known sequences of templates in enzyme-mediated syntheses, or through standard sequencing techniques. Typically, a sequence will be accompanied by MS data that establish the molecular weight.

Example: Product was isolated upon column chromatography [dry flash (SiO_2, eluent EA, EA/MeOH gradient 95/5 → 9/1, EA/MeOH/NH_3 gradient 18/0.5/0.5 → 9/1/1, and flash chromatography (Biotage SP1, RP column, eluent MeOH/H_2O gradient 75/25 → 95/5, N-H column, eluent EA/Hex gradient 6/3 → EA). was obtained after flash column chromatography (Biotage SP NH column, eluent hexane/EA 4:6 → 2:6). Yield 968.4 mg (95 %). Colorless foam softens at 96-101 °C. $[\alpha]^{20}$; D = +0,163 (c =2.0×10^{-3} g/mL, CH_2Cl_2). IR (ATR): 3376w, 2949m, 2868w, 2802w, 1731s, 1611w, 1581s, 1528m, 1452m, 1374s, 1331w, 1246s, 1171m, 1063w, 1023m, 965w, 940w, 881w, 850w, 807w, cm^{-1}. ^1H NMR (500 MHz, $CDCl_3$, δ): 8.46 (*d*, 1H, J = 5.4, H-2'), 7.89 (*s*, 1H, J = 2.0, H-8'), 7.71 (*d*, 1H, J = 8.9, H-5'), 7.30 (*dd*, 1H, J_1 = 8.8, J_2 = 2.1, H-6'), 6.33 (*d*, 1H, J = 5.4, H-3'), 6.07 (*s*, HN-Boc, exchangeable with D_2O), 5.06 (*s*, 1H, H-12), 4.92-4.88 (*m*, 1H, H-7), 4.42 (*bs*, H-3), 3.45 (*s*,CH_3-N), 3.33 (*bs*, H-9'), 3.05-2.95 (*m*, 2H, H-11'), 2.70-2.43 (*m*, 2H, H-24) and HN, exchangeable with D_2O), 2.07 (*s*, CH_3COO), 2.04 (*s*, CH_3COO), 1.42 (*s*, 9H, $(CH_3)_3$C-N(Boc)), 0.88 (*s*, 3H, CH_3-10), 0.79 (*d*, 3H,J = 6.6, CH_3-20), 0.68 (*s*, 3H, CH_3-13). ^{13}C NMR (125 MHz, $CDCl_3$, δ): 170.34, 170.27, 151.80, 149.92, 148.87, 134.77, 128.36, 125.11, 121.43, 117.29, 99.98, 75.41, 70.82, 50.43, 49.66, 47.60, 47.33, 44.97, 43.30, 41.83, 41.48, 37.65, 36.35, 35.44, 34.89,

34.19, 33.23, 31.24, 28.79, 28.35, 27.25, 26.45, 25.45, 22.74, 22.63, 21.57, 21.31, 17.85, 12.15. (+)ESI-HRMS (*m/z*): calculated for $[C_{45}H_{67}ClN_4O_6 + H]^+$ 795.48219, observed 795.48185. Combustion analysis for $C_{45}H_{67}ClN_4O_6$: Calculated. C 67.94, H 8.49, N 7.04; found C 67.72, H 8.63, N 6.75. HPLC purity: method A: RT 1.994, area 99.12 %; method C: RT 9.936, area 98.20 %.

Purity **-** Evidence for documenting compound purity should include one or more of the following:

a) Well-resolved high field 1D ^{1}H NMR spectrum showing at most only trace peaks not attributable to the assigned structure and a standard 1D proton-decoupled ^{13}C NMR spectrum. Copies of the spectra should be included as figures in the Supporting Information.
b) Quantitative gas chromatographic analytical data for distilled or vacuum-transferred samples, or quantitative HPLC analytical data for materials isolated by column chromatography or separation from a solid support. HPLC analyses should be performed in two diverse systems. The stationary phase, solvents (HPLC), detector type, and percentage of total chromatogram integration should be reported; a copy of the chromatograms may be included as a figure in the Supporting Information.
c) Electrophoretic analytical data obtained under conditions that permit observing impurities present at the 5 % level.

HRMS data may be used to support a molecular formula assignment **but cannot be used as a criterion of purity**.

4. Biological Data

Quantitative biological data are required for all tested compounds. Biological test methods must be referenced or described in sufficient detail to permit the experiments to be repeated by others. Detailed descriptions of biological methods should be placed in the experimental section. Standard compounds or established drugs should be tested in the same system for comparison. Data may be presented as numerical expressions or in graphical form; biological data for extensive series of compounds should be presented in tabular form. Tables consisting primarily of negative data will not usually be accepted; however, for purposes of documentation they may be submitted as supporting information. Active compounds obtained from combinatorial syntheses should be resynthesized and retested to verify that the biology conforms to the initial observation.

Statistical limits (statistical significance) for the biological data are usually required. If statistical limits cannot be provided, the number of determinations and some indication of the variability and reliability of the results should be given. References to statistical methods of calculation should be included. Doses and concentrations should be expressed as molar quantities (*e.g.*, mol/kg, μmol/kg, M, mM). The routes of administration of test compounds and vehicles used should be indicated, and any salt forms used (hydrochlorides, sulfates, *etc.*) should be noted. The physical state of the compound dosed (crystalline, amorphous; solution, suspension) and the formulation for dosing (micronized, jet-milled, nanoparticles) should be indicated. For those compounds found to be inactive, the highest concentration (*in vitro*) or dose level (*in vivo*) tested should be indicated.

- The RESULTS AND DISCUSSION should include concisely presented results and there significance discussed and compared to relevant literature data. The results and discussion may be combined or kept separate.
- The inclusion of a CONCLUSION section, which briefly summarizes the principal conclusions, is recommended.
- NOMENCLATURE is optional but, if the authors wish, a list of employed symbols may be included.
- REFERENCES should be numbered sequentially as they appear in the text. Please note that any reference numbers appearing in the Illustrations and/or Tables and corresponding captions must follow the numbering sequence of the paragraph in which they appear for the first time. When cited, the reference number should be superscripted in Font 12, following any punctuation mark. In the reference list, they should be in normal position followed by a full stop. Reference entry must not be formatted using Carriage returns (enter key; ↵ key) or multiple space key. The formatting of references to published work should follow the *Journal'*s style as follows:

Journals[a]:	A. B. Surname1, C. D. Surname2, *J. Serb. Chem. Soc.* **Vol** (Year) first page Number (https://doi.org/doi)[b]
Books:	A. B. Surname1, C. D. Surname2, *Name of Book*, Publisher, City, Year, pp. 100-101 (https://doi.org/doi)[b]
Compilations:	A. B. Surname1, C. D. Surname2, in *Name of Compilation*, A. Editor1, C. Editor2, Ed(s)., Publisher, City, Year, p. 100 (https://doi.org/doi)[b]
Proceedings:	A. B. Surname1, C. D. Surname2, in *Proceedings of Name of the Conference or Symposium*, (Year), Place of the Conference, Country, *Title of the Proceeding*, Publisher, City, Year, p. or Abstract No. 100
Patents:	A. B. Inventor1, C. D. Inventor2, (Holder), Country Code and patent number (registration year)
Chemical Abstracts:	A. B. Surname1, C. D. Surname2, *Chem. Abstr*. CA 234 567a; For non-readily available literature, the Chemical Abstracts reference should be given in square brackets: [C.A. 139/2003 357348t] after the reference
Standards:	EN ISO 250: *Name of the Standard* (Year)
Websites:	Title of the website, URL in full (date accessed)

[a] When citing Journals, the International Library Journal abbreviation is required. Please consult, *e.g.*, https://images.webofknowledge.com/WOK46/help/WOS/A_abrvjt.html

[b] doi should be replaced by doi number of the Article, for example: http://dx.doi.org/10.2298/JSC161212085B (as active link). If doi do not exist, provide the link to the online version of the publication.

Only the last entry in the reference list should end with a full stop.

The names of all authors should be given in the list of references; the abbreviation *et al.* may only be used in the text. The original journal title is to be retained in the case of publications published in any language other than English (please denote the language in parenthesis after the reference). Titles of publications in non-Latin alphabets should be transliterated. Russian references are to be transliterated using the following transcriptions:

ж→zh, х→kh, ц→ts, ч→ch, ш→sh, щ→shch, ы→y, ю→yu, я→ya, э→e, й→i, ь→’.

Supplementary material

Authors are encouraged to presentthe information and results non-essential to the understanding of their paper as SUPPLEMENTARY MATERIAL (can be uploaded inStep 4 of Online Submission). This material may include as a rule, but is not limited to, the presentation of analytical and spectral data demonstrating the identity and purity of synthesized compounds, tables containing raw data on which calculations were based, series of figures where one example would remain in the main text, etc. The Editorial Board retain the right to assign such information and results to the Supplementary material when deemed fit. Supplementary material does not appear in printed form but can be downloaded from the web site of the JSCS.

Mathematical and chemical equations should be given in separate lines and must be numbered, Arabic numbers, consecutively in parenthesis at the end of the line. All equations should be embedded in the text Complex equations (fractions, integrals, matrix…) should be prepared with the aid of the Microsoft Equation 3.0 (or higher) or MathType (Do not use them to create simple equations and labels). Using the Insert -> Equation option, integrated in MS Office 2010 and MS Office 2013, as well as insertion of equation objects within paragraph text IS NOT ALLOWED.

Deposition of crystallographic data

Prior to submission, the crystallographic data included in a manuscript presenting such data should be deposited at the appropriate database. Crystallographic data associated with organic and metal-organic structures should be deposited at the Cambridge Crystallographic Data Centre (CCDC) by e-mail to **deposit@ccdc.cam.ac.uk**

Crystallographic data associated with inorganic structures should be deposited with the Fachinformationszentrum Karlsruhe (FIZ) by e-mail to **crysdata@fiz-karlsruhe.de**. A deposition number will then be provided, which should be added to the reference section of the manuscript.

For detailed instructions please visit the JSCS website:
https://www.shd-pub.org.rs/index.php/JSCS/Instructions

ARTWORK INSTRUCTIONS

JSCS accepts only **TIFF** or **EPS** formats, as well as **JPEG** format (only for colour and greyscale photographs) for electronic artwork and graphic files. **MS files** (Word, PowerPoint, Excel, Visio) **NOT acceptable**. Generally, scanned instrument data sheets should be avoided. Authors are responsible for the quality of their submitted artwork. Every single Figure or Scheme, as well as any part of the Figure (A, B, C…) should be prepared according to following instructions (every part of the figure, A, B, C…, must be submitted as an independent single graphic file):

TIFF

Virtually all common artwork and graphic creation software is capable of saving files in TIFF format. This 'option' can normally be found under 'the 'Save As...' or 'Export...' commands in the 'File' menu.

TIFF (Tagged Image File Format) is the recommended file format for bitmap, greyscale and colour images.

- Colour images should be in the RGB mode
- When supplying TIFF files, please ensure that the files are supplied at the correct resolution:
    1. Line artwork: minimum of 1000 dpi
    2. RGB image: minimum of 300 dpi
    3. Greyscale image: minimum of 300 dpi
    4. Combination artwork (line/greyscale/RGB): minimum of 500 dpi
- Images should be tightly cropped, without frame and any caption.
- If applicable please re-label artwork with a font supported by JSCS (Arial, Helvetica, Times, Symbol) and ensure it is of an appropriate font size.
- Save an image in TIFF format with LZW compression applied.
- It is recommended to remove Alpha channels before submitting TIFF files.
- It is recommended to flatten layers before submitting TIFF files.

Please be sure that quality of an image cannot be increased by changing the resolution from lower to higher, but only by rescanning or exporting the image with higher resolution, which can be set in usual "settings" facilities.

EPS

Virtually all common artwork creation software, such as Canvas, ChemDraw, CorelDraw, SigmaPlot, Origin Lab…, are capable of saving files in EPS format. This 'option' can normally be found under the 'Save As...' or 'Export...' commands in the 'File' menu.

For vector graphics, EPS (Encapsulated PostScript) files are the preferred format as long as they are provided in accordance with the following conditions:

- when they contain bitmap images, the bitmaps should be of good resolution (see instructions for TIFF files)
- when colour is involved, it should be encoded as RGB
- an 8-bit preview/header at a resolution of 72 dpi should always be included
- embed fonts should always included and only the following fonts should be used in artwork: Arial, Helvetica, Times, Symbol
- the vertical space between the parts of an illustration should be limited to the bare necessity for visual clarity
- no data should be present outside the actual illustration area
- line weights should range from 0.35 pt to 1.5 pt
- when using layers, they should be reduced to one layer before saving the image (Flatten Artwork)

JPEG

Virtually all common artwork and graphic creation software is capable of saving files in JPEG format. This 'option' can normally be found under 'the 'Save As...' or 'Export...' commands in the 'File' menu.

JPEG (Joint Photographic Experts Group) is the acceptable file format **only for colour and greyscale photographs**. JPEG can be created with respect to photo quality (low, medium, high; from 1 to 10), ensuring file sizes are kept to a minimum to aid easy file transfer. Images should have a minimum resolution of 300 dpi. Image width: minimum 3.0 cm; maximum 12.0 cm.

Please be sure that quality of an image cannot be increased by changing the resolution from lower to higher, but only by rescanning or exporting the image with higher resolution, which can be set in usual "settings" facilities.

SIZING OF ARTWORK

- JSCS aspires to have a uniform look for all artwork contained in a single article. Hence, it is important to be aware of the style of the journal.
- Figures should be submitted in black and white or, if required, colour (charged). If coloured figures or photographs are required, this must be stated in the cover letter and arrangements made for payment through the office of the Serbian Chemical Society.
- As a general rule, the lettering on an artwork should have a finished, printed size of 11 pt for normal text and no smaller than 7 pt for subscript and superscript characters. Smaller lettering will yield a text that is barely legible. This is a rule-of-thumb rather than a strict rule. There are instances where other factors in the artwork, (for example, tints and shadings) dictate a finished size of perhaps 10 pt. Lines should be of at least 1 pt thickness.
- When deciding on the size of a line art graphic, in addition to the lettering, there are several other factors to address. These all have a bearing on the reproducibility/readability of the final artwork. Tints and shadings have to be printable at the finished size. All relevant detail in the illustration, the graph symbols (squares, triangles, circles, *etc*.) and a key to the diagram (to explain the explanation of the graph symbols used) must be discernible.
- The sizing of halftones (photographs, micrographs,...) normally causes more problems than line art. It is sometimes difficult to know what an author is trying to emphasize on a photograph, so you can help us by identifying the important parts of the image, perhaps by highlighting the relevant areas on a photocopy. The best advice that can be given to graphics suppliers is not to over-reduce halftones. Attention should also be paid to magnification factors or scale bars on the artwork and they should be compared with the details inside. If a set of artwork contains more than one halftone, again please ensure that there is consistency in size between similar diagrams.

General sizing of illustrations which can be used for the Journal of the Serbian Chemical Society:

- Minimum fig. size: 30 mm width
- Small fig. size - 60 mm width
- Large fig. size - 90 mm width
- Maximum fig. size - 120 mm width

Pixel requirements (width) per print size and resolution for bitmap images:

	Image width	A	B	C
Minimal size	30 mm	**354**	**591**	**1181**
Small size	60 mm	**709**	**1181**	**2362**
Large size	90 mm	**1063**	**1772**	**3543**
Maximal size	120 mm	**1417**	**2362**	**4724**

A: 300 dpi > RGB or Greyscale image
B: 500 dpi > Combination artwork (line/greyscale/RGB)
C: 1000 dpi> Line artwork

The designation of physical quantities and graphs formatting

The designation of physical quantities on figures must be in italic, whereas the units are in upright letters. They should be in Times New Roman font. In graphs a slash should be used to separate the designation of a physical quantity from the unit (example: p / kPa, t °C, T_0 / K, τ / h, ln (j / mA cm^{-2})…). Designations such as: p (kPa), t [min]…, are not acceptable. However, if the full name of a physical quantity is unavoiable, it should be given in upright letters and separated from the unit by a comma (example: Pressure, kPa, Temperature, K…). Please do not use the axes of graphs for additional explanations; these should be mentioned in the figure captions and/or the manuscript (example: "pressure at the inlet of the system, kPa" should be avoided). The axis name should follow the direction of the axis (the name of y-axis should be rotated by 90°). Top and right axes should be avoided in diagrams, unless they are absolutely necessary. Decimal numbers must have decimal points and not commas in the axis labels in graphical presentations of results. Thousands are separated, if at all, by a comma and not a point.

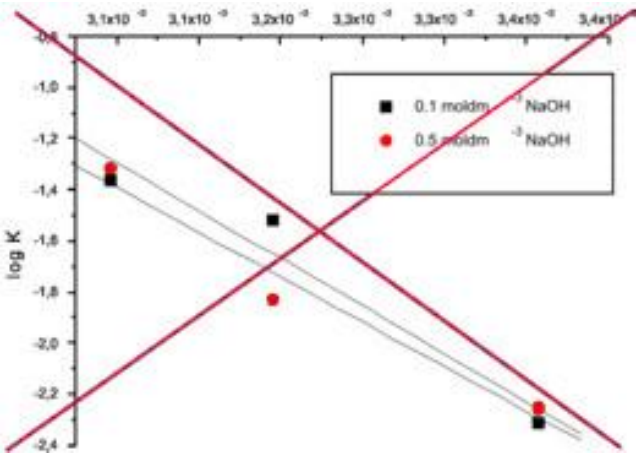

INCORRECT

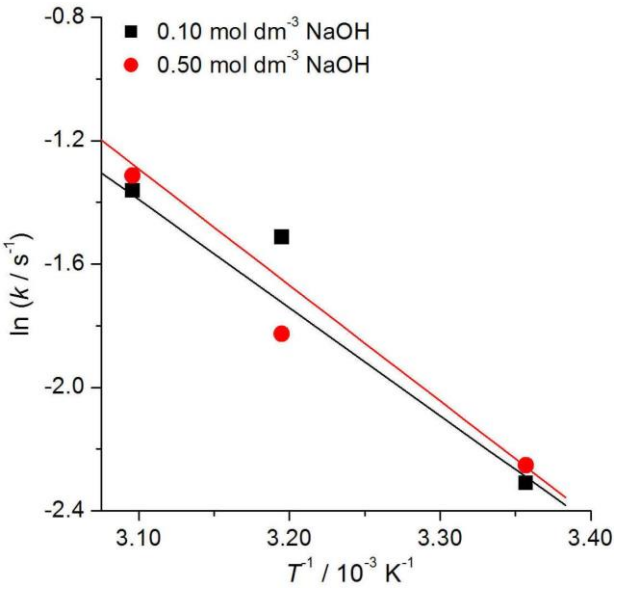

CORRECT

Journal of the Serbian Chemical Society
JSCS-info@shd.org.rs • www.shd.org.rs/JSCS

J. Serb. Chem. Soc. Vol. 87, No. 10 (2022)

CONTENTS*

Published by the Serbian Chemical Society
Karnegijeva 4/III, P.O. Box 36, 11120 Belgrade, Serbia
Printed by the Faculty of Technology and Metallurgy
Karnegijeva 4, P.O. Box 35-03, 11120 Belgrade, Serbia

* For colored figures in this issue please see electronic version at the Journal Home Page: http://www.shd.org.rs/JSCS/

(CC) 2022 SCS.

Journal of the Serbian Chemical Society
JSCS@tmf.bg.ac.rs • www.shd.org.rs/JSCS
J. Serb. Chem. Soc. *87* (10) 1109–1116 (2022)
JSCS–5581
Original scientific paper
Published 1 August 2022

Synthesis of novel fluorinated 1,5-benzothiazepine derivatives and their biological evaluation as anticancer and antibacterial agents

SONAL R. BHABAL, SARFARAZ F. SHAIKH, ISHITA P. YELLAPURKAR, GANESH S. PAVALE and MUCHELI M. V. RAMANA*

Department of Chemistry, University of Mumbai, Santacruz (E), Mumbai 400 098, India

(Received 28 April 2021, revised 28 April, accepted 10 May 2022)

Abstract: A series of novel fluorinated 1,5-benzothiazepine derivatives were synthesized, characterized and evaluated for *in vitro* anticancer and antibacterial activity. The *in vitro* anticancer activity of the synthesized compounds **4a**–**h** was evaluated against four human cancer cell lines namely lung (A549), breast (MCF-7), liver (HEPG2) and prostate (PC-3). Compounds **4c**, **4d**, **4g** and **4h** exhibited good activity with GI_{50} <10 μg ml^{-1} against all four human cancer cell lines which was comparable to standard drug adriamycin. Additionally, antibacterial activity of synthesized compounds was estimated using Resazurin Microtiter Assay (REMA) and compared with standard drug ampicillin. Among the synthesized compounds, **4c**, **4d**, **4g** and **4h** showed good antibacterial activity and all the synthesized compounds were found to be more active towards gram negative than gram positive bacteria. These promising results obtained from *in vitro* anticancer and antibacterial activity, inferred that the synthesized compounds are capable of being anticancer as well as antibacterial agents.

Keywords: *in vitro*; lung cancer cell line; breast cancer cell line; liver cancer cell line; prostate cancer cell line.

INTRODUCTION

One of the major world problems is cancer; due to the increased cancer cases and deaths. In the year 2020, it was anticipated that there will be 19.3 million new cancer cases and 10.0 million deaths worldwide.[1] Despite the fact that chemotherapy is most commonly used to treat cancer, the failure of existing chemotherapeutics to treat cancer highlights the need for new chemical entities to be developed.[2] Additionally, chemotherapy in cancer treatment is usually associated with various side effects and appearance of resistance.[3] Moreover, despite

* Corresponding author. E-mail: mmvramana@yahoo.co.in
https://doi.org/10.2298/JSC210428041B

Available on line at www.shd.org.rs/JSCS/
(CC) 2022 SCS.

of progressive development in cancer chemotherapy, there are still insufficient cytotoxic agents that act selectively to cancer cells.

Infections are one of the reasons for compromised immunity among cancer patients. They make patient vulnerable which leads to disturbance in treatment.[4] Infectious diseases put public life in jeopardy and are responsible for a large number of deaths globally. The major issue is the resistance of pathogenic microorganisms to the available antimicrobial agents, which makes it difficult to treat with conventional antibiotics and force clinicians to rely on restricted options.[5] Therefore, the development of both new anticancer and antimicrobial entities is a necessity.

In the last decades, owing to their structural properties and wide range of biological activities, benzothiazepines have piqued the interest of researchers.[6,7] 1,5-Benzothiazepine scaffold has been used as anticancer,[8–11] antimicrobial,[11–14] anti-inflammatory,[14] anticonvulsant[15] and anti-HIV[16,17]agent. Also, 1,5-benzothiazepine scaffold is reported as acetylcholinesterase inhibitor,[18] butyrylcholinesterase inhibitor,[19] VRV-PL-8a and H^+/K^+ ATPase inhibitor.[20] Clentiazem, diltiazem, thiazesim and quetiapine are among the commercially available drugs which contain the 1,5-benzothiazepine skeleton.

Heterocycles containing fluorine atoms have a wide range of applications in pharmaceutical industry.[21] The presence of a fluorine atom alters certain physicochemical properties such as basicity, lipophilicity, bioavailability as well as binding affinity of a drug molecule to the target protein.[22] Ciprofloxacin (antibiotic), fluconazole (antifungal), 5-fluorouracil (anticancer), paroxetine (antidepressant), linezolid (antibacterial), favipiravir (antiviral) and midazolam (sedative) are some of the marketed drugs that contain fluorine atom. Prasada Rao *et al.* reported compounds with fluorinated 1,5 Benzothiazepine skeleton as anti-cancer agents.[23] Similarly, Upreti *et al.* reported 8-fluoro-1,5-benzothiazepine as promising anti-AIDS agent.[24] A series of 1,5-benzothiazepines with fluorine and 4-fluorophenyl groups have also been reported for the treatment of cancer metastasis.[25]

Based on the wide spectrum of biological activities, 1,5-benzothiazepines are good candidate and could be taken in consideration as promising anticancer and antimicrobial agents. Herein we report the synthesis, anticancer and antibacterial activity of fluorinated 1,5-benzothiazepines. Anticancer activity was evaluated *in vitro* using four different cell lines namely human lung cancer cell line (A549), human breast cancer cell line (MCF-7), human liver cancer cell line (HEPG2) and human prostate cancer cell line (PC-3). Similarly, antibacterial activity was performed using two Gram-positive strains and two Gram-negative strains.

(CC) 2022 SCS.

EXPERIMENTAL

Materials and method

All reagents and chemicals were of analytical grade, procured from Sigma Aldrich (India), and used without further purification. Melting points are uncorrected and were recorded on Centrofix Syndicate MP apparatus. Merck silica gel 60 F254 TLC plates were used to monitor the reaction. FTIR spectra were recorded on Perkin Elmer, Frontier equipment with ATR. ^{1}H- (300 MHz) and ^{13}C-NMR (75 MHz) were recorded on Bruker Avance II using TMS as the internal standard in $CDCl_3$ and DMSO-d_6. ESI mass spectra were recorded on AB SCIEX 3200 QTRAP mass spectrometer. Elemental analysis (CHNS) was carried out on model EA300, Euro Vector, Italy. *Staphylococcus aureus* (ATCC 25923), *Bacillus subtilis* (ATCC 6633), *Salmonella typhi* (ATCC 23564) and *Escherichia coli* (ATCC 25922) cultures were procured from National Chemical Technology, Pune, Maharashtra and were used for antibacterial assay.

Analytical and spectral data are given in the Supplementary material to this paper.

Chemistry

Synthesis of α,β-*unsaturated ketone derivatives (**3a**–**h**).*[26] A mixture of 3,4-difluorobenzaldehyde derivative (5 mmol) and acetophenone derivative (6 mmol) were dissolved in 15 ml ethanol, then NaOH 40 % solution (5 ml) was added dropwise. The temperature of reaction was maintained below 10 °C and the reaction mixture was stirred until precipitation of solid. The precipitate was then filtered, washed several times with cold water and recrystallized from aqueous ethanol.

*Synthesis of 1,5-benzothiazepine derivatives (**4a**–**h**), Scheme 1.* A mixture of *α,β*-unsaturated ketone (5 mmol) and 2-aminothiophenol (5 mmol) were taken in methanol (10 ml) containing catalytic amount of glacial acetic acid. The reaction mixture was allowed to reflux until completion as indicated by TLC. After completion, the reaction was allowed to cool to room temperature and the solid obtained was filtered, washed several times with methanol and recrystallized using ethanol to afford yellow solid.

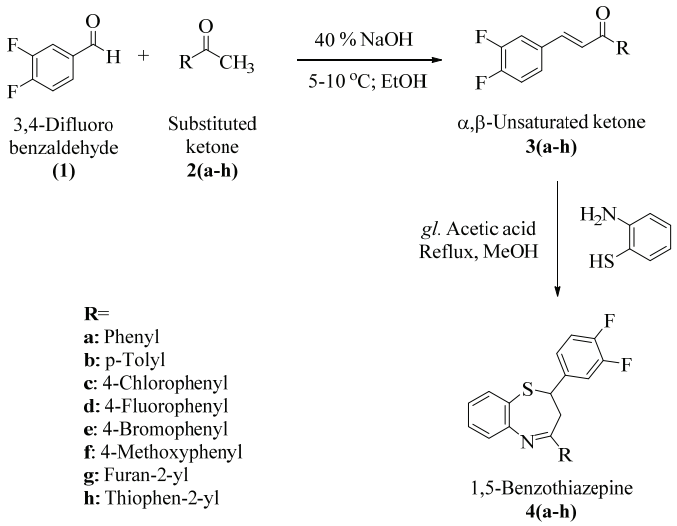

Scheme 1. Synthetic pathway of fluorinated 1,5-benzothiazepine derivatives.

(CC) 2022 SCS.

Biology

In vitro *anticancer activity*. The sulforhodamine B (SRB) assay was used to test the anticancer activity of the synthesized derivatives against four human cancer cell lines namely lung (A549), breast (MCF-7), liver (HEPG2) and prostate (PC-3) cancer.[27] The cell lines were grown in RPMI 1640 medium for 24 h before being inoculated into 96-well plates and incubated at 37 °C. After that, the cells were fixed with 10 % trichloroacetic acid (TCA) and tested with drugs at four dose levels (10, 20, 40, and 80 μg ml^{-1}) with doxorubicin serving as a control. After adding the compounds, the plates were incubated for 48 h until the assay was terminated with the addition of cold TCA. TCA (30 %) was used to fix the cells, which were then incubated at 4 °C for 1 h before being stained with SRB solution for 20 min. Further, the excess dye was discarded by washing with 1 % acetic acid and air dried. The protein-bound dye was then eluted with a 10mM Tris base, and the absorbance was measured at 540 nm using a plate reader. Growth was calculated and expressed as the ratio of average absorbance of the test well (T_i) to the average absorbance of the control wells (C):

$$\text{Growth inhibition} = 100(T_i/C) \quad (1)$$

where C = control growth and T_i = test growth in the presence of drug at the four concentration levels. The experiment was done in triplicate and the average values were plotted as control growth versus drug concentrations.

Antibacterial assay

The antimicrobial activity of synthesized compounds was investigated using the resazurin microtiter assay (REMA) in aseptic conditions using a 96 well microtitre plate as described previously.[28] 50 μl solution of test material dissolved in 2 % DMSO was added after filling all the wells of the microtiter plate with 50 μl of nutrient broth. Two-fold serial dilution was achieved by transferring 50 μl test material from the top well of the first row to the following wells in the next row of the same column and resulted in a graded sequence of concentrations (500, 250, 125, 62.5, 31.25, 15.63, 7.81 and 3.90 μg ml^{-1}). After that, 50 μl of bacterial suspension were added to each well, resulting in a final concentration of 0.5 Mcfarland standard cfu ml^{-1}. Later, all plates containing test materials were incubated for 24 h at 37 °C. After 24 h, each well was given 0.2 % resazurin, and a visual change in colour was observed in the wells. The transition from purple to pink/colorless was taken as a positive. The *MIC* value for that particular sample was recorded, as the lowest concentration in the column containing the sample at which no color shift occurred, and compared to the standard drug ampicillin.

RESULTS AND DISCUSSION

Chemistry

Synthesis of fluorinated 1,5-benzothiazepines **4a**–**h** followed the path shown in Scheme 1. The compounds were synthesized by reaction of *α*,*β*-unsaturated ketone with 2-aminothiophenol in presence of catalytic amount of glacial acetic acid. The synthesized novel compounds **4a**–**h** were verified by various techniques like IR, NMR (^{1}H and ^{13}C), MS and elemental analyses (CHN).

FTIR spectra of the synthesized compounds **4a**–**h** showed appearance of C–H in the range of 2844–3105 cm^{-1}, a characteristic band in the range of 1595––1608 cm^{-1} confirms presence of C=N bond in the synthesized compound, also presence of band in range of 1311–1322 cm^{-1} indicates presence of C–N.

(CC) 2022 SCS.

Presence of band in the range of 681–688 cm^{-1} indicates formation of C–S–C bond. ^{1}H-NMR spectra of synthesized compounds shows presence of three characteristics peaks apart from aromatic protons (δ 8.12–6.50 ppm). The three peaks in the aliphatic region are due to CH_2 and CH. Two protons of CH_2 are diastereotopic in nature (H_a and H_b), H_a shows triplet at δ 2.88–2.99 ppm with J_{ab} value 12.4–12.7 Hz and the other H_b along with C<u>H</u> (H_x) shows doublet of doublet at δ 3.19–3.28 ppm with J_{bx} in range12.9–13.0 Hz; J_{ab} in range 4.8–5.1 Hz and δ 4.88–4.99 ppm with J_{ax} in range 11.8–12.5 Hz; J_{ab} in range 4.6–5.1 Hz, respectively, due to abx system. The ^{13}C-NMR showed characteristics peak at δ 37–38 ppm denoting <u>C</u>H and at δ = 59 ppm confirming presence of <u>C</u>H_2. Hence, the interpreted data obtained from the spectra corroborated with the structure of synthesized compound. For further verification, ESI-MS was performed, *m*/*z* values obtained were in good agreement with measured mass. Further elemental analysis confirmed the purity of the synthesized compounds as the experimental composition was found to be similar with the theoretical composition.

Biology

In vitro *anticancer activity*. The *in vitro* anticancer activity of the synthesized compounds **4a**–**h** was assessed using sulforhodamine B (SRB) assay with adriamycin as standard drug. The results were described in terms of GI_{50} (concentration that reduces total cell growth by 50 values) and are delineated in Table I. The results concluded that among the synthesized compounds, compound **4c**, **4d**, **4g** and **4h** exhibited good activity with $GI_{50} < 10$ μg ml^{-1} against all four cell lines, while rest of the compounds exhibited moderate to poor activity with $GI_{50} > 10$ μg ml^{-1}.

TABLE I. *In vitro* anticancer activity (GI_{50} / μg ml^{-1}); GI_{50} = concentration of drug causing 50 % inhibition of cell grow. For pure compounds, GI_{50} value ≤ 10 μg ml^{-1} is considered to demonstrate activity

Compound	Cell line			
	A549	MCF-7	HEP G2	PC-3
4a	68.2	68.6	57.6	>80
4b	27.8	48.2	32.6	28.1
4c	<10	<10	<10	<10
4d	<10	<10	<10	<10
4e	22.1	<10	16.9	<10
4f	32.3	35.1	33.4	11.6
4g	<10	<10	<10	<10
4h	<10	<10	<10	<10
Adriamycin	<10	<10	<10	<10

From the structure activity relationship, the activity of heterocyclic and halogenated compounds was outstanding when compared to other substituents. The

(CC) 2022 SCS.

compounds were found to be in the order: –F group > –Cl group > –Br group > > –OMe group > –Me group > –H denoting that the compounds having electronegative groups showed excellent activity.

Antibacterial assay. The antibacterial activity of the synthesized compounds **4a**–**h** were evaluated against two Gram-positive (*Staphylococcus aureus* and *Bacillus subtilis*) and two Gram-negative (*Escherichia coli* and *Salmonella typhi*) bacteria using REMA. Ampicillin was taken as positive control. The antibacterial potential of the synthesized compounds were assessed by minimum inhibitory concentration (*MIC*) values and are displayed in Table II. Result obtained indicates that all the synthesized compounds are potent antibacterial agents. Among which, compound **4c**, **4d**, **4g** and **4h** exhibited excellent activity w.r.t the standard (ampicillin) against all the bacterial strains inferring that hetero and halogenated substances show excellent results. The results outlined suggested that the synthesized compounds are more active towards Gram-negative strain than Gram-positive strain.

TABLE II. *In vitro* bacterial activity using REMA method (*MIC* / μg ml^{-1})

Compound	Strain			
	Gram-positive		Gram-negative	
	S. aureus	*B. subtilis*	*E. coli*	*S. typhi*
4a	62.5	62.5	62.5	62.5
4b	62.5	125	62.5	62.5
4c	31.25	31.25	15.625	31.25
4d	15.625	15.625	15.625	15.625
4e	62.5	125	62.5	62.5
4f	62.5	125	62.5	62.5
4g	15.625	31.25	15.625	15.625
4h	15.625	15.625	31.25	15.625
Ampicillin	31.25	31.25	15.625	31.25

CONCLUSION

To conclude, we synthesized series of fluorinated 1,5-benzothiazepine derivatives **4a**–**h**. The synthesized compounds were evaluated for *in vitro* anticancer and antibacterial activity. The *in vitro* anticancer activity was performed using four human cancer cell lines namely A549, MCF-7, HEPG2 and PC-3. Compounds **4c**, **4d**, **4g** and **4h** exhibited excellent activity with GI_{50} <10 μg ml^{-1} against all four cell lines which is comparable to standard drug adriamycin. Further, the synthesized compounds were subjected to antibacterial activity using resazurin microtiter assay (REMA) with ampicillin as standard drug. The compounds **4c**, **4d**, **4g** and **4h** exhibited elegant antibacterial activity and the synthesized compounds were found to be more active towards Gram-negative than

(CC) 2022 SCS.

Gram-positive bacteria. Hence, the synthesized fluorinated 1,5-benzothiazepine derivatives have potential to be an anticancer as well as antibacterial agents.

SUPPLEMENTARY MATERIAL

Additional data and information are available electronically at the pages of journal website: https://www.shd-pub.org.rs/index.php/JSCS/article/view/10712, or from the corresponding author on request.

Acknowledgements. We are thankful to Microanalytical Laboratory, University of Mumbai, for providing characterization facilities. We are also thankful to Advanced Centre for Treatment Research and Education in Cancer (ACTREC) Anti-Cancer Drug Screening Facility (ACDSF), Kharghar, Navi Mumbai, for providing anticancer activity.

ИЗВОД

СИНТЕЗА НОВИХ ФЛУОРИСАНИХ ДЕРИВАТА 1,5-БЕНЗОТИАЗЕПИНА И ЊИХОВА БИОЛОШКА ПРОЦЕНА КАО АНТИКАНЦЕРОГЕНИХ И АНТИБАКТЕРИЈСКИХ СРЕДСТАВА

SONAL R. BHABAL, SARFARAZ F. SHAIKH, ISHITA P. YELLAPURKAR, GANESH S. PAVALE и MUCHELI M. V. RAMANA

Department of Chemistry, University of Mumbai, Santacruz (E), Mumbai 400 098, India

Синтетисана је серија флуорованих деривата 1,5-бензотиазепина, једињења су окарактерисана и испитана је њихова *in vitro* антиканцерска и антибактеријска активност. *In vitro* антиканцерска активност једињења **4a**–**h** испитана је према ћелијским линијама хуманог канцера плућа (A549), груди (MCF-7), јетре (HEPG2) и простате (PC-3). Једињења **4c**, **4d**, **4g** и **4h** имају добру активност, која износи GI_{50} < 10 μg ml^{-1} према свим испитиваним ћелијским линијама, и блиска је активности стандардног лека адриамицина. Такође, антибактеријска активност једињења је испитана употребом ресазурин микротитар есеја (resazurin microtiter assay, REMA) и добијене вредности су упоређене са активношћу стандардног лека ампицилина. Од синтетисаних једињења, једињења **4c**, **4d**, **4g** и **4h** показују добру антибактеријску активност и утврђено је да су сва синтетисана једињења активнија према грам-негативним него према грам-позитивним бактеријама. Резултати добијени из *in vitro* антиканцерске и антибактеријске активности су охрабрујући и указују да би синтетисана једињења могла да буду добри антиканцерски и антибактеријски агенси.

(Примљено 28. априла 2021, ревидирано 28. априла, прихваћено 10. маја 2022)

REFERENCES

1. H. Sung, J. Ferlay, R. L. Siegel, M. Laversanne, I. Soerjomataram, A. Jemal, F. Bray, *CA. Cancer J. Clin.* (2021) 1 (https://doi.org/10.3322/caac.21660)
2. A. Kamal, D. Dastagiri, M. Janaki Ramaiah, J. Surendranadha Reddy, E. Vijaya Bharathi, M. Kashi Reddy, M. Victor Prem Sagar, T. Lakshminarayan Reddy, S. N. C. V. L. Pushpavalli, M. Pal-Bhadra, *Eur. J. Med. Chem.* **46** (2011) 5817 (https://doi.org/10.1016/j.ejmech.2011.09.039)
3. B. Mansoori, A. Mohammadi, S. Davudian, S. Shirjang, B. Baradaran, *Adv. Pharm. Bull.* **7** (2017) 339 (https://doi.org/10.15171/apb.2017.041)
4. S. Bhat, S. Muthunatarajan, S. S. Mulki, K. Archana Bhat, K. H. Kotian, *Int. J. Microbiol.* **2021** (2021) (https://doi.org/10.1155/2021/8883700)

(CC) 2022 SCS.

5. R. J. Fair, Y. Tor, *Perspect. Medicin. Chem.* (2014) 25 (https://doi.org/10.4137/PMC.S14459)
6. S. G. Jagadhani, S. G. Kundlikar, B. K. Karale, *Orient. J. Chem.* **31** (2015) 601 (https://doi.org/10.13005/ojc/310177)
7. F. L. Ansari, S. Umbreen, L. Hussain, T. Makhmoor, S. A. Nawaz, M. A. Lodhi, S. N. Khan, F. Shaheen, M. I. Choudhary, Atta-ur-Rahman, *Chem. Biodivers.* **2** (2005) 487 (https://doi.org/10.1002/cbdv.200590029)
8. A. B. Shaik, P. R. Yejella, S. Nissankararao, S. Shahanaaz, *Anticancer. Agents Med. Chem.* **20** (2020) 1115 (https://doi.org/10.2174/1871520620666200130091142)
9. K. L. Ameta, N. S. Rathore, B. Kumar, *J. Serb. Chem. Soc.* **77** (2012) 725 (https://doi.org/10.2298/JSC110715219A)
10. A. Sharma, G. Singh, A. Yadav, L. Prakash, *Molecules* **2** (1997) 129 (https://doi.org/10.3390/20900129)
11. V. R. Vutla, R.P. Yejella, R. Nadendla *Int. J. Pharm. Sci. Res.* **5** (2014) 453 (http://dx.doi.org/10.13040/IJPSR.0975-8232.5(2).453-62)
12. M. Mostofi, G. Mohammadi Ziarani, N. Lashgari, *Bioorganic Med. Chem.* **26** (2018) 3076 (https://doi.org/10.1016/j.bmc.2018.02.049)
13. G. Singh, N. Kumar, A. K. Yadav, A. K. Mishra, *Heteroat. Chem.* **13** (2002) 620 (https://doi.org/10.1002/hc.10051)
14. B. V. Kendre, M. G. Landge, S. R. Bhusare, *Arab. J. Chem.* **12** (2019) 2091 (https://doi.org/10.1016/j.arabjc.2015.01.007)
15. G. De Sarro, A. Chimirri, A. De Sarro, R. Gitto, S. Grasso, M. Zappalà, *Eur. J. Med. Chem.* **30** (1995) 925 (https://doi.org/10.1016/0223-5234(96)88311-5)
16. R. Di Santo, R. Costi, *Farmaco* **60** (2005) 385 (https://doi.org/10.1016/j.farmac.2005.03.006)
17. G. Grandolini, L. Perioli, V. Ambrogi, *Eur. J. Med. Chem.* **34** (1999) 701 (https://doi.org/10.1016/S0223-5234(99)00223-8)
18. S. A. Nawaz, S. Umbreen, A. Kahlid, F. L. Ansari, M. I. Choudhary, *J. Enzyme Inhib. Med. Chem.* **23** (2008) 206–212 (https://doi.org/10.1080/14756360701533080)
19. F. L. Ansari, F. Iftikhar, Ihsan-ul-Haq, B. Mirza, M. Baseer, U. Rashid, *Bioorg. Med. Chem.* **16** (2008) 7691 (https://doi.org/10.1016/j.bmc.2008.07.009)
20. D. M. Lokeshwari, N. D. Rekha, B. Srinivasan, H. K. Vivek, A. K Kariyappa, *Bioorg. Med. Chem. Lett.* **27** (2017) 3048 (https://doi.org/10.1016/j.bmcl.2017.05.059)
21. N. C. Desai, H. V. Vaghani, B. Y. Patel, T. J. Karkar, *Ind. J. Pharm. Sci.* **80** (2018) 242 (https://doi.org/10.4172/pharmaceutical-sciences.1000351)
22. H. J. Böhm, D. Banner, S. Bendels, M. Kansy, B. Kuhn, K. Müller, U. Obst-Sander, M. Stahl, *ChemBioChem* **5** (2004) 637 (https://doi.org/10.1002/cbic.200301023)
23. P. M. M. C. Rao, S. A. Rahaman, P. R. Yejella, *Asian J. Pharm. Anal. Med. Chem.* **4** (2016) 175
24. M. Upreti, S. Pant, A. Dandia, U. C. Pant, *Phosphorus Sulfur Silicon Relat. Elem.* **113** (1996) 165 (https://doi.org/10.1080/10426509608046387)
25. A. Dandia, M. Sati, A. Loupy, *Green Chem.* **4** (2002) 599 (https://doi.org/10.1039/b207004a)
26. H. Suwito, Jumina, Mustofa, P. Pudjiastuti, M. Z. Fanani, Y. Kimata-Ariga, R. Katahira, T. Kawakami, T. Fujiwara, T. Hase, H. M. Sirat, N. N. T. Puspaningsih, *Molecules* **19** (2014) 21473 (https://doi.org/10.3390/molecules191221473)
27. V. Vichai, K. Kirtikara, *Nat. Protoc.* **1** (2006) 1112 (https://doi.org/10.1038/nprot.2006.179)
28. S. F. Shaikh, P. P. Dhavan, P. R. Singh, S. P. Vaidya, B. L. Jadhav, M. M. V. Ramana *Russ. J. Bioorg. Chem.* **47** (2021) 571 (https://doi.org/10.1134/S1068162021020242).

(CC) 2022 SCS.

Journal of the Serbian Chemical Society
JSCS@tmf.bg.ac.rs • www.shd.org.rs/JSCS
J. Serb. Chem. Soc. 87 (10) S331–S353 (2022) *Supplementary material*

SUPPLEMENTARY MATERIAL TO

Synthesis of novel fluorinated 1,5-benzothiazepine derivatives and their biological evaluation as anticancer and antibacterial agents

SONAL R. BHABAL, SARFARAZ F. SHAIKH, ISHITA P. YELLAPURKAR, GANESH S. PAVALE and MUCHELI M. V. RAMANA*

Department of Chemistry, University of Mumbai, Santacruz (E), Mumbai 400 098, India

J. Serb. Chem. Soc. 87 (10) (2022) 1109–1116

SPECTROSCOPIC DATA

*2-(3,4-difluorophenyl)-4-phenyl-2,3-dihydrobenzo[*b*][1,4]thiazepine (**4a**)*

Yellow solid, Yield: 91 %, M.P. = 145-147 °C, IR (υ_{max}/cm^{-1}): 2918 (C-H), 1605 (C=N), 1322 (C-N), 685 (C-S-C). ^{1}H NMR (300 MHz, $CDCl_3$) δ = 8.04 (dd, *J*= 7.6, 1.7 Hz, 2H, Ar-H), 7.60 (dd, *J*= 7.7, 0.9 Hz, 1H, Ar-H), 7.49 (dt, *J*= 8.7, 4.3 Hz, 4H, Ar-H), 7.31 (dd, *J*= 7.9, 1.0 Hz, 1H, Ar-H), 7.21- 6.97 (m, 4H, Ar-H), 4.92 (dd, J_{ax}= 12.5, J_{ab}= 4.7 Hz, 1H, CH), 3.28 (dd, J_{bx}= 12.9, J_{ab}= 4.8 Hz, 1H, CH_2), 2.97 (t, J_{ab}= 12.7 Hz, 1H, CH_2). ^{13}C NMR (75 MHz, $CDCl_3$) δ = 168.51, 152.39, 150.23 (dd, $^1J_{FC}$= 249.2, 12.8 Hz), 149.74 (dd, $^1J_{FC}$= 248.8, 12.5 Hz), 141.77- 139.95 (m), 137.49, 134.99, 131.25, 130.08, 128.83, 127.37, 125.48, 122.08 (t, *J* = 4.9 Hz), 117.43 (d, $^2J_{FC}$= 17.4 Hz), 115.25 (d, $^2J_{FC}$= 17.8 Hz), 59.28 (CH), 37.52 (CH_2). MS (ESI) *m/z*: 352.5 $(M+1)^+$. Elemental analysis for $C_{21}H_{15}F_2NS$: C, 71.78; H, 4.30; N, 3.99; S, 9.12; found: C, 71.65; H, 4.28; N, 3.82; S, 9.09.

*2-(3,4-difluorophenyl)-4-(p-tolyl)-2,3-dihydrobenzo[*b*][1,4]thiazepine (**4b**)*

Yellow solid, Yield: 93 %, M.P.= 157-159 °C, IR (υ_{max}/cm^{-1}): 2901 (C-H), 1604 (C=N),1319 (C-N), 684 (C-S-C). ^{1}H NMR (300 MHz, $CDCl_3$) δ = 7.93 (d, J= 8.1 Hz, 2H, Ar-H), 7.58 (d, *J*= 7.6 Hz, 1H, Ar-H), 7.47 (t, *J*= 7.6 Hz, 1H, Ar-H), 7.29 (d, *J*= 8.0 Hz, 3H, Ar-H), 7.08 (ddd, *J*= 14.7, 11.3, 6.0 Hz, 4H, Ar-H), 4.89 (dd, J_{ax}= 12.5, J_{ab}= 4.7 Hz, 1H, CH), 3.26 (dd, J_{bx}= 12.9, J_{ab}= 4.8 Hz, 1H, CH_2), 2.95 (t, J_{ab}= 12.7 Hz, 1H, CH_2), 2.43 (s, 3H, CH_3). ^{13}C NMR (75 MHz, $CDCl_3$) δ = 168.33, 152.52, 150.22 (dd, $^1J_{FC}$= 249.0, 12.8 Hz), 149.72 (dd, $^1J_{FC}$= 248.8, 12.6 Hz), 141.74, 141.12, 134.96, 134.74, 130.04, 129.55, 127.37, 125.38 (d, $^3J_{FC}$= 9.7 Hz), 122.07 (t, *J*= 4.8 Hz), 117.40 (d, $^2J_{FC}$=17.5 Hz), 115.24 (d, $^2J_{FC}$=17.7 Hz), 59.24 (CH), 37.42 (CH_2), 21.47 (CH_3). MS (ESI) *m/z*: 366.5 $(M+1)^+$. Elemental analysis for $C_{22}H_{17}F_2NS$: C, 72.31; H, 4.69; N, 3.83; S, 8.77; found: C, 72.20; H, 4.54; N, 3.63; S, 8.68.

*4-(4-chlorophenyl)-2-(3,4-difluorophenyl)-2,3-dihydrobenzo[*b*][1,4]thiazepine (**4c**)*

Yellow solid, Yield: 90 %, M.P. = 149-151 °C, IR (υ_{max}/cm^{-1}): 2902 (C-H), 1605 (C=N), 1321 (C-N), 685 (C-S-C). ^{1}H NMR (300 MHz, $CDCl_3$) δ = 7.96 (d, *J*= 8.7 Hz, 2H, Ar-H),

* Corresponding author. E-mail: mmvramana@yahoo.co.in

Available on line at www.shd.org.rs/JSCS/
(CC) 2022 SCS.

7.59 (dd, *J*= 7.7, 1.2 Hz, 1H, Ar-H), 7.53-7.40 (m, 3H, Ar-H), 7.29 (dd, *J*= 7.9, 1.2 Hz, 1H, Ar-H), 7.22- 6.93 (m, 4H, Ar-H), 4.89 (dd, J_{ax}= 12.4, J_{ab}= 4.8 Hz, 1H, CH), 3.22 (dd, J_{bx}= 13.0, J_{ab}= 4.9 Hz, 1H, CH_2), 2.96 (t, J_{ab}= 12.7 Hz, 1H, CH_2). ^{13}C NMR (75 MHz, $CDCl_3$) δ = 167.26, 152.16, 150.23 (dd, $^1J_{FC}$= 249.0, 12.8 Hz), 149.77 (dd, $^1J_{FC}$=248.9, 12.7 Hz), 141.30-140.18 (m), 137.48, 135.90, 135.03, 130.15, 129.03, 128.69, 125.57 (d, J= 16.1 Hz), 122.07 (dd, *J*= 6.0, 3.2 Hz), 117.48 (d, $^2J_{FC}$= 17.4 Hz), 115.23 (d, $^2J_{FC}$= 17.8 Hz), 59.27 (CH), 37.36 (CH_2). MS (ESI) *m/z*: 385.7 $(M)^+$. Elemental analysis for $C_{21}H_{14}ClF_2NS$: C, 65.37; H, 3.66; N, 3.63; S, 8.31; found: C, 65.29; H, 3.58; N, 3.50; S, 8.23.

*2-(3,4-difluorophenyl)-4-(4-fluorophenyl)-2,3-dihydrobenzo[*b*][1,4]thiazepine (**4d**)*

Yellow solid, Yield: 89 %, M.P. = 143-145 °C, IR (υ_{max}/cm^{-1}): 2905 (C-H), 1601 (C=N), 1311 (C-N), 683 (C-S-C). ^{1}H NMR (300 MHz, $CDCl_3$) δ = 8.12- 7.92 (m, 2H, Ar-H), 7.59 (d, *J*= 7.6 Hz, 1H, Ar-H), 7.48 (dd, *J*= 11.0, 4.3 Hz, 1H, Ar-H), 7.29 (d, *J*= 7.8 Hz, 1H, Ar-H), 7.22- 6.88 (m, 6H, Ar-H), 4.89 (dd, J_{ax}= 12.4, J_{ab}= 4.8 Hz, 1H, CH), 3.23 (dd, J_{bx}= 13.0, J_{ab}= 4.8 Hz, 1H, CH_2), 2.96 (t, J_{ab}= 12.7 Hz, 1H, CH_2). ^{13}C NMR (75 MHz, $CDCl_3$) δ = 167.21, 164.76 (d, $^1J_{FC}$= 252.3 Hz), 152.25, 150.23 (dd, $^1J_{FC}$= 249.3, 12.8 Hz), 149.76 (dd, $^1J_{FC}$= 248.9, 12.7 Hz), 141.87- 139.82 (m), 135.01, 133.71 (d, *J*= 3.1 Hz), 130.14, 129.55 (d, $^3J_{FC}$= 8.7 Hz), 125.50 (d,$^3J_{FC}$=8.6 Hz), 122.08 (dd, *J*= 7.2, 4.5 Hz), 117.46 (d, $^2J_{FC}$=17.3 Hz), 115.84 (d, *J*= 21.8 Hz), 115.25 (d, $^2J_{FC}$= 17.8 Hz), 59.21 (CH), 37.42 (CH_2). MS (ESI) *m/z*: 370.4 (M+1) $^+$. Elemental analysis for $C_{21}H_{14}F_3NS$: C, 68.28; H, 3.82; N, 3.79; S, 8.68; found: C, 68.20; H, 3.75; N, 3.70; S, 8.52.

*4-(4-bromophenyl)-2-(3,4-difluorophenyl)-2,3-dihydrobenzo[*b*][1,4]thiazepine (**4e**)*

Yellow solid, Yield: 90 %, M.P. = 164-166 °C, IR (υ_{max}/cm^{-1}): 2901 (C-H), 1604 (C=N),1320 (C-N), 684 (C-S-C). ^{1}H NMR (300 MHz, $CDCl_3$) δ = 7.89 (d, *J*= 8.3 Hz, 2H, Ar-H), 7.66-7.54 (m, 3H, Ar-H), 7.48 (t, *J*= 7.6 Hz, 1H, Ar-H), 7.29 (d, *J*= 7.8 Hz, 1H, Ar-H), 7.21-6.91 (m, 4H, Ar-H), 4.88 (dd, J_{ax}= 12.4, J_{ab}= 4.6 Hz, 1H, CH), 3.21 (dd, J_{bx}= 13.0, J_{ab}= 4.8 Hz, 1H, CH_2), 2.95 (t, J_{ab}= 12.7 Hz, 1H, CH_2). ^{13}C NMR (75 MHz, $CDCl_3$) δ = 167.27, 152.24, 150.28 (dd, $^1J_{FC}$= 248.9, 12.6 Hz), 149.82 (dd, $^1J_{FC}$= 248.5, 12.7 Hz), 140.75, 136.50, 134.97, 131.98, 130.08, 128.88, 125.92, 125.53 (d, $^3J_{FC}$=11.1 Hz), 122.09, 117.44 (d, $^2J_{FC}$= 17.2 Hz), 115.26 (d, $^2J_{FC}$=17.9 Hz), 59.33 (CH), 37.31 (CH_2). MS (ESI) *m/z:* 430.2 $(M+1)^+$. Elemental analysis for $C_{21}H_{14}BrF_2NS$: C, 58.62; H, 3.28; N, 3.26; S, 7.45; found: C, 58.40; H, 3.25; N, 3.08; S, 7.30.

*2-(3,4-*difluorophenyl*)-4-(4-methoxyphenyl)-2,3-dihydro benzo[*b*][1,4]thiazepine (**4f**)*

Yellow solid, Yield: 92 %, M. P.= 137-139 ºC, IR (υ_{max}/cm^{-1}): 2844 (C-H), 1595 (C=N), 1322 (C-N), 684 (C-S-C). ^{1}H NMR (300 MHz, $CDCl_3$) δ = 8.00 (d, *J*= 8.9 Hz, 2H, Ar-H), 7.58 (dd, *J*= 7.7, 1.2 Hz, 1H, Ar-H), 7.47 (td, *J*= 7.8, 1.4 Hz, 1H, Ar-H), 7.29 (dd, *J*= 7.9, 1.2 Hz, 1H, Ar-H), 7.20- 7.06 (m, 3H, Ar-H), 7.06- 6.94 (m, 3H, Ar-H), 4.89 (dd, J_{ax}= 12.4, J_{ab}= 4.7 Hz, 1H, CH), 3.87 (d, *J*= 6.6 Hz, 3H, OCH_3), 3.25 (dd, J_{bx}= 12.9, J_{ab}= 4.8 Hz, 1H, CH_2), 2.95 (t, J_{ab}= 12.7 Hz, 1H, CH_2). ^{13}C NMR (75 MHz, $CDCl_3$) δ = 167.65, 162.22, 152.64, 150.23 (dd, $^1J_{FC}$= 251.1, 10.9 Hz), 149.71 (dd, $^1J_{FC}$= 248.7, 12.7 Hz), 141.15 (d, $^4J_{FC}$= 4.3 Hz), 141.09 (d, $^4J_{FC}$= 4.6 Hz), 134.95, 130.05, 129.13, 125.43, 125.16, 122.12 (d, $^3J_{FC}$= 9.5 Hz), 122.04, 117.41 (d, $^2J_{FC}$= 17.1 Hz), 115.25 (d, $^2J_{FC}$= 17.7 Hz), 114.14, 59.18 (CH), 55.47 (OCH_3), 37.26 (CH_2).MS (ESI) *m/z*: 382.8 (M+1) $^+$. Elemental analysis for $C_{22}H_{17}F_2NOS$: C, 69.27; H, 4.49; N, 3.67; S, 8.40; found: C, 69.15; H, 4.33; N, 3.59; S, 8.37.

(CC) 2022 SCS.

*2-(3,4-difluorophenyl)-4-(furan-2-yl)-2,3-dihydrobenzo[*b*][1,4]thiazepine (**4g**)*

Yellow solid, Yield: 88 %, M.P. = 125-127 °C, IR (υ_{max}/cm^{-1}): 3105 (C-H), 1605 (C=N), 1319 (C-N), 681 (C-S-C). ^{1}H NMR (300 MHz, $CDCl_3$) δ = 7.66-7.57 (m, 2H, Ar-H), 7.54-7.43 (m, 1H, Ar-H), 7.37-7.30 (m, 1H, Ar-H), 7.22- 6.99 (m, 5H, Ar-H), 6.68- 6.50 (m, 1H, Ar-H), 4.96 (dd, J_{ax}= 11.8, J_{ab}= 5.1 Hz, 1H, CH), 3.19 (dd, J_{bx}= 12.9, J_{ab}= 5.1 Hz, 1H, CH_2), 2.88 (t, J_{ab}= 12.4 Hz, 1H, CH_2). ^{13}C NMR (75 MHz, $CDCl_3$) δ = 159.26, 152.45, 150.29 (d, $^1J_{FC}$= 249.2 Hz), 149.71 (dd, $^1J_{FC}$= 248.7, 12.7 Hz), 145.75, 140.80, 135.04, 130.14, 125.74 (d, J= 23.6 Hz), 122.64, 122.20 (dd, J= 6.3, 3.6 Hz), 117.40 (d, $^2J_{FC}$= 17.3 Hz), 115.36 (d, $^2J_{FC}$= 17.9 Hz), 113.93, 112.48, 59.38 (CH), 37.52 (CH_2). MS (ESI) *m/z*: 342.1 $(M+1)^+$. Elemental analysis for $C_{19}H_{13}F_2NOS$: C, 66.85; H, 3.84; N, 4.10; S, 9.39; found: C, 66.82; H, 3.75; N, 4.06; S, 9.25.

*2-(3,4-difluorophenyl)-4-(thiophen-2-yl)-2,3-dihydrobenzo[*b*][1,4]thiazepine (**4h**)*

Yellow solid, Yield: 87 %, M.P. = 149-151 °C, IR (υ_{max}/cm^{-1}): 2917 (C-H), 1599 (C=N),1322 (C-N), 688 (C-S-C). ^{1}H NMR (300 MHz, $CDCl_3$) δ = 7.66-7.53 (m, 2H, Ar-H), 7.53- 7.40 (m, 2H, Ar-H), 7.37-7.27 (m, 1H, Ar-H), 7.24-6.99 (m, 5H, Ar-H), 4.99 (dd, J_{ax}= 11.9, J_{ab}= 5.0 Hz, 1H, CH), 3.23 (dd, J_{bx}= 13.0, J_{ab}= 5.0 Hz, 1H, CH_2), 2.99 (t, J_{ab}= 12.5 Hz, 1H, CH_2). ^{13}C NMR (75 MHz, $CDCl_3$) δ = 163.24, 151.53, 150.12 (d, $^1J_{FC}$= 242.5 Hz), 140.80, 134.96, 131.46, 130.10, 128.83, 127.91, 125.75, 125.57, 122.62, 122.12, 117.45 (d, $^2J_{FC}$= 17.4 Hz), 115.37 (d, $^2J_{FC}$= 17.9 Hz), 59.18 (CH), 38.46 (CH_2). MS (ESI) *m/z*: 359.7 $(M+2)^+$. Elemental analysis for $C_{19}H_{13}F_2NS_2$: C, 63.85; H, 3.67; N, 3.92; S, 17.94; found: C, 63.75; H, 3.56; N, 3.88; S, 17.81.

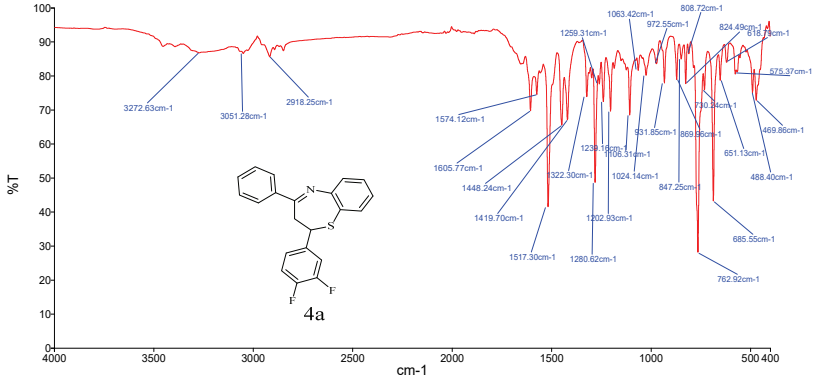

Fig. S-1. FTIR Spectrum of Compound **4a**

(CC) 2022 SCS.

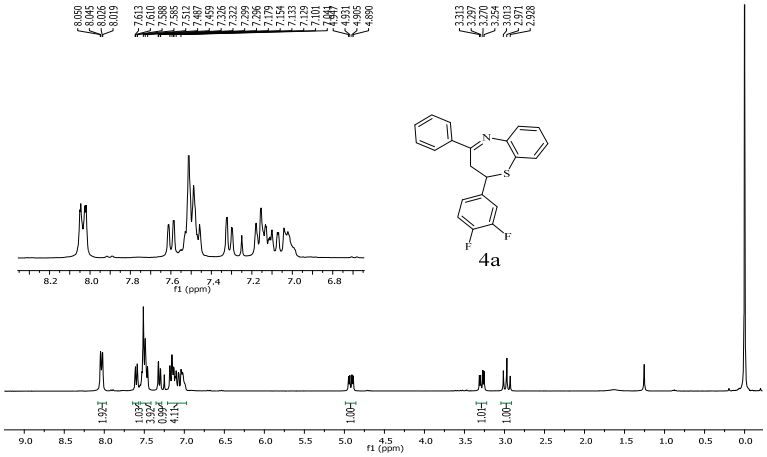

Fig. S-2. ^{1}H-NMR spectrum of compound **4a** (300 MHz, $CDCl_3$)

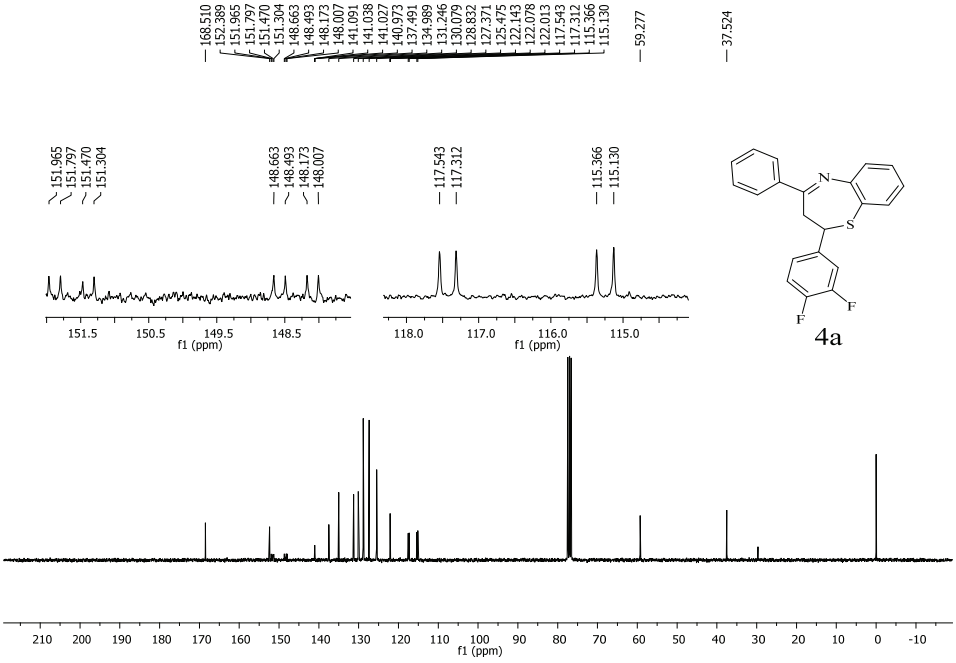

Fig. S-3. ^{13}C-NMR spectrum of compound **4a** (75 MHz, $CDCl_3$)

(CC) 2022 SCS.

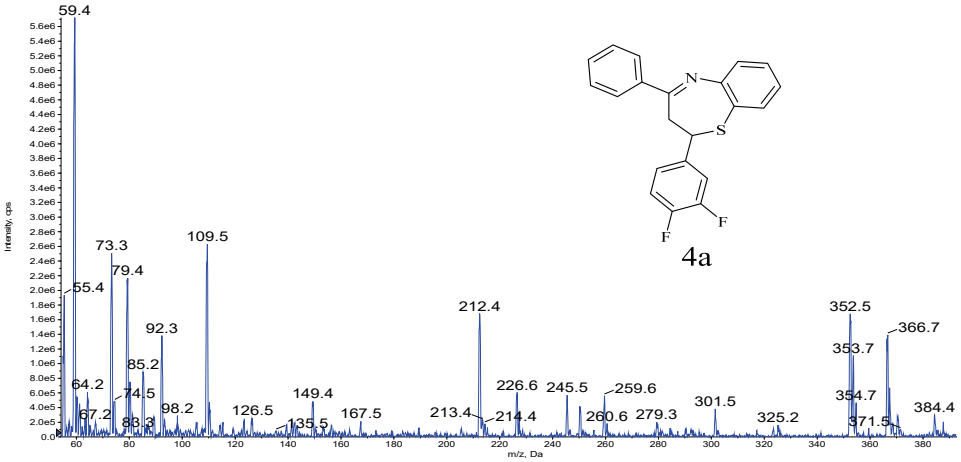

Fig. S-4. Mass spectrum of compound **4a**

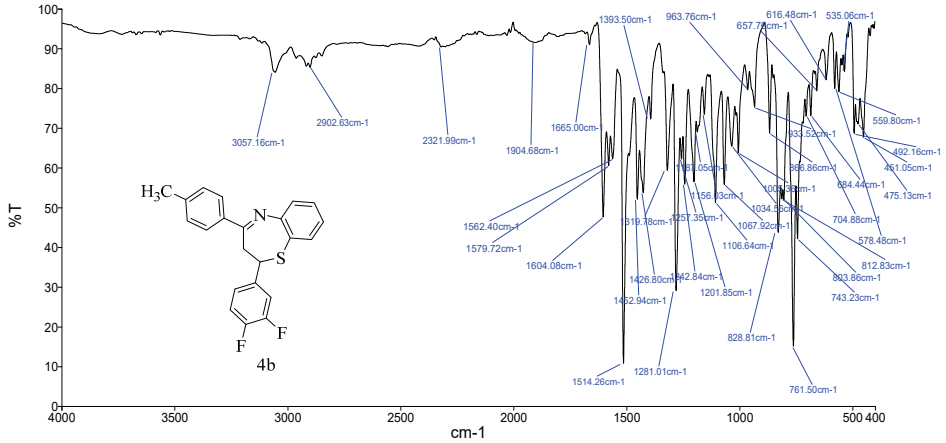

Fig. S-5. FTIR Spectrum of Compound **4b**

(CC) 2022 SCS.

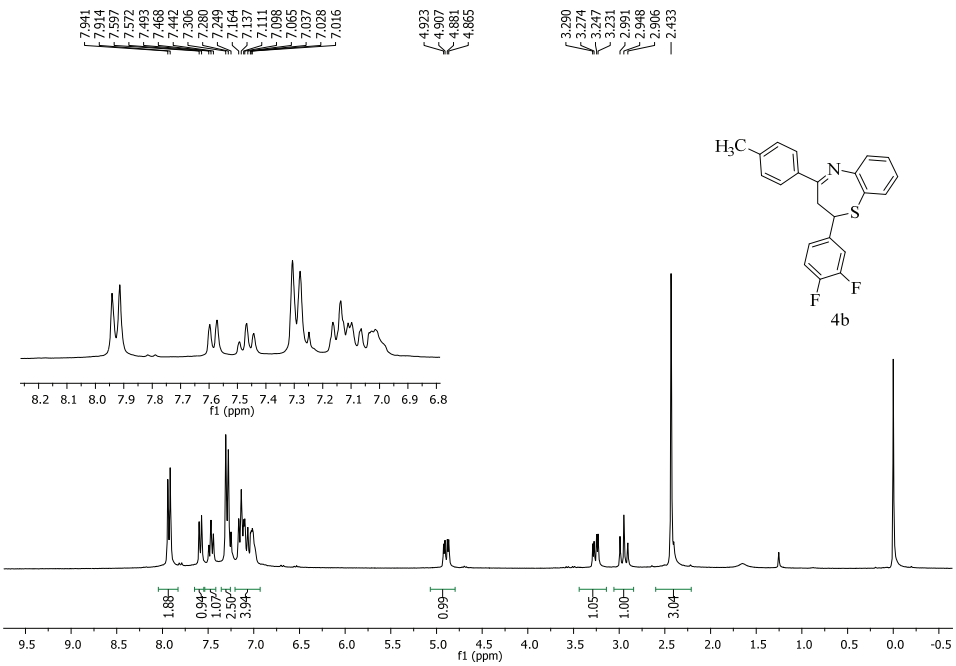

Fig. S-6. ^{1}H-NMR spectrum of compound **4b** (300 MHz, $CDCl_3$)

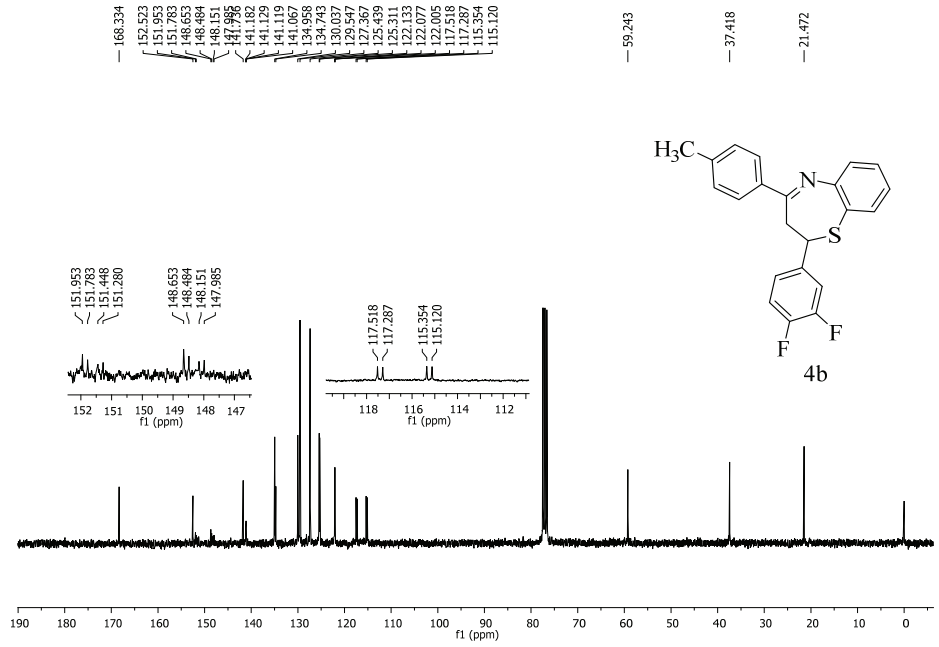

Fig. S-7. ^{13}C-NMR spectrum of compound **4b** (75 MHz, $CDCl_3$)

(CC) 2022 SCS.

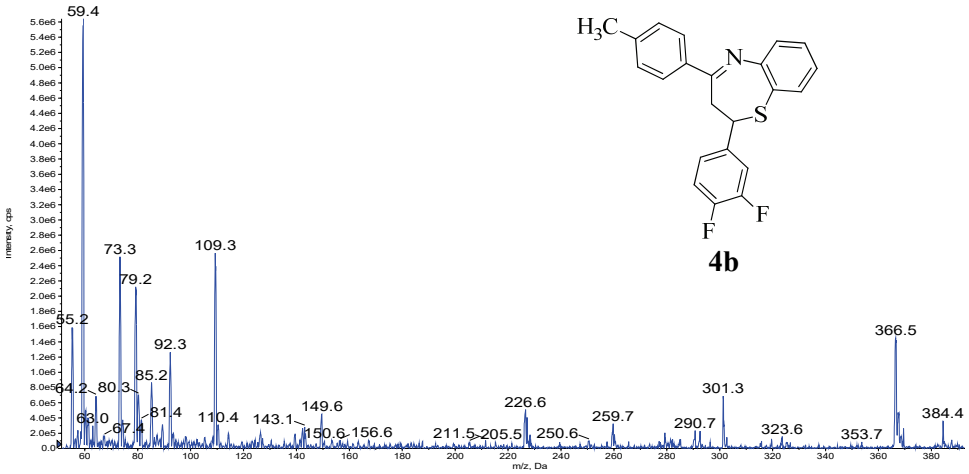

Fig. S-8. Mass spectrum of compound **4b**

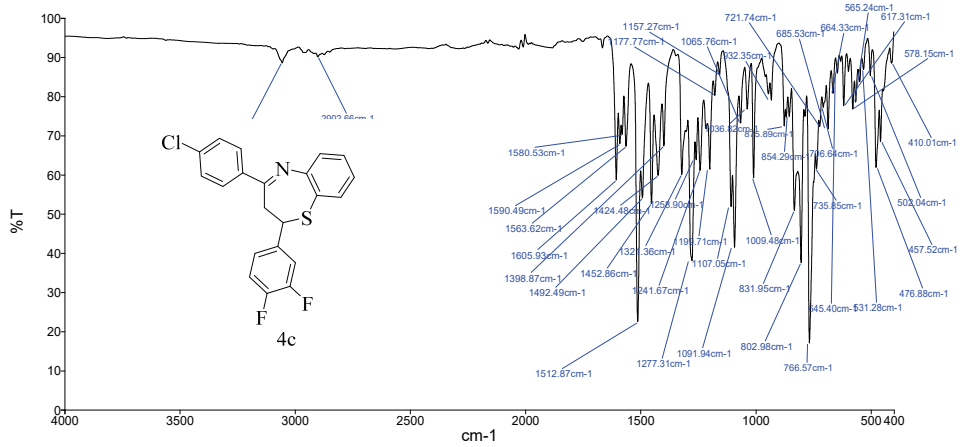

Fig. S-9. FTIR spectrum of compound **4c**

(CC) 2022 SCS.

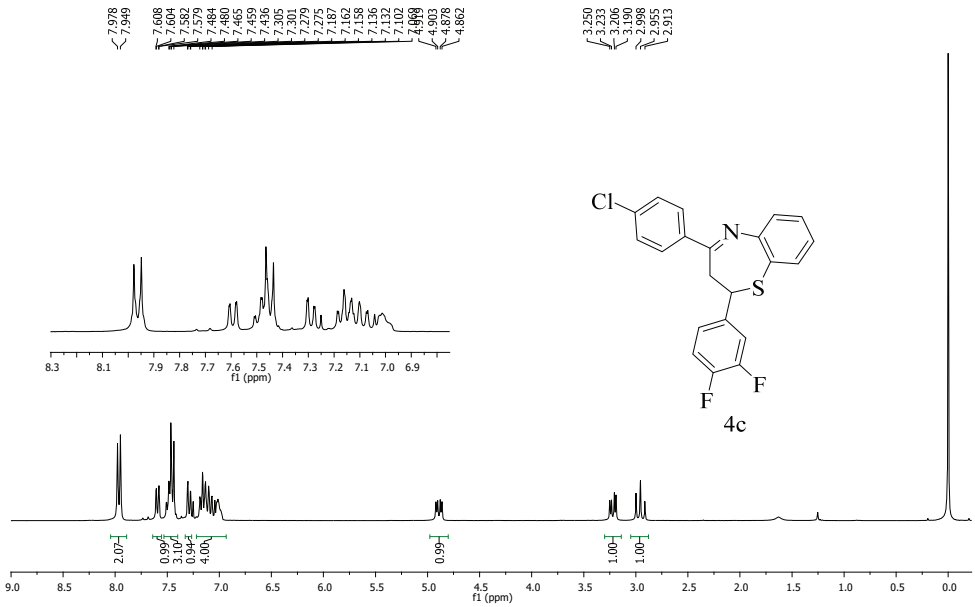

Fig. S-10. ^{1}H-NMR spectrum of compound **4c** (300 MHz, $CDCl_3$)

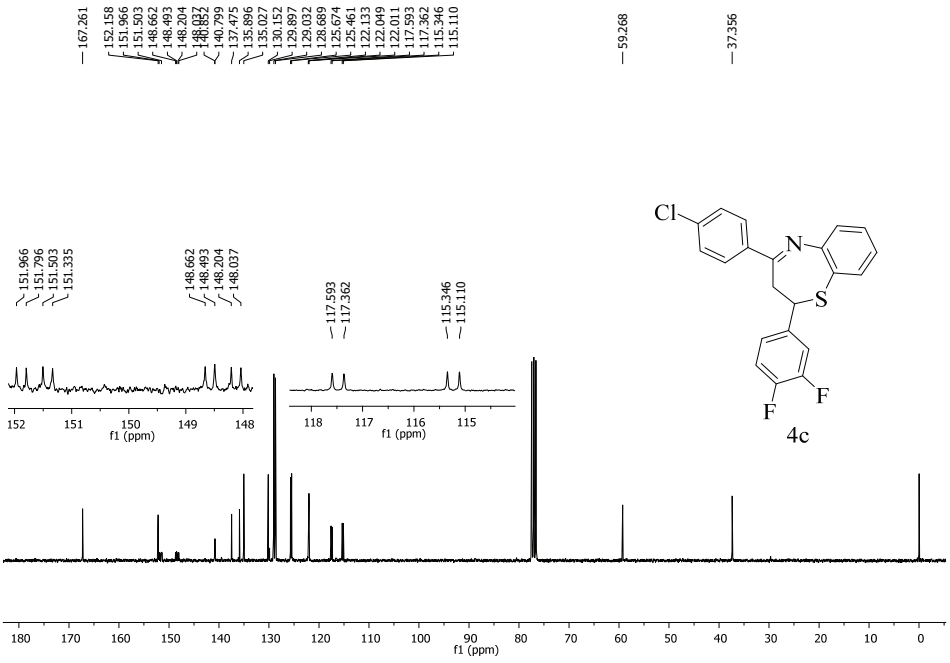

Fig. S-11. ^{13}C-NMR spectrum of compound **4c** (75 MHz, $CDCl_3$)

(CC) 2022 SCS.

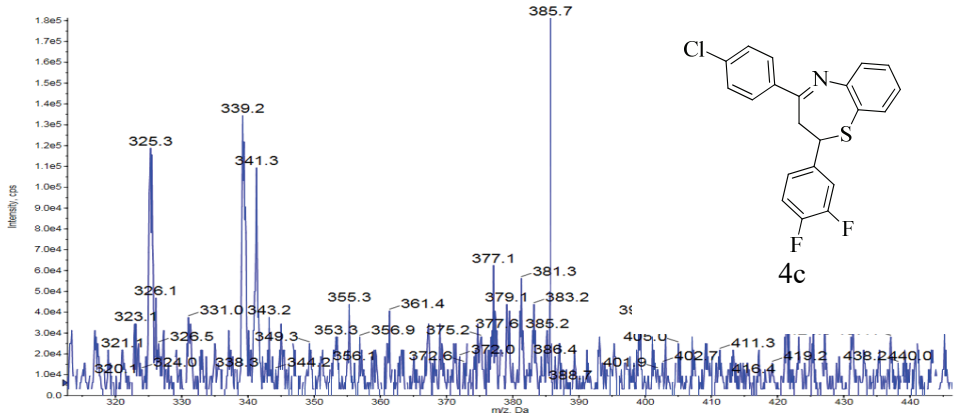

Fig. S-12. Mass spectrum of compound **4c**

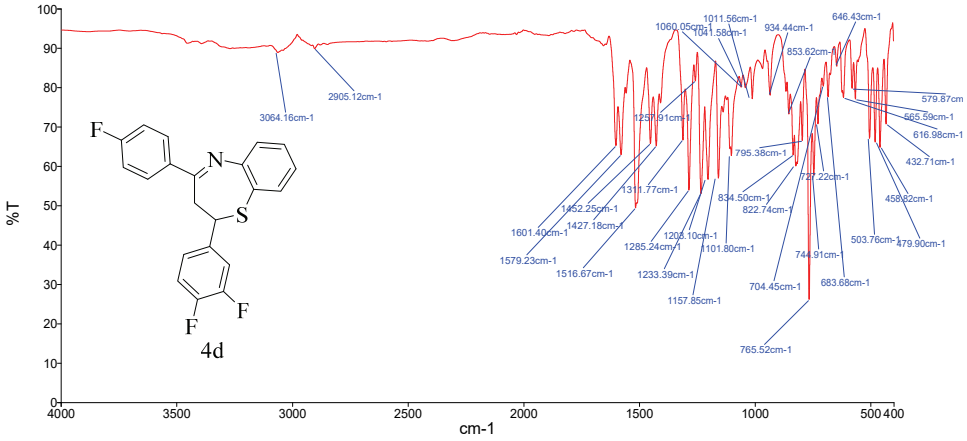

Fig. S-13. FTIR spectrum of Compound **4d**

(CC) 2022 SCS.

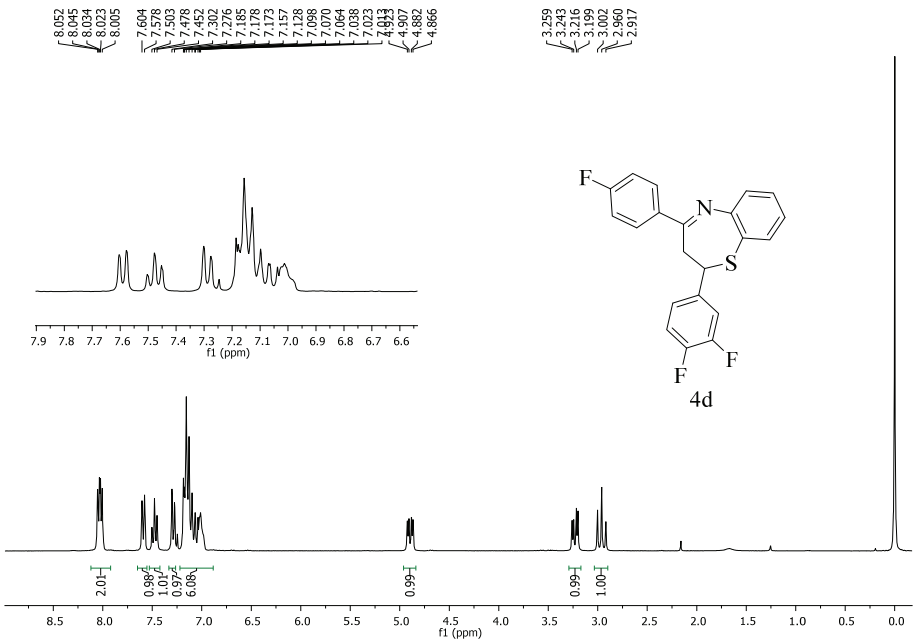

Fig. S-14. ^{1}H-NMR spectrum of compound 4d (300 MHz, $CDCl_3$)

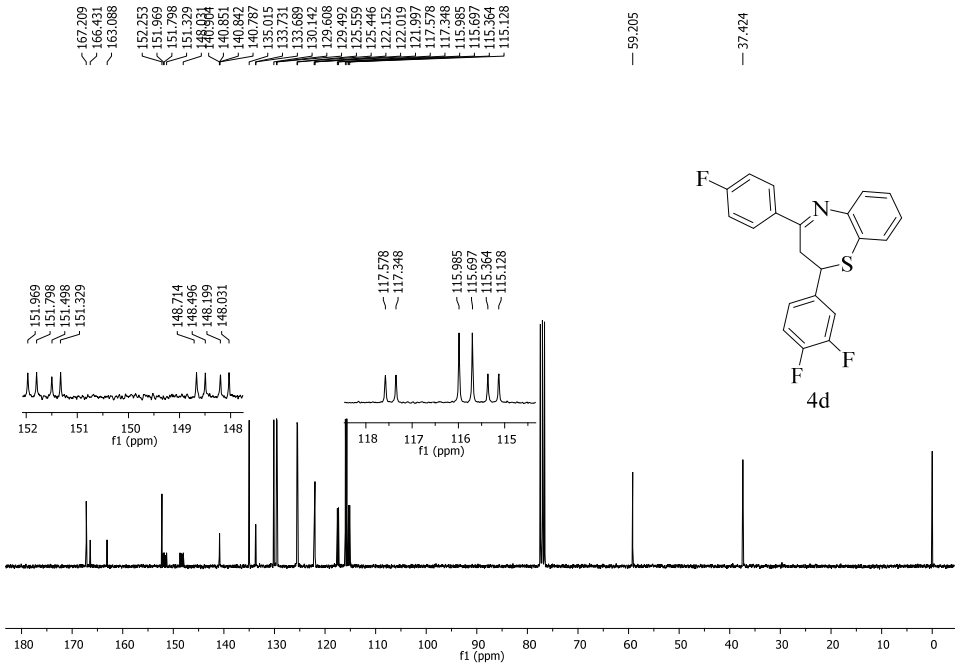

Fig. S-15. ^{13}C-NMR spectrum of compound **4d** (75 MHz, $CDCl_3$)

(CC) 2022 SCS.

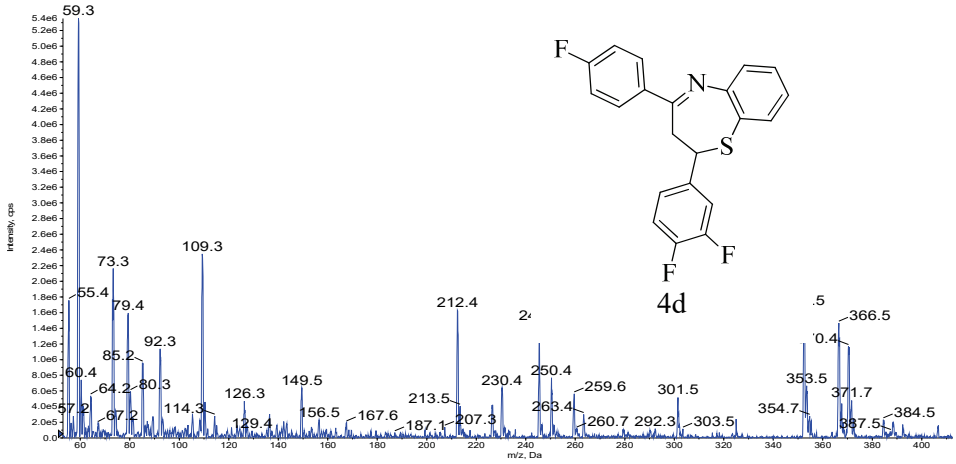

Fig. S-16. Mass spectrum of compound **4d**

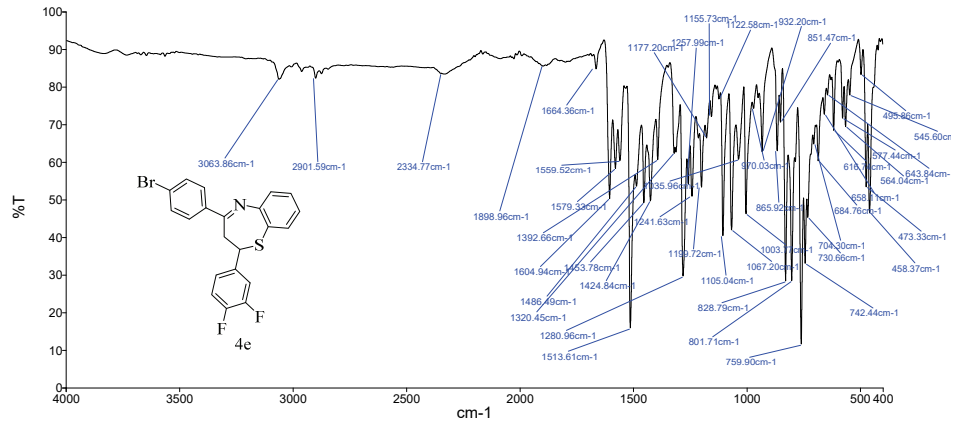

Fig. S-17. FTIR spectrum of compound **4e**

(CC) 2022 SCS.

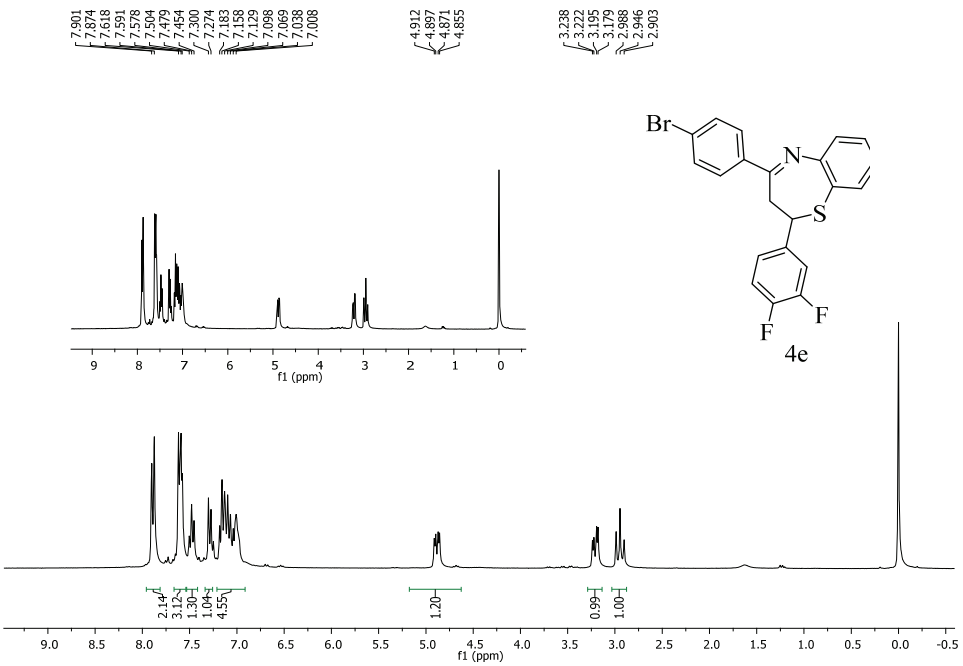

Fig. S-18. ^{1}H-NMR spectrum of compound **4e** (300 MHz, $CDCl_3$)

(CC) 2022 SCS.

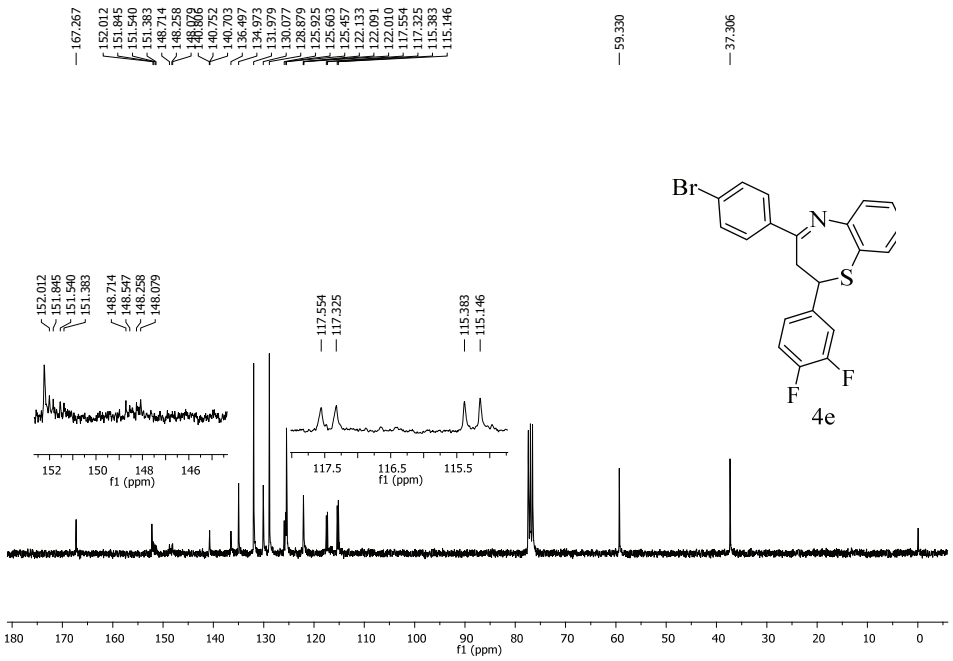

Fig. S-19. ^{13}C-NMR spectrum of compound 4e (75 MHz, $CDCl_3$)

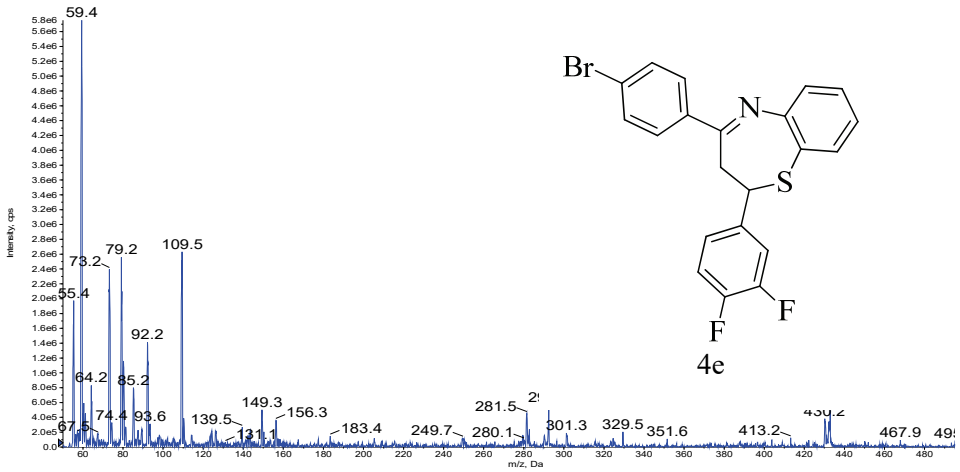

Fig. S-20. Mass spectrum of compound **4e**

(CC) 2022 SCS.

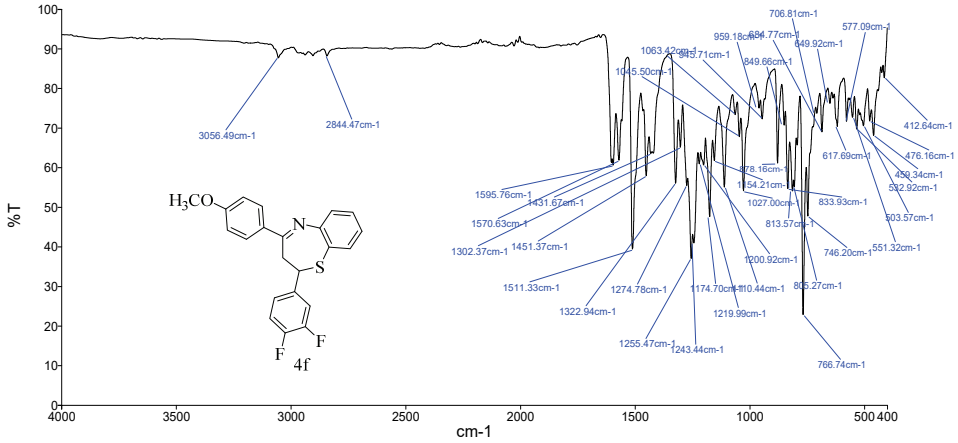

Fig. S-21. FTIR spectrum of compound 4f

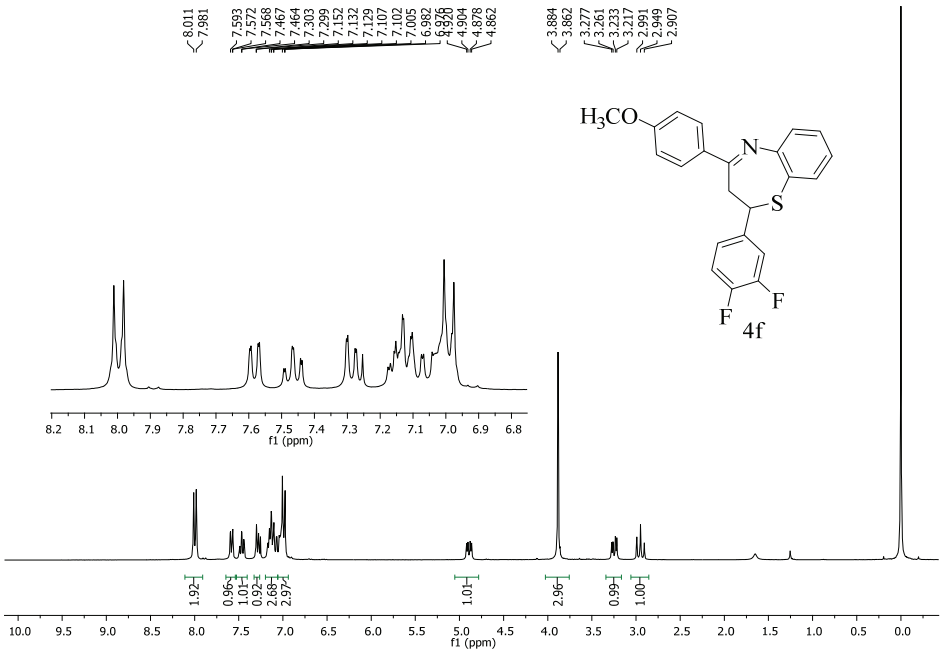

Fig. S-22. ^{1}H-NMR spectrum of compound **4f** (300 MHz, $CDCl_3$)

(CC) 2022 SCS.

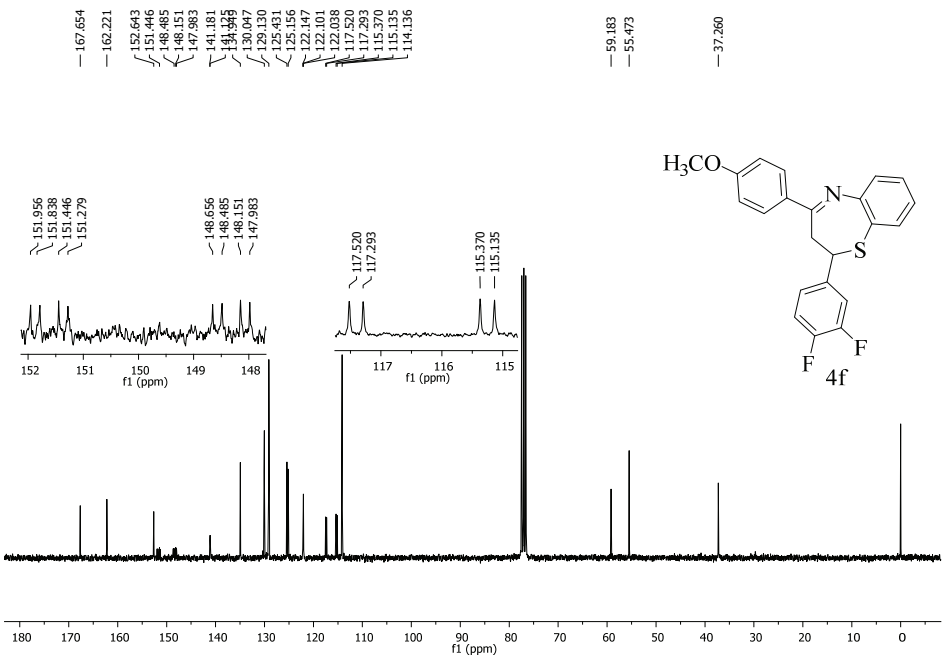

Fig. S-23. ^{13}C-NMR spectrum of compound **4f** (75 MHz, $CDCl_3$)

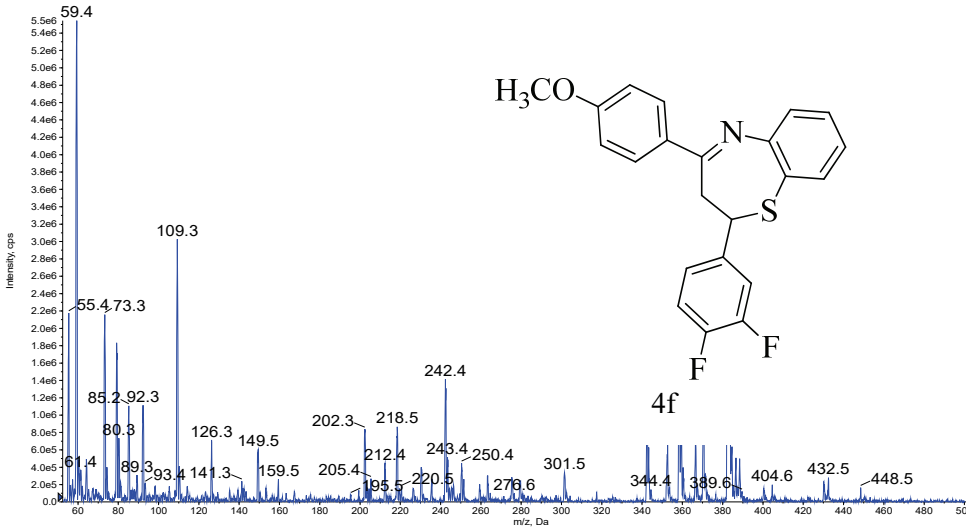

Fig. S-24. Mass spectrum of compound **4f**

(CC) 2022 SCS.

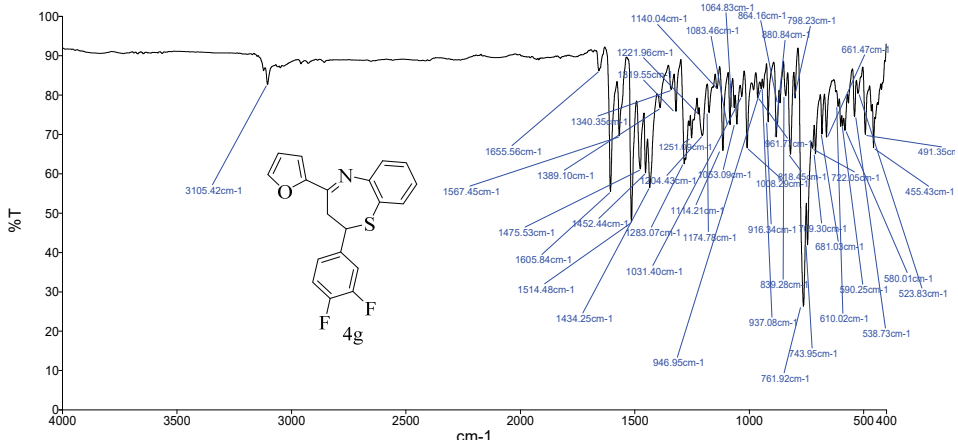

Fig. S-25. FTIR spectrum of compound **4g**

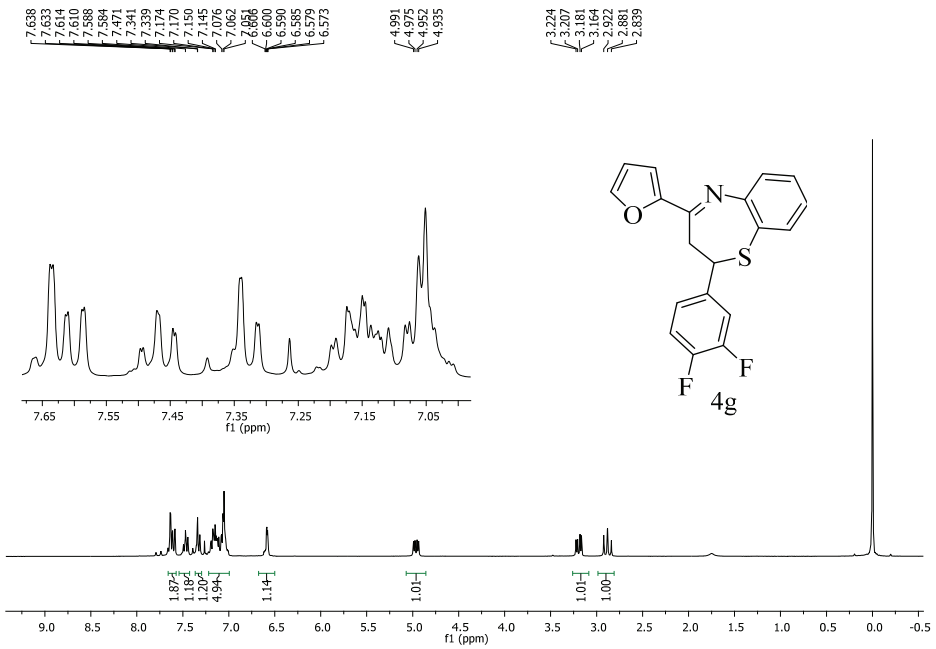

Fig. S-26. ^{1}H-NMR spectrum of compound **4g** (300 MHz, $CDCl_3$)

(CC) 2022 SCS.

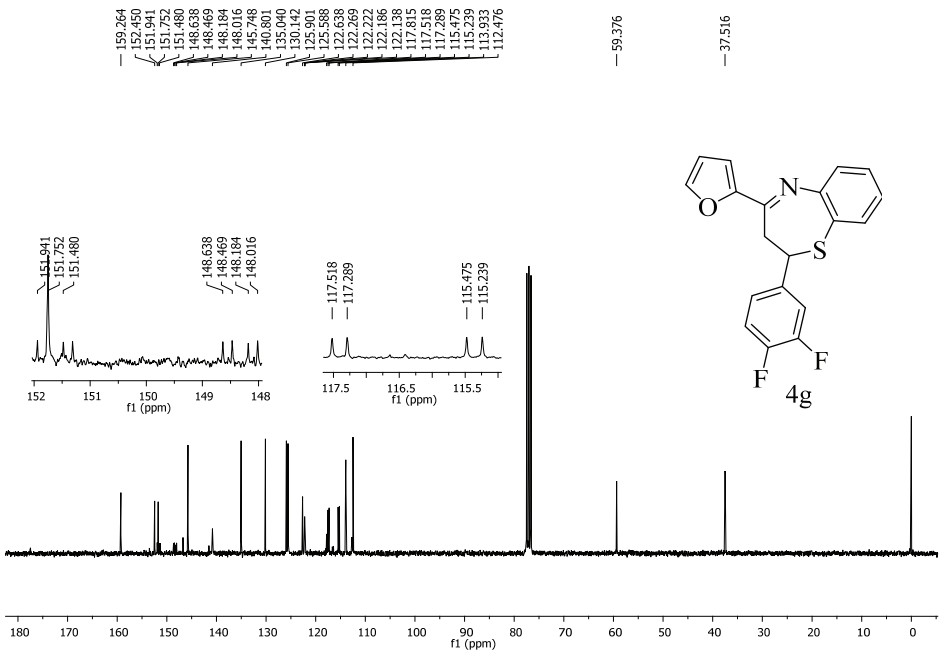

Fig. S-27. ^{13}C-NMR spectrum of compound **4g** (75 MHz, $CDCl_3$)

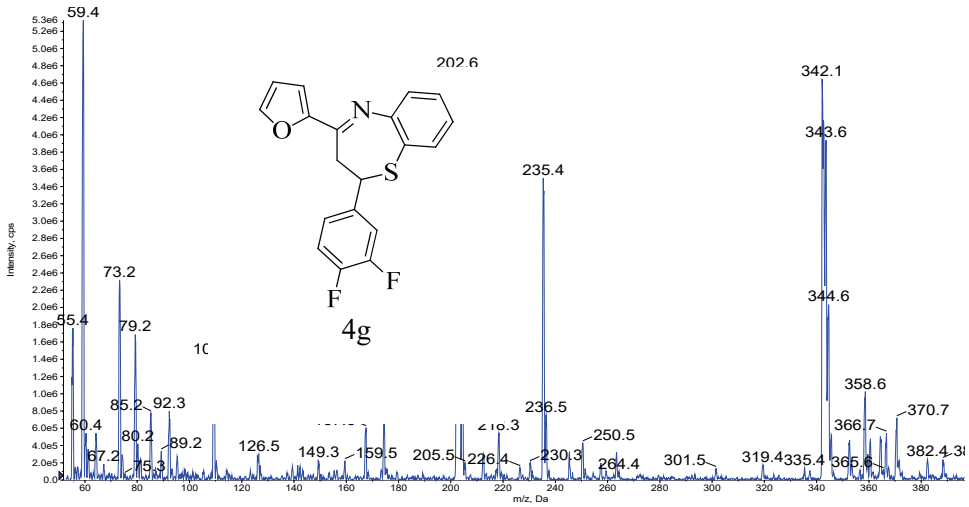

Fig. S-28. Mass spectrum of compound **4g**

(CC) 2022 SCS.

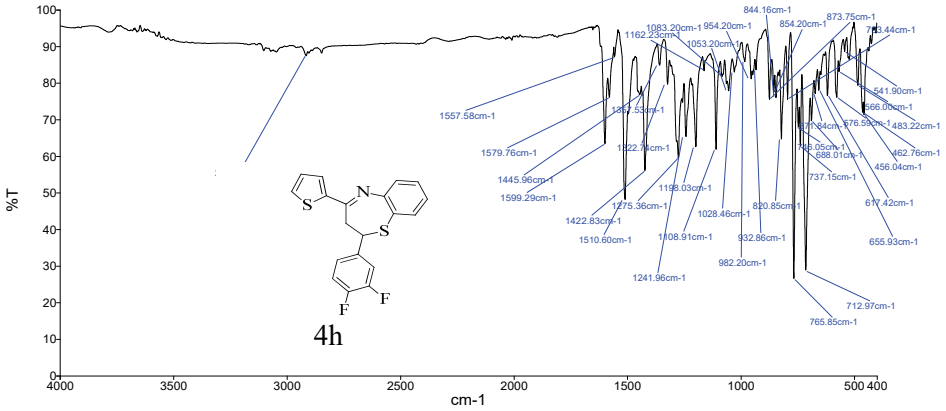

Fig. S-29. FTIR Spectrum of compound **4h**

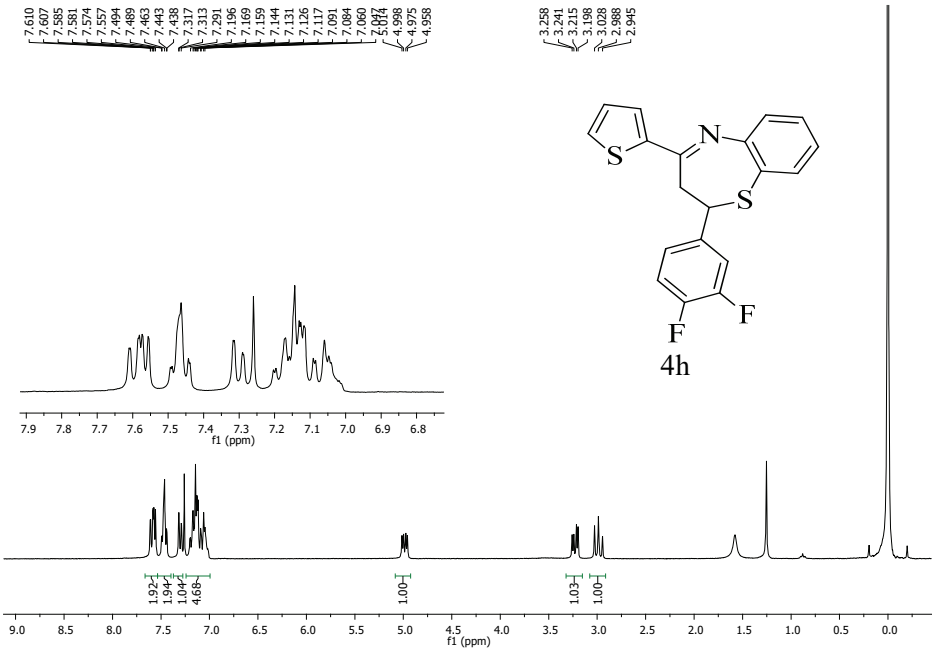

Fig. S-30. ^{1}H-NMR spectrum of compound **4h** (300 MHz, $CDCl_3$)

(CC) 2022 SCS.

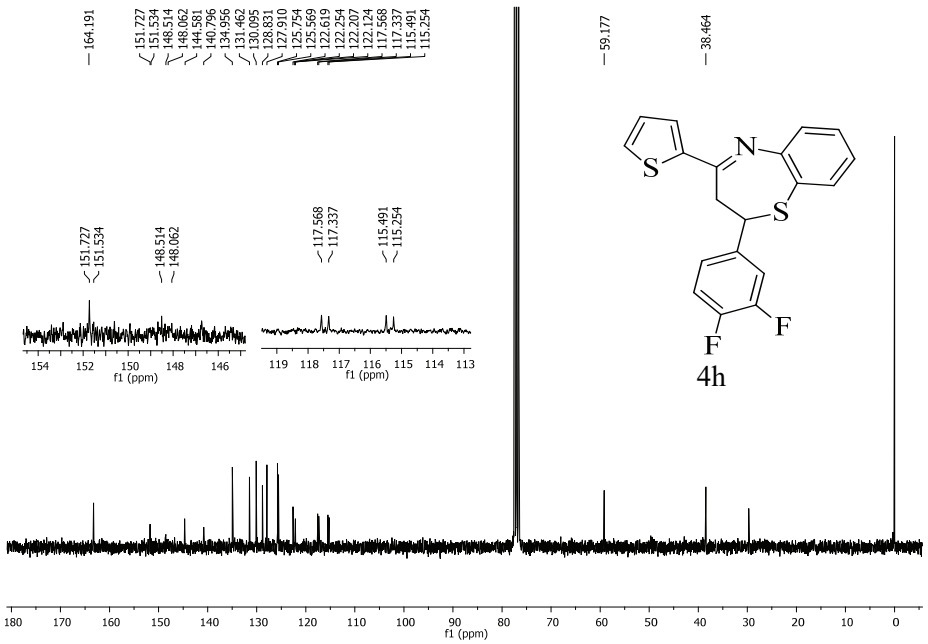

Fig. S-31. ^{13}C-NMR spectrum of compound **4h** (75 MHz, $CDCl_3$)

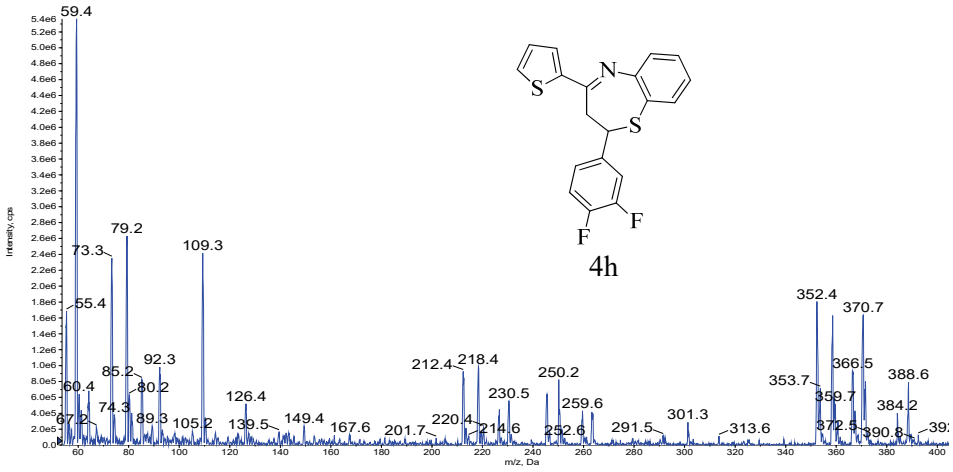

Fig. S-32. Mass spectrum of compound **4h**

(CC) 2022 SCS.

Anticancer activity

Table S-I. Control growth against human lung cancer cell line A549

Compound	Experiment 1				Experiment 2				Experiment 3			
	Control growth, %											
	10	20	40	80	10	20	40	80	10	20	40	80
	Drug concentration, μg ml^{-1}											
4a	79.8	69.7	54.9	28.2	89.9	80.8	72.7	35.1	96.7	91.9	85.1	46.2
4b	92.5	80.7	46.9	11.5	75.7	56.6	27.3	8.1	80.2	71.5	30.5	10.1
4c	59.7	24.6	3.6	-10.4	71.3	30.3	4.8	-18.1	84.4	41.1	9.3	-24.6
4d	51.2	18.3	1.7	-42.3	36.1	10.9	0.9	-30.7	24.6	9.5	3.1	-19.4
4e	72.5	52.2	48.5	1.6	65.4	37.1	33.7	1.2	81.4	67.9	58.2	0.5
4f	91.3	86.9	61.2	-12.2	87.5	78.6	55.1	-5.8	78.6	69.7	37.3	-1.5
4g	26.3	13.9	-11.2	-43	12.5	4.2	-3.5	-36	5.9	1.4	-1.2	-11
4h	40.1	24.4	15.8	-12.7	18.9	10.8	5.4	-5.8	10.3	6.2	2.5	-1.9
ADR	12.6	0.7	-16.9	-50	8.5	1.0	-12.3	-41	4.1	1.6	-6.2	-35

Table S-II. Average control growth against human lung cancer cell line A549

Compound	Average control growth, %				GI_{50} / μg ml^{-1}
	10	20	40	80	
	Drug concentration, μg ml^{-1}				
4a	88.8	80.8	70.9	36.5	69.23
4b	82.8	69.6	34.9	9.9	27.88
4c	71.8	32.0	5.9	-17.7	<10
4d	37.3	12.9	1.9	-30.8	<10
4e	73.1	52.4	46.8	1.1	22.07
4f	85.8	78.4	51.2	-6.5	32.33
4g	14.9	6.5	-5.3	-30	<10
4h	23.1	13.8	7.9	-6.8	<10
ADR	8.4	1.1	-11.8	-42	<10

Table S-III. Control growth against human breast cancer cell line MCF-7

Compound	Experiment 1				Experiment 2				Experiment 3			
	Control growth, %											
	10	20	40	80	10	20	40	80	10	20	40	80
	Drug concentration, μg ml^{-1}											
4a	109.9	91.1	70.1	55.8	95.7	82.6	58.6	42.3	89.9	70.5	46.2	30.6
4b	95.6	93.8	83.1	37.1	75.9	74.5	70.2	14.1	61.6	60.9	55.2	8.8
4c	60.7	26.3	11.5	-18.9	52.4	16.3	5.7	-11.1	24.9	6.9	2.3	-7.2
4d	49.8	18.9	-9.2	-56.2	25.1	11.9	-3.8	-41.1	11.2	7.6	-1.1	-35.6
4e	65.3	32.4	17.3	11.7	50.1	15.2	11.2	7.5	42.4	9.7	4.2	2.1
4f	82.5	70.2	64.5	51.5	62.2	55.4	50.1	42.2	50.9	42.1	36.3	30.5
4g	42.7	30.1	27.7	-15.2	29.5	16.4	14.5	-6.7	12.1	9.3	4.9	-2.4
4h	51.4	31.4	10.5	-41.2	42.6	19.9	4.3	-26.4	15.2	10.8	1.1	-14.6
ADR	14.3	1.6	-15.3	-43.4	8.3	1.1	-11.5	-29.1	5.3	0.9	-7.1	-17.8

(CC) 2022 SCS.

Table S-IV. Average control growth against human breast cancer cell line MCF-7

Compound	Average control growth, %				GI_{50}/μg ml^{-1}
	10	20	40	80	
	Drug concentration, μg ml^{-1}				
4a	98.5	81.4	58.3	42.9	68.59
4b	77.7	76.4	69.5	20	48.23
4c	46	16.5	6.5	-12.4	<10
4d	28.7	12.8	-4.7	-44.3	<10
4e	52.6	19.1	10.9	7.1	<10
4f	83.6	51.8	47.9	37.3	35.05
4g	28.1	18.6	15.7	-8.1	<10
4h	36.4	20.7	5.3	-27.4	<10
ADR	9.3	1.2	-11.3	-30.1	<10

Table S-V. Control growth against human liver cancer cell line HEPG2

Compound	Experiment 1				Experiment 2				Experiment 3			
	Control growth, %											
	10	20	40	80	10	20	40	80	10	20	40	80
	Drug concentration, μg ml^{-1}											
4a	95.4	88.3	70.7	49.3	87.3	79.1	56.9	41.1	76.2	64.5	45.8	30.2
4b	89.8	69.7	60.1	52.9	77.8	57.2	41.6	39.5	70.9	37.8	23.7	22.2
4c	69.1	46.5	20.3	-17.2	52.9	31.6	12.1	-10.2	45.7	24.2	5.4	-4.1
4d	30.6	16.2	-50.7	-48.1	20.1	6.7	-38.5	-34.8	16.5	3.8	-29.9	-14.9
4e	94.2	65.5	62.1	49.5	82.7	50.6	51.8	36.5	73.9	39.3	29.8	25.9
4f	79.6	70.2	46.2	-11.2	68.4	61.1	32.1	-8.6	57.5	31.6	14.1	-2.1
4g	59.2	40.4	21.9	-36.3	48.6	31.1	13.3	-27.8	34.4	19.7	8.9	-16.3
4h	21.8	9.1	-12.3	1.1	17.3	7.2	-10.1	0.7	10.1	2.3	-6.1	2.1
ADR	11.9	9.1	-5.3	-30.9	8.7	5.2	-3.2	-21.6	4.3	1.3	-1.4	-10.2

Table S-VI. Average control growth against human liver cancer cell line HEPG2

Compound	Average control growth, %				GI_{50}/μg ml^{-1}
	10	20	40	80	
	Drug concentration, μg ml^{-1}				
4a	86.3	77.3	57.8	40.2	57.69
4b	79.5	54.9	41.8	38.2	32.6
4c	55.9	34.1	12.6	-10.5	<10
4d	22.4	8.9	-39.7	-32.6	<10
4e	68.5	54.3	30.8	-7.3	16.98
4f	65.2	55.9	50.3	41.4	33.46
4g	47.4	30.4	14.7	-26.8	<10
4h	16.4	6.2	-9.5	1.3	<10
ADR	8.3	5.2	-3.3	-20.9	<10

(CC) 2022 SCS.

Table S-VII. Control growth against human prostate cancer cell line PC-3

Compound	Experiment 1				Experiment 2				Experiment 3			
	Control growth, %											
	10	20	40	80	10	20	40	80	10	20	40	80
	Drug concentration, μg ml^{-1}											
4a	109.2	90.5	88.7	60.1	100.7	81.2	70.9	50.3	89.8	69.8	61.8	33.9
4b	90.2	63.2	51.5	42.8	74.9	47.9	46.1	30.9	67.1	36.2	32.9	21.1
4c	45.3	41.1	31	22.4	36.4	24.7	19	14.2	25.1	13.4	10	5.1
4d	40.2	35.6	4.2	-12.4	25.2	20.4	2.8	-9.1	17.4	11.2	1.1	-3.1
4e	70.2	31.8	9.4	-39.4	54.1	23.5	7.2	-27.2	46.1	11.3	3.5	-18.6
4f	58.1	52	43.5	11.8	45.9	41	29.2	7.2	39.1	27	17.6	2.3
4g	39.1	32.4	22.8	15.2	30.4	20.5	11.1	8.9	20.2	13.7	6.3	5.6
4h	59.6	40.9	15.5	-11.2	45.8	32.6	11.7	-7.9	37.7	16.5	3.1	-2.2
ADR	13.6	1.1	-12.1	-28.8	9.2	0.7	-7.5	-22.1	5.1	1.8	-5.3	-11.8

Table S-VIII. Average control growth against human prostate cancer cell line PC-3

Compound	Average control growth, %				GI_{50} /μg ml^{-1}
	10	20	40	80	
	Drug concentration, μg ml^{-1}				
4a	99.9	80.5	73.8	48.1	92.93
4b	77.4	49.1	43.5	31.6	28.19
4c	35.6	26.4	20	13.9	<10
4d	27.6	22.4	2.7	-8.2	<10
4e	56.8	22.2	6.7	-28.4	<10
4f	47.7	40	30.1	7.1	11.59
4g	29.9	22.2	13.4	9.9	<10
4h	47.7	30	10.1	-7.1	<10
ADR	9.3	1.2	-8.3	-20.9	<10

Antibacterial activity

Gram positive

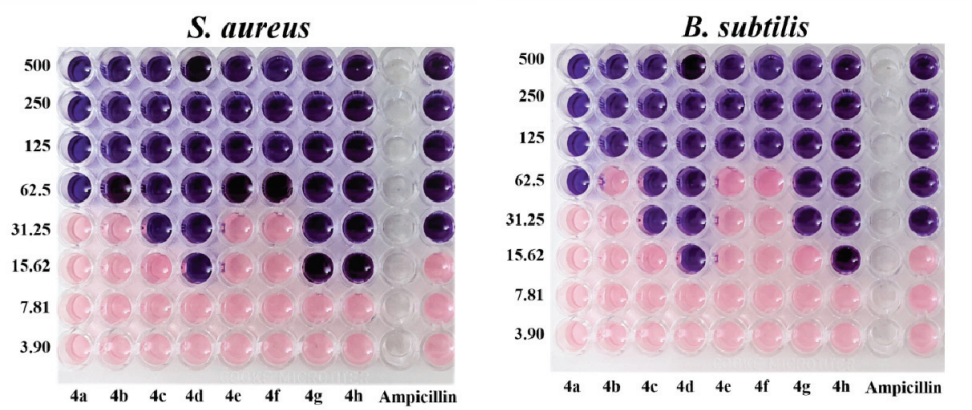

Fig. S-33. Antibacterial activity of synthesized compounds against gram positive strains

(CC) 2022 SCS.

Gram negative

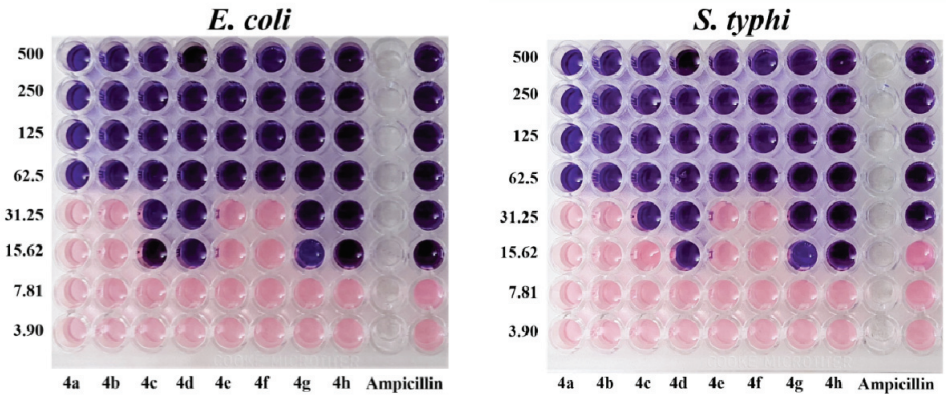

Fig. S-34. Antibacterial activity of synthesized compounds against gram negative strains

(CC) 2022 SCS.

Journal of the Serbian Chemical Society
JSCS@tmf.bg.ac.rs • www.shd.org.rs/JSCS
J. Serb. Chem. Soc. *87* (10) 1117–1123 (2022)
JSCS–5582
Short communication
Published 1 August 2022

SHORT COMMUNICATION

Optimization of the reaction conditions for the synthesis of 2,3,5-trimethylpyridine from 3-amino-2-methylpropenal and methylethylketone

JOVICA UROŠEVIĆ[1], MIROSLAV MITIĆ[1], BILJANA ARSIĆ[2]* and GORDANA STOJANOVIĆ[2#]

[1]*Chemical-technological school "Božidar Đorđevic Kukar", Vlajkova 94, 16000 Leskovac, Serbia and* [2]*University of Niš, Faculty of Sciences and Mathematics, Department of Chemistry, Višegradska 33, 18000 Niš, Serbia*

(Received 18 September 2021, revised 26 April, accepted 10 May 2022)

Abstract: The influence of temperature, reaction time, and type of the catalyst on the yield of the 2,3,5-trimethylpyridine (collidine) from 3-amino-2-methylpropenal and methylethylketone was investigated. 3-Amino-2-methylpropenal was synthesized from 3-ethoxy-2-methylacrolein previously synthesized from methylmalondialdehyde tetraethyl acetal, obtained from triethyl orthoformate and propenyl ether. The optimal conditions for the investigated synthesis were temperature of 150 °C, reaction time 24 h, and the CH_3COOH/pTsOH catalyst. This synthesis is the first successful attempt to synthesize 2,3,5-trimethylpyridine in an acid medium.

Keywords: cyclic condensation; GC–MS; side reactions.

INTRODUCTION

The importance of 2,3,5-trimethylpyridine (collidine) is reflected in the fact that it is the starting compound for the synthesis of esomeprazole which is used to treat symptoms of gastroesophageal reflux disease (GERD, Fig. 1).[1]

The production of 2,3,5-trimethylpyridine can be achieved either from natural products or synthesis. 2,3,5-Trimethylpyridine was isolated at the beginning of the 20th century from the tar of the stone coal,[2,3] and then from shales[4] by the fraction distillation at 186–190 °C with the yield of 7 %.

According to the literature, there are few published works on the synthesis of 2,3,5-trimethylpyridine. They can be divided into two groups: 1) the synthesis in the gaseous phase and 2) the synthesis in the liquid phase (solution).

* Corresponding author. E-mail: Biljana.Arsic@pmf.edu.rs
# Serbian Chemical Society member.
https://doi.org/10.2298/JSC210918042U

Available on line at www.shd.org.rs/JSCS/
(CC) 2022 SCS.

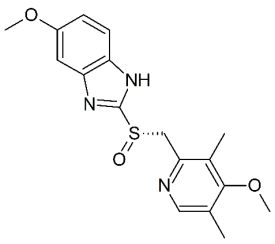

Fig. 1. Structure of esomeprazole.

The synthesis of 2,3,5-trimethylpyridine in the gaseous phase

The synthesis belongs to the condensation reactions of aldehydes and ammonia and can be delivered in homogenous or heterogeneous media.

Homogenous synthesis[5] occurs under high pressure and high temperature with the propionaldehyde, paraformaldehyde, and concentrated ammonia in an autoclave, followed by fraction distillation in a vacuum with the yield up to 14 %.

The heterogeneous synthesis produces 2,3,5-trimethylpyridine from methylethyl acrolein, ethanol, ammonia, and the catalyst (SiO_2, Al_2O_3) at elevated temperature and pressure for a longer time with the yield of up to 28.5 %.[6]

The synthesis of 2,3,5-trimethylpyridine in the liquid phase (solution)

The characteristic of reactions in the solution is that all of them happened in numerous stages, so the overall yield is modest.

Some of the most representative examples are synthesis *via* 3-carbetoxy-2,5--dimethyl-6-hydroxypyridine (the overall yield 8 %),[7] cyclic condensation *via* 3-carbetoxy-2,5-dimethylpyridine (the overall yield 22 %).[8]

Direct synthesis of collidine from mono-substituted acetylenes and nitriles in the presence of cobaltocene was achieved (yield in this step 45%), and the composition of the reaction mixture was estimated using gas–liquid chromatography (GLC).[9] Srinivas *et al.* reported a synthesis of 2,3,5-trimethylpyridine from 2-butanone, formaldehyde, ammonia and zeolite 5% PbZSM-5 (Si/Al = 15) as a shape selective catalyst with a yield of 43 %.[10] Substituted pyridines syntheses were reported from allylamines and alkynes *via* Cu(II) promoted oxidation and C–H bond activation by Rh (III).[11] Good yield of substituted pyridines was achieved in the reaction of Rh (III)-catalysed decarboxylative coupling of α,β--unsaturated carboxylic acid and α,β-unsaturated *O*-pivaloyl oximes.[12]

Given the low yields or complex conditions for the synthesis and the importance of 2,3,5-trimethyl pyridine, optimization of the reaction conditions for its synthesis from 3-amino-2-methylpropenal and methylethylketone was set for the purpose of this study.

(CC) 2022 SCS.

EXPERIMENTAL

*Synthesis of methylmalondialdehyde tetraethyl acetate (**1**)*

In Kolbe's flask with three necks, 13 mL boron trifluoride at 30 °C was added in drops for 1 h to the mixture of triethyl orthoformate and propenyl ether (4 kg, 16.73 mol) in the inert atmosphere in a stream of nitrogen. Then the reaction mixture was stirred for an additional 6 h at 30–40 °C and left overnight. Sodium carbonate (100 g, 0.94 mol) was added to the reaction mixture and stirred for 1 h at room temperature. After that, the mixture was filtered through a sintered glass filter, and the filtrate was distilled in a vacuum.[13] The first fraction (56–110 °C)/30 mmHg was triethyl orthoformate (around 5 kg), which can be used again, and the second was methylmalondialdehyde tetraethyl acetyl as the main product (Scheme 1, **1**) at 118––122 °C/30 mmHg (3.93 kg (83 %), n_D^{20} = 1.4130, where n_D^{20} is a refractive index at 20 °C and a dimensionless number.

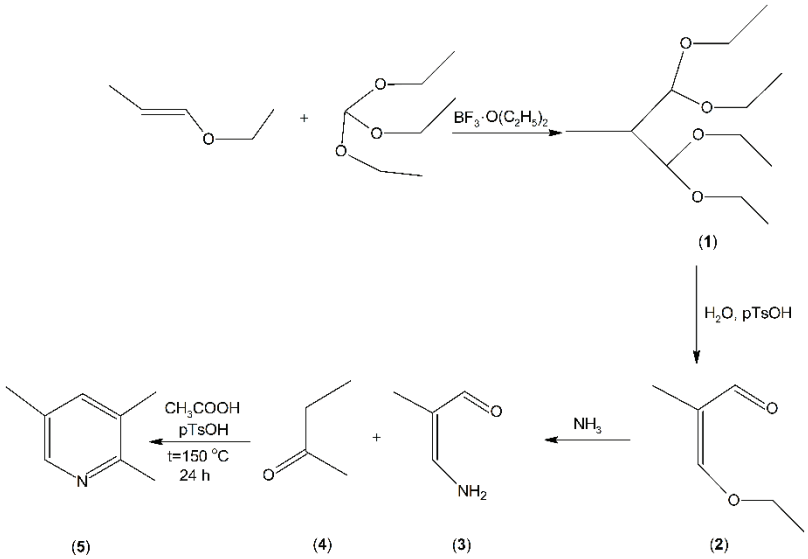

Scheme 1. The synthesis of compounds **1**–**5**.

*Synthesis of 3-ethoxy-2-methylacrolein (**2**)*

Methyl malondialdehyde tetraethyl acetal (2.34 kg, 9.99 mol), *p*-toluenesulfonic acid (5.4 g, 0.03 mol), and 180 mL water were mixed at 80 °C until the disappearance of the aqueous phase. Afterward, the reaction mixture was left for 2 h at 80 °C, then to cool down, and finally, with stirring, sodium bicarbonate was added (50 g, 0.6 mol) for 2 h at room temperature. The reaction mixture was filtered, the solid residue was washed with ethanol, and the filtrate and the ethanolic extract were distilled in a vacuum.[13] The first fraction (~115 g) at 34–78 °C/14 mm Hg was ethanol (n_D^t = 1.3788), the second (1.050 kg, 92 %) at 78–81 °C/14 mm Hg was 3-ethoxy-2-methylacrolein (Scheme 1, **2**), n_d^{22} = 1.4738, the maximum absorption in UV (ultraviolet) spectrum is at 242 nm.

*Synthesis of 3-amino-2-methylacrolein (**3**)*

3-Ethoxy-2-methylacrolein (114 g, 1 mol) and 750 mL conc. solution of ammonia (25 %) was emulsified at –10 °C with mixing and cooling using a mixture of ice and sodium chlo-

(CC) 2022 SCS.

ride for 6 h. After that, the temperature was allowed to reach 25 °C with constant stirring. The yellow solution was evaporated, using a rotary vacuum evaporator, to dryness and the remaining raw yellow solid was recrystallized from ethanol (100 mL) with the addition of 200–300 mL carbon tetrachloride. The obtained product was filtered and washed with petroleum ether at 30–50 °C and dried in a vacuum desiccator (p = 1.33 kPa) under the influence of phosphorus pentoxide at room temperature.[14] The yield of 3-amino-2-methylacrolein (Scheme 1, **3**) is 0.9 mol (103 g), 90 %, m.p., 113–114 °C, IR.[15]

The total yield of the synthesis of 3-amino-2-methylacrolein was 68 %.

*Synthesis of 2,3,5-trimethylpyridine (**5**)*

The reaction mixture consisted of 3-amino-2-methylacrolein (2.3 g, 0.025 mol), methylethylketone (2.5 g, 0.03 mol), glacial acetic acid (4.4 g, 0.075 mol), *p*-toluenesulfonic acid (0.02 g, 0.09 mmol), was refluxed for 24 h at 150 °C under the inert atmosphere of nitrogen, and then distilled in vacuum (p = 40 kPa). The fraction after 105 °C, yellow oily liquid, in quantity 1.60 g (49 %) represented the raw product, *i.e.*, the mixture of pyridine derivatives. There is 48 % 2,3,5-trimethylpyridine in the mixture separated and identified from the rest of the components by GC–MS, so the total yield of 2,3,5-trimethylpyridine (Scheme 1, **5**) is nearly 24 %, b.p., 187 °C, d_4^{25} = 0.9310, n_d^{25} = 1.5057.

Analysis of the products of the reaction

After distillation in a vacuum, the analysis of the reaction mixture was performed using GC–MS.

Gas chromatography

Instrument: gas chromatograph HP 5890 series II Hewlett Packard; integrator: HP 3396A Hewlett Packard; detector: FID (flame ionization); column: length 2.0 m, Chromosorb: W-HP 80/100; liquid phase: FFAP 10 %, gaseous phase: nitrogen (80 kPa); temperature: 120–220 °C (5 °C min^{-1}); sample: 0.2 μL.

Mass spectrometer was operated in electron-impact (EI) mode. The scan range was 33––651 amu (atomic mass unit), and the ionization energy was 70 eV.

MS spectra of the compounds, with a content higher than 1% in the mixture, are available as the Supplementary material to this paper (Figs. S-1–S-10).

RESULTS AND DISCUSSION

Numerous experiments of the synthesis of 2,3,5-trimethylpyridine from 3--amino-2-methylpropenal and methylethylketone were carried out to optimize the reaction conditions: temperature, reaction time and type of the catalyst. The results are presented in Table I.

TABLE I. Reaction conditions used

Serial No.	Temperature, °C	Reaction time, h	Yield of the 2,3,5-trimethylpyridine in the mixture, %
1	200	12	10
2	230	12	14
3	150	20	39
4	150	24	42.6
5	150	24	48

(CC) 2022 SCS.

The synthesis was investigated under the influence of different catalysts: glacial CH_3COOH, resin Lewiatit-80, $CH_3COOH/C_6H_5NO_2$, CH_3COOH/CH_3COONH_4 and in the inert atmosphere in a stream of nitrogen. The best yields were achieved with acetic acid and pTsOH, so other parameters were varied only with this catalyst.

According to the obtained results, the following conditions were optimal: temperature 150 °C, reaction time 24 h, and the catalyst CH_3COOH/pTsOH.

Analysis of the products of the reactions was performed using GC–MS (Table II) because the separation of the products was not possible either with fraction distillation or thin-layer chromatography. The identification of the components of the reaction mixture was performed based on their mass spectra, available as Supplementary material (Figs. S-1–S-10).

TABLE II. Components from the reaction mixture with a percentage of more than 1 %; component area contribution, % = 100×Area of the component/Total area of all components

Component area contribution, %	t_R / min	Compound
1.9	1.354	Lutidine (2,3-dimethylpyridine)
6.3	4.756	3,7-Dimethyl-1,5-diazocine
43.5	6.876	Collidine
2.3	2.321	2-Ethyl-5-methylpyridine
6.8	7.10	Lutidine (3,5-dimethylpyridine)
15.5	7.51	3,5-Dimethylpyridine-2-carbonitrile
1.3	7.948	(5-Methylpyridin-2-yl)acetonitrile
14.88	8.45	(2*E*)-3-{(*Z*)-[(2*Z*)-3-{(*Z*)-[(2*E*)-3-Amino-2--methylprop-2-en-1-ylidene]amino}-2-methyl-prop-2-en-1-ylidene]amino}-2-methylprop-2-enal
2	8.925	Polycondensate
1	9.228	3-Methylfuro[3,4-*b*]pyridine-5,7-dione

Peak with the retention time $t_R = 6.88$ min represents the main product (43.47 %), and it is 2,3,5-trimethylpyridine.

Other peaks of the components in the reaction mixture with more than 1 % represent the side products.

Mechanism of the reaction

The reaction of the cyclic condensation is analogous to the addition in weakly acidic media of carbonyl compounds with H_2N–R derivatives. In case of this condensation, R–NH_2 as a nucleophile can attack the carbonyl compound's conjugated acid, which is in acid media in the form of the enol more stable due to the conjugation effect (Scheme 2).

CONCLUSION

2,3,5-Trimethyl pyridine was synthesized using cyclic condensation under the influence of the acid catalyst in one phase from 3-amino-2-methylpropenal and

(CC) 2022 SCS.

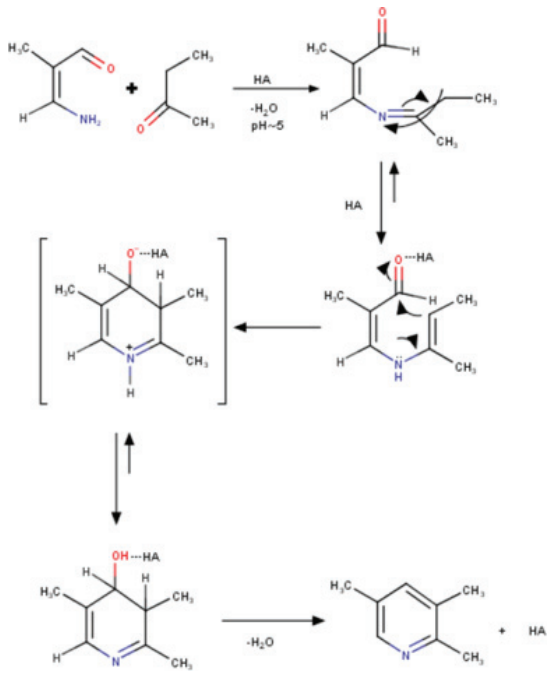

Scheme 2. Proposed mechanism of the reaction.

2-butanone. In this synthesis, 2,3,5-trimethyl pyridine was the main component in the mixture with some other pyridine derivatives. The advantage of this method is that it occurs in one phase with approximately the same yield to those of most published syntheses.

SUPPLEMENTARY MATERIAL

Additional data and information are available electronically at the pages of journal website: https://www.shd-pub.org.rs/index.php/JSCS/article/view/11174, or from the corresponding author on request.

Acknowledgement. Biljana Arsić and Gordana Stojanović want to thank for the financial support for this work to the Ministry of Education, Science and Technological Development of the Republic of Serbia (contract number 451-03-9/2021-14/200124).

ИЗВОД

ОПТИМИЗАЦИЈА РЕАКЦИОНИХ УСЛОВА СИНТЕЗЕ 2,3,5-ТРИМЕТИЛПИРИДИНА ИЗ 3-АМИНО-2-МЕТИЛПРОПЕНАЛА И МЕТИЛЕТИЛКЕТОНА

ЈОВИЦА УРОШЕВИЋ[1], МИРОСЛАВ МИТИЋ[1], БИЉАНА АРСИЋ[2] и ГОРДАНА СТОЈАНОВИЋ[2]

[1]*Хемијско-технолошка школа „Божидар Ђорђевић Кукар“, Влајкова 94, 16000 Лесковац и* [2]*Универзитет у Нишу, Природно–математички факултет, Департман за хемију, Вишеградска 33, 18000 Ниш*

Проучаван је утицај температуре, времена реакције и типа катализатора на принос 2,3,5-триметилпиридина (колидина) из 3-амино-2-метилпропенала и метилетилкетона.

(CC) 2022 SCS.

3-Амино-2-метилпропенал је синтетисан из 3-етокси-2-метилакролеина претходно синтетисаног из метилмалондиалдехид-тетраетил-ацетала, који је добијен из триетил-ортоформата и пропенил-етра. Нађени оптимални услови за синтезу су били температура од 150 °C, време реакције 24 h, и катализатор CH_3COOH/pTsOH. Ова синтеза је први успешни покушај синтезе 2,3,5-триметилпиридина у киселој средини.

(Примљено 18. септембра 2021, ревидирано 26. априла, прихваћено 10. маја 2022)

REFERENCES

1. J. C. Sih (Upjohn Co.), US4575554 (1986)
2. A. Eckert, S. Loria, *Monatsh. Chem.* **38** (1917) 225 (https://doi.org/10.1007/BF01524213)
3. M. P. Oparina, *Ber. Dtsch. Chem. Ges.*, *B* **64** (1931) 562 (https://doi.org/10.1002/cber.19310640311)
4. T. Eguchi, *Bull. Chem. Soc. Jpn.* **3** (1928) 235 (https://doi.org/10.1246/bcsj.3.235)
5. J. Herzenberg, G. Boccato, *Chim. Ind. (Paris)* **80** (1958) 248
6. K. Tsuda, N. Ikekawa, H. Mishima, A. Iino, T. Morishige, *Pharm. Bull.* **1** (1953) 122 (https://doi.org/10.1248/cpb1953.1.122)
7. G. Errera, *Ber. Dtsch. Chem. Ges.* **34** (1901) 3691 (https://doi.org/10.1002/cber.19010340367)
8. E. Breitmaier, S. Gassenmann, *Chem. Ber.* **104** (1971) 665 (https://doi.org/10.1002/cber.19711040234)
9. Y. Wakatsuki, H. Yamazaki, *Synthesis* **1976** (1976) 26 (https://doi.org/10.1055/s-1976-23943)
10. N. Srinivas, V. Radha Rani, S. J. Kulkarni, K. V. Raghavan, *J. Catal.* **208** (2002) 332 (https://doi.org/10.1006/jcat.2002.3538)
11. D.-S. Kim, J.-W. Park, C.-H. Jun, *Chem. Commun.* **48** (2012) 11334 (https://doi.org/10.1039/C2CC36699A)
12. J. M. Neely, T. Rovis, *J. Am. Chem. Soc.* **136** (2014) 2735 (https://doi.org/10.1021/ja412444d)
13. V. T. Klimko, T.V. Protopopova, N.V. Smirnova, A.P. Skoldinov, *Zh. Obshch. Khim.* **32** (1962) 2961
14. V. T. Klimko, T.V. Protopopova, A. P. Skoldinov, SU136351A1 (1960)
15. J. Vymetal, Z. Hejda, *Collect. Czech. Chem. Commun.* **43** (1978) 3024 (https://doi.org/10.1135/cccc19783024).

(CC) 2022 SCS.

Journal of the Serbian Chemical Society
JSCS@tmf.bg.ac.rs • www.shd.org.rs/JSCS
J. Serb. Chem. Soc. 87 (0) S354–S359 (2022) *Supplementary material*

SUPPLEMENTARY MATERIAL TO

Optimization of the reaction conditions for the synthesis of 2,3,5-trimethylpyridine from 3-amino-2-methylpropenal and methylethylketone

JOVICA UROŠEVIĆ[1], MIROSLAV MITIĆ[1], BILJANA ARSIĆ[2]* and GORDANA STOJANOVIĆ[2]

[1]*Chemical-technological school "Božidar Đorđevic Kukar", Vlajkova 94, 16000 Leskovac, Serbia and* [2]*University of Niš, Faculty of Sciences and Mathematics, Department of Chemistry, Višegradska 33, 18000 Niš, Serbia*

J. Serb. Chem. Soc. 87 (10) (2022) 1117–1123

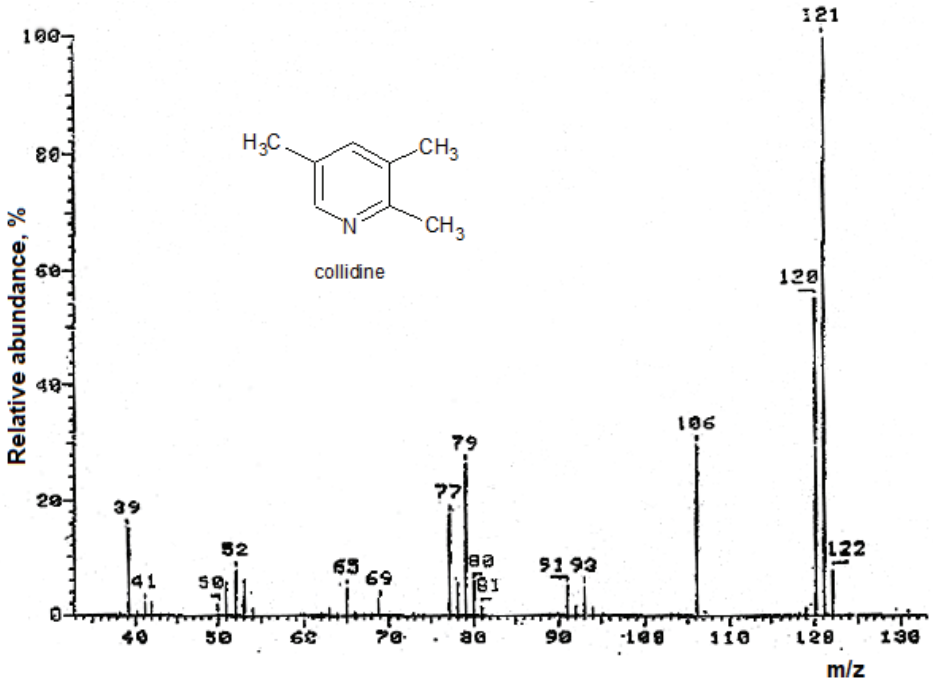

Fig. S-1. Mass spectrum of collidine detected from the reaction mixture.

* Corresponding author. E-mail: Biljana.Arsic@pmf.edu.rs

Available on line at www.shd.org.rs/JSCS/
(CC) 2022 SCS.

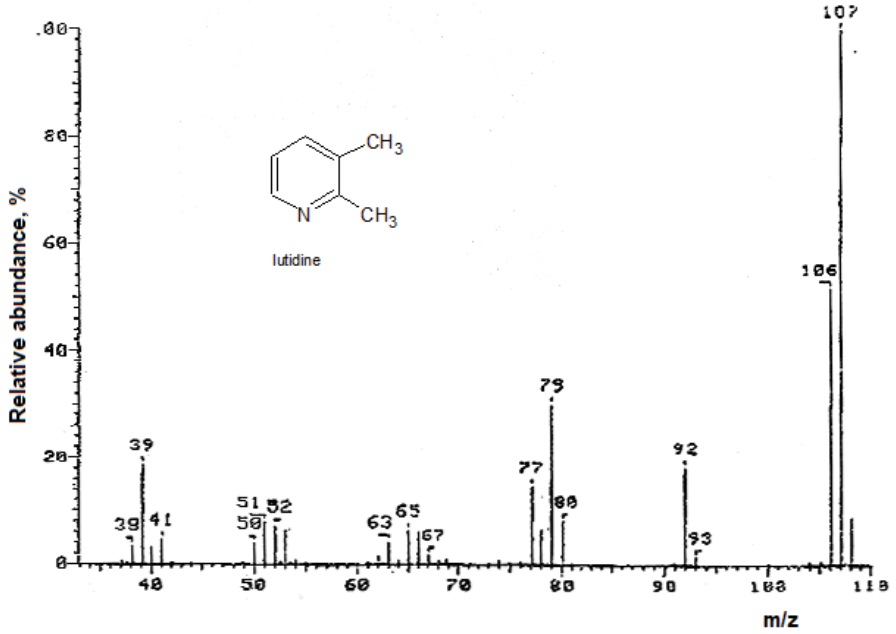

Fig. S-2. Mass spectrum of lutidine (2,3-dimethylpyridine) detected from the reaction mixture.

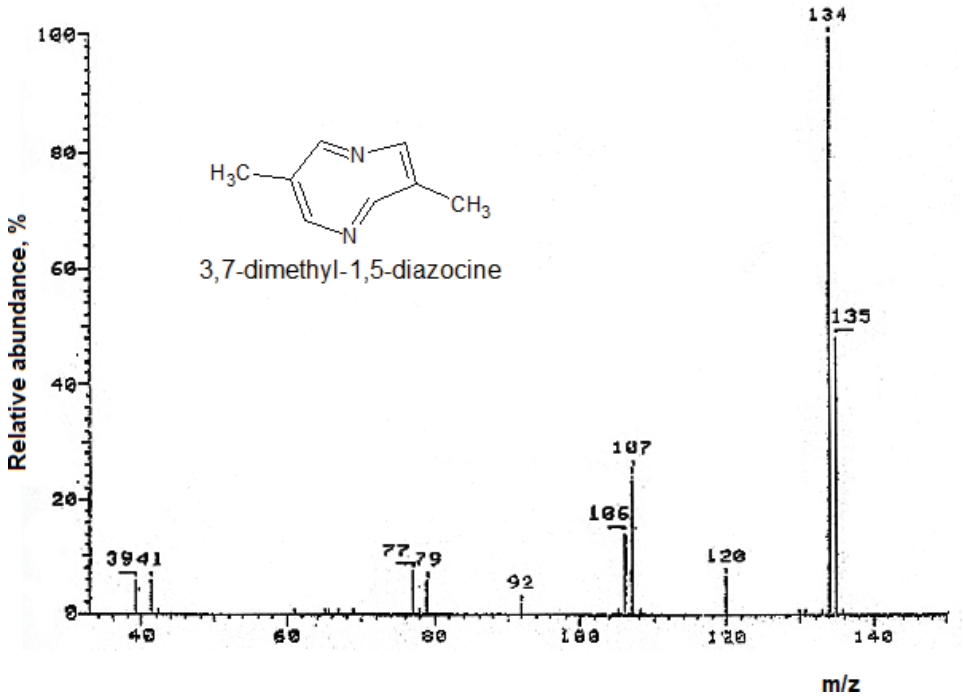

Fig. S-3. Mass spectrum of 3,7-dimethyl-1,5-diazocine detected from the reaction mixture.

(CC) 2022 SCS.

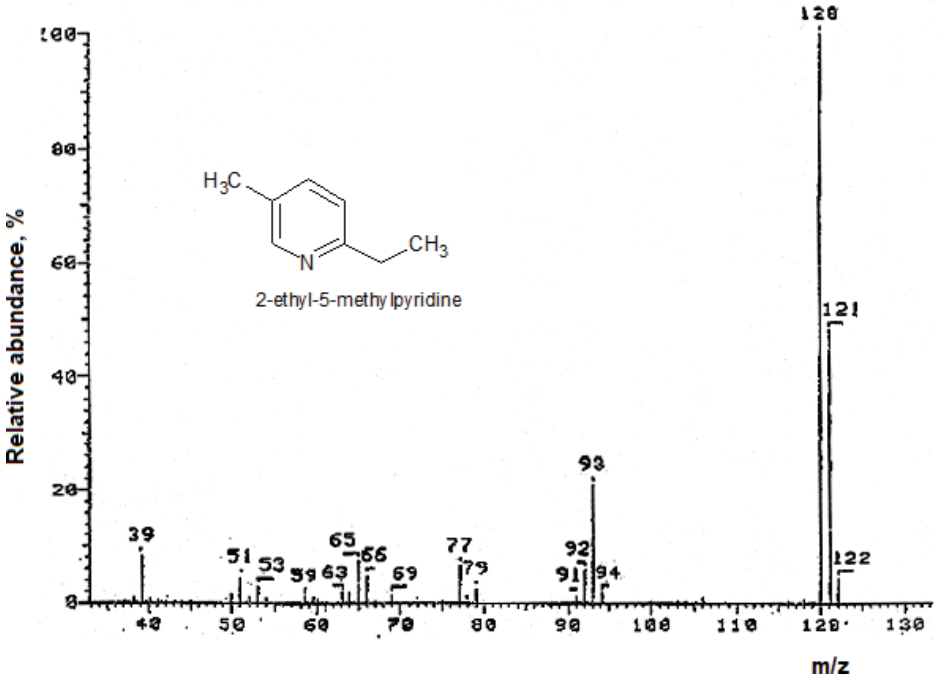

Fig. S-4. Mass spectrum of 2-ethyl-5-methylpyridine detected from the reaction mixture.

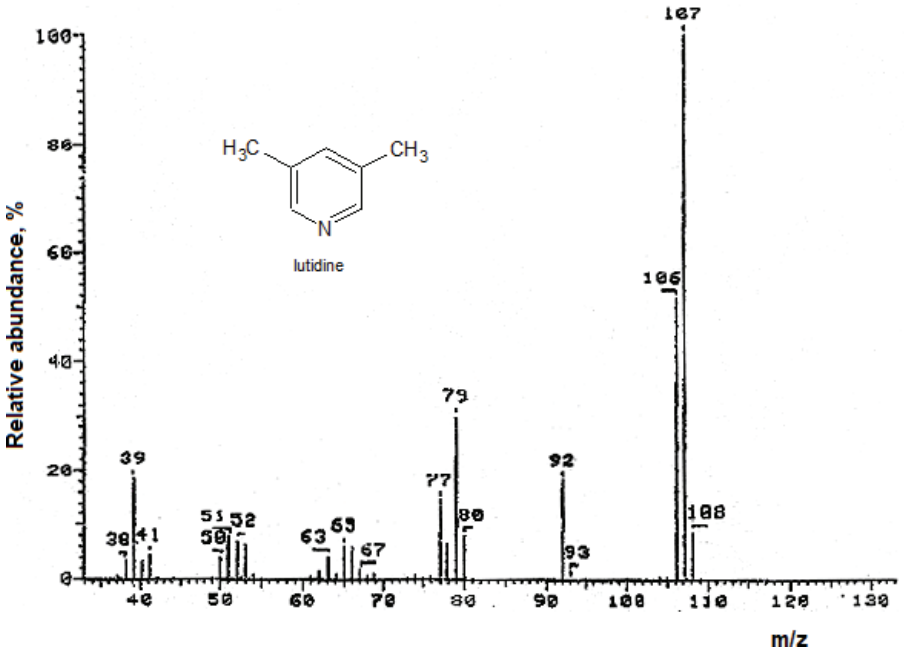

Fig. S-5. Mass spectrum of lutidine (3,5-dimethylpyridine) detected from the reaction mixture.

(CC) 2022 SCS.

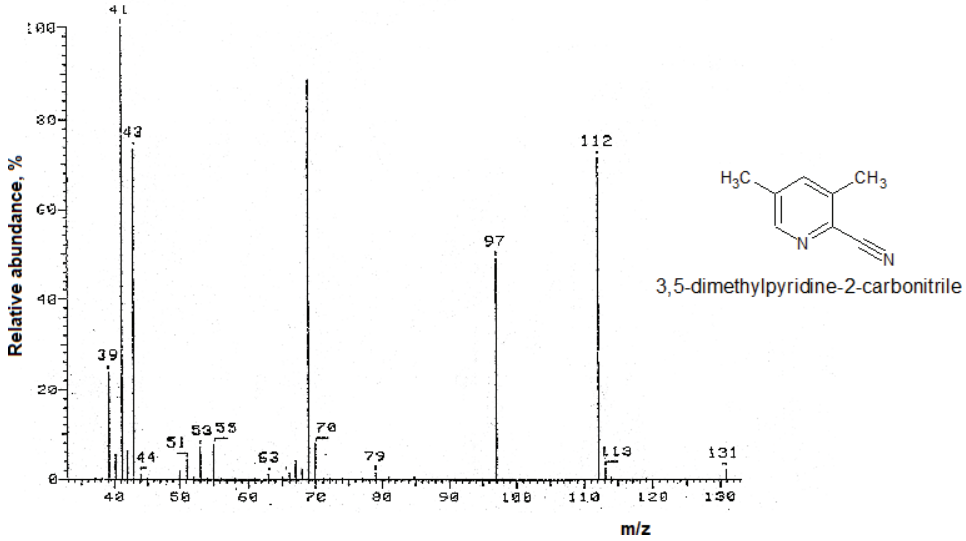

Fig. S-6. Mass spectrum of 3,5-dimethylpyridine-2-carbonitrile detected from the reaction mixture.

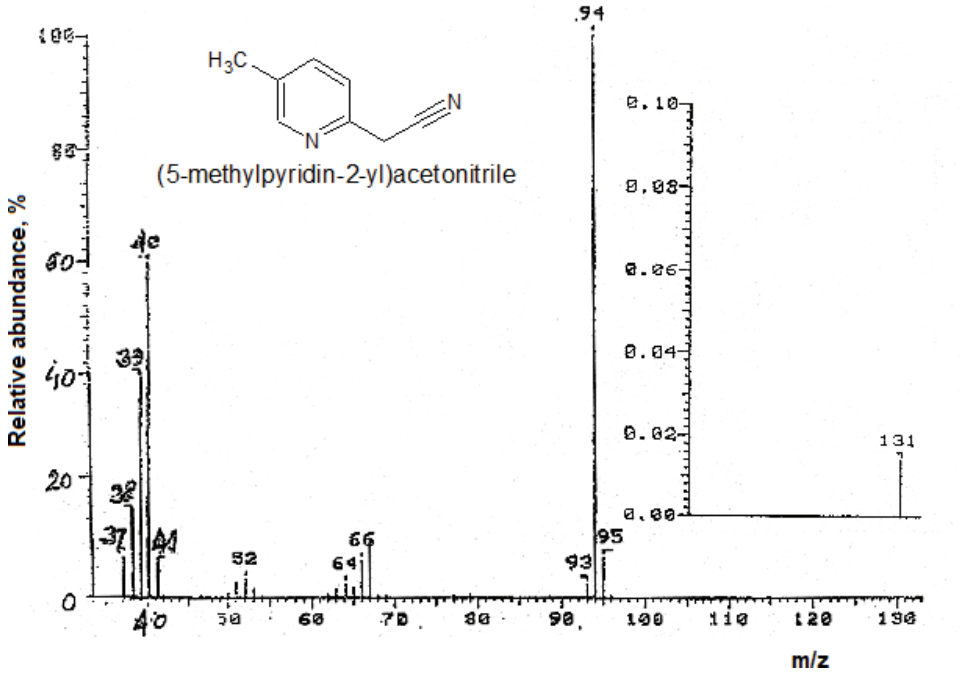

Fig. S-7. Mass spectrum of (5-methylpyridin-2-yl)acetonitrile detected from the reaction mixture.

(CC) 2022 SCS.

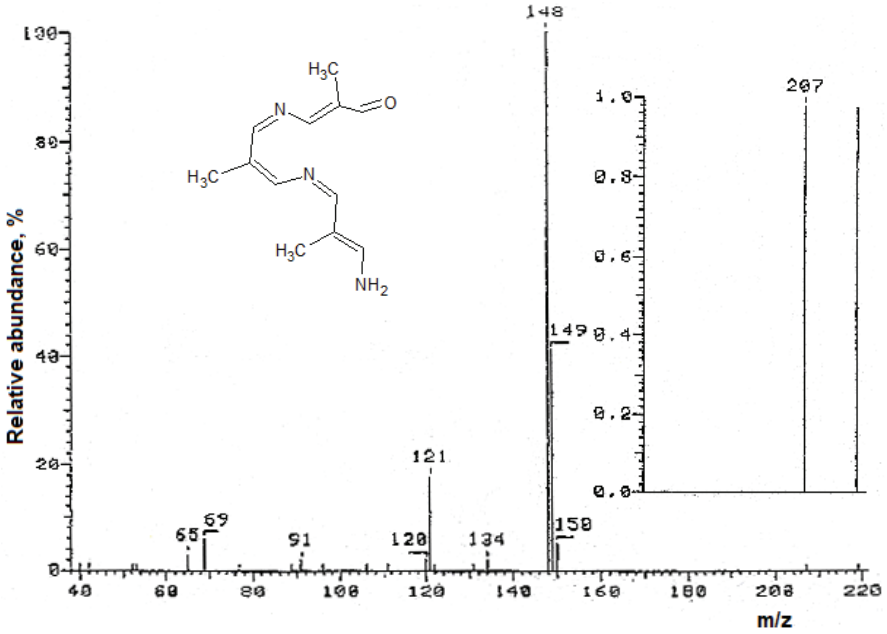

Fig. S-8. Mass spectrum of (2*E*)-3-{(*Z*)-[(2*Z*)-3-{(*Z*)-[(2*E*)-3-amino-2-methylprop-2-en-1-ylidene]amino}-2-methylprop-2-en-1-ylidene]amino}-2-methylprop-2-enal detected from the reaction mixture.

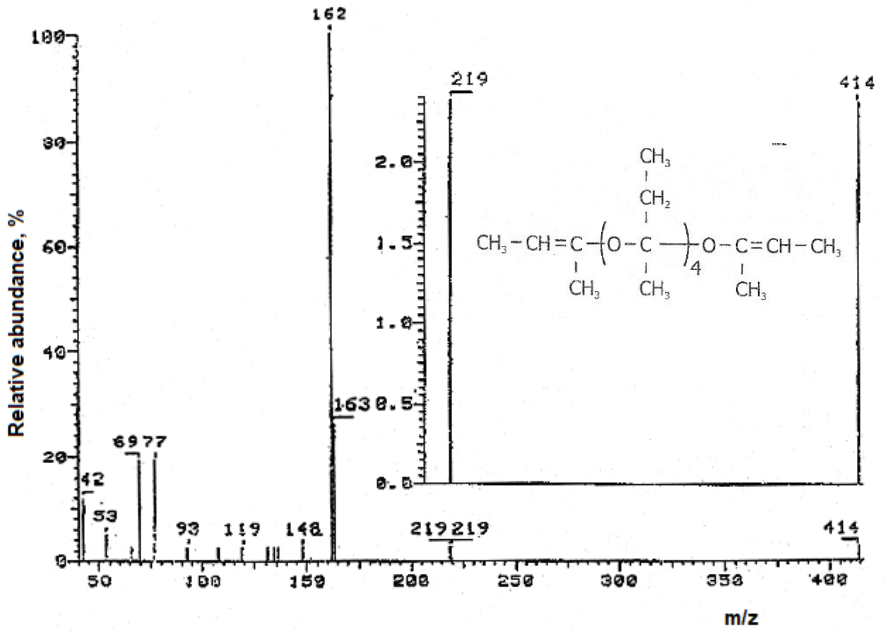

Fig. S-9. Mass spectrum of polycondensate detected from the reaction mixture.

(CC) 2022 SCS.

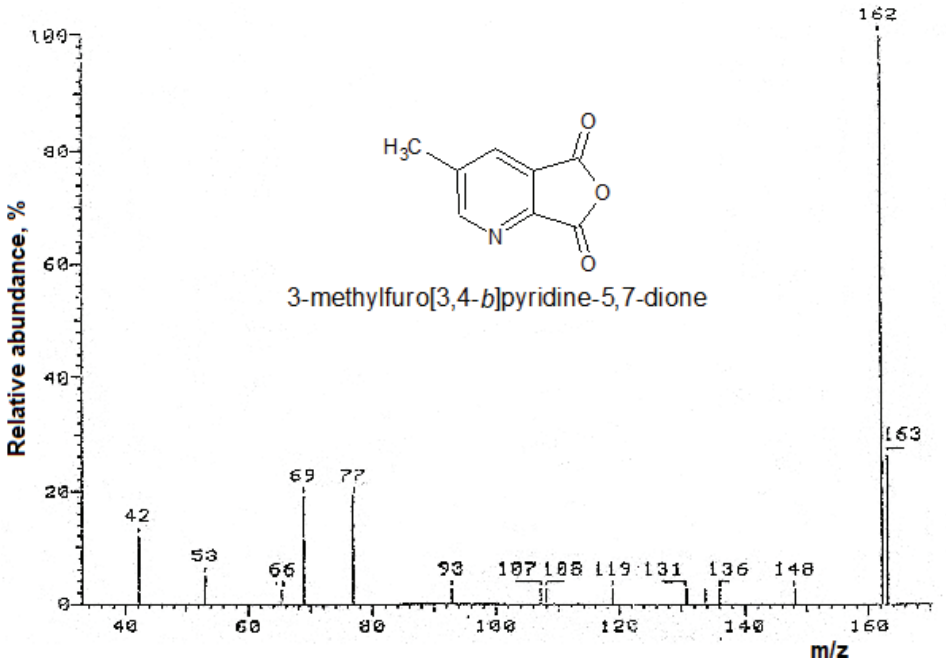

Fig. S-10. Mass spectrum of 3-methylfuro[3,4-*b*]pyridine-5,7-dione detected from the reaction mixture.

(CC) 2022 SCS.

Journal of the Serbian Chemical Society
JSCS@tmf.bg.ac.rs • www.shd.org.rs/JSCS
J. Serb. Chem. Soc. *87* (10) 1125–1142 (2022)
JSCS–5583
Original scientific paper
Published 1 August 2022

Synthesis of some benzylidene thiosemicarbazide derivatives and evaluation of their cytotoxicity on U87, MCF-7, A549, 3T3 and HUVEC cell lines

TOUBA ESLAMINEJAD[1], YAGHOUB POURSHOJAEI[1,2], MAHMOOD NAGHIZADEH[2], HODA ESLAMI[2], MOHAMMAD DANESHPAJOUH[2] and ABDOLREZA HASSANZADEH[1,2]*

[1]*Pharmaceutics Research Centre, Institute of Neuropharmacology, Kerman University of Medical Sciences, Kerman, Iran and* [2]*Department of Medicinal Chemistry, Faculty of Pharmacy, Kerman University of Medical Sciences, Kerman, Iran*

(Received 30 June 2021, revised 15 January, accepted 24 February 2022)

Abstract: Iron homeostasis is altered in tumours in response to a perturbation in the expression of iron-dependent proteins. Therefore, iron chelators make cancerous cells more vulnerable to iron deficiency. Compounds having thiosemicarbazide scaffold with the ability to metal complex formation have the potential to act as anticancer. A series of thiosemicarbazide derivatives were designed, synthesized successfully and their cytotoxicity was then tested on some cancerous as well as laboratory normal model systems by using colorimetric assay based on WST-1 reagent. According to the cytotoxicity results, some compounds showed high toxicity effect on both the cancerous and healthy cell lines. The results of toxicity assays on U87 and A549 cell lines showed the survivability less than 50 % at all concentrations higher than 10 ppm for all the synthesized compounds. The MCF-7 cell line exhibited approximately the same behaviour and had survivability less than 60 %. The 3T3 in compared with HUVEC cell line showed a completely different behaviour against the synthesized compounds and had survivability more than 50 %. The selectivity index was also measured and based on the study results it could be concluded that the cytotoxicity profile of the synthesized compounds on 3T3 cell line shows a significant difference, indicating a good anticancer effect of these compounds.

Keywords: *meta* and *para*-substituted benzylidene thiosemicarbazides; cytotoxicity assessment; cancerous and normal cell lines; WST-1 assay.

* Corresponding author. E-mail: a_hassanzadeh@kmu.ac.ir
https://doi.org/10.2298/JSC210630016E

Available on line at www.shd.org.rs/JSCS/
(CC) 2022 SCS.

INTRODUCTION

Have been known for years that cancer cells have modified metabolic pathways compared to their normal cell counterparts. For instance, there is general agreement that cancer cells, at least in a large number of solid ones, benefit from an enhancement in aerobic glycolysis over oxidative phosphorylation.[1–3] Also glutamines play a major role in the cancer cells either as a supplier for building blocks of macromolecules or through increasing the activity of the glutaminolysis pathways enhancing the ATP supply through the Krebs cycle.[4] Furthermore, while de novo fatty acid synthesis is usually suppressed in normal cells, tumour cells synthesize fatty acids at high rates.[3] NADPH can contribute to fatty acid biosynthesis as well as ROS scavenging of reactive oxygen species in tumour cells.[2,5] Tumour proliferations also need more ribose-5-phosphate, cofactors and relevant enzymes to enhance nucleotide synthesis and DNA repair.[3]

One of the different characteristics of cancer cells that can be used to design anti-cancer drugs is expression of high levels of the transferrin receptor 1 (TfR1) and internalization of iron (Fe) from transferrin (Tf) at an extraordinary rate in response to the high requirement of tumor cells for Fe.[6,7] The monoclonal antibody designated 42/6, has been reported to act as an agent with the potential to Fe deprivation through transferrin binding inhibition to its receptor, resulting in in vitro growth suppression of the human T leukemic cell line.[8]

Disorders that impair iron homeostasis are one of the most common human diseases that cancer is one of them.[9] Ribonucleotide reductase (a Fe-containing enzyme required for the conversion of ribonucleotides into deoxynucleotides for DNA synthesis) is a key enzyme in the rate limiting step of DNA synthesis.[10] It has been reported that desferrithiocin and desferrioxamine, as iron chelators, target cancerous cells in the S phase or the early S phase of the cell proliferation cycle.[10–12] Iron chelation therapy is a new strategy to cure cancers, especially those resistant, by using iron chelators depriving tumour cells from nutrient Fe.[13–15] This issue is based on the finding that the ribonucleotide reductase shows an enhanced activity in tumour cells compared to normal cells.[16–18]

Thiosemicarbazides are considered as a class of biological compounds with a wide range of activity and have been studied for their activity against viruses,[19–22] bacteria,[20,23–26] fungi[27] and cancerous cells.[20,28–30] Triapine and marboran (methisazone, Fig. 1) are two synthetic analogues of thiosemicarbazides already in market.[20] Triapine, first synthesized by Liu and co-workers[30] and still under clinical phase I/II studies,[31–33] is a more potent ribonucleotide reductase and cancer cell growth inhibitor than the antineoplastic drug, hydroxyurea.[34] Marboran is also a good anti-viral agent.[35–37] The ability of thiosemicarbazones to form chelators with metal ions, especially iron, has led researchers to synthesize derivatives of these compounds and investigate their anti-cancer effects.[38,39] As part of an ongoing research program on the synthesis of new thiosemicarbazide

(CC) 2022 SCS.

derivatives as biologically active compounds, we herein report the synthesis and cytotoxicity assessment of some thiosemicarbazide derivatives on U87, MCF-7, A549, 3T3 and HUVEC cell lines.

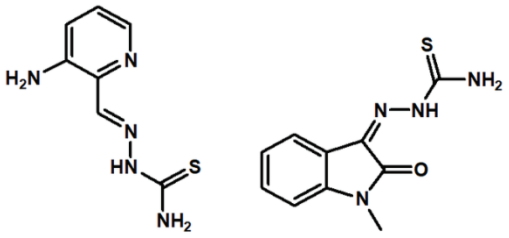

Fig. 1. Two synthetic analogues of thiosemicarbazides already in market.

EXPERIMENTAL

All chemicals, reagents and solvents were commercially available and were used without further purification. An electrothermal IA9100 melting point apparatus fixed at 1 °C/min was used to determine melting point. The IR spectra were recorded on an FT-IR Tensor 27 infrared spectrophotometer (Bruker) using KBr as a matrix. ^{1}H-NMR and ^{13}C-NMR spectra were taken by an FT-NMR Bruker Avance ultra shield Spectrometer (300 and 75 MHz in frequencies for ^{1}H and ^{13}C, respectively) using DMSO-d_6 as solvent. Also, TLC-grade silica gel G/UV 254 nm plates were used for monitoring reaction progress by the use of EtOAc/*n*-hexane (1:2 volume ratio) as eluent. Standard laboratory chemicals and a selection of reagents were obtained from the Sigma–Aldrich Company including Dulbecco's modified eagle's medium F12 (DMEM), fetal bovine serum (FBS), penicillin-streptomycin (100 μg/ml), and phosphate-buffered saline (PBS), trypan blue dye solution, and trypsin- EDTA solution. 2-(2--methoxy-4-nitrophenyl)-3-(4-nitrophenyl)-5-(2,4-disulfophenyl)-2*H*-tetrazolium. WST-1 reagent was prepared from Roche Holding AG. Cytotoxicity assay kit II was prepared from the LDH bioscience source. All eukaryote cells were obtained from Pasteur Institute of Iran.

General procedures for the synthesis of compounds ***1–13***

To a solution of 0.1 g NaOH in 5 mL water, 1 mmol corresponding aldehyde was added under stirring. Then 1 mmol thiosemicarbazide was gradually added to the solution and under room temperature the mixture was stirred overnight. Then 5 mL ethyl alcohol was poured into the mixture, and refluxed for 1 h. After completion of the reaction, monitored by TLC using EtOAc/*n*-hexane (1:2) as eluent, the reaction mixture was filtered off to separate precipitate. Next, the precipitate was recrystallized from boiling ethanol to afford pure crystalline. The structure of novel compounds was confirmed by application of spectroscopic methods (The data are given in the Supplementary material to this paper).

Cell culture

Human breast cancer cells (MCF-7), human primary glioblastoma cells (U87), adenocarcinomic human alveolar basal epithelial cells (A549), human umbilical vein endothelial cells (HUVEC) and mouse embryonic fibroblast cell (3T3) as two normal cell lines were obtained from Pasteur Institute (Tehran, Iran) and incubated at 37 °C and 5 % CO_2 until flaunted the 75 % of the culture plate. Cells lines were grown in DMEM-F12 supplemented with 10 % FBS, 100 U mL^{-1} of penicillin-streptomycin.

(CC) 2022 SCS.

Cytotoxicity studies

For cytotoxicity assay, a cell suspension containing 10^4 cells of each cell line were seeded into each well of a flat-bottomed 96-well plate and incubated for 24 h. On the following day, the medium was aspirated and 100 µl of each concentration (1000, 100, 10, 1, 0.1, 0.01, 0.001 ppm) of examined compounds were added into each well. Then plates were incubated 24 h at 37 °C and 5 % CO_2 atmosphere. On the next day 10 µl of WST-1 solution was added to each well and incubated for 4 h. Then the optical density (*OD*) was measured at 420 nm using an Elisa reader (BioTek Elx800). Cell viability was expressed as 100 % for untreated cells (control). All measures were performed in triplicates and the survival rate (%) was calculated as:[40]

$$\text{Survival rate} = 100(OD \text{ in treatment group}/OD \text{ in control group}) \quad (1)$$

The inhibitory concentration required for 50 % cytotoxicity (IC_{50}) was calculated using the Prism dose-response histogram (Graphpad Prism, Prism 9, version 9.3.0 (463) for Windows, 1992–2021 GraphPad Software, LLC), obtained by plotting the percentage of survival versus the concentration.

To further support the results obtained by WST-1 assay, the lactate dehydrogenase (LDH) release of U87, MCF-7 and 3T3 cells after 24 h incubation with compounds number 7, 9, 11 and 12 (as representative compounds) at 10, 100 and 1000 µg mL^{-1} concentrations were measured using the supernatant of the cell culture media by LDH cytotoxicity detection kit. A 10 µl of culture media on the cell was moved to a 96-well plate and 100 µl of LDH reaction mix was added to each well. The plate was then incubated at room temperature for 30–60 min when absorbance was read using the microplate reader. The absorbance was read at 492 nm using an automatic analyzer RA-1000 (Technicon, Ireland). Triton X (1 %) was used as positive control. The 650 nm reference absorbance was subtracted from the 450 nm absorbance reading to give the well absorbance. The cytotoxicity percentage was calculated as:

$$\text{Cytotoxicity} = 100[(A_{\text{sample}} - A_{\text{low control}})/(A_{\text{high control}} - A_{\text{low control}})] \quad (2)$$

where: low control was un-treated cells (control) and high control was treated cells with triton X 1 %.

Statistical analysis

The data obtained from the WST-1 assay were evaluated by one-way ANOVA followed by Tukey's test in SPSS (statistical package for social sciences). Results were expressed as percentages of the control as the mean ± *SD*, and differences from the control groups were considered significant with $p < 0.05$. In addition, IC_{50} values of the substances were calculated by nonlinear regression analysis of triplicate experiments by the software Graphpad Prism.

RESULTS AND DISCUSSION

Chemistry

The target compounds were synthesized as outlined in Scheme 1. The condensation reaction between thiosemicarbazide and a variety of different substituted benzaldehyde or benzyloxybenzaldehyde compounds afforded the corresponding target benzylidene thiosemicarbazide derivatives (Table I). The identity of target compounds was confirmed by melting point, IR, ^{1}H- and ^{13}C-NMR spectra.

(CC) 2022 SCS.

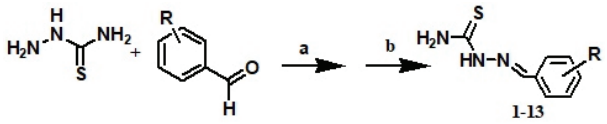

Scheme 1. Synthetic route for the target compounds. Reagents and conditions: a) NaOH solution, rt, overnight; b) EtOH, reflux, 1 h.

TABLE I. The structure of the synthesized compounds

Cmpd. No.	Structure	Cmpd. No.	Structure
1	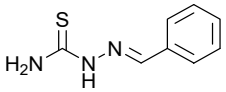	**8**	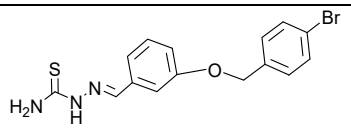
2	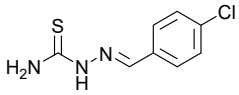	**9**	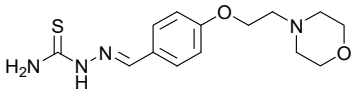
3	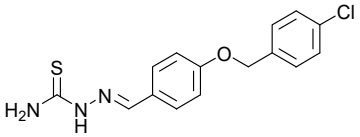	**10**	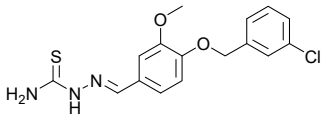
4	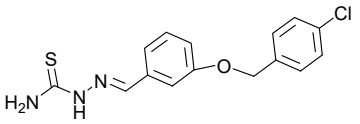	**11**	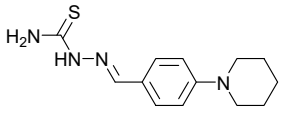
5	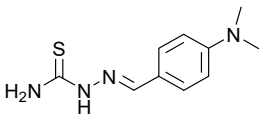	**12**	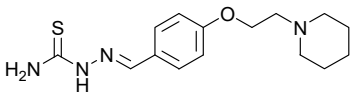
6	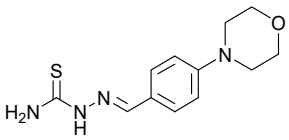	**13**	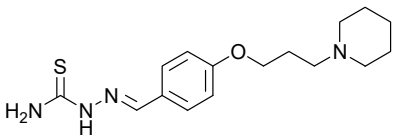
7	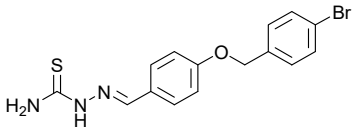		

Cytotoxicity assay

The cytotoxic effect of thiosemicarbazide derivatives (13 compounds) on MCF-7, U87, A549, HUVEC and 3T3 cell lines was determined by WST-1 and LDH assays. The toxicity of the synthesized compounds was investigated in the concentration range of 0.001 to 1000 mg L^{-1}. However, to be in line with the published results on the medicinal chemistry, the concentration of compounds in

(CC) 2022 SCS.

micromolar ranged from the least 2.75×10^{-3} (cmpd. **7**) to 5590 μM (Cmpd. **1**) which is shown in Table II. The WST-1 results are depicted as dose-response histograms in Figs. 2 and 3 and IC_{50} values in Table III. The dose-response histograms shown in Figs. 2 and 3 indicate that MCF-7 and HUVEC cell lines are the most sensitive ones against all tested compounds. Also, 3T3 and U87 cell lines were considered as the most resistant ones against all compounds at concentrations ≤ 10 μg mL^{-1}. In addition, compounds **5** with IC_{50} = 7.3 μM against MCF-7, **7** with IC_{50} = 24.73 μM against U-87, and **11** with IC_{50} of 46.37 and 46.60 μM against A549 and MCF-7, respectively, accounted for compounds with the most effective toxicity profiles. Based on statistical analysis, the results showed that the compounds used in the concentration ranges 0.001–1000 mg L^{-1} tested on MCF-7, A549 and HUVEC cell lines exhibited a significant difference ($p < 0.05$).

TABLE II. The concentration of studied compounds applied in biological assays and IC_{50} in terms of μM

Cmpd. No.	c / mg L^{-1}						
	0.001	0.01	0.1	1	10	100	1000
1	5.59×10^{-3}	5.59×10^{-2}	5.59×10^{-1}	5.59	55.9	559	5590
2	4.68×10^{-3}	4.68×10^{-2}	4.68×10^{-1}	4.68	46.8	468	4680
3	3.13×10^{-3}	3.13×10^{-2}	3.13×10^{-1}	3.13	31.3	313	3130
4	3.13×10^{-3}	3.13×10^{-2}	3.13×10^{-1}	3.13	31.3	313	3130
5	4.50×10^{-3}	4.50×10^{-2}	4.50×10^{-1}	4.50	45	450	4500
6	3.79×10^{-3}	3.79×10^{-2}	3.79×10^{-1}	3.79	37.9	379	3790
7	2.75×10^{-3}	2.75×10^{-2}	2.75×10^{-1}	2.75	27.5	275	2750
8	2.75×10^{-3}	2.75×10^{-2}	2.75×10^{-1}	2.75	27.5	275	2750
9	3.25×10^{-3}	3.25×10^{-2}	3.25×10^{-1}	3.25	32.5	325	3250
10	2.86×10^{-3}	2.86×10^{-2}	2.86×10^{-1}	2.86	28.6	286	2860
11	3.82×10^{-3}	3.82×10^{-2}	3.82×10^{-1}	3.82	38.2	382	3820
12	3.27×10^{-3}	3.27×10^{-2}	3.27×10^{-1}	3.27	32.7	327	3270
13	3.12×10^{-3}	3.12×10^{-2}	3.12×10^{-1}	3.12	31.2	312	3120

It is known that the free electrons on elements such as N, S, and O have a high tendency to bind to metal ions such as iron and copper. Because cells need metallic elements such as iron, zinc, and magnesium to grow, especially in the G/S1 phase of cell proliferation, so iron deficiency stops cell proliferation and growth.[41]

Cancer cells tend to multiply rapidly thus iron deficiency can affect them much more. Therefore, iron chelators can have anti-tumor effects.[42]

Metal chelators have the potential to inhibit iron uptake from iron-carrying proteins, inhibit the expression of iron-containing enzymes such as ribonucleotide reductase, and inhibit the formation of redox-active iron complexes that produce reactive oxygen species.[41,43] In this project, MCF-7, among cancer cell lines,

(CC) 2022 SCS.

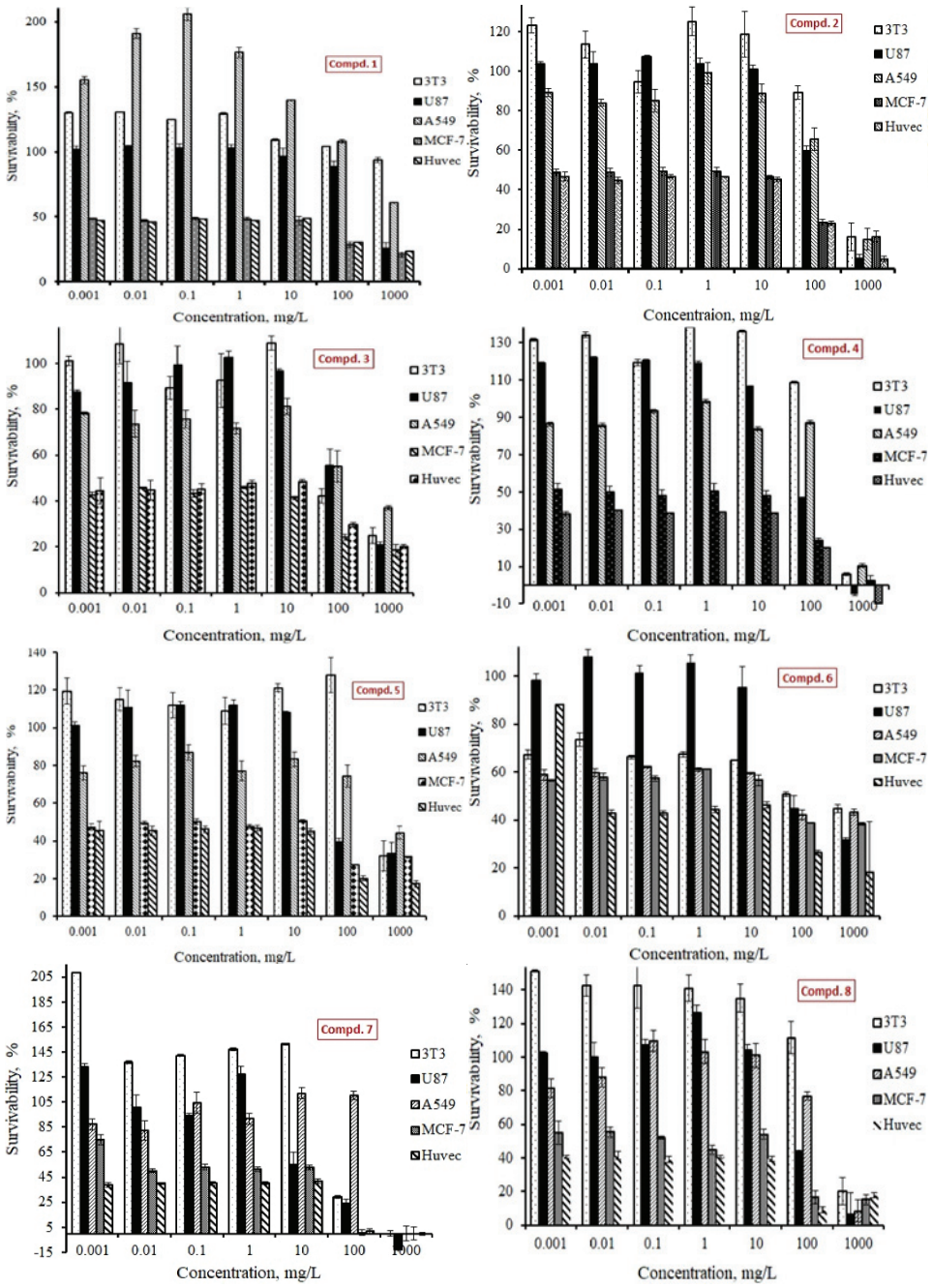

Fig. 2. The dose-response histogram of compounds 1-8 on MCF-7, U87, A549, HUVEC and 3T3 cell lines determined by WST-1 assay.

(CC) 2022 SCS.

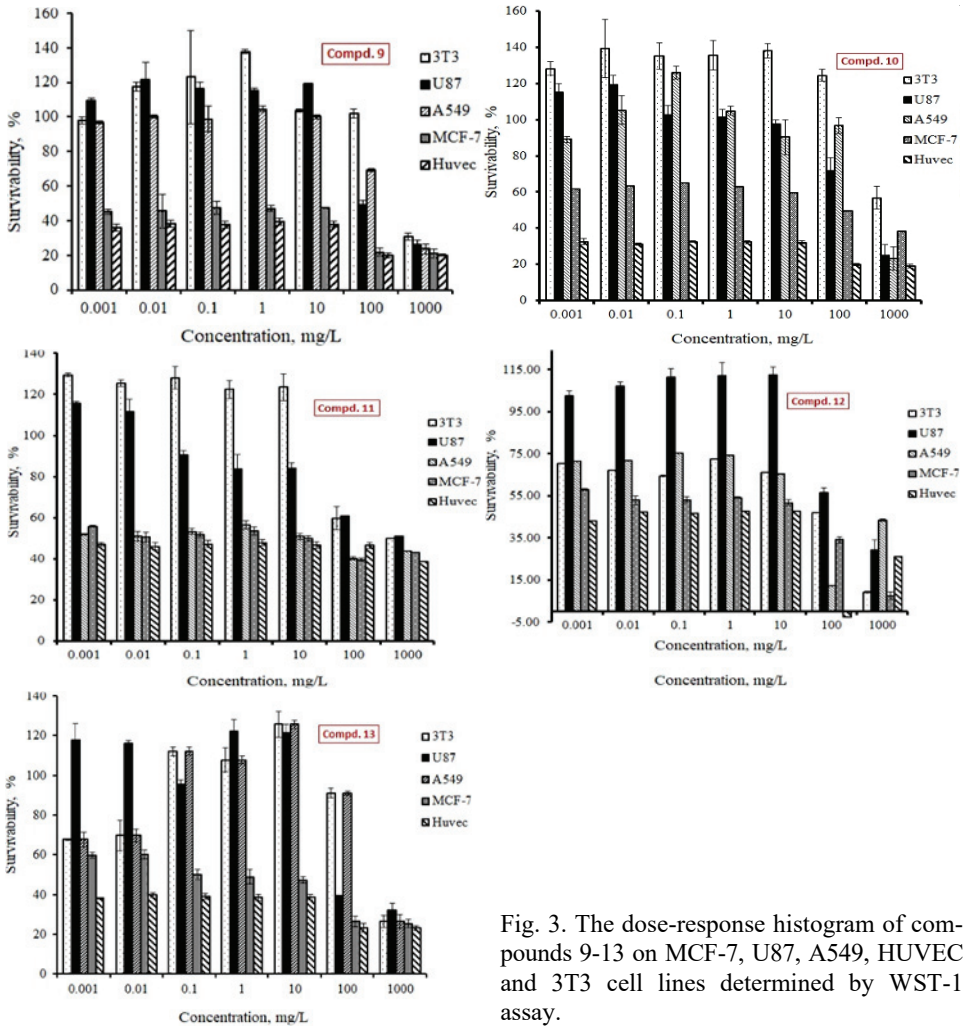

Fig. 3. The dose-response histogram of compounds 9-13 on MCF-7, U87, A549, HUVEC and 3T3 cell lines determined by WST-1 assay.

was the most sensitive cell line against all concentrations of synthesized compounds. In contrast, U87 cell line was resistant to almost all compounds at concentrations below 100 ppm and showed cell survival of more than 80 %. On the other hand, healthy cell lines showed completely different behaviour. For example, the cell line 3T3, which originates from mouse fibroblasts, showed resistance to all compounds at all concentrations, while HUVEC cell line, originating from the human umbilical cord, appeared to be sensitive to all compounds, even at low concentrations, this cell line did not show high cell survival. This sensitivity and resistance phenomena may be due to the cellular origin and the type of tissue from which the cells were extracted.

(CC) 2022 SCS.

TABLE III. The IC_{50} values of studied compounds

Cmpd. No.		A549	MCF-7	U-87	3T3	HUVEC
1	IC_{50} / μM	344.53	330.34	1509.44	67.04	506.82
	IC_{50} / mg L^{-1}	61.67	59.13	270.19	12	90.72
2	IC_{50} / μM	689.46	218.97	602.81	569.09	414.75
	IC_{50} / mg L^{-1}	147.20	46.75	128.70	121.50	88.55
3	IC_{50} / μM	305.76	133.05	305.10	265.73	290.89
	IC_{50} / mg L^{-1}	97.69	42.51	97.48	84.90	92.94
4	IC_{50} / μM	1114.65	283.41	265.20	416.59	396.56
	IC_{50} / mg L^{-1}	356.13	90.55	84.73	133.10	126.70
5	IC_{50} / μM	598.65	7.30	201.13	3862.61	180.45
	IC_{50} / mg L^{-1}	132.90	1.62	44.65	857.50	40.06
6	IC_{50} / μM	53.18	84.55	147.05	158.41	339.51
	IC_{50} / mg L^{-1}	14.04	22.32	38.82	41.82	89.63
7	IC_{50} / μM	1929.12	62.75	24.73	128.30	188.76
	IC_{50} / mg L^{-1}	702.20	22.84	9.00	46.70	68.71
8	IC_{50} / μM	346.43	175.25	200.00	350.14	52.80
	IC_{50} / mg L^{-1}	126.10	63.79	72.80	127.45	19.22
9	IC_{50} / μM	380.52	216.69	275.91	513.47	51.30
	IC_{50} / mg L^{-1}	117.20	66.74	84.98	158.15	15.80
10	IC_{50} / μM	603.95	317.31	383.69	410.30	186.29
	IC_{50} / mg L^{-1}	211.08	110.90	134.10	143.40	65.11
11	IC_{50} / μM	46.37	46.60	762.21	174.31	907.79
	IC_{50} / mg L^{-1}	12.15	12.21	199.70	45.67	237.84
12	IC_{50} / μM	350.65	540.20	296.05	354.58	754.38
	IC_{50} / mg L^{-1}	107.30	165.30	90.59	108.50	230.84
13	IC_{50} / μM	217.13	108.94	230.25	827.69	102.78
	IC_{50} / mg L^{-1}	69.48	34.86	73.68	264.86	32.89

The study carried out by Potůčková and co-workers has shown that the compound 2-benzoylpyridine-4-ethyl-3-thiosemicarbazone reveals high toxicity effects on HL-60 (human leukemia), MCF-7 and HCT116 (human colon cancer) and moderate toxicity on A549 and healthy cell line H9C2 (neonatal mouse heart cell). They claimed that 3T3 fibroblasts were the most resistant of all the cell-types to every agent examined.[44] In the research by Serda and co-workers[28] on thiosemicarbazide skeletons, derivatives that exhibited good activity as anti-cancer agents were introduced, among those the two compounds, depicted in Fig. 4, displayed the greatest promise. They attributed the anti-cancer ability of their compounds to the complexing power of thiosemicarbazides. Their study on the structure-activity relationship showed that the combination of donor atoms N, N, S in thiosemicarbazone backbone had a crucial role in the anti-cancer activity of their compounds, rather than the existence of different fragments in R position. Also, thiosemicarbazones appear to elevate the level of reactive oxygen species that disrupt the antioxidant activity of mitochondria triggering apoptosis pro-

(CC) 2022 SCS.

cess.[45] The presence of aromatic rings, attached to thiosemicarbazone moiety, increase the anti-cancer activity by DNA intercalating ability.[44]

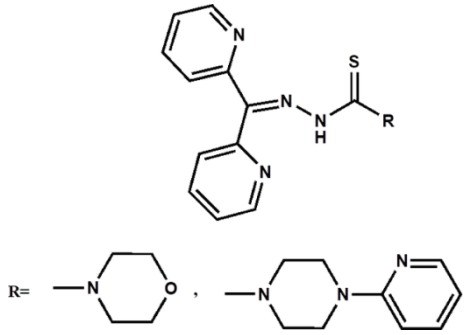

Fig. 4. Two thiosemicarbazones with good antiproliferative activity from Serda and co-workers' work.[28]

The cytotoxicity determinations were performed to confirm the toxycity effects of the synthesized compounds by WST-1 and LDH assays. Fig. 5 shows the cell viability (WST-1 assay) and cell mortality (LDH assay) results of three cell lines (MCF-7, U87 and 3T3) after treatment with four representative compounds (No. **7**, **9**, **11** and **12**) at 10, 100 and 1000 μg mL^{-1} concentrations.

First of all, WST-1 assay was done at different concentrations to recognize the IC_{50} values. All of the examined compounds showed a quality of being toxic to cells. The WST-1 technique is a common colorimetric approach to assess cytotoxicity or cell viability through determination of mitochondrial function of cell by measuring activity of mitochondrial enzymes. Also, to confirm the cell membrane damaging effects of the synthesized materials, the LDH enzyme activity was measured on the cells after being treated with three of the highest concentrations used in this project, which showed toxicity to all the cells.

Considering our WST-1 results that 3T3 and U87 cells below concentrations less than 10 μg mL^{-1} were evaluated as the most resistant cells, hence for LDH assay these cells were used in concentrations above 10. From the other cells that appeared as sensitive cells in this project, MCF-7 cell was also selected for LDH assay. Also, since the synthesizad compounds exerted high toxicity on most of the cells at high concentrations, only three high concentrations were used for LDH assay. Among all 13 synthesized compounds, only 4 representative ones were used that had good toxicity profiles on the three selected cell lines.

According to the results, all of the examined compounds showed some disturbing effect on the cell membrane and secreted more LDH enzyme. The LDH assay is used for the assessment of cytotoxicity mediated by toxic compounds and the LDH enzyme release from damaged cells. In this method, if the cells are attacked aggressively, due to the membrane destruction and cell damage, there would be more enzyme level secretion and the subsequent mortality is reported to be higher.[46] However, if cells are attacked by cellular mechanisms, low enzyme release is reported due to the lack of cell damage.

(CC) 2022 SCS.

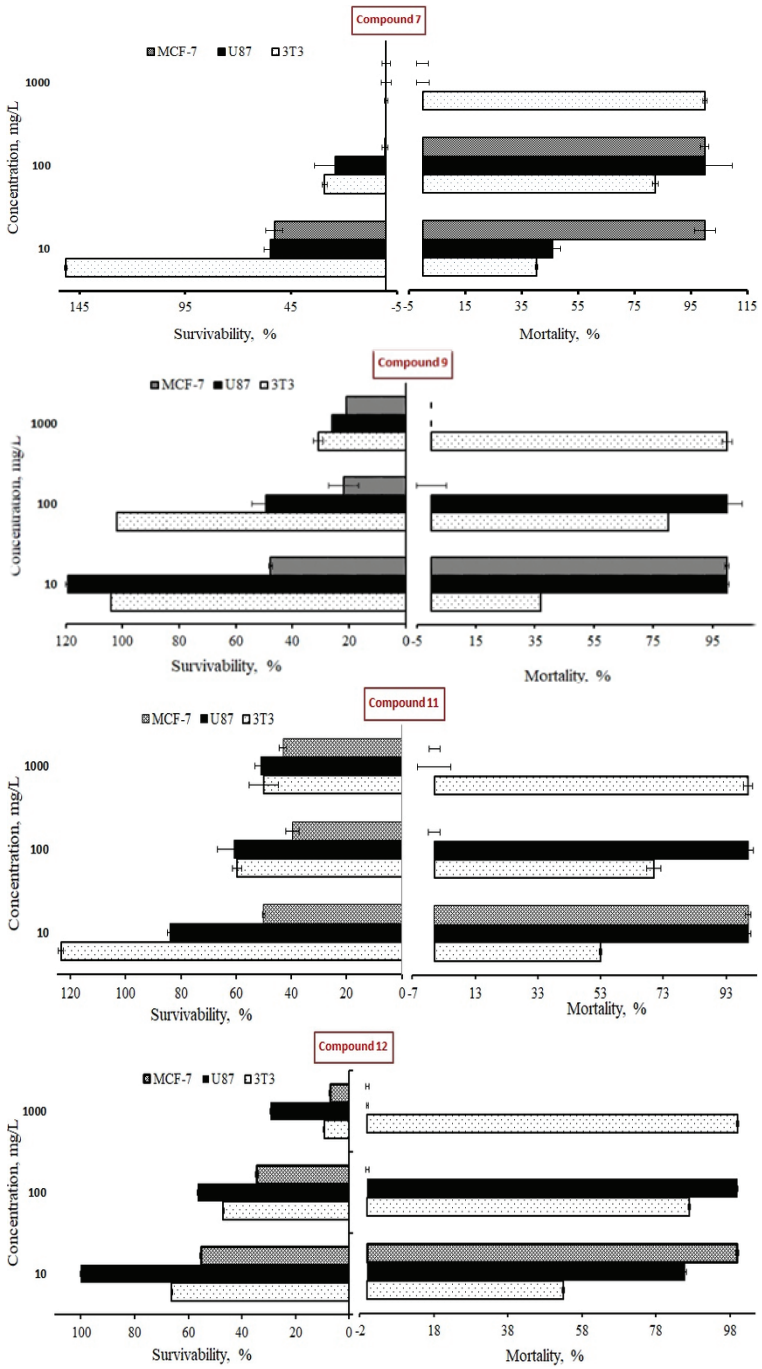

Fig. 5. The MCF-7, U87 and 3T3 cells viability (WST-1) and mortality (LDH) after treatment with various concentrations of compounds No. **7**, **9**, **11** and **12**.

(CC) 2022 SCS.

The results shown in Fig. 5 indicate that the mechanism of action of cytotoxicity of benzylidene thiosemicarbazides on cells can be addressed differently.

Against 3T3 cells, the studied compounds show their toxicity by the mechanism of cell damage and cell destruction. In a way, the more toxic the compound, the lower the cell survival rate, the higher the LDH release, which results in a higher mortality rate because cell death is achieved through cell destruction.

At high concentration, *i.e.*, 1000 mg L^{-1}, the studied compounds displayed their toxicity against U87 and MCF-7 cell lines through intracellular mechanisms and not through cell membrane damage, so that despite the low cell survival rate at this concentration, the level of LDH secretion is at its lowest level. These intracellular mechanisms can be attributed as though specified complexes probably induce apoptotic death. Compounds **9**, **11** and **12** at concentration of 100 mg L^{-1} also induced MCF-7 cell death by intracellular mechanism, but at low concentration of 10, all four benzylidene thiosemicarbazide derivatives appear to induce cell destruction leading to the death of U87 and MCF-7 cells, and consequently the rate of LDH release is proportional with the rate of cell death.

Based on Fig. 5, the behavior of U87 cell after treatment with compounds **9**, **11** and **12** at a concentration of 10 mg L^{-1} is strange. Whether this can be addressed as false positive WST-1 result – due to variable metabolic behavior under different cell culture conditions,[54] or impermeability of WST-1 and its reduction reaction at the cell surface or at the level of the plasma membrane *via* trans-plasma membrane electron transport[55] – or whether this is attributed to high LDH release – due to high spontaneous release caused by poor condition of the cells used,[56] or variability of LDH activity within different cell types[57] or other conflicting parameters are involved , this remains open for further investigations.

*Selectivity index (*SI*)*

The selectivity index (*SI*) is a measure of how differentiated a compound is against cancer cells compared to healthy cells. To evaluate the toxicity of the studied compounds, the equation 2 was used to calculate the selectivity index:[47]

$$SI = \frac{IC_{50}(\text{healty cell})}{IC_{50}(\text{cancer cell})} \quad (2)$$

The results of the selectivity index calculation are shown in Table IV. Theoretically the higher the *SI*, the safer a compound would be during treatment for a given infection and the higher the potential to be developed as a safe drug.[48] According to the acceptance criteria for selectivity index, selective compounds against cancer cells should have $SI > 10$; and compounds with *SI* lower than 10 but higher than 1 could be considered as non-selective.[47] A lower *SI* value (≥ 3) has been proposed by Weerapreeyakul *et al.* for classifying a promising anti-cancer agents.[49] However Angel Quispe *et al.* a further lower *SI* value (> 1) and rec-

(CC) 2022 SCS.

ommended for substances to be more cytotoxic to tumor cells than to normal cells.[50] Vonthron-Sénécheau *et al.* suggested an acceptance criterion of $SI \geq 10$ for plant extracts with promising antimalarial activity.[51] Compounds with $SI < 2$ are not considered as good candidates for antimalarial activity.[48] However, recently Famuyide *et al*. described $SI > 1$ for plant extracts with antibacterial effect as bioactive and non-toxic agents.[52] Due to many variations that have been presented about the selectivity acceptance criteria in different journals as mentioned above, compounds with SI below 1 are not recommended for further studies.

TABLE IV. The selectivity index values based on 3T3 or HUVEC as healthy cells

Cmpd. No.	Based on 3T3			Based on HUVEC			
	A549	MCF-7	U-87	A549	MCF-7	U-87	3T3
1	0.19	0.20	0.04	1.47	1.53	0.34	0.13
2	0.83	2.60	0.94	0.60	1.89	0.69	1.37
3	0.87	2.00	0.87	0.95	2.19	0.95	0.91
4	0.37	1.47	1.57	0.36	1.40	1.50	1.05
5	6.45	529.32	19.20	0.30	24.73	0.90	21.41
6	2.98	1.87	1.08	6.38	4.02	2.31	0.47
7	0.07	2.04	5.19	0.10	3.01	7.63	0.68
8	1.01	2.00	1.75	0.15	0.30	0.26	6.63
9	1.35	2.37	1.86	0.13	0.24	0.19	10.01
10	0.68	1.29	1.07	0.31	0.59	0.49	2.20
11	3.76	3.74	0.23	19.58	19.48	1.19	0.19
12	1.01	0.66	1.20	2.15	1.40	2.55	0.47
13	3.81	7.60	3.59	0.47	0.94	0.45	8.05

In the study of the selectivity index of the studied compounds in relation to HUVEC as healthy cell, these compounds showed the best selectivity characterrization against MCF-7 cancer cell line. Against MCF-7, the *SI* of compounds **5** and **11** far exceeded the value of 10 (more cytotoxic for tumor cells), unlike compound **9**, with the least *SI* value, which only reached a value of 0.24 (more cytotoxic for normal HUVEC cell). Also, compound **11** displayed a $SI = 19.58$, as the most promising compound against A549 and at the same time compound **7** with $SI = 7.63$ accounted for the most selective one against U-87 when compared with HUVEC. Also compounds **6** and **11** exerted a $SI > 2$ and > 1, respectively, against all three cell lines, when selectivity ratio was measured based on HUVEC cytotoxicity.

Instead, all compounds had selective toxicity against cancer cells in relation to 3T3 cells. According to this, all compounds except **1** and **12**, presented $SI > 1$ against MCF-7. Compounds **5** and **13** exerted a relatively good safe margin and promising anti-MCF-7 activity; compounds **5** and **7** against U-87 and compounds **5**, **13** and **11** against A549 showed the same selectivity profile when their cytotoxicity was compared with 3T3 cytotoxicity. In general, compound **5** presented

(CC) 2022 SCS.

the least cytotoxicity against all three cancer cell lines and the highest cytotoxicity against 3T3. In the next ranks, compounds **13**, **9** and **6** had respectively acceptable toxicity ($SI > 1$) against all three cancer cell lines compared to 3T3. Based on 3T3, compound **7** was considered as the most cytotoxic agent against A549 ($SI = 0.07$); compound **1** against MCF-7 with $SI = 0.20$ and compound **11** against U-87 with $SI = 0.23$ were considered toxic, too.

Generally, compounds **6** and **11** among other compounds showed the best selectivity against all three cancer cells. This is while compounds **6** and **11** displayed relatively low IC_{50} against all three cancer cells.

By determining the selectivity of these compounds against HUVEC,[53] the effect of the synthesized compounds on angiogenesis can be carefully estimated. By measuring the selectivity index of the compounds against HUVEC in relation to 3T3 cell, a cautious estimation of their anti-angiogenic potential can be apprized, although specific test for anti-angiogenesis evaluation should be performed to speak certainty in this regard.

Looking at the last column in the selectivity indices in Table IV, it can be said that compounds **5** and **9** (*SI* of 21.41 and 10.01, respectively) can be strongly considered as anti-angiogenic agents. Compounds **13** and **8** (*SI* of 8.05 and 6.63, respectively) are in the second place and compounds **10**, **2** and **4** with respective *SI* of 2.2, 1.37 and 1.05 ranked the third place. The other compounds can be considered as general toxic.

CONCLUSION

In this study, a series of benzylidene thiosemicarbazide derivatives were synthesized and tested for their cytotoxicity against three different cancer cell lines as well as two different normal cell lines. Although most of the derivatives possessed weak cytotoxic activity against U-87 and, to somehow, A549 cell lines, they exhibited good activity against MCF-7. Among healthy cell lines the 3T3 cell line showed resistance to all compounds at all concentrations, while HUVEC cell line appeared to be sensitive to all compounds, even at low concentrations. Based on this study, compound **5** was found to be the most potent cytotoxic agent against MCF-7 and compounds B and B against A549 and MCF-7 showed the highest cytotoxicity. This is while compounds **6** and **11** displayed the best selectivity profiles. Based on LDH results, we can say that benzylidene thiosemicarbazides show toxicity through different actions. At high concentrations they show their toxicity by possible formation of specified complexes inducing apoptotic mechanisms whist at low concentration, they follow destructive approaches.

SUPPLEMENTARY MATERIAL

Additional data and information are available electronically at the pages of journal website: https://www.shd-pub.org.rs/index.php/JSCS/article/view/10908, or from the corresponding author on request.

(CC) 2022 SCS.

ИЗВОД

СИНТЕЗА НЕКИХ ДЕРИВАТА БЕНЗИЛИДЕН-ТИОСЕМИКАРБАЗИДА И ПРОЦЕНА ЊИХОВЕ ЦИТОТОКСИЧНОСТИ НА U87, MCF-7, A549, 3T3 И HUVEC ЋЕЛИЈСКИМ ЛИНИЈАМА

TOUBA ESLAMINEJAD[1], YAGHOUB POURSHOJAEI[1,2], MAHMOOD NAGHIZADEH[2], HODA ESLAMI[2], MOHAMMAD DANESHPAJOUH[2] и ABDOLREZA HASSANZADEH[1,2]

[1]*Pharmaceutics Research Centre, Institute of Neuropharmacology, Kerman University of Medical Sciences, Kerman, Iran и* [2]*Department of Medicinal Chemistry, Faculty of Pharmacy, Kerman University of Medical Sciences, Kerman, Iran*

Хомеостаза гвожђа се мења у туморима као одговор на поремећај у експресији протеина зависних од гвожђа. Због тога, хелатори гвожђа чине ћелије рака рањивијим на недостатак гвожђа. Једињења која имају тиосемикарбазидну структуру са способношћу формирања металних комплекса имају потенцијал да делују антиканцерно. Серија деривата тиосемикарбазида је дизајнирана и успешно синтетизована, а њихова цитотоксичност је затим тестирана на неким канцерогеним, као и на лабораторијским нормалним моделним системима, коришћењем колориметријског теста заснованог на WST-1 реагенсу. Према резултатима цитотоксичности, нека једињења су показала висок токсични ефекат и на канцерогене и на здраве ћелијске линије. Резултати испитивања токсичности на ћелијским линијама U87 и A549 су показали преживљавање мање од 50 % при свим концентрацијама већим од 10 ppm за сва синтетизована једињења. Ћелијска линија MCF-7 је показала приближно исто понашање и имала је преживљавање мање од 60 %. 3T3 у поређењу са HUVEC ћелијском линијом показао је потпуно другачије понашање у односу на синтетизована једињења и имао је преживљавање више од 50 %. Измерен је и индекс селективности и на основу резултата студије може се закључити да профил цитотоксичности синтетизованих једињења на 3T3 ћелијској линији показује значајну разлику, што указује на добар антиканцерогени ефекат ових једињења.

(Примљено 30. јуна 2021, ревидирано 15. јануара, прихваћено 24. фебруара 2022)

REFERENCES

1. N. D. Amoêdo, J. P. Valencia, M. F. Rodrigues, A. Galina, F. D. Rumjanek, *Biosci. Rep.* **33** (2013) e00080 (https://doi.org/10.1042/BSR20130066)
2. G. Kroemer, J. Pouyssegur, *Cancer Cell* **13** (2008) 472 (https://doi.org/10.1016/j.ccr.2008.05.005)
3. S. Romero-Garcia, J. S. Lopez-Gonzalez, J. L. B´ez-Viveros, D. Aguilar-Cazares, H. Prado-Garcia, *Cancer Biol. Ther.* **12** (2011) 939 (https://doi.org/10.4161/cbt.12.11.18140)
4. V. Ganapathy, M. Thangaraju, P. D. Prasad, *Pharmacol. Ther.* **121** (2009) 29 (https://doi.org/10.1016/j.pharmthera.2008.09.005)
5. E. S. Cho, Y. H. Cha, H. S. Kim, N. H. Kim, J. I. Yook, *Biomol. Ther.* (*Seoul*) **26** (2018) 29 (https://doi.org/10.4062/biomolther.2017.179)
6. J. C. Kwok, D. R. Richardson, *Crit. Rev. Oncol. Hematol.* **42** (2002) 65 (https://doi.org/10.1016/S1040-8428(01)00213-X)
7. R. Luria-Pérez, G. Helguera, J. A. Rodríguez, *Bol. Med. Hosp. Infant Mex.* **73** (2016) 372 (https://doi.org/10.1016/j.bmhimx.2016.11.004)
8. I. S. Trowbridge, F. Lopez, *Proc. Natl. Acad. Sci. U.S.A.* **79** (1982) 1175 (https://doi.org/10.1073/pnas.79.4.1175)
9. N. C. Andrews, *Nat. Rev. Genet.* **1** (2000) 208 (https://doi.org/10.1038/35042073)

(CC) 2022 SCS.

10. A. Kicic, A. C. Chua, E. Baker, *Br. J. Pharmacol*. **135** (2002) 1393 (https://doi.org/10.1038/sj.bjp.0704507)
11. C. Brodie, G. Siriwardana, J. Lucas, R. Schleicher, N. Terada, A. Szepesi, E. Celfand, P. Seligman, *Cancer Res*. **53** (1993) 3968 (https://pubmed.ncbi.nlm.nih.gov/8358725/)
12. L. Dezza, M. Cazzola, M. Danova, C. Carlo-Stella, G. Bergamaschi, S. Brugnatelli, R. Invernizzi, G. Mazzini, A. Riccardi, E. Ascari, *Leukemia* **3** (1989) 104 (https://pubmed.ncbi.nlm.nih.gov/2911202/)
13. D. S. Kalinowski, D. R. Richardson, *Pharmacol. Rev*. **57** (2005) 547 (https://doi.org/10.1124/pr.57.4.2)
14. N. T. Le, D. R. Richardson, *Biochim. Biophys. Acta* **1603** (2002) 31 (https://doi.org/10.1016/S0304-419X(02)00068-9)
15. J. L. Buss, B. T. Greene, J. Turner, F. M. Torti, S. V. Torti, *Curr. Top. Med. Chem*. **4** (2004) 1623 (https://doi.org/10.2174/1568026043387269)
16. C. R. Chitambar, P. A. Seligman, *J. Clin. Invest*. **78** (1986) 1538 (https://doi.org/10.1172/jci112746)
17. L. Witt, T. Yap, R. L. Blakley, *Adv. Enzyme Regul*. **17** (1979) 157 (https://doi.org/10.1016/0065-2571(79)90012-8)
18. G. Weber, *New Engl. J. Med*. **296** (1977) 486 (https://www.nejm.org/doi/full/10.1056/NEJM197703032960905)
19. T. R. Bal, B. Anand, P. Yogeeswari, D. Sriram, *Bioorg. Med. Chem. Lett*. **15** (2005) 4451 (https://doi.org/10.1016/j.bmcl.2005.07.046)
20. D. R. Patel, S. M. Divatia, E. Clercq, *Indian J. Chem., B* **52** (2013) 535 (http://nopr.niscair.res.in/handle/123456789/16888)
21. D. J. Bauer, *Chemotherapy of Virus Diseases*, Pergamon Press, Oxford, 1972 (ISBN: 0080169619)
22. C. C. Pacca, R.E. Marques, J. W. P. Espindola, G. B. O. O Filho, A. C. L. Leite, M. M Teixeira, M. L. Nogueira, *Biomed. Pharmacother*. **87** (2017) 381 (https://doi.org/10.1016/j.biopha.2016.12.112)
23. M. Sheikhy, A. Jalilian , A. Novinrooz, F. Motamedi-Sedeh, *J. Biomed. Sci. Eng*. **5** (2012) 39 (http://dx.doi.org/10.4236/jbise.2012.52006)
24. A. M. Omar, H. N. Eshba, H. M. Salama, *Arch. Pharm. (Weinheim)* **317** (1984) 701 (https://doi.org/10.1002/ardp.19843170810)
25. M. D. Hall, N. K. Salam, J. L. Hellawell, H. M. Fales, C. B. Kensler, J. A. Ludwig, G. Szakács, D. E. Hibbs, M. M. Gottesman, *J. Med. Chem*. **52** (2009) 3191 (https://doi.org/10.1021/jm800861c)
26. X.-M. Zhang, H. Guo, Z.-S. Li, F.-H. Song, W.-M. Wang, H.-Q. Dai, L.-X. Zhang, J.-G. Wang, *Eur. J. Med. Chem*. **101** (2015) 419 (https://doi.org/10.1016/j.ejmech.2015.06.047)
27. F. Degola, C. Morcia, F. Bisceglie, F. Mussi, G. Tumino, R. Ghizzoni, G. Pelosi, V. Terzi, A. Buschini, F. M. Restivo, T. Lodi, *Int. J. Food. Microbiol*. **200** (2015) 104 (https://doi.org/10.1016/j.ijfoodmicro.2015.02.009)
28. M. Serda, D. S. Kalinowski, N. Rasko, E. Potůčková, A. Mrozek-Wilczkiewicz, R. Musiol, J. G. Małecki, M. Sajewicz, A. Ratuszna, A. Muchowicz, J. Gołąb, T. Simůnek, D. R. Richardson, J. Polanski, *PLoS One* **9** (2014) e110291 (https://doi.org/10.1371/journal.pone.0110291)
29. D. R. Richardson, P. C. Sharpe, D. B. Lovejoy, D. Senaratne, D. S. Kalinowski, M. Islam, P. V. Bernhardt, *J. Med. Chem*. **49** (2006) 6510 (https://doi.org/10.1021/jm0606342)

(CC) 2022 SCS.

30. M. C. Liu, T. S. Lin, A. C. Sartorelli, *J. Med. Chem*. **35** (1992) 3672 (https://doi.org/10.1021/jm00098a012)
31. C. A. Kunos, S. Waggoner, V. von Gruenigen, E. Eldermire, J. Pink, A. Dowlati, T. J. Kinsella, *Clin. Cancer.* Res. **16** (2010) 1298 (https://clincancerres.aacrjournals.org/content/16/4/1298)
32. C. A. Kunos, T. Radivoyevitch, S. Waggoner, R. Debernardo, K. Zanotti, K. Resnick, N. Fusco, R. Adams, R. Redline, P. Faulhaber, A. Dowlati, *Gynecol. Oncol*. **130** (2013) 75 (https://doi.org/10.1016/j.ygyno.2013.04.019)
33. C. A. Kunos, T. M. Sherertz, *Front. Oncol*. **4** (2014) 184 (https://doi.org/10.3389/fonc.2014.00184)
34. J. Shao, B. Zhou, A. J. Di Bilio, L. Zhu, T. Wang, C. Qi, J. Shih, Y. Yen, *Mol. Cancer. Ther*. **5** (2006) 586 (https://mct.aacrjournals.org/content/5/3/586)
35. D. J. Bauer, L. Stvincent, C .H. Kempe, A. W. Downie, *Lancet* **2** (1963) 494 (https://doi.org/10.1016/S0140-6736(63)90230-7)
36. D. J. Bauer, *Ann. N.Y. Acad. Sci.* **130** (1965) 110 (https://doi.org/10.1111/j.1749-6632.1965.tb12545.x)
37. L. Sebastian, A. Desai, M. N. Shampur, Y. Perumal, D. Sriram, R. Vasanthapuram, *Virol. J*. **5** (2008) 64 (https://doi.org/10.1186/1743-422X-5-64)
38. S. Arora, S. Agarwal, S. Singhal. *Int. J. Pharm. Pharm. Sci*. **6** (2014) 34 (https://innovareacademics.in/journals/index.php/ijpps/article/view/1837)
39. Y. Yu, D. S. Kalinowski, Z. Kovacevic, A. R. Siafakas, P. J. Jansson, C. Stefani, D. B. Lovejoy, P. C. Sharpe, P. V. Bernhardt, D. R. Richardson. *J. Med. Chem*. **52** (2009) 5271 (https://doi.org/10.1021/jm900552r)
40. T. Eslaminejad, S. N. Nematollahi-Mahani, M. Ansari, *J. Magn. Magn. Mater*. 402 (2016) 34 (https://doi.org/10.1016/j.jmmm.2015.11.037)
41. Y. Yu, D. S. Kalinowski, Z. Kovacevic, A. R. Siafakas, P. J. Jansson, C. Stefani, D. B. Lovejoy, P. C. Sharpe, P. V. Bernhardt, D. R. Richardson, *J. Med. Chem*. **52** (2009) 5271 (https://doi.org/10.1021/jm900552r)
42. M. Whitnall, J. Howard, P. Ponka, D. R. Richardson, *Proc. Natl. Acad. Sci. U.S.A*. **103** (2006) 14901 (https://doi.org/10.1073/pnas.0604979103)
43. L. M. Bystrom, M. L. Guzman, S. Rivella, *Antioxid. Redox. Signal*. **20** (2014) 1917 (https://doi.org/10.1089/ars.2012.5014)
44. E. Eliška Potůčková, J. Roh, M. Macháček, S. Sahni, J. Stariat, V. Šesták, H. Jansová, P. Hašková, A. Jirkovská, K. Vávrová, P. Kovaříková, D. S. Kalinowski , D. R. Richardson, T. Šimůnek, *PLoS One* **10** (2015) e0139929 (https://doi.org/10.1371/journal.pone.0139929)
45. K. Malarz, A. Mrozek-Wilczkiewicz, M. Serda, M. Rejmund, J. Polanski, R. Musiol, *Oncotarget*. **9** (2018) 17689 (https://doi.org/10.18632/oncotarget.24844)
46. T. Decker, M. L. Lohmann-Matthes, *J. Immunol. Methods* **115** (1988) 61 (https://doi.org/10.1016/0022-1759(88)90310-9)
47. O. A. Peña-Morán, M. L. Villarreal, L. Álvarez-Berber, A. Meneses-Acosta, V. Rodríguez-López, *Molecules* **21** (2016) 1013 (https://doi.org/10.3390/molecules21081013)
48. F. Nogueira, V. E. do Rosário, *Rev. Pan-Amaz. Saúde* **1** (2010) 109 (https://doi.org/10.5123/S2176-62232010000300015)
49. N. Weerapreeyakul, A. Nonpunya, S. Barusrux, T. Thitimetharoch, B. Sripanidkulchai, *Chin. Med*. **7** (2012) 15 (https://doi.org/10.1186/1749-8546-7-15)

(CC) 2022 SCS.

50. M. Angel Quispe, C. David Zavala, C. José Rojas, R. Margarita Posso, W. Abraham Vaisberg, *Rev. Perú Med. Exp. Public Health* **23** (2006) 265 (http://www.scielo.org.pe/scielo.php?script=sci_arttext&pid=S1726-46342006000400006&lng=es)
51. C. Vonthron-Sénécheau, B. Weniger, M. Ouattara, F. T. Bi, A. Kamenan, A. Lobstein, R. Brun, R. Anton, *J. Ethnopharmacol*. **87** (2003) 221 (https://doi.org/10.1016/s0378-8741(03)00144-2)
52. I. M. Famuyide, A. O. Aro, F. O. Fasina, J. N. Eloff, L. J. McGaw, *BMC Complement. Altern. Med*. **19** (2019) 141 (https://doi.org/10.1186/s12906-019-2547-z)
53. B. Y. A. El-Aarag, T. Kasai, M. A. H. Zahran, N. I. Zakhary, T. Shigehiro, S. C. Sekhar, H. S. Agwa, A. Mizutani, H. Murakami, H. Kakuta, M. Seno, *Int. Immunopharmacol*. **21** (2014) 283 (https://doi.org/10.1016/j.intimp.2014.05.007)
54. S. Akter, R. Addepalli, M. E. Netzel, U. Tinggi, M. T. Fletcher, Y. Sultanbawa, S. A. Osborne, *Antioxidants* **8** (2019) 191 (https://doi.org/10.3390/antiox8060191)
55. M. V. Berridge, P. M. Herst, A. S. Tan, *Biotechnol. Ann. Rev*. **11** (2005) 127 (https://doi.org/10.1016/S1387-2656(05)11004-7)
56. Cat. #MK401, Takara, Shiga, Japan, 2019 (https://www.takarabio.com/documents/User%20Manual/MK401/MK401_e.v1906.pdf)
57. S. Kaja, A. J. Payne, Y. Naumchuk, P. Koulen, *Curr. Protoc. Toxicol*. **72** (2017) 2.26.1 (https://doi.org/10.1002/cptx.21).

(CC) 2022 SCS.

Journal of the Serbian Chemical Society
JSCS@tmf.bg.ac.rs • www.shd.org.rs/JSCS
J. Serb. Chem. Soc. 87 (10) S360–S378 (2022) *Supplementary material*

SUPPLEMENTARY MATERIAL TO

Synthesis of some benzylidene thiosemicarbazide derivatives and evaluation of their cytotoxicity on U87, MCF-7, A549, 3T3 and HUVEC cell lines

TOUBA ESLAMINEJAD[1], YAGHOUB POURSHOJAEI[1,2], MAHMOOD NAGHIZADEH[2], HODA ESLAMI[2], MOHAMMAD DANESHPAJOUH[2] and ABDOLREZA HASSANZADEH[1,2]*

[1]*Pharmaceutics Research Centre, Institute of Neuropharmacology, Kerman University of Medical Sciences, Kerman, Iran and* [2]*Department of Medicinal Chemistry, Faculty of Pharmacy, Kerman University of Medical Sciences, Kerman, Iran*

J. Serb. Chem. Soc. 87 (10) (2022) 1125–1142

EXPERIMENTAL DETAILS

The crude products obtained during the synthesis reactions were first recrystallized from ethanol and then their purity was checked by a TLC-Grade silica gel-G/UV 254 nm plate using EtOAc/n-hexane (1:2) as eluent. Melting points were determined on an electrothermal IA9100 melting point apparatus and were not corrected. In the case of known compounds, their melting points were compared with the reference and their IR spectra was analysed for identification purpose. The IR spectra were recorded on an FT-IR Tensor 27 infrared spectrophotometer (Bruker) using KBr as a matrix. For the novel compounds, in addition to IR spectra, ^{1}H & ^{1}3C NMR spectra were also recorded. ^{1}H NMR and ^{13}C NMR spectra were taken by an FT-NMR Bruker Avance Ultra Shield Spectrometer (300 and 75 MHz in frequencies for ^{1}H and ^{13}C, respectively) using DMSO-d_6 as solvent and as the internal standard. Chemical shifts are expressed in ppm (δ / ppm) values and coupling constants in Hz (J / Hz).

General procedures for the synthesis of compounds 1-13

To a solution of 0.1 g NaOH in 5 mL water, 1 mmol corresponding aldehyde was added under stirring. Then 1 mmol thiosemicarbazide was gradually added to the solution and under room temperature the mixture was stirred overnight. Then 5 mL ethyl alcohol was poured into the mixture, and it was refluxed for 1 h. After completion of the reaction, monitored by TLC using EtOAc/n-hexane (1:2) as eluent, the reaction mixture was filtered off to separate precipitate. Next, the precipitate was recrystallized from boiling ethanol to afford pure crystalline. The structure of novel compounds was confirmed by application of spectroscopic methods.

* Corresponding author. E-mail: a_hassanzadeh@kmu.ac.ir

Available on line at www.shd.org.rs/JSCS/
(CC) 2022 SCS.

*(E)-1-benzylidenethiosemicarbazide (**1**):*

Yield 75 %; m.p. 160-161 °C (literature data: 162-165 °C[1,2]); IR (KBr) ν_{max} (cm^{-1}): 3423 (NH), 3253, 3156 (NH_2), 1590 (C=N), 1299 (C=S).

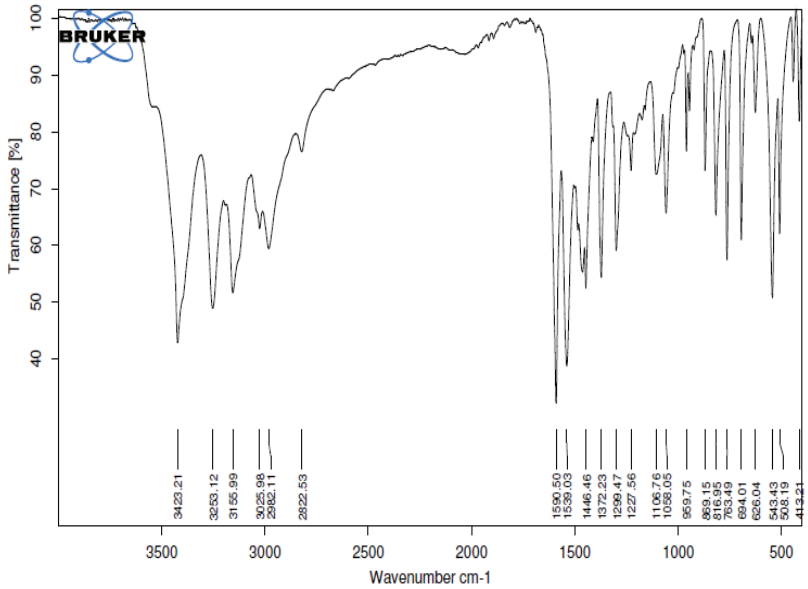

Fig S-1. IR spectrum of compound **1**

*(E)-1-(4-chlorobenzylidene)thiosemicarbazide (compound **2**)*

Yield 90 %; m.p. 222-225 °C (literature data: 217-220 °C[3]); IR (KBr) ν_{max} (cm^{-1}): 3436 (NH), 3280, 3164 (NH_2), 1600 (C=N), 1281 (C=S), 815 (C-Cl).

(CC) 2022 SCS.

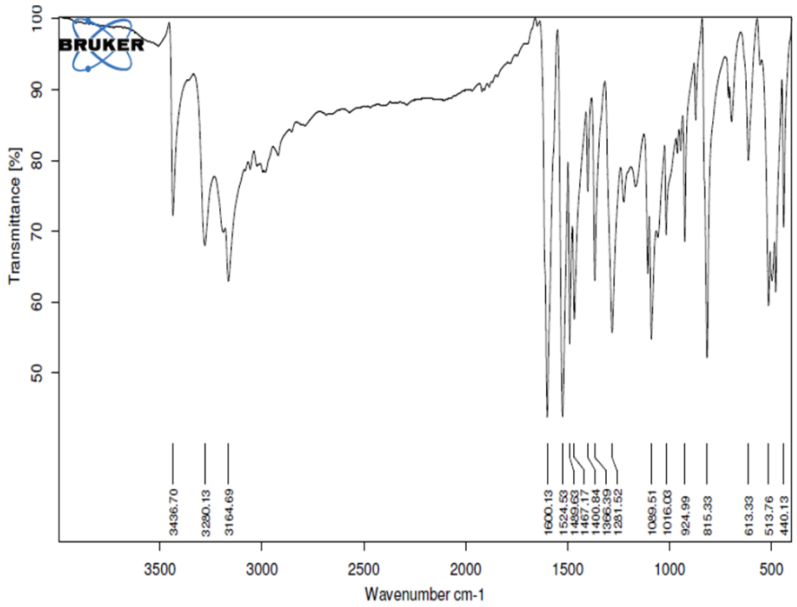

Fig. S-2. IR spectrum of compound **2**

*(E)-1-(4-(4-chlorobenzyloxy)benzylidene)thiosemicarbazide (compound **3**)*

Yield 85 %; m.p. 194-195 °C (literature data: 194 °C[4]); IR (KBr) ν_{max} (cm^{-1}): 3419 (NH), 3288, 3165 (NH_2), 1594 (C=N), 1231 (C=S). ^{1}H NMR (300 MHz, DMSO-d_6) δ (ppm): 11.36 (1H, s, NH), 8.15 (1H, s, NH), 8.02 (1H, s, NH), 7.95 (1H, s, CH), 7.77 (2H, d, J = 9 Hz, 2CHAr), 7.52-7.45 (4H, m, 4CHAr), 7.04 (2H, d, J = 9 Hz, 2CHAr), 5.16 (2H, s, OCH_2). ^{13}C NMR ($CDCl_3$, 75 MHz) δ (ppm): 178.1, 160.0, 142.5, 136.3, 132.9, 130.0, 129.3, 128.9, 127.5, 115.4, 68.9 (CH_2).

(CC) 2022 SCS.

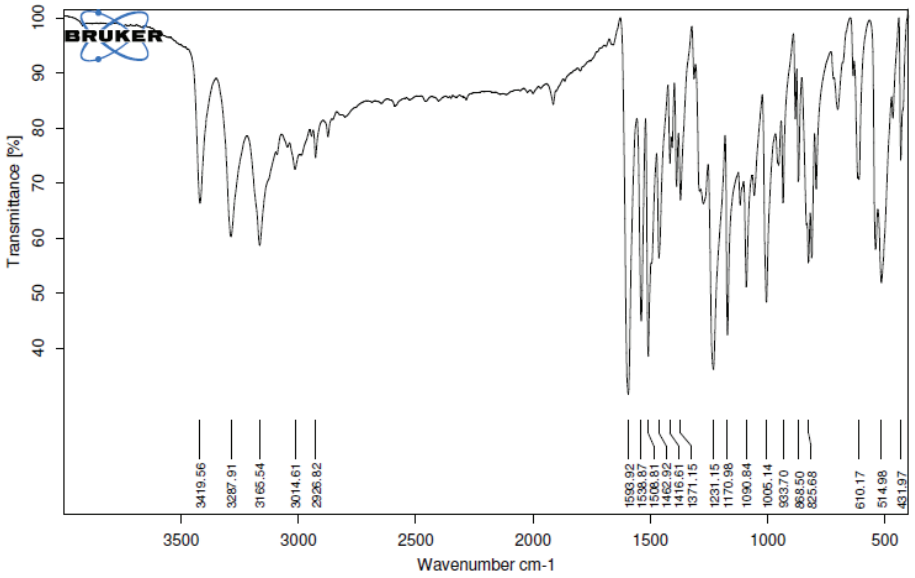

Fig. S-3. IR spectrum of compound **3**

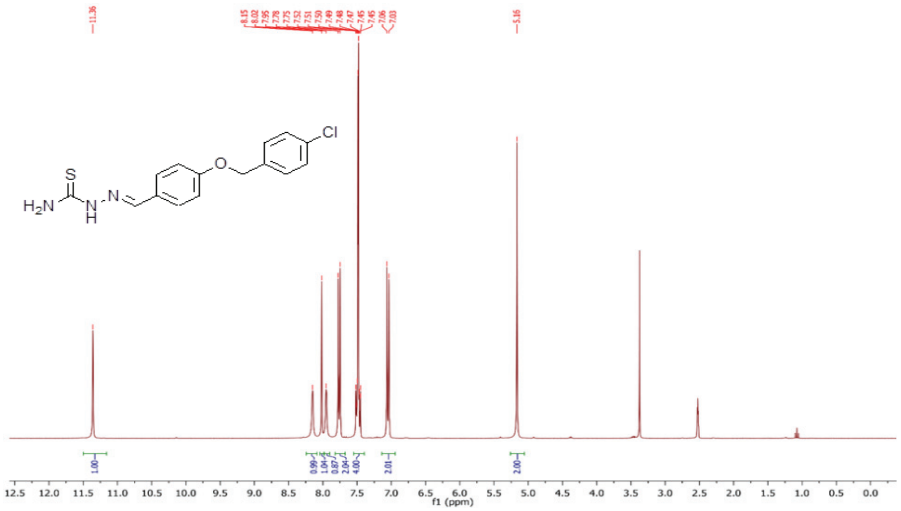

Fig S-4. ^{1}H NMR spectrum of compound **3**

(CC) 2022 SCS.

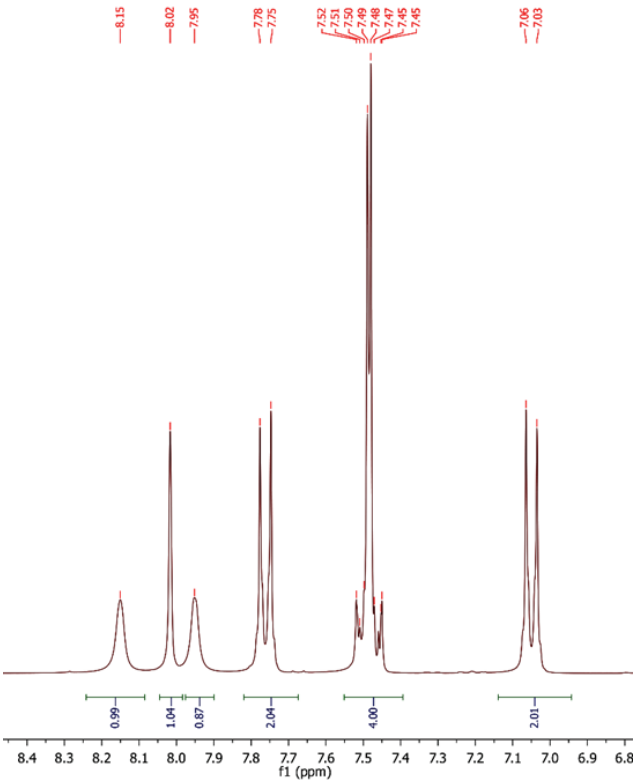

Fig S-5. ^{1}H NMR expanded spectrum of compound **3**

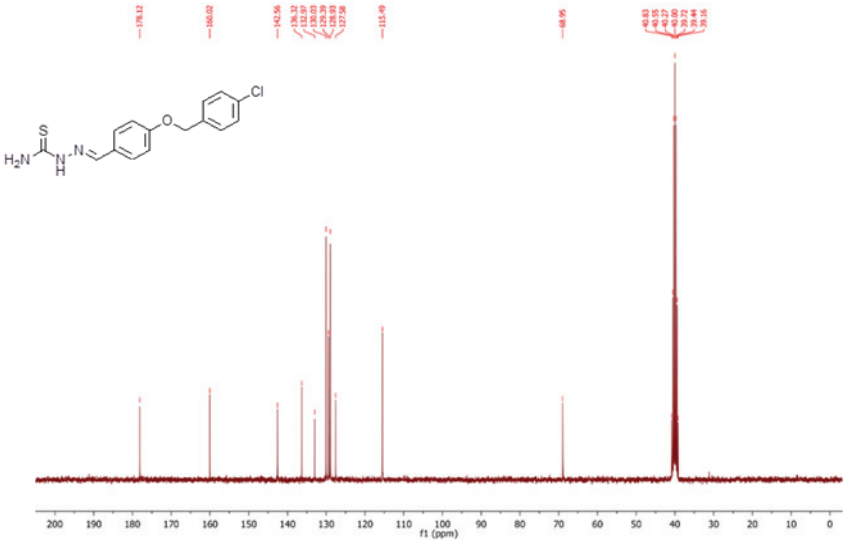

Fig S-6. ^{13}C NMR spectrum of compound **3**

(CC) 2022 SCS.

*(E)-1-(3-(4-chlorobenzyloxy)benzylidene)thiosemicarbazide (compound **4**)*

Yield 85%; m.p. 165-167 °C (literature data: 160 °C[5]); IR (KBr) ν_{max} (cm^{-1}): 3429 (NH), 3252, 3155 (NH_2), 1610(C=N), 1269 (C=S). ^1H NMR (300 MHz, DMSO-d_6) δ (ppm): 11.47 (1H, s, NH), 8.26 (1H, s, NH), 8.1 (1H, s, NH), 8.04 (1H,s, CHAr), 7.6 (1H, s, CHAr), 7.54-7.46 (4H, m, 4CHAr), 7.36-7.27 (2H, m, 2CHAr), 7.06-7.03(1H, m, CHAr), 5.17(2H, s, OCH_2). ^{13}C NMR ($CDCl_3$, 75 MHz) δ (ppm): 178.4, 158.9, 142.4, 136.5, 136.1, 132.9, 130.2, 130.1, 128.9, 121.5, 117.4, 112.2, 68.9 (CH_2).

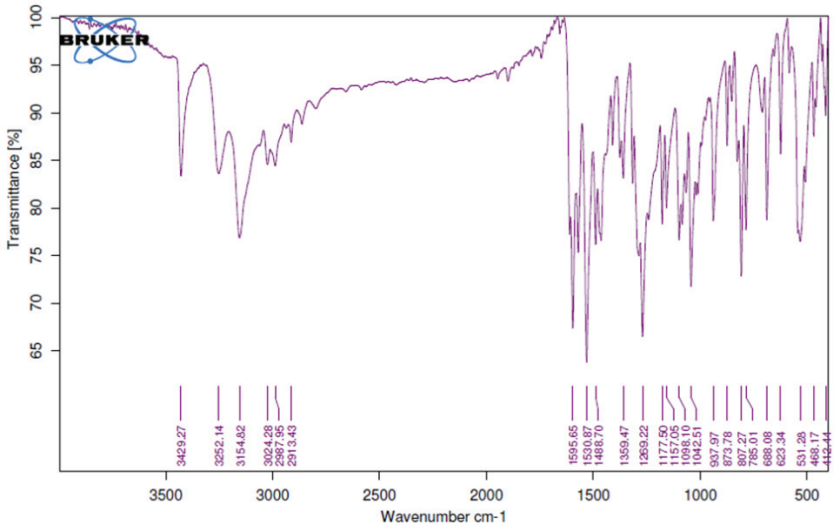

Fig S-7. IR spectrum of compound **4**

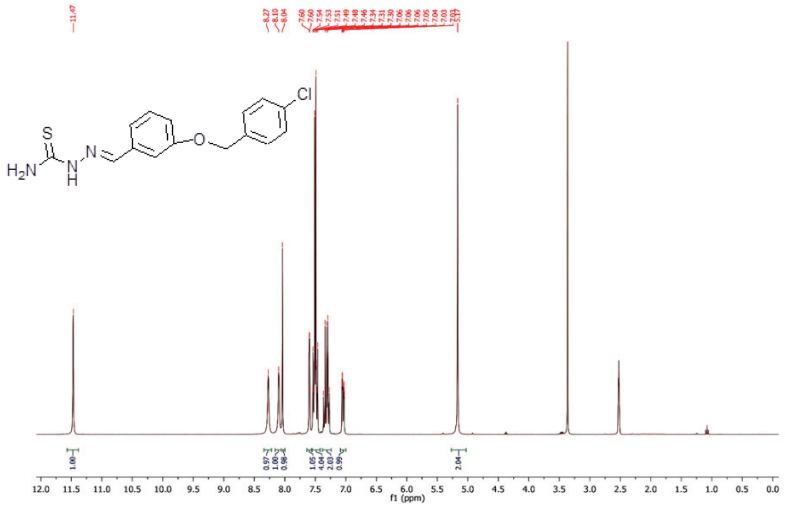

Fig S-8. ^1H NMR spectrum of compound **4**

(CC) 2022 SCS.

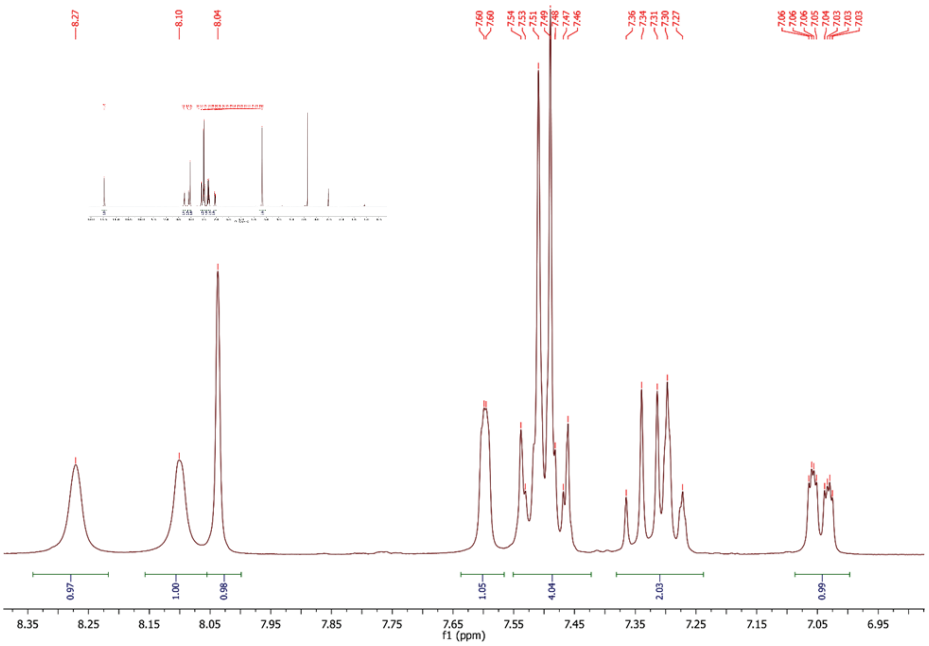

Fig S-9. ^{1}H NMR expanded spectrum of compound **4**

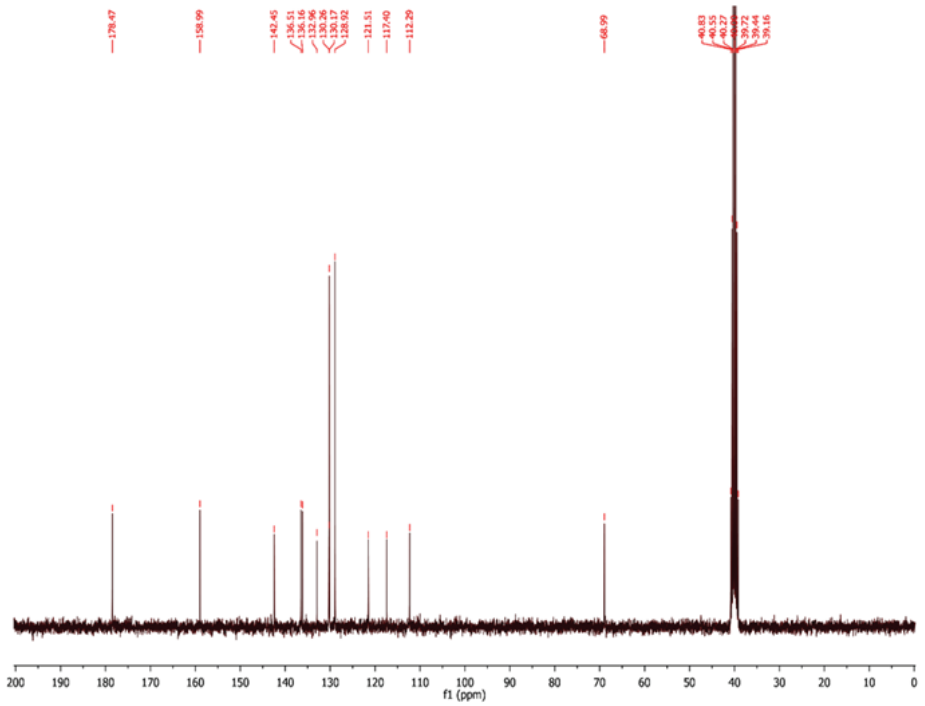

Fig S-10. ^{13}C NMR spectrum of compound **4**

(CC) 2022 SCS.

*(E)-1-(4-(dimethylamino)benzylidene)thiosemicarbazide (compound **5**)*

Yield 80 %; m.p. 209-212 °C (literature data: 210-211 °C[6,7]); IR (KBr) ν_{max} (cm^{-1}): 3378 (NH), 3257, 3157 (NH_2), 1598 (C=N), 1229 (C=S).

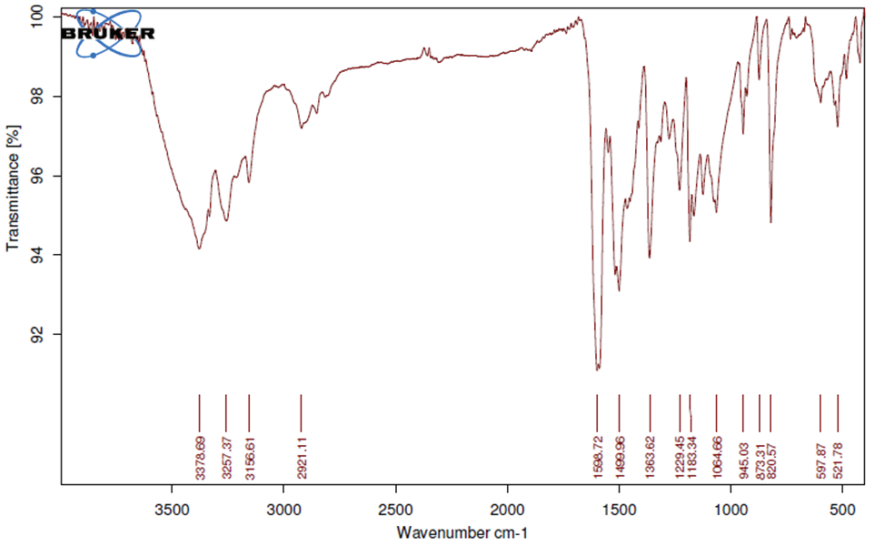

Fig S-11. IR spectrum of compound **5**

*(E)-1-(4-morpholinobenzylidene)thiosemicarbazide (compound **6**)*

Yield 80 %; m.p 210-213 °C (decomp.) (literature data: 208.5 °C with decomposition[8]); IR (KBr) ν_{max} (cm^{-1}): 3375 (NH), 3266, 3157 (NH_2), 1605 (C=N), 1230 (C=S).

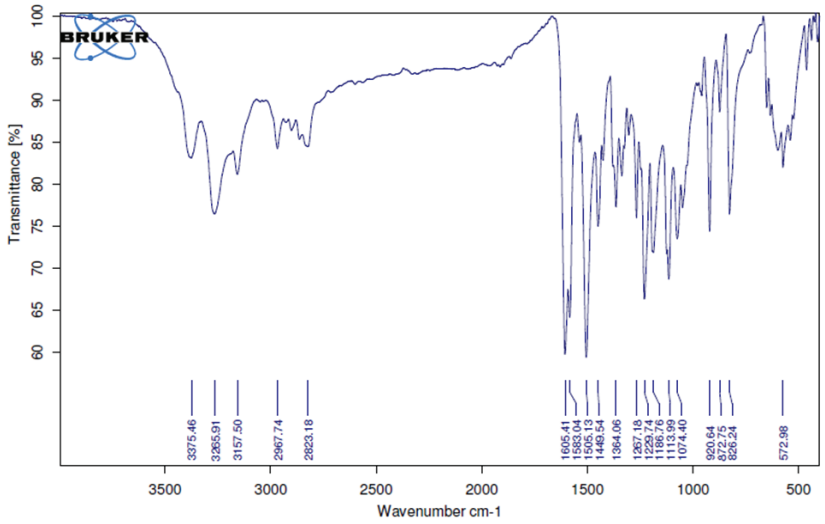

Fig S-12. IR spectrum of compound **6**

(CC) 2022 SCS.

(E)-1-(4-(4-bromobenzyloxy)benzylidene)thiosemicarbazide (compound 7)

Yield 85 %; m.p. 199-201 °C (literature data: 187 ºC[4]); IR (KBr) ν_{max} (cm^{-1}): 3419 (NH), 3289, 3161 (NH_2), 1601 (C=N), 1583, 1244 (C=S). ^{1}H NMR (300 MHz, DMSO-d6) δ (ppm): 11.36 (1H, s, NH), 8.15 (H, s, NH), 8.02 (1H, s, CH), 9.95 (1H, s, NH), 7.77 (2H, d, J = 9 Hz, 2CHAr), 7.61 (2H, d, J = 9 Hz, 2CHAr), 7.44 (2H, d, J = 9 Hz, 2CHAr), 7.05 (2H, d, J = 9 Hz, 2CHAr), 5.15 (2H, s, OCH_2). ^{13}C NMR (75 MHz, $CDCl_3$) δ (ppm): 178.5, 158.9, 142.5, 136.9, 136.2, 131.8, 130.5, 130.3, 121.9, 117.4, 112.3, 69.0 (CH_2).

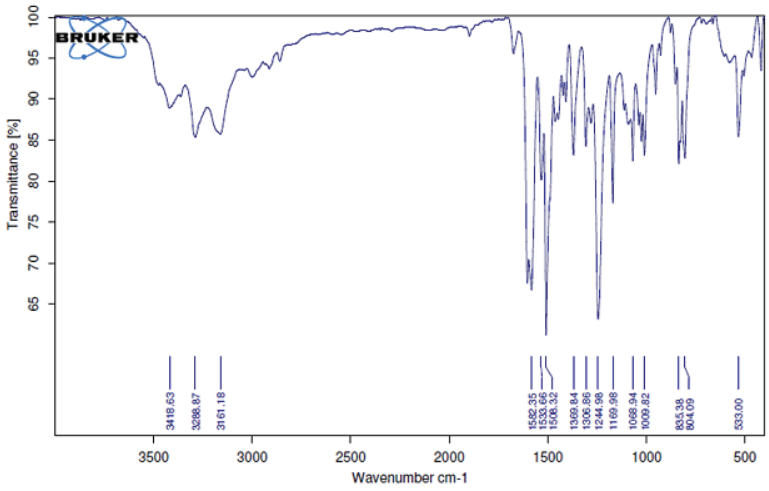

Fig S-13. IR spectrum of compound **7**

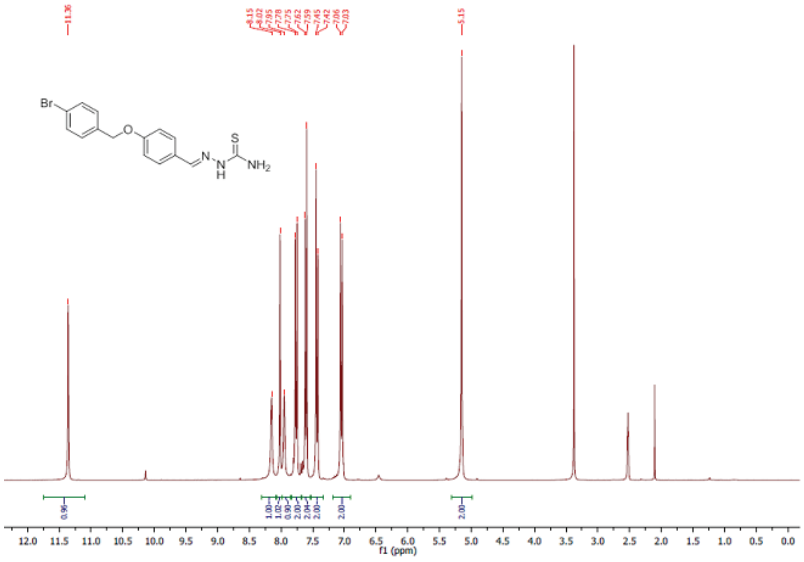

Fig S-14. ^{1}H NMR spectrum of compound **7**

(CC) 2022 SCS.

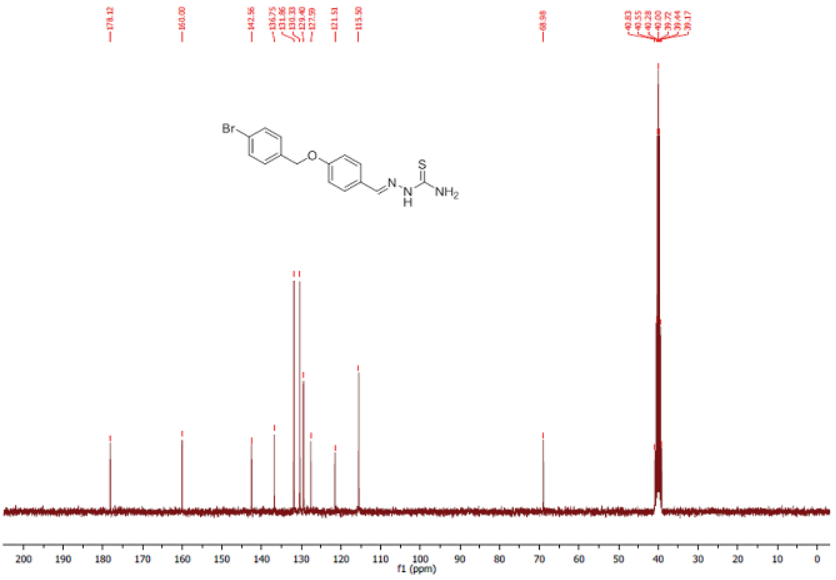

Fig S-15. ^{13}C NMR spectrum of compound **7**

*(E)-1-(3-(4-bromobenzyloxy)benzylidene)thiosemicarbazide (compound **8**)*

Yield 85%; m.p. 171-173.5 °C (literature data: 165 °C[5]); IR (KBr) ν_{max} (cm^{-1}): 3393 (NH), 3242, 3160 (NH_2), 1600 (C=N), 1262 (C=S). ^{1}H NMR (300 MHz, DMSO-d_6) δ (ppm): 11.48 (1H, s, NH), 8.27 (H, s, NH), 8.10 (1H, s, NH), 8.04 (1H, s, CH), 7.61 (3H, d, J = 6 Hz, 3CHAr), 7.46 (2H, d, J = 9 Hz, 2CHAr), 7.35 (2H, d, J = 6 Hz, 2CHAr), 7.32 (2H, m, 2CHAr), 7.04 (1H, m, CHAr), 5.15 (2H, s, OCH_2). ^{13}C NMR (75 MHz, $CDCl_3$) δ (ppm): 178.1, 160.0, 142.6, 136.8, 131.9, 130.3, 129.4, 127.9, 121.5, 115.9, 68.9 (CH_2).

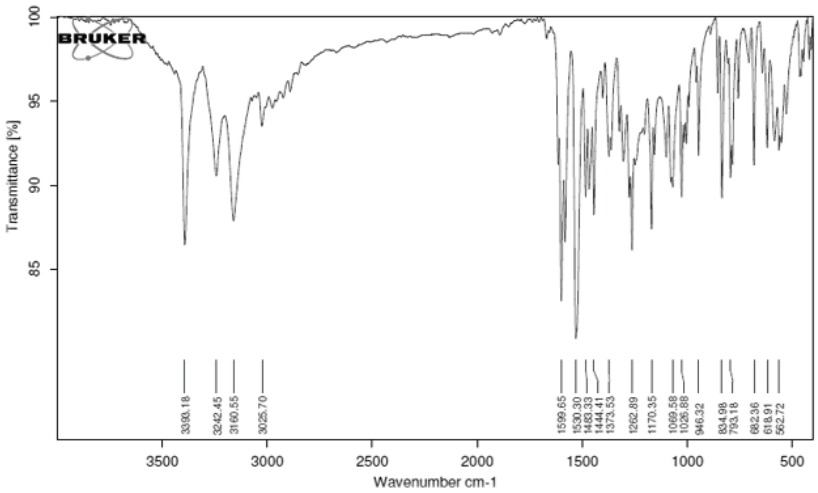

Fig S-16. IR spectrum of compound **8**

(CC) 2022 SCS.

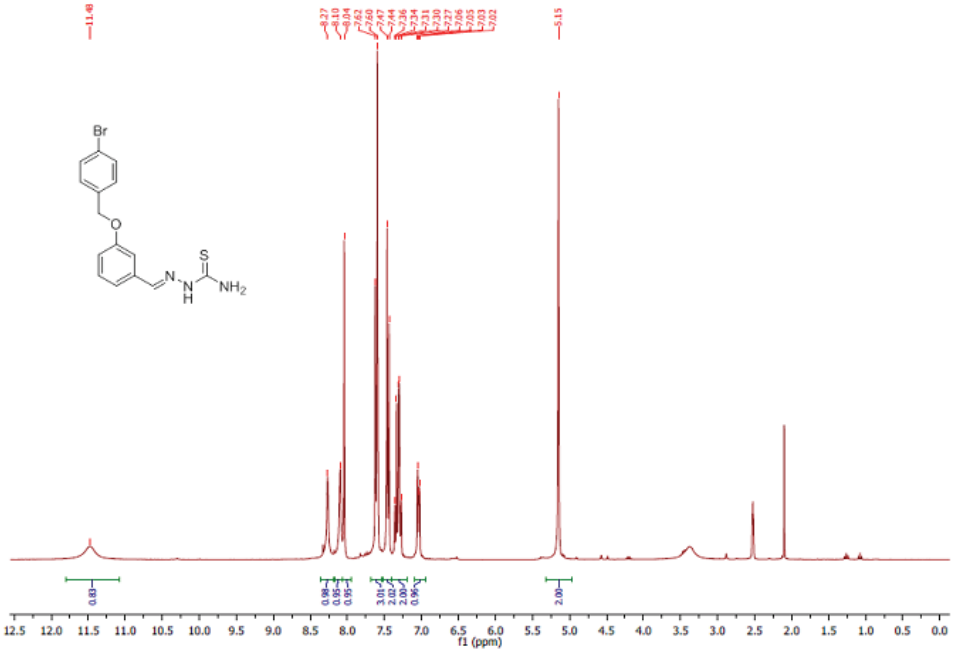

Fig S-17. ^{1}H NMR spectrum of compound **8**

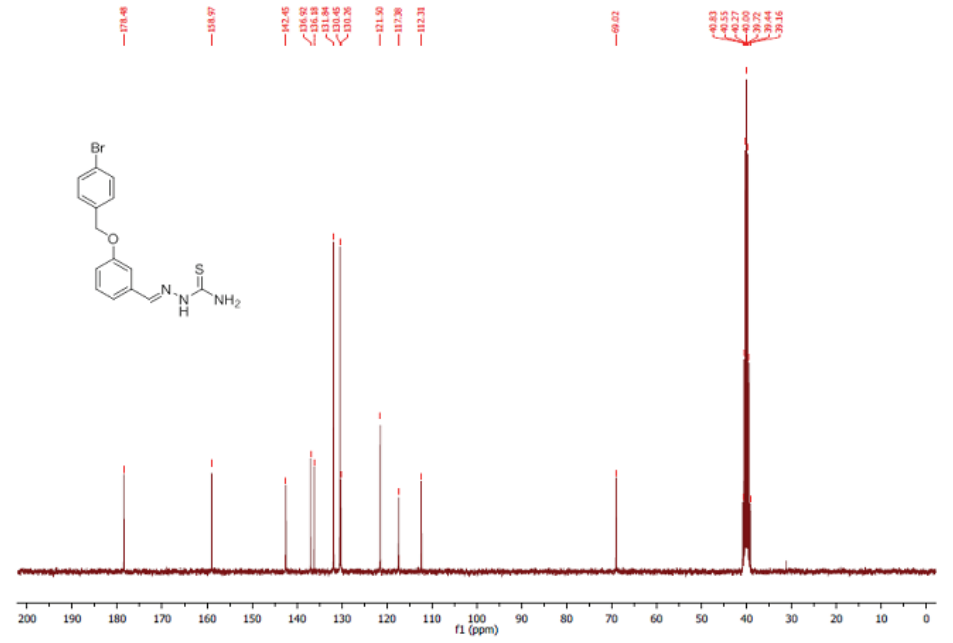

Fig S-18. ^{13}C NMR spectrum of compound **8**

(CC) 2022 SCS.

*(E)-1-(4-(2-morpholinoethoxy)benzylidene)thiosemicarbazide (compound **9**)*

Yield 80 %; m.p. 216-217.4 °C (literature data: 216-217 °C[9]); IR (KBr) ν_{max} (cm^{-1}): 3438 (NH), 3204, 3113 (NH_2), 1599 (C=N), 1243 (C=S).

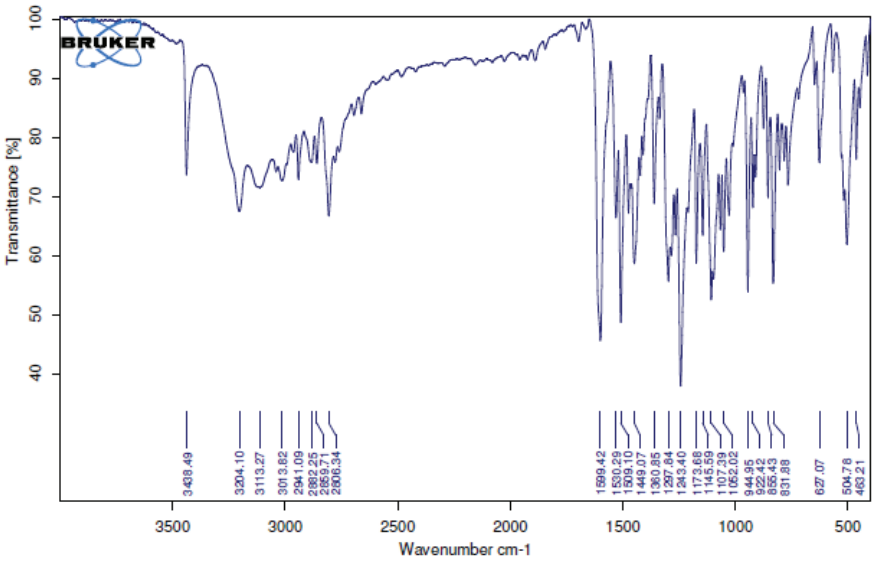

Fig S-19. IR spectrum of compound **9**

*(E)-1-(4-(3-chlorobenzyloxy)-3-methoxybenzylidene)thiosemicarbazide (compound **10**)*

Yield 85 %; m.p. 174-176 °C; IR (KBr) ν_{max} (cm^{-1}): 3421 (NH), 3308, 3144 (NH_2), 1599 (C=N), 1268 (C=S). ^{1}H NMR (300 MHz, DMSO-d_6) δ (ppm): 11.35 (1H, s, NH), 8.19 (H, s, NH), 8.05 (1H, s, NH), 7.96 (1H, s, CH), 7.55 (1H, d, J =1.8 Hz, 1CHAr), 7.51 (1H, t, J = 2.1 Hz, 1CHAr), 7.40-7.44 (3H, m, 3CHAr), 7.13 (1H, dd, J = 1.8, 8.3 Hz, 1CHAr), 7.03 (1H, d, J = 8.4 Hz, 1CHAr), 5.14 (2H, s, OCH_2), 3.84 (3H, s, OCH_3). ^{13}C NMR (75 MHz, $CDCl_3$) δ (ppm): 177.6, 149.4, 149.2, 142,4, 139.5, 133.1, 130.4, 127.9, 127.5, 126.4, 122.0, 68.9 (CH_2), 55.8 (CH_3).

(CC) 2022 SCS.

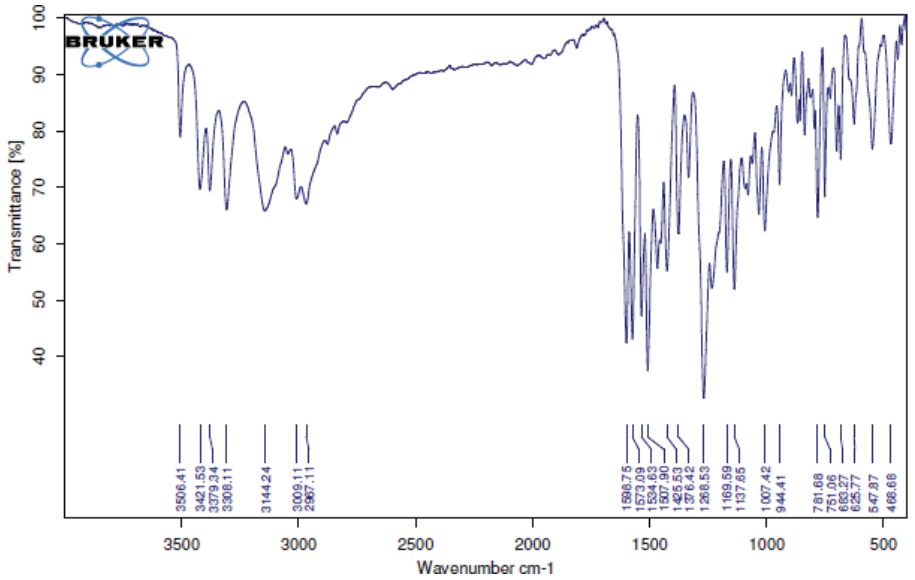

Fig S-20. IR spectrum of compound **10**

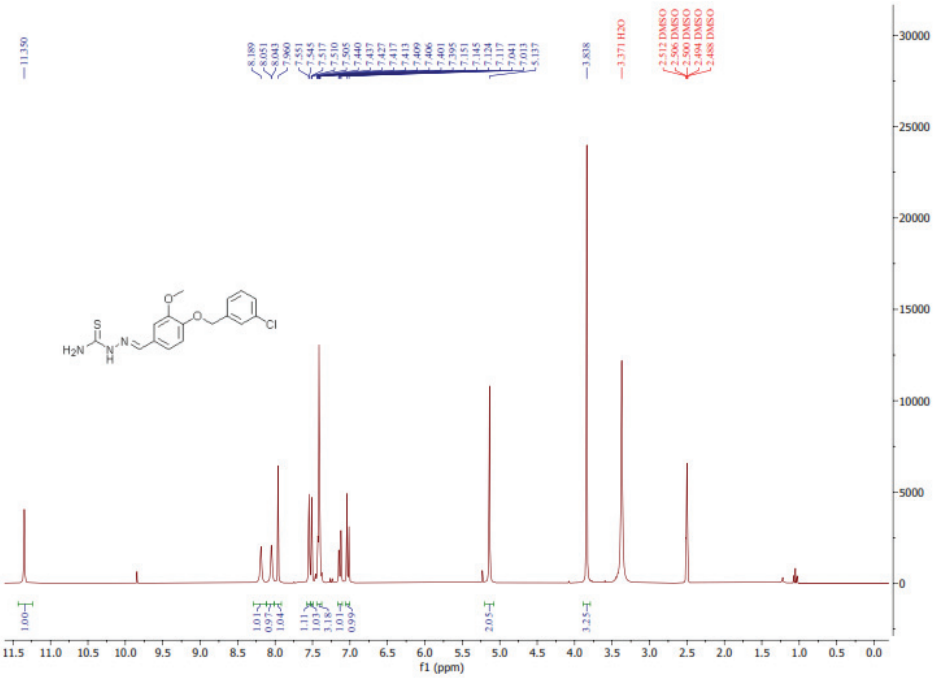

Fig S-21. ^{1}H NMR spectrum of compound **10**

(CC) 2022 SCS.

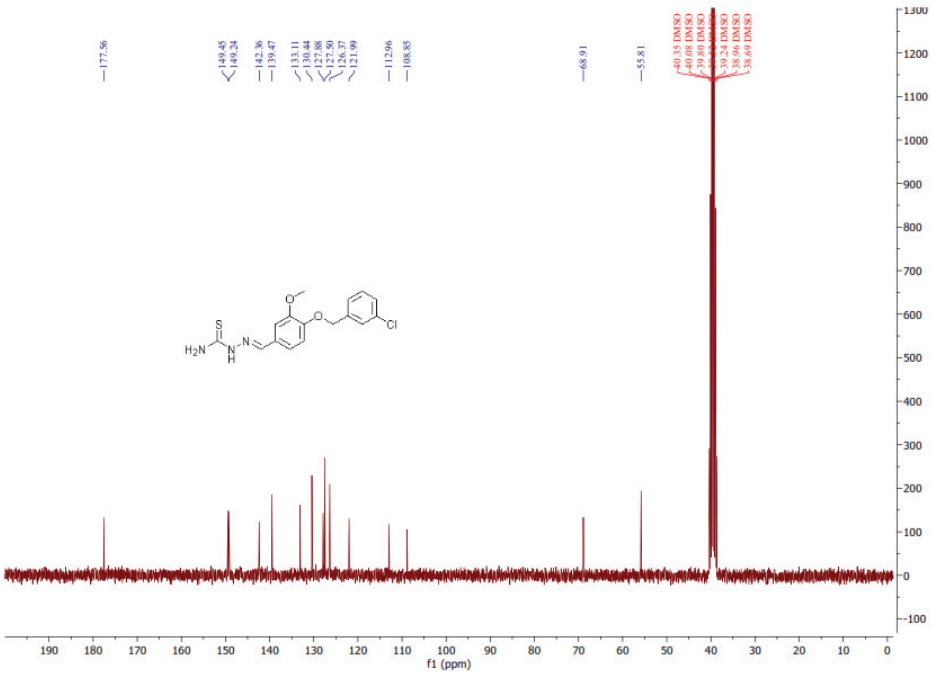

Fig S-22. ^{13}C NMR spectrum of compound **10**

*(E)-1-(4-(piperidin-1-yl)benzylidene)thiosemicarbazide (compound **11**)*

Yield 95 %; m.p. 99-101 °C (literature data: 105-106 °C[10]); IR (KBr) ν_{max} (cm^{-1}): 3371 (NH), 3266, 3160 (NH_2), 1604 (C=N), 1530, 1227 (C=S).

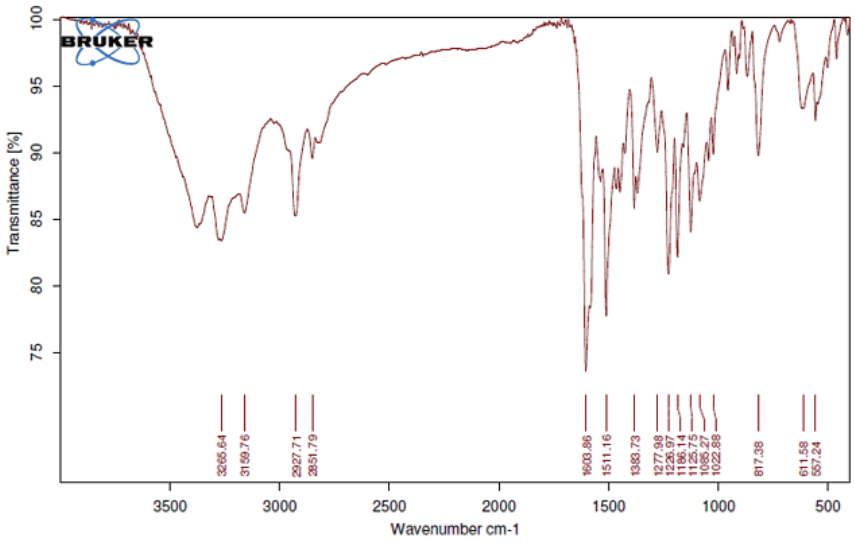

Fig S-23. IR spectrum of compound **11**

(CC) 2022 SCS.

*(E)-1-(4-(2-(piperidin-1-yl)ethoxy)benzylidene)thiosemicarbazide (compound **12**)*

Yield 90 %; m.p. 166.166.6 °C; IR (KBr) ν_{max} (cm^{-1}): 3442 (NH), 3320, 3159 (NH_2), 1607 (C=N), 1247 (C=S). ^{1}H NMR (300 MHz, DMSO-d_6) δ (ppm): 11.33 (1H, s, NH), 8.12 (1H, s, NH), 8.01 (H, s, CH), 7.93 (H, s, NH), 7.74 (2H, d, J = 9 Hz, 2CHAr), 6.98 (2H, d, J = 9 Hz, 2CHAr), 4.11 (2H, t, J = 6 Hz, OCH_2), 2.66 (2H, t, J = 6 Hz, NCH_2), 2.43 (4H, t, J = 6 Hz, CH_2NCH_2), 1.5 (4H, quint, J = 6 Hz, CH_2), 1.40 (2H, t, J = 6 Hz, CH_2). ^{13}C NMR (75 MHz, $CDCl_3$) δ (ppm): 178.1, 160.4, 142.9, 129.4, 127.2, 115.2, 66.2, 57.8, 54.9, 26.1, 24.4.

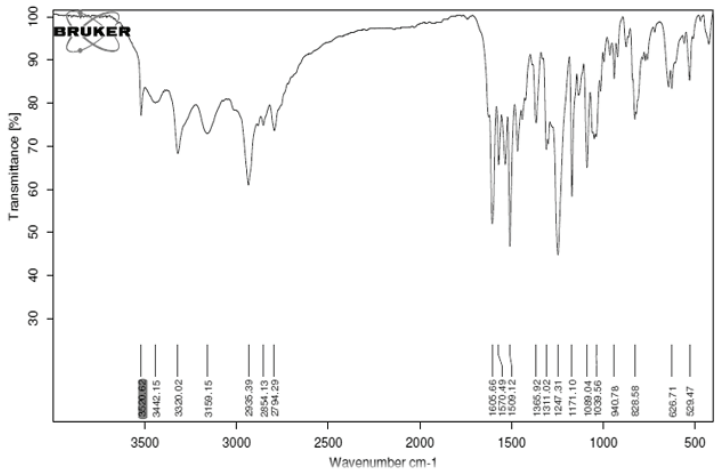

Fig S-24. IR spectrum of compound **12**

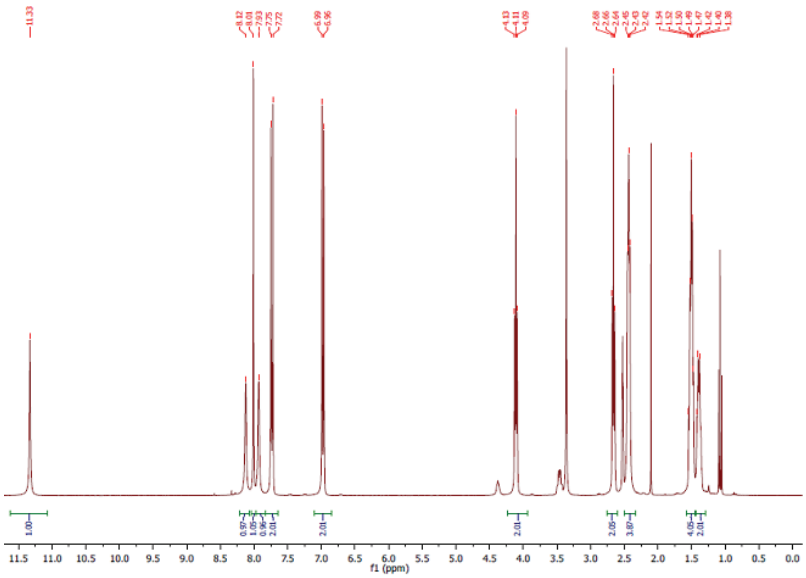

Fig S-25. ^{1}H NMR spectrum of compound **12**

(CC) 2022 SCS.

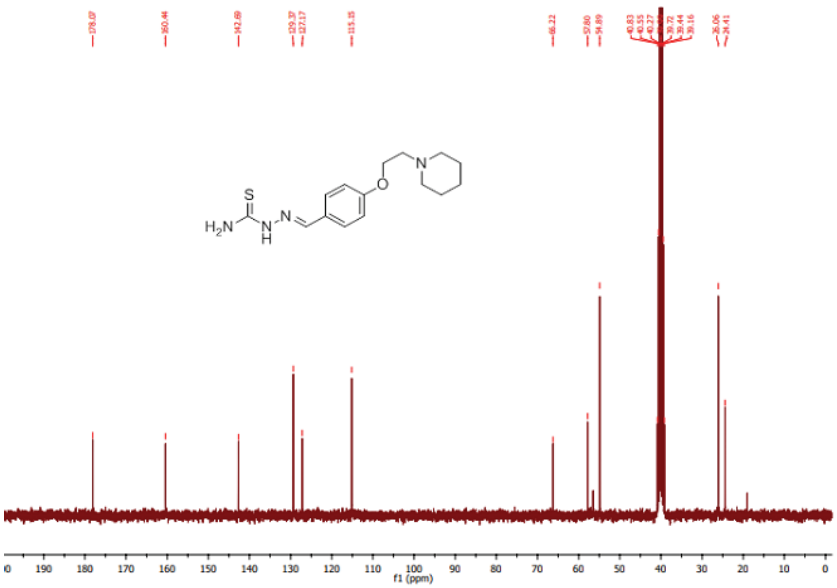

Fig S-26. ^{13}C NMR spectrum of compound **12**

*(E)-1-(4-(3-(piperidin-1-yl)propoxy)benzylidene)thiosemicarbazide (compound **13**)*

Yield 90%; m.p. 137-139 °C (decomp.); IR (KBr) ν_{max} (cm^{-1}): 3476 (NH), 3302, 3160 (NH_2), 1602 (C=N), 1253 (C=S). ^{1}H NMR (300 MHz, DMSO-d_6) δ (ppm): 11.33 (1H, s, NH), 8.13 (H, s, NH), 8.02 (1H, s, NH), 7.92 (1H, s, CH), 7.73 (2H, d, J = 9 Hz, 2CHAr), 6.97 (2H, d, J = 9 Hz, 2CHAr), 4.04 (2H, t, J = 6 Hz, OCH_2), 2.39 (2H, t, J = 6 Hz, CH_2), 2.34 (2H, t, CH_2), 1.87 (2H, quint, J = 6 Hz, CH_2), 1.52-1.39 (6H, m, $3CH_2$). ^{13}C NMR (75 MHz, $CDCl_3$) δ (ppm): 178.0, 160.5, 142.7, 129.3, 127.1, 115.0, 66.5, 55.5, 54.5, 26.6, 26.0, 24.6.

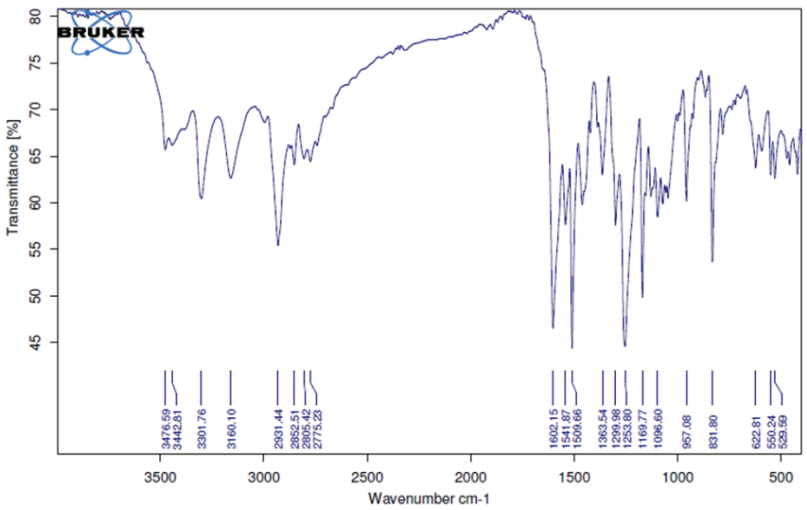

Fig S-27. IR spectrum of compound **13**

(CC) 2022 SCS.

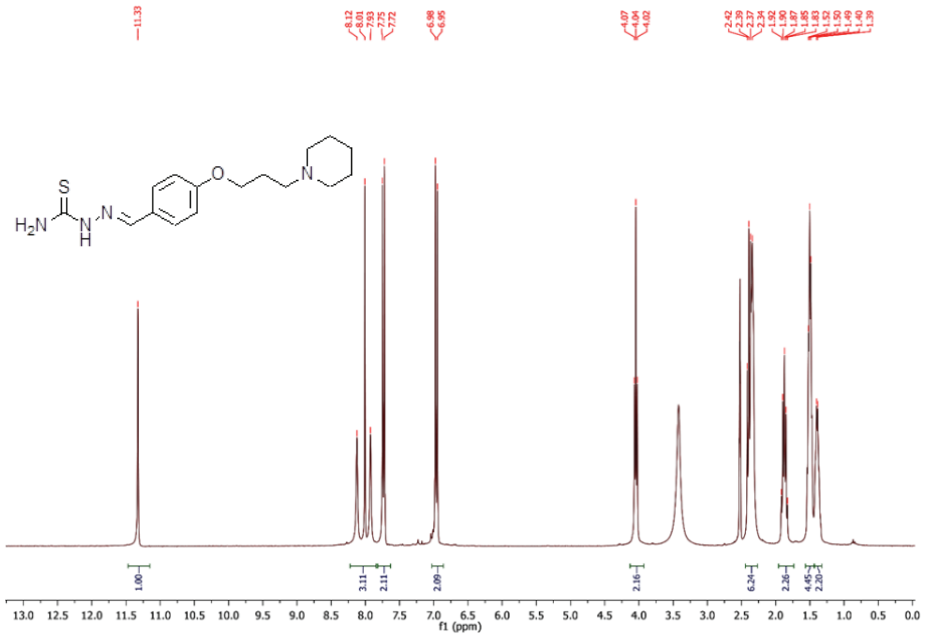

Fig S-28. ^{1}H NMR spectrum of compound **13**

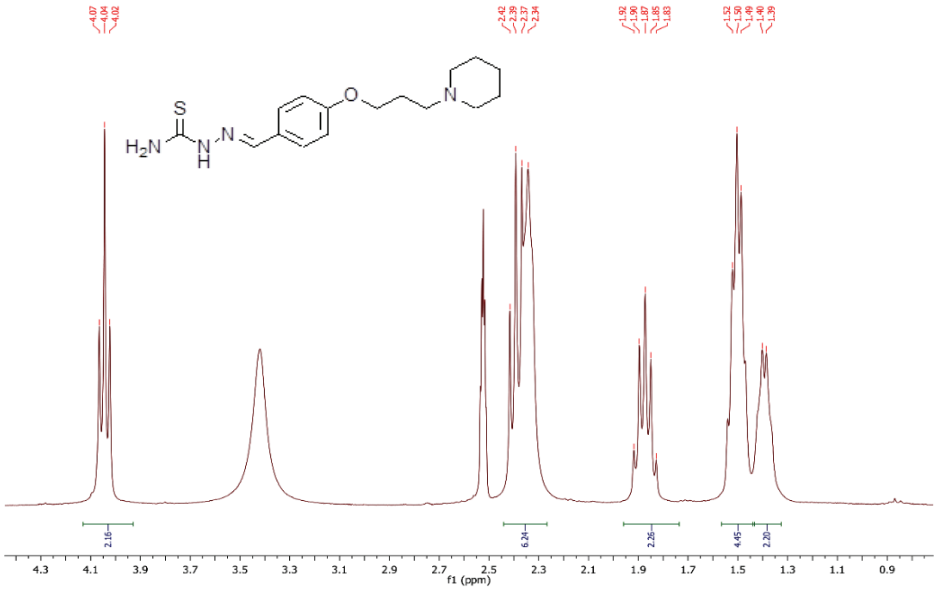

Fig S-29. ^{1}H NMR expanded spectrum of compound **13**

(CC) 2022 SCS.

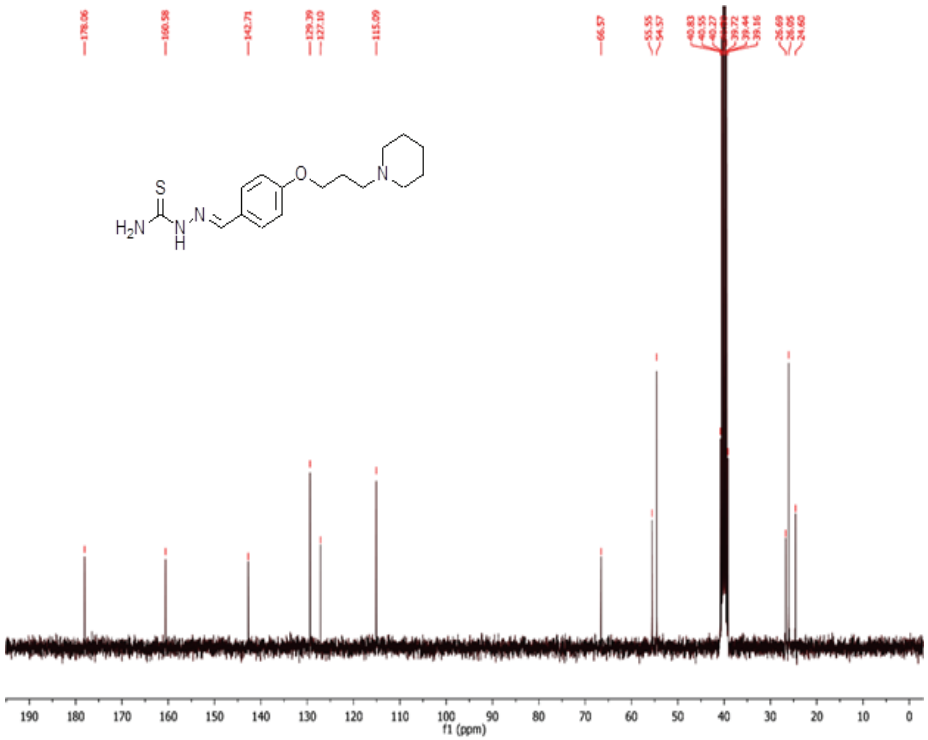

Fig S-30. ^{13}C NMR spectrum of compound **13**

REFERENCES

1. H. R. Fatondji, S. Kpoviessi, F. Gbaguidi, J. Bero, V. Hannaert, J. Quetin-Leclercq, J. Poupaert, M. Moudachirou, G. C. Accrombessi, *Med. Chem. Res*. **22** (2013) 2151 (https://doi.org/10.1007/s00044-012-0208-6)
2. N. H. Nam, T. L. Huong, T. M. Dung do, P. T. Dung, D .T. Oanh, S. H. Park, K. Kim, B. W. Han, J. Yun, J. S. Kang, Y. Kim, S. B. Han, *J. Enzyme Inhib. Med. Chem*. **29** (2014) 611 (https://doi.org/10.3109/14756366.2013.832238)
3. J. B. da Silva, D. M. Navarro, A. G. da Silva, G. K. Santos, K. A. Dutra, D. R. Moreira, M. N. Ramos, J. W. Espíndola, A. D. de Oliveira, D. J. Brondani, A. C. Leite, M. Z. Hernandes, V. R. Pereira, L. F. da Rocha, M. C. de Castro, B. C. de Oliveira, Q. Lan, K. M. Jr. Merz, *Eur. J. Med. Chem*. **100** (2015) 162 (https://doi.org/10.1016/j.ejmech.2015.04.061)
4. Ng. Ph. Buu-Hoi, M. Welsch, G. Dechamps, H. Le. Bihan, F. Binon, Ng. D. Xuong, *J. Org. Chem*. **18** (1953) 121 (https://doi.org/10.1021/jo01130a001)
5. Ng. Ph. Buu-Hoi, Ng. D. Xuong, F. Binon, *J. Chem. Soc*. (*Resumed*) **1956**, 713 (https://doi.org/10.1039/JR9560000713)
6. M. E. Abd El-Fattah, *Indian. J. Chem.- Sec. B*. **45B** (2006) 2523 (http://nopr.niscair.res.in/bitstream/123456789/6764/1/IJCB%2045B%2811%29%202523-2533.pdf)
7. R. Wilson, G. R. Revankar, R. L. Tolman, *J. Med. Chem*. **17** (1974) 760 (https://doi.org/10.1021/jm00253a025

(CC) 2022 SCS.

8. N.Ö. Can, D. Osmaniye, S. Levent, B. N. Sağlik, B. Korkut, Ö. Atli, Y. Özkay, Z. A. Kaplancikli, *Eur. J. Med. Chem*. **144** (2018) 68 (https://doi.org/10.1016/j.ejmech.2017.12.013)
9. H. D. Cossey, C. J. Sharpe, F. F. Stephens, *J. Chem. Soc. (Resumed)* **1963**, 4322 (https://doi.org/10.1039/JR9630004322
10. M. S. A. El-Gaby, *J. Chin. Chem. Soc*. **51** (2004) 125 (https://doi.org/10.1002/jccs.200400020).

(CC) 2022 SCS.

Journal of the Serbian Chemical Society
JSCS@tmf.bg.ac.rs • www.shd.org.rs/JSCS
J. Serb. Chem. Soc. *87* (10) 1143–1156 (2022)
JSCS–5584
Original scientific paper
Published 1 August 2022

The effect of non-specific binding of Pd(II) complexes with *N*-heteroaromatic hydrazone ligands on the protein structure

NEMANJA D. MIJIN[1#], JELICA MILOŠEVIĆ[1], NENAD R. FILIPOVIĆ[2#], DRAGANA MITIĆ[3#], KATARINA ANĐELKOVIĆ[1#], NATALIJA Đ. POLOVIĆ[1#] and TAMARA R. TODOROVIĆ[1*#]

[1]University of Belgrade – Faculty of Chemistry, Studentski trg 12–16, 11000 Belgrade, Serbia, [2]University of Belgrade – Faculty of Agriculture, Nemanjina 6, 11000 Belgrade, Serbia and [3]Innovation Centre of University of Belgrade – Faculty of Chemistry, Studentski trg 12–16, 11000 Belgrade, Serbia

(Received 18 May, revised 29 May, accepted 11 June 2022)

Abstract: Previously, the cytotoxic actions of five Pd(II) complexes with bidentate *N*-heteroaromatic chelators (complexes **1**–**5**) on a palette of several cancer cell lines were investigated. However, the results of the cytotoxic activity did not correlate with the hydrophobic character of the complexes. To gain further insight into the structure–activity relationship, essential for the design of novel potential drugs, other factors, such as non-specific interactions with cellular proteins, have to be taken into account. To explore the potential non-specific influence of the complexes on protein structures, ovalbumin (OVA) was chosen as a model system to mimic cellular non-specific crowding environments with high protein concentrations. A Fourier-transform infrared spectroscopy study implied that the binding of **3** and **4** led to only moderate alternations in the secondary structures of the protein, without the possibility to penetrate into hydrophobic core of the protein and disruption of protein native fold. Contrary, the effect of complex **5** on OVA secondary structures was concentration-dependent. While the lower concentration of complex **5** had no effect on OVA structure, a doubled concentration of complex **5** led to complete disruption of the content native-like secondary structures. The concentration-dependent effect of complex **5** on the changes in secondary structures and considerable increase in the exposure of OVA hydrophobic surfaces to water may be related to a potential crosslinking that leads to OVA aggregation.

Keywords: ovalbumin model system; protein aggregation; DMSO effect; ligand hydrophobicity.

* Corresponding author. E-mail: tamarat@chem.bg.ac.rs
# Serbian Chemical Society member.
https://doi.org/10.2298/JSC220518050M

Available on line at www.shd.org.rs/JSCS/
(CC) 2022 SCS.

INTRODUCTION

The coordination compound cis-diamminedichloroplatinum(II), known as cisplatin or CDDP, is a blockbuster anticancer drug that entered the market a half-century ago as the first metal-based chemotherapeutic (MBC).[1] Cisplatin is used to treat various types of solid tumors[2] and proved to be especially active against testicular cancer, with a 90% cure rate.[3] For all so called 'platins' – platinum(II)-based chemotherapeutics, including cisplatin, that entered the market, DNA was identified as a primary target. Their mechanism of action includes covalent binding of platinum to DNA bases, with formation of mainly intrastrand cross links, which eventually leads to apoptosis.[4] In order to overcome the side effects of cisplatin, such as nephrotoxicity and development of tumor resistance, novel MBCs based on platinum and other metals were developed.[1,4,5] Among them, palladium(II) complexes have been studied due to significant similarity of coordination chemistry of Pt(II) and Pd(II).[6,7] The advantage of Pd(II) complexes over analogues Pt(II) complexes is firstly the better solubility of the former.[8] In the terms of anticancer activity, Pd(II) complexes have shown comparable or even better activities than approved platinum-based chemotherapeutics, with reduced cross-resistance and decreased toxicity.[6,7,9] On the other hand, due to high reactivity, Pd-based complexes are often unable to reach their biological targets. Moreover, isomerization of active cis into trans isomers results most frequently in decreased activity of Pd(II) complexes. Preparation of Pd(II) complexes with *N*,*N*′ chelating ligands was proven to be an effective strategy for the prevention of isomerization.[8]

In previous studies, the cytotoxic action of several Pd(II) complexes with bidentate *N*-heteroaromatic chelators (complexes **1**–**5**, Scheme 1), which are the condensation products of ethyl hydrazinoacetate hydrochloride and quinoline-8--carboxaldehyde, quinoline-2-carboxaldehyde, 2-formylpyridine, 2-acetylpyridine and 2-benzoylpyridine, were investigated. The antiproliferative activity of the complexes was evaluated on a palette of several cancer cell lines.[9,10] Complex **1** with an q8a-based ligand (Scheme 1) appeared to be the most effective with an activity comparable to that of cisplatin in all the investigated cell lines. The observed antiproliferative effect was predominantly mediated through the induction of apoptotic cell death.

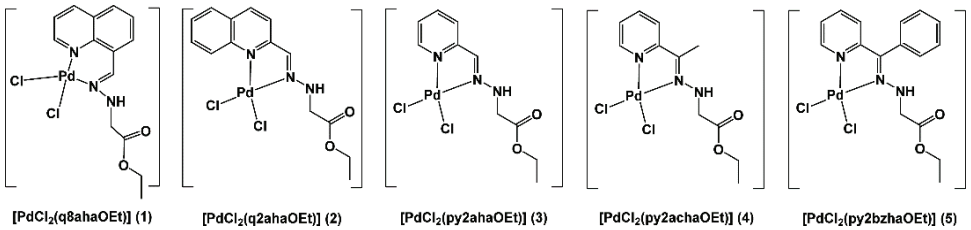

Scheme 1. Structures of Pd(II) complexes **1**–**5**.

(CC) 2022 SCS.

Generally, the antiproliferative activity of a compound could be related, in part, to its log *P* value, as a measure of lipophilic character. Since **1**–**5** all possess a $PdCl_2$ core, the liphophilicity should vary only as a function of the log *P* value of the ligands. The calculated log *P* values for the ligands in **1**–**5** are: 2.12, 2.24, 1.16, 1.48 and 2.48, respectively.[9,11,12] Based only on the log *P* values, it would be expected that **5** possesses the most pronounced antiproliferative effect, since the resulting hydrophobicity may contribute to an increased uptake of the compound by the cells.[13] However, despite a favorable log *P* value, **5** showed no anticancer activity against acute monocytic leukemia (THP-1) and mammary adenocarcinoma (MCF-7) cell lines, while complex **3**, with the lowest log *P* value, induced apoptosis in the investigated cell lines.[10] Thus, it was hypothesize that reduction of the cytotoxic action within this group of similar complexes could be related to non-specific interactions with cellular proteins. Thus, complexes **3**–**5** were selected for further studies. In order to explore the potential non-specific influence of **3**–**5** on protein structure, ovalbumin (*Gallus gallus*) was chosen as a model system. Ovalbumin (OVA) is a 45 kDa reserve protein expressed in chicken egg whites. Based on its homology, it belongs to the serpin family of proteins, which includes certain inhibitors of serine proteases.[14] OVA accounts for about 50 % of hen egg white proteins, which makes it an easily available model system for studying protein behavior, including protein conformational changes.[15–17] Even though OVA is an extensively studied protein, there are no reports about its natural ligands. Another common protein model system, human serum albumin (HSA), is a transport protein that has many binding sites for various natural ligands and, hence, it is likely to bind structurally related molecules including potential therapeutics under investigation. The low affinity of binding of diverse molecules makes OVA a better model system for studying the effect of different compounds on a protein structure. Due to its low specificity, OVA is even used to mimic cellular non-specific crowding environments with protein concentrations up to above 300 g L^{-1}.[18,19]

EXPERIMENTAL

Materials and methods

Ethyl hydrazinoacetate hydrochloride (98 %), 2-formylpyridine (98 %), 2-acetylpyridine (97 %) and 2-benzoylpyridine (98 %) were obtained from Acros Organics (BVBA, Geel, Belgium), while potassium tetrachloropalladate(II) (98%) was obtained from Aldrich. All solvents (reagent grade) were obtained from commercial suppliers and used without further purification.

Elemental analyses (C, H, N) were performed by standard micromethods using a Elementar Vario ELIII C,H,N,S/O analyser, and their results were found to be in good agreement (±0.4 %) with the calculated values. NMR spectra were obtained on a Bruker Avance 500 instument equipped with a broad-band direct probe. All spectra were measured at 298 K in $CDCl_3$ or DMSO-d_6. Chemical shifts are given on δ scale (ppm) relative to tetramethylsilane (TMS) as an internal standard for ^1H and ^{13}C.

(CC) 2022 SCS.

*Synthesis of ethyl (*E*)-((pyridin-2-ylmethylene)amino)glycinate-*N,N*-dichloridopalladium(II) [PdCl$_2$py2ahaOEt] (**3**), ethyl (*E*)-((1-(pyridin-2-yl)ethylidene)amino)glycinate-*N,N*-dichloridopalladium(II) [PdCl$_2$py2achaOEt] (**4**) and ethyl (*E*)-((phenyl(pyridin-2-yl)methylene)amino)glycinate-*N,N*-dichloridopalladium(II) [PdCl$_2$py2bzhaOEt] (**5**)*

The complexes **3**–**5** were synthesized as described previously[9,10] by the template reaction of ethyl hydrazinoacetate hydrochloride, the corresponding carbonyl compound and potassium tetrachloropalladate(II) (mole ratio 1:1:1). The purity of the complexes was checked by elemental analysis and NMR spectroscopy (Supplementary material to this paper).

Calculation of absorption, distribution, metabolism, and excretion (ADME) parameters and pan assay interference compounds (PAINS) evaluation

Physicochemical properties, lipophilicity, water solubility, pharmacokinetics, druglikeness and medicinal chemistry parameters were determined using the free SwissADME tools available at the website of the Swiss Institute of Bioinformatics (http://www.swissadme.ch/).[11] The structures of the complexes obtained by X-ray diffraction studies were converted to Sybyl Mol2 format using the Mercury 2022.1.0 program.[20] Input SMILES formats of the complexes were constructed using the Open Babel Package v3.1.1.[21]

Protein purification

OVA was extracted from hen egg whites by a two-step method according to a previously published protocol.[22] The globulins were first precipitated using a 50 % saturation solution of ammonium sulfate, after which they were removed *via* 30 min of centrifugation at 3000*g*. Thereafter, the OVA was precipitated from the received supernatant by adjusting the pH to its isoelectric point of 4.6 through titration with 2 M acetic acid. The precipitate was separated by centrifugation (30 min at 3000*g*) and then resuspended in 100 mM Tris-HCl buffer (pH 7.4). The obtained OVA solution was then dialysed against 100 mM Tris-HCl buffer (pH 7.4) for 16 h in order to remove excess salts. The OVA was then stored at –20 °C. The OVA concentration was determined *via* the Bradford assay, using bovine serum albumin (BSA) as the standard.

8-Anilinonaphthalene-1-sulphonic acid (ANS) fluorescence measurements

The binding of ANS fluorescent dye was measured using a FluoroMax-4 Jobin Yvon spectrofluorimeter. The dye was dissolved in 100 mM Tris-HCl buffer (pH 7.4) with a concentration of 8 mM. Mixtures containing 200 μL of ANS, 1900 μL of the 100 mM Tris-HCl buffer (pH 7.4), and 100 μL of the samples (containing the protein and each of the complex in equimolar ratio) were prepared. The concentrations used were based on already published IC_{50} values of the selected complexes and were 50 μM for complex **3**, and 100 μM for complexes **4** and **5**. Complex **5** was also tested in a concentration of 50 μM. Emission spectra (wavelength range 440–550 nm) were obtained, with the excitation wavelength set to 390 nm.[23]

Fourier transform infrared spectroscopy (FTIR)

Infrared spectra of the OVA-Pd complex samples (in 100 mM Tris-HCl buffer, pH 7.4 and DMSO) were collected using a Thermo Fisher Scientific Nicolet Summit FTIR Spectrometer in the ATR mode. Aliquots of 1.0 μL were applied to the diamond crystal, and their solvents were evaporated *via* a mild stream of argon. Thereafter, composite spectra in the mid-IR region (400–4000 cm^{-1}) were collected in 32 scans using a DTGS KBr detector, with a scanning resolution of 2 cm^{-1}. The received spectra were automatically corrected for background absorption. FTIR corrections (automatic ATR correction and automatic baseline cor-

(CC) 2022 SCS.

rection) were performed using OMNIC32 software. The amide I region was deconvoluted to its constituents corresponding to certain secondary structures using the same software, essentially as described previously.[22]

RESULTS AND DISCUSSION

ADME parameters and PAINS evaluation

The *in-silico* ADME profiles of complexes **1**–**5** were assessed through the robust SwissADME program and the results are presented in Table I. All compounds showed the desirable Lipinski rule principles such as MW ≤ 500, number

TABLE I. Pharmacological profiles, medicinal chemistry principles and lead-likeness properties of compounds **1**–**5**; ++: high; +: activity; –: no activity

Parameter	Compound				
	1	**2**	**3**	**4**	**5**
Physicochemical properties					
Molecular weight	434.61	434.61	384.56	398.58	460.56
#Heavy atoms	22	22	18	19	24
#Aromatic heavy atoms	10	10	6	6	12
Fraction Csp^3	0.21	0.21	0.30	0.36	0.19
#Rotatable bonds	5	5	5	5	6
#H-bond acceptors	2	2	2	2	2
#H-bond donors	1	1	1	1	1
Molar Refractivity	88.74	88.74	71.23	76.04	95.72
Topological polar surface area (TPSA), $Å^2$	55.62	55.62	55.62	55.62	55.62
log $P_{o/w}$	1.55	1.61	0.69	0.98	1.94
Pharmacokinetics					
GI absorption	++	++	++	++	++
BBB permeant	+	+	+	+	+
P-gp substrate	–	–	–	–	–
CYP1A2 inhibitor	+	+	–	–	+
CYP2C19 inhibitor	+	+	+	+	+
CYP2C9 inhibitor	–	–	–	–	–
CYP2D6 inhibitor	+	+	–	–	+
CYP3A4 inhibitor	–	–	–	–	+
log (K_p / cm s^{-1})	–6.00	–5.77	–6.41	–6.27	–5.47
Druglikeness					
Lipinski #violations	0	0	0	0	0
Ghose #violations	0	0	0	0	0
Veber #violations	0	0	0	0	0
Egan #violations	0	0	0	0	0
Muegge #violations	0	0	0	0	0
Bioavailability score	0.55	0.55	0.55	0.55	0.55
Medicinal chemistry					
PAINS #alerts	0	0	0	0	0
Leadlikeness (1 violation: $MW > 350$)	No	No	No	No	No
Synthetic accessibility	3.72	3.77	3.64	3.69	3.92

(CC) 2022 SCS.

of atoms that act as hydrogen bond acceptors ≤ 10 and number of hydrogen bond donors ≤ 5.[24] Other physicochemical properties, such as number of rotatable bonds (≤ 10), molar refractivity (from 40 to 130) and topological polar surface area (TPSA ≤ 140 Å^2), were also found within the acceptable range. All compounds were predicted to be highly absorbed by the gastrointestinal (GI) system after oral administration, while some of them are likely to inhibit cytochrome P450 gene isoforms (*i.e.*, CYP1A2, CYP219). Relevant strategies for selection of molecules with preferred drug-like profiles examined by SwissADME indicate that the all complexes represent drug candidates since they possess important functional groups and bioavailability. Finally, according to a recently published editorial,[25] in order to remove suspicion of artificial activity, in addition to SwissADME, the compounds were evaluated by the ZINC PAINS pattern identifier.[26] The applied algorithms did not report the compounds as potential PAINS or covalent inhibitors, although due to *MW* > 350 none of the compounds represent potential lead compound, which is usually the case for MBCs with nontrivial organic ligands.

However, one of the most important drug-likeness descriptors is related to the lipophilic character of the drug candidate. This property is usually measured by 1-octanol/water partition coefficient (log $P_{o/w}$). The calculated log $P_{o/w}$ for the complexes given in Table I represent the average value of five computational models.[12,24,27–30] The order of the log $P_{o/w}$ values for the complexes is the same as for the parent ligands, where complex **5** possesses the highest hydrophobic character and lipo-solubility. However, the results of the cytotoxic activity do not correlate with the hydrophobic character of the complexes. In order to gain insight into the structure–activity relationship, other factors, such as non-specific interactions with cellular proteins, have to be taken into account. Thus, for the further studies, complex **3**, which showed to be more potent apoptosis inducer than cisplatin in THP-1 and MCF-7 cell lines, and complexes **4** and **5**, which showed no activity, were chosen.

The effect of DMSO on OVA secondary structures

In exploring the biological effect of potential medicinal therapeutics on biological systems including proteins, nucleic acids and cells, usually the presence of co-solvent is needed to enable dissolution of the potential therapeutics in simulated physiological conditions (aqueous buffers). For this purpose, DMSO is commonly used in final concentrations up to 5 %.[10] FTIR spectroscopy was employed to monitor the changes in the secondary structures of OVA in the absence and presence of different concentration of DMSO (1, 2 and 4 %) in order to explore whether any change in DMSO concentration could influence the protein structure in a non-specific way. The obtained spectra are shown in Fig. 1.

(CC) 2022 SCS.

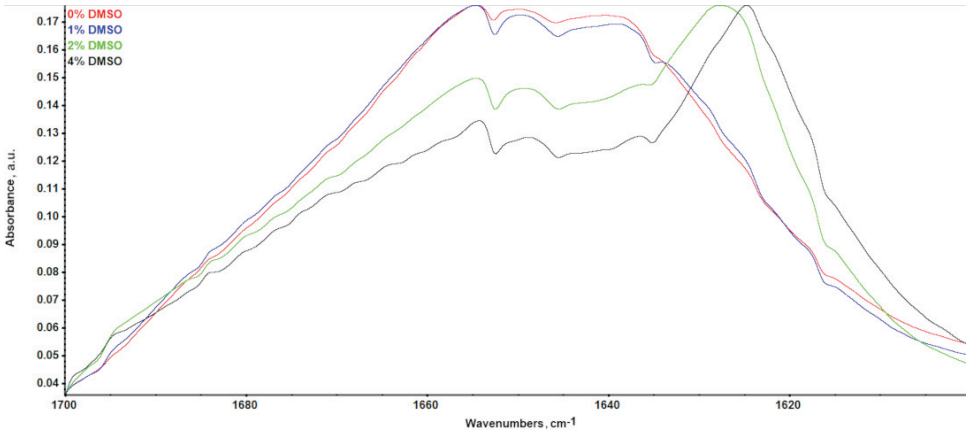

Fig. 1. FTIR spectra of OVA in the presence of 0–4% DMSO.

The most commonly used spectral region within an IR spectrum is the amide I region. The associated absorption bands, which are almost entirely the result of C=O stretching vibrations of the peptide bonds, make this region the most sensitive for the analysis of the secondary structure of proteins.[31] Bands attributed to the most abundant native-like secondary structures were identified according to previously published data: native-like β-sheets (1636 cm^{-1}),[22,32] random coils (1646 cm^{-1}),[22] α-helices (1653 cm^{-1}),[22] unordered structures (1662–1675 cm^{-1})[33] and β-turns (1683 cm^{-1}).[34] Additional bands, which were barely visible in the spectrum of the starting OVA sample, were also identified as side-chain peaks (1611 cm^{-1}), and low-frequency and high-frequency aggregation specific β-sheets (1625 and 1695 cm^{-1}, respectively).[17,35,36]

Qualitative examination of the spectra showed that 1 % DMSO appeared not to affect the OVA structure, while 2 and 4 % DMSO induced concentration-dependent conformational changes in OVA. Peaks attributed to native-like secondary structures are less prominent in favor of low frequency aggregation specific β-sheets (1622–1625 cm^{-1}). For quantitative determination of secondary structures, second order derivatives of the deconvoluted amide I peaks were created and the respective secondary structure percentages are given in Table II.

TABLE II. The effect of DMSO concentration on the content of secondary structure (contribution of polypeptide chain total structure, %) in OVA

OVA	Structure				
	β-Sheets	Unordered	α-Helix	β-Turn	Error
0 % DMSO	37.2	29.5	25.5	7.8	1.0
1 % DMSO	36.7	30.3	25.0	8.0	1.2
2 % DMSO	41.7	27.3	23.6	7.4	0.9
4 % DMSO	50.3	21.2	19.4	9.1	0.7
X-Ray structure	37.9	28.1	26.3	7.7	–

(CC) 2022 SCS.

While the control of OVA and OVA treated with 1 % DMSO showed a content of secondary structures similar to that of the crystal structure of the protein, higher DMSO concentrations led to significant structural rearrangements. Specifically, the total β-sheet content was elevated by about 13 % at the expense of other secondary structures in 4 % DMSO, such as α-helices and unordered structures.

It was noted in several studies that DMSO has a potential influence on various protein properties at higher DMSO concentrations[37–40] by inducing changes in the binding and biochemical properties of proteins[41] through the indirect disruption of protein–solvent interactions, thus causing subsequent protein denaturation.[37,39,42] However, it has also been shown that DMSO may have such an effect on several protein systems at considerably lower concentrations (0.1–3 vol. % DMSO).[41] Despite the similarly noticeable trend of α-helix to β-sheet conversion in these studies,[43] based on our findings and research it is believe that, in the present *in vitro* system, DMSO concentrations of up to 1% are adequate, as they do not display such a denaturing influence on considerably lower protein concentrations.

*The effect of the complexes **3**–**5** on OVA secondary structures*

Even a simple inspection of the protein IR spectra (Fig. 2) implied that the binding of **3** and **4** led to only moderate alternations in the protein secondary structures. This conclusion was fortified by insignificant changes in the well-described content of protein secondary structures (Table III).

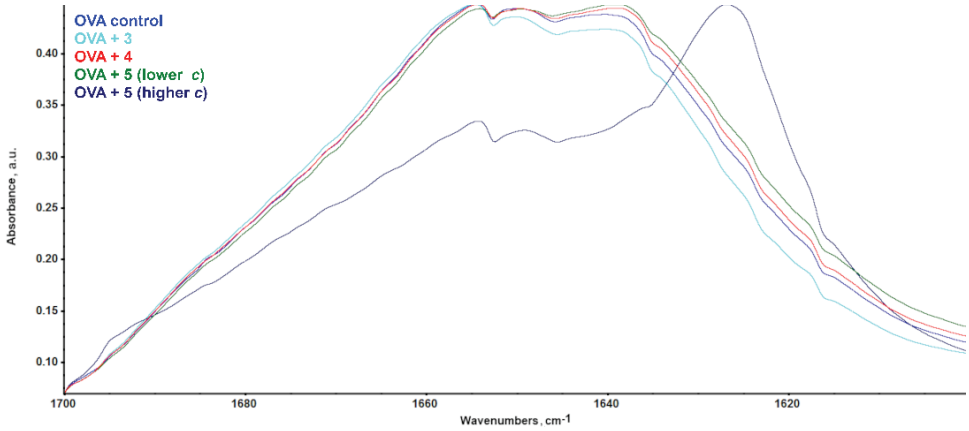

Fig. 2. FTIR spectra of OVA in the presence of the complexes **3**–**5** in 1 % DMSO.

On the other hand, the effect of complex **5** on OVA secondary structures was concentration-dependent. While lower concentration of complex **5** did not have any effect on the OVA structure, even though present in equimolar ratio, doubled

(CC) 2022 SCS.

concentration of complex **5** led to complete disruption of native like secondary structures. In this higher concentration, complex **5** induced a shift toward *β*-fold at the expense of native-like secondary structures, such as *α*-helices and unordered chain (Table III). Elevated intensity of peaks at frequencies of 1625 and 1695 cm^{-1} suggested denaturation and aggregation of OVA (Fig. 2).[22,23]

TABLE III. The effect of the complexes **3**–**5** on the content of OVA secondary structures (Contribution of polypeptide chain total structure, %)

Sample	Structure				
	β-Sheets	Unordered	*α*-Helix	*β*-Turn	Error
OVA control	36.7	30.3	25.0	8.0	1.2
OVA + **3**	34.8	31.5	25.3	8.4	1.5
OVA + **4**	34.2	30.2	27.0	8.6	1.4
OVA + **5** (lower *c*)	37.5	29.5	24.1	8.9	0.9
OVA + **5** (higher *c*)	51.8	19.9	20.1	8.2	1.7

*The effect of complexes **3**–**5** on OVA water exposed hydrophobic surface*

To address such a wide range effects of complexes **3**–**5** on the native structure of OVA, from none to denaturation, the potential effect on their preferential binding to the protein surface was explored by monitoring the water exposed hydrophobic surface of the protein in the absence and the presence of the complexes. Due to the effect of the present palladium complexes on the secondary structure of OVA, conformational changes in the level of exposure of hydrophobic amino acid residues to water were noted. These changes were established *via* the binding of ANS to water-exposed hydrophobic surfaces and are depicted in Fig. 3.

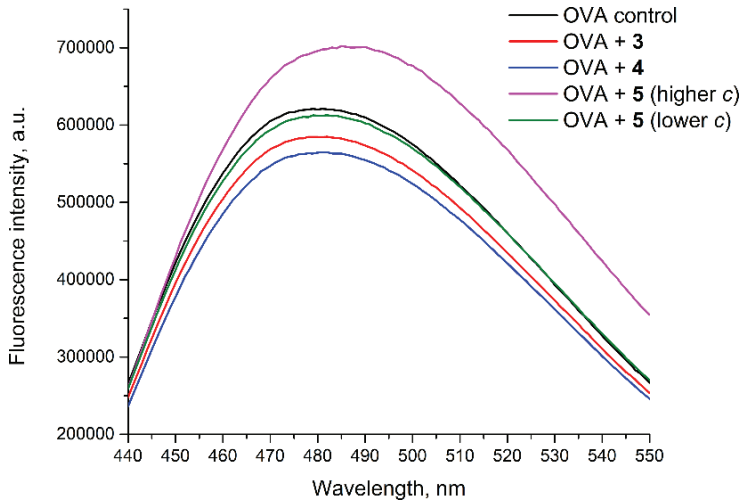

Fig. 3. The effect of complexes **3**–**5** on ANS fluorescence.

(CC) 2022 SCS.

A small but notable decrease of water-exposed hydrophobic protein surfaces may be observed in the cases of the complexes **3** and **4**. The observed change in water exposed protein surface is in line with non-specific, reversible binding of ligands to a protein surface.[44,45] In this sense, complexes **3** and **4** bind to water exposed hydrophobic patches on the OVA surface by weak hydrophobic interactions, thus lowering ANS binding. Bearing in mind their insignificant effect on the presence of protein structural motives (Table III), their binding suggested non-specificity and reversibility, without the possibility of penetration into hydrophobic core of the protein and disruption of the protein native fold. Beside secondary structures changes, binding of the complex **5** to OVA had a concentration-dependent controversial effect on the water exposed hydrophobic surface protein, as well. In the case of the sample with the lower concentration of **5**, only negligible changes in water exposed hydrophobic OVA surface could be observed (Fig. 3). This result is in line with insignificant changes in the content of protein secondary structures and implies that complex **5** does not bind to water exposed hydrophobic patches on protein surface, thus its presence does not interfere with ANS binding. Doubled concentration of both complex **5** and protein, however, induced a considerable increase in the exposure of hydrophobic surfaces to water, as may be observed in the case of sample with the higher concentration of **5**, hinting towards notable conformational changes, including exposure of parts of the hydrophobic core of the protein.

It is well documented that non-specific ligand binding can influence the protein native fold. Induction of protein conformational changes was proven to be in line with induced changes in protein flexibility and the hydrophobic nature of ligands.[46] Since complex **5** is the most hydrophobic among the tested complexes, the obtained results fit well. However, the concentration-dependent effect of complex **5** on secondary structures changes and considerable increase in the exposure of hydrophobic surfaces of OVA to water may be related to a potential crosslinking that leads to OVA aggregation. Exposure of at least parts of hydrophobic core is well documented because that leads to changes in the secondary structures and the consequential aggregation of the denatured proteins.[22,23,31]

CONCLUSIONS

The calculated pharmacological profiles, medicinal chemistry principles and lead-likeness properties of investigated Pd(II) complexes with bidentate *N*-heteroaromatic chelators **1**–**5** indicated that the all complexes represent drug candidates since they possess important functional groups and bioavailability. However, the previously obtained results of the cytotoxic activity do not correlate with the hydrophobic character of the complexes. To gain more insight into structure–activity relationship, essential for design of novel potential drugs, the potential non-specific influence of the complexes on the OVA structure, as a

(CC) 2022 SCS.

model system used to mimic cellular non-specific crowding environments with high protein concentrations were explored. FTIR study implied that the binding of **3** and **4** led to only moderate alternations in OVA secondary structures, without a possibility to penetrate into hydrophobic core of the protein and disruption of the protein native fold. On the contrary, the effect of complex **5** on OVA secondary structures was concentration-dependent. While a lower concentration of complex **5** did not have any effect on OVA structure, doubled the concentration of complex **5** led to complete disruption of the contents of native like secondary structures. Concentration-dependent effect of complex **5** on secondary structures changes and considerable increase in the exposure of OVA hydrophobic surfaces to water may be related to a potential crosslinking which leads to OVA aggregation. It has been demonstrated that a non-specific influence of a compound on a protein structure could be successfully assessed using OVA as a model system. In addition to ADME parameter calculation, this experimental test run at concentrations close to the anticipated or determined IC_{50} values could serve as experimental pre-evaluation of a potential drug candidate and could aid in the selection of a lead compound.

SUPPLEMENTARY MATERIAL

Additional data and information are available electronically at the pages of journal website: https://www.shd-pub.org.rs/index.php/JSCS/article/view/11863, or from the corresponding author on request.

Acknowledgement. The authors acknowledge the financial support of the Ministry of Education, Science and Technological Development of the Republic of Serbia (Contract Nos. 451-03-68/2022-14/200168 and 451-03-68/2022-14/200288).

ИЗВОД

ЕФЕКАТ НЕСПЕЦИФИЧНОГ ВЕЗИВАЊА КОМПЛЕКСА ПАЛАДИЈУМА(II) СА *N*-ХЕТЕРОАРОМАТИЧНИМ ХИДРАЗОНСКИМ ЛИГАНДИМА НА СТРУКТУРУ ПРОТЕИНА

НЕМАЊА Д. МИЈИН[1], ЈЕЛИЦА МИЛОШЕВИЋ[1], НЕНАД Р. ФИЛИПОВИЋ[2], ДРАГАНА МИТИЋ[3], КАТАРИНА АНЂЕЛКОВИЋ[1], НАТАЛИЈА Ђ. ПОЛОВИЋ[1] и ТАМАРА Р. ТОДОРОВИЋ[1]

[1]Универзитет у Београду – Хемијски факултет, Студентски трг 12–16, 11000 Београд, [2]Универзитет у Београду – Пољопривредни факултет, Немањина 6, 11000 Београд и [3]Иновациони центар Универзитета у Београду – Хемијског факултета, Студентски трг 12–16, 11000 Београд

Наша претходна истраживања су била усмерена ка испитивању цитотоксичног дејства пет Pd(II) комплекса са бидентатним *N*-хетероароматичним хелаторима (комплекси **1**–**5**) на палети од неколико туморских ћелијских линија. Међутим, резултати цитотоксичне активности нису били у корелацији са хидрофобним карактером комплекса. Како би се стекао бољи увид у однос између структуре и активности, који је од суштинског значаја за дизајн нових потенцијалних лекова, потребно је узети у обзир и друге факторе, као што су неспецифичне интеракције са ћелијским протеинима. У циљу проучавања потенцијалног неспецифичног утицаја комплекса на структуру протеина, овалбумин (OVA) је изабран као модел систем који опонаша ћелијско неспецифично окружење са високим концентрацијама протеина. Резултати инфрацрвене спектро-

(CC) 2022 SCS.

скопија са Фуријe трансформацијом су указали на то да је везивање **3** и **4** довело до умерених промена у секундарним структурама протеина, без могућности продирања у хидрофобно језгро протеина и поремећаја нативног типа увијања протеина. Насупрот томе, ефекат комплекса **5** на секундарне структуре OVA био је зависан од концентрације. Комплекс **5** при мањој концентрацији није имао утицај на структуру OVA, али је при двоструко већој концентрацији довео до потпуног поремећаја садржаја нативних секундарних структура. Овакав концентрационо-зависан ефекат комплекса **5** на промене секундарних структура и значајно повећање изложености хидрофобних површина OVA протеина молекулима воде може бити повезан са потенцијалним умрежавањем које доводи до агрегације OVA.

(Примљено 18. маја, ревидирано 29. маја, прихваћено 11. јуна 2022)

REFERENCES

1. D. M. Cheff, M. D. Hall, *J. Med. Chem.* **60** (2017) 4517 (https://doi.org/10.1021/acs.jmedchem.6b01351)
2. S. Dasari, P. Bernard Tchounwou, *Eur. J. Pharmacol.* **740** (2014) 364 (https://doi.org/10.1016/j.ejphar.2014.07.025)
3. N. J. Wheate, S. Walker, G. E. Craig, R. Oun, *Dalton Trans.* **39** (2010) 8113 (https://doi.org/10.1039/c0dt00292e)
4. T. C. Johnstone, K. Suntharalingam, S. J. Lippard, *Chem. Rev.* **116** (2016) 3436 (https://doi.org/10.1021/acs.chemrev.5b00597)
5. S. Medici, M. Peana, V. M. Nurchi, J. I. Lachowicz, G. Crisponi, M. A. Zoroddu, *Coord. Chem. Rev.* **284** (2015) 329 (https://doi.org/10.1016/j.ccr.2014.08.002)
6. M. N. Alam, F. Huq, *Coord. Chem. Rev.* **316** (2016) 36 (https://doi.org/10.1016/J.CCR.2016.02.001)
7. A. R. Kapdi, I. J. S. Fairlamb, *Chem. Soc. Rev.* **43** (2014) 4751 (https://doi.org/10.1039/C4CS00063C)
8. M. Fanelli, M. Formica, V. Fusi, L. Giorgi, M. Micheloni, P. Paoli, *Coord. Chem. Rev.* **310** (2016) 41 (https://doi.org/10.1016/j.ccr.2015.11.004)
9. N. Filipovicć, S. Grubišić, M. Jovanović, M. Dulović, I. Marković, O. Klisurić, A. Marinković, D. Mitić, K. Anđelković, T. Todorović, *Chem. Biol. Drug Des.* **84** (2014) 333 (https://doi.org/10.1111/cbdd.12322)
10. S. K. Bjelogrlić, T. R. Todorović, M. Kojić, M. Senćanski, M. Nikolić, A. Višnjevac, J. Araškov, M. Miljković, C. D. Muller, N. R. Filipović, *J. Inorg. Biochem.* **199** (2019) 110758 (https://doi.org/10.1016/j.jinorgbio.2019.110758)
11. ,A. Daina, O. Michielin, V. Zoete, *Sci. Rep.* **7** (2017) 42717 (https://doi.org/10.1038/srep42717)
12. A. Daina, O. Michielin, V. Zoete, *J. Chem. Inf. Model.* **54** (2014) 3284 (https://doi.org/10.1021/CI500467K)
13. M. G. Mendoza-Ferri, C. G. Hartinger, M. A. Mendoza, M. Groessl, A. E. Egger, R. E. Eichinger, J. B. Mangrum, N. P. Farrell, M. Maruszak, P. J. Bednarski, F. Klein, M. A. Jakupec, A. A. Nazarov, K. Severin, B. K. Keppler, *J. Med. Chem.* **52** (2009) 916 (https://doi.org/10.1021/JM8013234)
14. J. A. Huntington, P. E. Stein, *J. Chromatogr., B* **756** (2001) 189 (https://doi.org/10.1016/S0378-4347(01)00108-6)
15. H. Y. Hu, H. N. Du, *J. Protein Chem.* **19** (2000) 177 (https://doi.org/10.1023/A:1007099502179)

(CC) 2022 SCS.

16. M. Sogami, S. Era, T. Koseki, N. Nagai, *J. Pept. Res.* **50** (1997) 465 (https://doi.org/10.1111/J.1399-3011.1997.TB01210.X)
17. C. Lara, S. Gourdin-Bertin, J. Adamcik, S. Bolisetty, R. Mezzenga, *Biomacromolecules* **13** (2012) 4213 (https://doi.org/10.1021/BM301481V)
18. J. Li, S. Zhang, C. C. Wang, *J. Biol. Chem.* **276** (2001) 34396 (https://doi.org/10.1074/JBC.M103392200)
19. B. Van Den Berg, R. J. Ellis, C. M. Dobson, *EMBO J.* **18** (1999) 6927 (https://doi.org/10.1093/EMBOJ/18.24.6927)
20. C. F. MacRae, I. Sovago, S. J. Cottrell, P. T. A. Galek, P. McCabe, E. Pidcock, M. Platings, G. P. Shields, J. S. Stevens, M. Towler, P. A. Wood, *J. Appl. Crystallogr.* **53** (2020) 226 (https://doi.org/10.1107/S1600576719014092)
21. N. M. O'Boyle, M. Banck, C. A. James, C. Morley, T. Vandermeersch, G. R. Hutchison, *J. Cheminform.* **3** (2011) 1 (https://doi.org/10.1186/1758-2946-3-33/TABLES/2)
22. J. Milošević, J. Petrić, B. Jovčić, B. Janković, N. Polović, *Spectrochim. Acta, A* **229** (2020) 117882 (https://doi.org/10.1016/J.SAA.2019.117882)
23. J. Milošević, R. Prodanović, N. Polović, *Molecules* **26** (2021) 970 (https://doi.org/10.3390/MOLECULES26040970)
24. C. A. Lipinski, F. Lombardo, B. W. Dominy, P. J. Feeney, *Adv. Drug Deliv. Rev.* **46** (2001) 3 (https://doi.org/10.1016/S0169-409X(00)00129-0)
25. C. Aldrich, C. Bertozzi, G. I. Georg, L. Kiessling, C. Lindsley, D. Liotta, K. M. Merz, A. Schepartz, S. Wang, *ACS Cent. Sci.* **3** (2017) 143 (https://doi.org/10.1021/ACSCENTSCI.7B00069)
26. T. Sterling J. J. Irwin, *J. Chem. Inf. Model.* **55** (2015) 2324 (https://doi.org/10.1021/ACS.JCIM.5B00559)
27. R. Wang, Y. Fu, L. Lai, *J. Chem. Inf. Comput. Sci.* **37** (1997) 615 (https://doi.org/10.1021/CI960169P)
28. S. A. Wildman, G. M. Crippen, *J. Chem. Inf. Comput. Sci.* **39** (1999) 868 (https://doi.org/10.1021/CI990307L)
29. I. Moriguchi, H. Hirano, I. Nakagome, *Chem. Pharm. Bull.* **42** (1994) 976 (https://doi.org/10.1248/CPB.42.976)
30. I. Moriguchi, S. Hirono, Q. Liu, Izum. Nakagome, Y. Matsushita, *Chem. Pharm. Bull.* **40** (1992) 127 (https://doi.org/10.1248/CPB.40.127)
31. B. Rašković, N. Babić, J. Korać, N. Polović, *J. Serb. Chem. Soc.* **80** (2015) 613 (https://doi.org/10.2298/JSC140901007R)
32. A. Dong, J. D. Meyer, J. L. Brown, M. C. Manning, J. F. Carpenter, *Arch. Biochem. Biophys.* **383** (2000) 148 (https://doi.org/10.1006/ABBI.2000.2054)
33. G. Vedantham, H. G. Sparks, S. U. Sane, S. Tzannis, T. M. Przybycien, *Anal. Biochem.* **285** (2000) 33 (https://doi.org/10.1006/ABIO.2000.4744)
34. D. Smith, V.B. Galazka, N. Wellner, I. G. Sumner, *Int J. Food Sci Tech* **35** (2000) 361 (https://doi.org/10.1046/j.1365-2621.2000.00395.x)
35. J. S. Cristóvão, B. J. Henriques, C. M. Gomes, *Methods Mol. Biol.* **1873** (2019) 3 (https://doi.org/10.1007/978-1-4939-8820-4_1)
36. A. Barth, *Biochim. Biophys. Acta - Bioenergy* **1767** (2007) 1073 (https://doi.org/10.1016/J.BBABIO.2007.06.004)
37. T. M. Greve, K. B. Andersen, O. F. Nielsen, *Spectroscopy* **22** (2008) 405 (https://doi.org/10.3233/SPE-2008-0358)
38. A. N. L. Batista, J. M. Batista, V. S. Bolzani, M. Furlan, E. W. Blanch, *Phys. Chem. Chem. Phys.* **15** (2013) 20147 (https://doi.org/10.1039/C3CP53525H)

(CC) 2022 SCS.

39. P. Huang, A. Dong, W. S. Caughey, *J. Pharm. Sci.* **84** (1995) 387 (https://doi.org/10.1002/JPS.2600840402)
40. S. Roy, B. Jana, B. Bagchi, *J. Chem. Phys.* **136** (2012) 115103 (https://doi.org/10.1063/1.3694268)
41. A. Tjernberg, N. Markova, W. J. Griffiths, D. Hallén, *J. Biomol. Screen.* **11** (2006) 131 (https://doi.org/10.1177/1087057105284218)
42. T. Arakawa, Y. Kita, S. N. Timasheff, *Biophys. Chem.* **131** (2007) 62 (https://doi.org/10.1016/J.BPC.2007.09.004)
43. S. Tunçer, R. Gurbanov, I. Sheraj, E. Solel, O. Esenturk, S. Banerjee, *Sci. Rep.* **8** (2018) 14828 (https://doi.org/10.1038/s41598-018-33234-z)
44. C. X. Wang, F. F. Yan, Y. X. Zhang, L. Ye, *J. Photochem. Photobiol., A* **192** (2007) 23 (https://doi.org/10.1016/J.JPHOTOCHEM.2007.04.032)
45. E. Schönbrunn, S. Eschenburg, K. Luger, W. Kabsch, N. Amrhein, *Proc. Natl. Acad. Sci. U.S.A.* **97** (2000) 6345 (https://doi.org/10.1073/PNAS.120120397)
46. M. S. Celej, G. G. Montich, G. D. Fidelio, *Protein Sci.* **12** (2003) 1496 (https://doi.org/10.1110/PS.0240003).

(CC) 2022 SCS.

Journal of the Serbian Chemical Society
JSCS@tmf.bg.ac.rs • www.shd.org.rs/JSCS
J. Serb. Chem. Soc. *87* (10) S379 (2022) *Supplementary material*

SUPPLEMENTARY MATERIAL TO

The effect of non-specific binding of Pd(II) complexes with *N*-heteroaromatic hydrazone ligands on the protein structure

NEMANJA D. MIJIN[1#], JELICA MILOŠEVIĆ[1], NENAD R. FILIPOVIĆ[2#], DRAGANA MITIĆ[3#], KATARINA ANĐELKOVIĆ[1#], NATALIJA Đ. POLOVIĆ[1#] and TAMARA R. TODOROVIĆ[1*#]

[1]University of Belgrade – Faculty of Chemistry, Studentski trg 12–16, 11000 Belgrade, Serbia, [2]University of Belgrade – Faculty of Agriculture, Nemanjina 6, 11000 Belgrade, Serbia and [3]Innovation Centre of University of Belgrade – Faculty of Chemistry, Studentski trg 12–16, 11000 Belgrade, Serbia

J. Serb. Chem. Soc. *87* (10) (2022) 1143–1156

SPECTRAL DATA OF COMPLEXES **3**–**5**

3: ^{1}H-NMR (500 MHz, DMSO-d_6, δ / ppm): 1.24 (3H, *t*), 4.19 (2H, *q*), 4.38 (2H, *d*), 7.55 (1H, *ddd*), 7.72 (1H, *s*), 7.73 (1H, *d*), 8.16 (1H, *dt*), 8.33 (1H, *t*), 8.76 (1H, *d*). ^{13}C-NMR (126 MHz, DMSO-d_6, δ / ppm): 13.91, 47.43, 61.21, 123.95, 124.23, 136.52, 141.11, 148.94, 157.44, 167.11.

4: ^{1}H-NMR (500 MHz, $CDCl_3$, δ / ppm): 1.25 (3H, *t*), 2.52 (3H, *s*), 7.95 (2H, *m*), 4.05 (2H, d), 8.31 (2H, m), 4.15 (2H, q), 7.21 (1H, t), 7.77 (1H, ddd), 8.12 (1H, dd), 8.37 (1H, *ddd*), 8.97 (1H, *dd*). ^{13}C-NMR (126 MHz, DMSO-d_6, δ / ppm): 14.24, 16.15, 51.65, 61.20, 126.62, 127.73, 141.59, 149.90, 156.35, 168.53, 168.71.

5: ^{1}H-NMR (500 MHz, DMSO-d_6, δ / ppm): 1.13 (3H, *t*), 3.52 (1H, *d*), 4.04 (1H, *q*), 7.05 (1H, *dd*), 7.56–7.52 (2H, *m*), 7.67–7.61 (3H, *m*), 7.70 (1H, *ddd*), 8.02 (1H, *t*), 8.11 (1H, *td*), 8.99 (1H, *dd*). ^{13}C-NMR (126 MHz, DMSO-d_6, δ / ppm): 13.11, 51.36, 61.14, 126.02, 126.16, 129.07, 129.52, 129.92, 131.11, 141.32, 149.64, 155.48, 157.63, 167.69.

* Corresponding author. E-mail: tamarat@chem.bg.ac.rs

Available on line at www.shd.org.rs/JSCS/
(CC) 2022 SCS.

Journal of the Serbian Chemical Society
JSCS-info@shd.org.rs • www.shd.org.rs/JSCS
J. Serb. Chem. Soc. *87* (10) 1157–1170 (2022)
JSCS–5585
Original scientific paper
Published 30 September 2022

Adsorption of bendamustine anti-cancer drug on Al/B–N/P nanocages: A comparative DFT study

NOSRAT MADADI MAHANI*, REZA BEHJATMANESH-ARDEKANI and ROYA YOSEFELAHI

Department of Chemistry, Payame Noor University (PNU), 19395-4697, Tehran, Iran

(Received 12 March, revised 25 May, accepted 26 May 2022)

Abstract: Anti-cancer drug delivery based on nanocages is important step in drug development process due to reducing side effects and drug-releasing near the tumor cell. We have studied the interaction of the bendamustine anti-cancer drug with the Al/B-N/P nanocages with utilization density functional theory (DFT) approach both in gas and water phases at the B3LYP/6-31G (d,p) level of theory. Results show that the nanocages quantum parameters were somewhat varied by the adsorption of the bendamustine drug. The bendamustine drug operates as an electrons donor and can adsorb in the site of the electron's acceptor of nanocages. The changes in Gibbs energy correspond to a chemisorption in both phases. The results indicated that the bond between studied nanocages and bendamustine is covalent. However, all studied nanocages may be favorable candidates for detecting the bendamustine drug. Yet, pristine $B_{12}P_{12}$ and $B_{12}N_{12}$ nanocages appeared to be more suitable for drug delivery than $Al_{12}P_{12}$ and $Al_{12}N_{12}$ based on their recovery times.

Keywords: drug delivery; recovery time; interaction; covalent; molecular electrostatic potential (*MEP*); Gibbs energy; nanostructure.

INTRODUCTION

Bendamustine belongs to alkylating agents[1] that can be used to treat various human cancers such as non-Hodgkin's lymphoma, multiple myeloma, chronic lymphocytic leukemia, lung cancer and sarcoma.[2]

Bendamustine contains a benzimidazole ring, a butyric acid side chain and a 2-chloroethylamine alkylating group (Fig. 1). Bendamustine is a chemotherapeutic drug with a different cytotoxicity type contrasted with typical alkylating agents. It has both alkylating and antimetabolite properties.[3] Nanocarriers could decrease toxic effects of drugs, especially anti-cancer drugs. In the past few years, the applications of boron nitride (BN) and aluminum nitride (AlN) nano-

* Corresponding author. E-mail: nmmadady@gmail.com
https://doi.org/10.2298/JSC220312046M

Available on line at www.shd.org.rs/JSCS/
(CC) 2022 SCS.

cages as drug delivery have increased due to their features such as high thermal stability, great adsorbing capacity and low toxicity.

Units of the boron nitride (BN) and aluminum nitride (AlN) create main groups of nanostructures, they are made in the combinations of nanosheets, nanoclusters, nano chains and nanocages.[4] Recently, it has been demonstrated that boron nitride (BN) and aluminum nitride (AlN) nanocages are nontoxic[5] and can be beneficial for pharmaceutical applications.

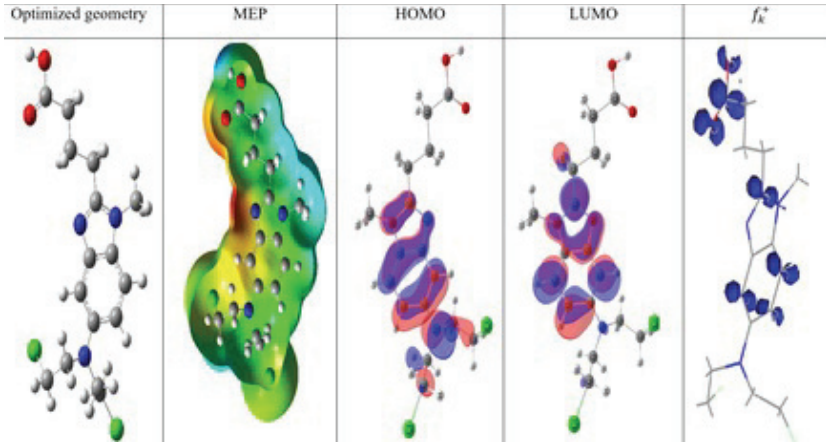

Fig. 1. Geometry optimization, molecular electrostatic potential *(MEP)*, F+ descriptor and HOMO–LUMO depictions of bendamustine drug (solvent).

Due to their excellent properties, boron nitride nanotubes have been used as a new carrier for the purposed magnetic carrier of the drugs.[6] The previous studies have illustrated that B atoms are more reactive than nitrogen atoms for N containing functional groups for BN systems.[7,8] Also, it was reported that lithium-doped fullerenes are more reactive than the pristine fullerenes in reactions of 1,3 dipolar cycloaddition.[9] Soltani *et al.*[10] have investigated the optical and electronic features of 5-AVA-functionalized BN nanoclusters by DFT calculations. Also, 5-ALA functioned with B16N16 and B12N12 nanoclusters have been studied to investigate the electronic and structural properties. DFT studies have been performed for investigation interaction of melphalan anticancer drug and 24 atoms nanoclusters.[11]

The adsorption of histidine and tyrosine amino acids on $Al_{12}N_{12}$ and $B_{12}N_{12}$ nanocages has been studied to develop biochemical sensors for these amino acids.[12] The interaction between adipic acid and Al/B-N/P nanocages was investigated by DFTapproach.[13] Soliman *et al.*[14] have studied adsorption of favipiravir drugs on fullerene and boron nitride nanocages by theoretical methods. Density functional theory studies have been carried out for the AlN nanotube, nanosheet and nanocage with benzoyl ethanamine drug.[15] Interaction between the jug-

(CC) 2022 SCS.

lone and its derivative as antioxidant agents with $B_{12}N_{12}$ nanocage have been investigated by density functional theory.[16] Also, DFT calculations have been performed for adsorption of guanine as a nucleobase on the surface of $Al_{12}N_{12}$, $Al_{12}P_{12}$, $B_{12}N_{12}$ and $B_{12}P_{12}$ nanocages.[17]

In the present study, we investigated and compared the interaction of bendamustine theoretically functionalized at $B_{12}N_{12}$, $B_{12}P_{12}$, $Al_{12}N_{12}$ and $Al_{12}P_{12}$ nanocages for the amelioration and design of nanocages ability for drug delivery. For investigation of the interaction between these nanocages with bendamustine drug, we studied quantum and thermodynamic descriptors. Free energies of binding, HOMO–LUMO frontier orbital diagrams, molecular electrostatic potential (*MEP*), density of state (DOS) plots, AIM and NBO analysis and time recovery for bendamustine drug desorption from studied nanocages.

EXPERIMENTAL

The initial structure of $B_{12}N_{12}$, $B_{12}P_{12}$, and $Al_{12}N_{12}$, $Al_{12}P_{12}$ and bendamustine drug were created using Gauss View 5.0 and optimized by density functional theory at the B3LYP/6-31g (d,p) level[18] of theory using the Gaussian 09 code[19] in the gas and the solvent phases. The formation a homogenous system, is one of the important parameters to achieve desired concentration of drug in systemic circulation for desired (anticipated) pharmacological response. As solvent (water) plays a major role in our body, it has been selected as a solvent in order to identify the interaction of bendumustine molecule with nanocages while passing through human bodies.

Thereinafter, complexes of bendamustine and nanocages were geometrically optimized. The B3LYP functional was an efficacious and accurate functional in nanostructure systems.[20] Frequency calculations were performed and demonstrated that there is no negative frequency in typical analyses. One of the aims of this research is foretelling the sensibility gap of the nanocages to the vicinity of bendamustine drug using the highest occupied (HOMO) and the lowest unoccupied molecular orbital (LUMO). The E_g is dependent on the conduction electron population (N) and can be applied as benchmarks for an adsorbing sensibility that can be used as a suitable criterion for their adsorption:[21]

$$N = AT^{3/2} \exp(-E_g / 2kT) \tag{1}$$

where k is the Boltzmann constant and A (electrons m^3 $K^{3/2}$) is a constant.

For the interaction of nanocages with bendamustine drug, the most stable complex nanocage–bendamustine was optimized on the gas phase and the water solvent employing the B3LYP/6-31G (d,p) level theory. The change in adsorption energy of bendamustine drug on nanocages has been obtained using the following equation:

$$\Delta G_{ad} = G_{nanocage/bendamustine} - (G_{bendamustine} + G_{nanocage}) \tag{2}$$

where $G_{nanocage/bendamustine}$ is the Gibbs energy of the complex, *i.e.*, the interaction between anti-cancer bendamustine drug ($G_{bendamustine}$) and the studied nanocages ($G_{nanocage}$).

To investigate the electronic structure and the nature of the interaction of complexes, molecular electrostatic potential (MEP), HOMO–LUMO frontier orbital diagrams and density of states (DOS) were presented. This approach has been proven to be beneficial in the previous literature.[22,23] Furthermore, the calculation of quantum theory of atoms in molecules (QTAIM)[24] was performed for detailed investigation on bonding characteristics and to probe

(CC) 2022 SCS.

the electron density of complexes. Atom in molecule (AIM) analysis was used to calculate intramolecular force. The electron density (ρ), Laplacian of electron densities ($\nabla^2\rho$) and ellipticity parameters (ε) at the bond critical points for nanocages–bendamustine were calculated from AIM calculations *via* the AIM studio program.

RESULTS AND DISCUSSION

The pristine nanocages consist of 6 tetragonal and 8 hexagonal rings that are not flattish.[25] Table I and Fig. 2 show the mean bond angles and bond lengths for Al–N, Al-P, B–N and B–P in tetragonal and hexagonal rings before and after adsorption. The mean bond lengths in the nanocages are longer in the $Al_{12}P_{12}$ in both the hexagonal and the tetragonal rings. Although, the bond lengths of the hexagonal ring in nanocages are shorter than the tetragonal rings due to the more tension in the tetragonal rings compared to the hexagonal ones.

TABLE I. Selected bond lengths (D_1 and D_2) and bond angles A_1, A_2, A_3 and A_4 for nanocages (PCM)

Property	Ring	$B_{12}N_{12}$	$B_{12}P_{12}$	$Al_{12}N_{12}$	$Al_{12}P_{12}$
D_1 / nm	6	0.1440	0.1910	0.1798	0.2343
D_2 / nm	4	0.1486	0.1929	0.1861	0.2343
A_1 / ° (Al–N(P)–Al/B–N(P)–B)	6	111.0402	101.9178	112.7974	101.9178
A_2 / ° (N(P)–Al–N(P)/N(P)–B–N(P))	6	125.7739	129.5436	125.5935	129.9199
A_3 / ° (N(P)–Al–N(P)/N(P)–B–N(P))	4	98.2291	98.8408	94.5483	99.0950
A_4 / ° (Al–N(P)–Al/B–N(P)–B)	4	80.5001	76.1199	84.5106	74.8137

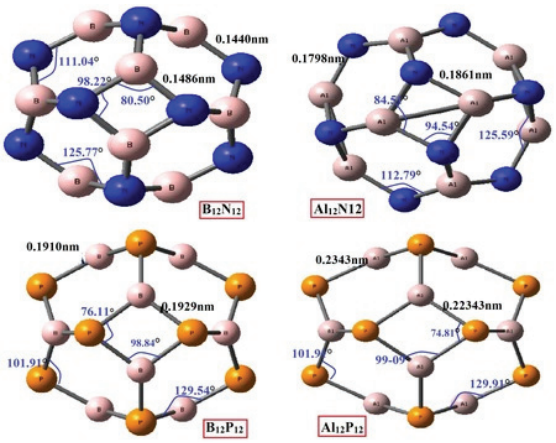

Fig. 2. Bond lengths and bond angles for nanocages (PCM).

The bond angles for N–Al–N in $Al_{12}N_{12}$ nanocage are A_2 = 125.59°, A_3 = = 94.54°. Also, the bond angles for Al–N–Al are, A_1 = 112.79° and A_4 = 84.51°, in the hexagonal and tetragonal rings, respectively. Whereas, in the $B_{12}N_{12}$ nanocage, the N–B–N angle has the values of A_2 = 125.77°, A_3 = 98.22° and the B–N–B angle has the values of A_1 = 111.04°, and A_4 = 80.46°, in the hexagonal ring and

(CC) 2022 SCS.

the tetragonal rings, respectively which are almost the same in both $Al_{12}N_{12}$ and $B_{12}N_{12}$ nanocages. The P–Al–P angle has the values of $A_2 = 129.91°$ and $A_3 = = 99.09°$ and the Al–P–Al angle has the values of $A_1 = 99.80°$ and $A_4 = 74.81°$, in the hexagonal ring and the tetragonal rings, respectively. While the P–B–P angle has the values of $A_2 = 129.54°$, $A_3 = 98.84°$ and the B–P–B angle has the values of $A_1 = 101.91°$ and $A_4 = 76.11°$ in the hexagonal ring and the tetragonal rings, respectively.

The lowest unoccupied molecular orbitals (LUMOs) and the highest occupied molecular orbitals (HOMOs) as the frontier molecular orbitals (FMOs) are the central orbitals that participate in chemical reactions. The HOMO signifies LUMO's capacity to supply an electron as an electron receptor.[26]

The difference between LUMO and HOMO, which is called the energy gap, displays structure stability.[27] Fig. 2 displays pictures of the HOMOs and LUMOs orbitals. The energy gap of the anti-cancer drug is observed to be 4.74 eV, which is reasonable for the pharmaceutical activity of the bendamustine drug.[28–30] Higher energy gap indicates less polarity of anticancer drug, which is recognized as a hard drug. Also, it indicates low chemical reactivity and suitable stability.

The strength of the vicinal charges, electrons and nuclei at a unique position was investigated by molecular electrostatic potential (*MEP*) in terms of colors.[31,32] *MEP* of the bendamustine drug in the PCM is illustrated in Fig. 2. The negative and positive positions are of the bendamustine drug are between $–7.930×10^{–2}$ and $7.93×10^{–2}$.

The most positive region, as the nucleophilic site, is demonstrated by blue color and the most negative region, as the electrophilic site, is displayed by red color. The bendamustine drug, near the nitrogen atom N39, is more the negative and demonstrated by the red color. Around COOH functional group are also somewhat negative. The other segments of the drug are illustrated in the nucleophilic region. Therefore, the reactive regions of the drug represent biological activity.

To recognize reactivity sites for bendamustine drug, Fukui functions for electrophilic and nucleophilic attacks (f_k^+, f_k^-) has been studied[33] based on Mulliken population analysis, which has been calculated as:

$$f_k^+ = (q(N+1) – q(N)) \text{ for nucleophilic attack} \quad (3)$$

$$f_k^- = (q(N) – q(N–1)) \text{ for electrophilic attack} \quad (4)$$

Also, dual descriptor $\Delta f(k)$ is obtained by following the formula:[34]

$$\Delta f(k) = f_k^+ – f_k^- \quad (5)$$

For the electrophilic attack, $\Delta f(k)$ is negative, and for the nucleophilic attack, $\Delta f(k)$ is positive.

Fukui indices for nucleophilic attack (Fukui (+)) *N* (39) is equal 0.085, and for electrophilic attack (Fukui (–)) is equal 0.006. The trend of the dual Fukui

(CC) 2022 SCS.

indices for nucleophilic attack is as follows N8 > N16 > N17. The negative dual descriptor for electrophilic attack is O21 > O22.

This study's primary purpose is to investigate the sensitivity of electronic properties of the $Al_{12}N_{12}$, $Al_{12}P_{12}$, $B_{12}N_{12}$ and $B_{12}P_{12}$ nanocages to the bendamustine drug. The results in Table II display that in all bendamustine/nanocage systems, the HOMO is unfixed, and the LUMO is fixed after the adsorption process of bendamustine drug; so, the E_g in them is reduced.

TABLE II. Chemical descriptors o in both the gas and the solvent phases

Compound	Phase	E_{HOMO} / eV	E_{LUMO} / eV	E_g / eV	η /eV	S / eV^{-1}	χ / eV
$B_{12}N_{12}$	GAS	–7.7098	–0.8617	6.8480	3.4240	0.2920	4.2858
	PCM	–7.6997	–0.8002	6.8995	3.4497	0.2898	4.2500
$B_{12}P_{12}$	GAS	–6.8301	–3.1315	3.6986	1.8493	0.5407	4.9808
	PCM	–6.6347	–2.9051	3.7296	1.8648	0.5362	4.7699
$Al_{12}N_{12}$	GAS	–6.4717	–2.5393	3.9323	1.9661	0.5086	4.5055
	PCM	–6.5177	–2.4607	4.0569	2.0284	0.4929	4.4892
$Al_{12}P_{12}$	GAS	–6.7462	–3.3633	3.3829	1.6914	0.5912	5.0548
	PCM	–6.4488	–2.9045	3.5443	1.7721	0.5642	4.6767
Drug	GAS	–5.1255	–0.3757	4.7497	2.3748	0.4210	2.7506
	PCM	–5.1522	–0.4473	4.7048	2.3524	0.4250	2.7998
$Al_{12}P_{12}$–B	GAS	–5.5756	–2.4199	3.1557	1.5778	0.6337	3.9977
	PCM	–5.4921	–2.5091	2.9829	1.4914	0.6704	4.0006
$B_{12}N_{12}$–B	GAS	–5.7721	–1.4359	4.3361	2.1680	0.4612	3.6040
	PCM	–5.5198	–1.1243	4.3954	2.1977	0.4550	3.3221
$B_{12}P_{12}$–B	GAS	–5.5805	–2.3646	3.2158	1.6079	0.6219	3.9726
	PCM	–5.5440	–2.5905	2.9535	1.4767	0.6771	4.0673
$Al_{12}N_{12}$–B	GAS	–5.5560	–1.7227	3.8332	1.9166	0.5217	3.6394
	PCM	–5.4444	–1.8525	3.5919	1.7959	0.5568	3.6485

The drug losses more electrons basis on NBO charge analysis in the liquid phase to the nanocages than in the gas phase. For instance, a charge of 0.45 e is conducted from the drug to the AlN nanocage complex, but that is 0.25 e in the gas phase. Finally, the charge transfer in the liquid phase is more prominent than in the gas phase, as shown in Table III. Accordingly, it can be deduced that nanocages can diagnose bendamustine most positive region as the nucleophilic site drug according to Eq. (2). Since the electrical conductivity of the nanocages increased by decreasing the E_g, which can be transformed into an electrical signal that supports the detection process.

According to Zhan *et al.*[35] gap energy equals to, $E_g = E_{LUMO} - E_{HOMO}$ chemical hardness equals to $\eta = E_g/2$, mulliken electronegativity equals to $\chi =$ $= E_{LUMO} + + E_{HOMO}$, and the chemical softness equals to $S = 1/\eta$ which is the opposite of hardness. The energy gap varies in the order BN > AlN > BP > AlP in pristine nanocages, also after complexation show the same trend.

(CC) 2022 SCS.

TABLE III. Values of Gibbs energy change, recovery time, dipole moments and ΔN for systems under study

Compound	Medium	ΔG / kJ mol^{-1}	τ / s	Dipole moment, D*	ΔN
$B_{12}N_{12}$–B	Gas	–70.50	2.14	9.85	–0.38
	PCM	–83.05	3.41×10^{2}	14.38	–0.41
$B_{12}P_{12}$–B	Gas	–45.77	10^{4}	11.49	–0.39
	PCM	–48.78	3.00×10^{4}	15.95	–0.42
$Al_{12}N_{12}$–B	Gas	–117.57	3.73×10^{8}	10.21	–0.27
	PCM	–126.18	1.20×10^{10}	20.69	–0.45
$Al_{12}P_{12}$–B	Gas	–98.95	2.05×10^{5}	16.14	–0.28
	PCM	–109.53	1.46×10^{7}	23.68	–0.33

The E_g is decreased in all nanocages complexes compared to the pristine nanocages. Consequently, it is possible that the bendamustine drug can be sensed by nanocages based on the Eq. (1). Because the electrical conductivity of the nanocages will rise by reducing the E_g and help the detection process.

HOMO and LUMO of nanocages are on N and P, and considerable variations are observed for HOMO and LUMO on complexation with bendamustine drug, which is like the adsorption of guanine on these nanocages.[36]

The hardness values of AlN/AlP/BN/BP–bendamustine complexes are 1.79, 1.49, 2.19 and 1.47 eV, respectively. This shows, for all systems, the softness will increase after adsorption, but the hardness is decreased after adsorption.

In bendamustine nanocage systems, HOMO of AlN– AlP– and BP–bendamustine is located on the drug except for COOH group, and LUMO is situated on ALN nanocage.

Nevertheless, in BN–bendamustine, both HOMO and LUMO are spread over drugs except the COOH group. The distributions of HOMO and LUMO can change the band gap. Change in band gap upon complexation is 2.5 eV in BN, but changes in band gap are smaller in another nanocage. Therefore, the nanocages can be used as useful sensors for bendamustine because their electronic properties mainly change. Also, to determine the chemical activity of complexes, the MEPs surface of bendamustine with nancages are investigated. Fig. 3 displays that N and P are negatively charged, while B and Al are positively charged.

The nanocages, due to the charge density, can act as the nucleophilic site. Dipole moments of pristine nanocages are zero. Significant changes are displayed in dipole moment after adsorption (Table III).

Dipole moments of AlN–bendamustine, AlP–bendamustine, BN–bendamustine, and BP–bendamustine are 20.69, 23.68, 14.37 and 15.94 D, respectively, in the solvent phase. The most increase is seen for AlP–bendamustine, followed by AlN–bendamustine nanocage. As well as BN–bendamustine complex has a low

* 1 D = 3.335×10^{30} C m

(CC) 2022 SCS.

dipole moment. In addition, low dipole moments for boron nanocages are due to the low charge of BN nanocage.

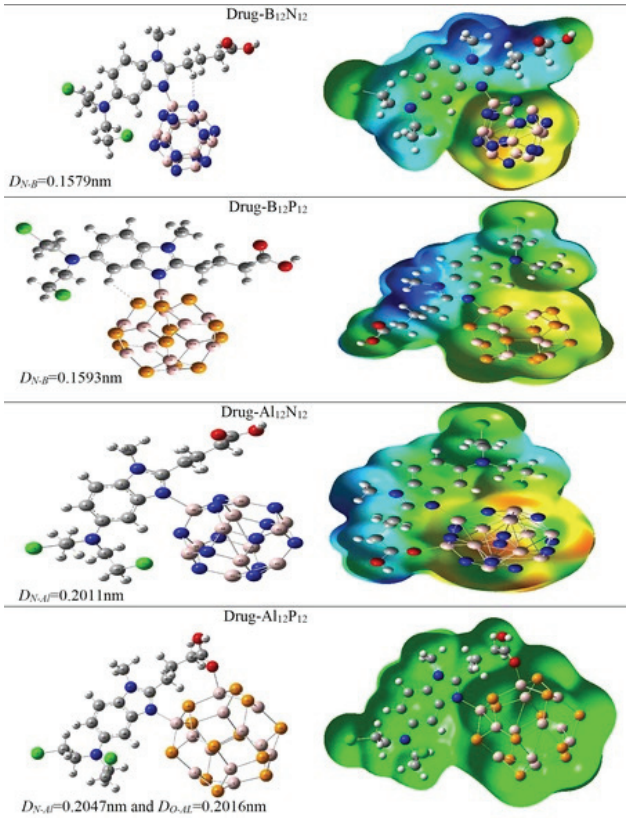

Fig. 3. Geometry optimizations and molecular electrostatic potential (MEP) maps of systems under study.

We investigated and assessed the active adsorption sites of the bendamustine drug-using Fukui function and MEPs analysis. The Gibbs energy changes (ΔG) according to Eq. (2), based on the most stable bendamustine nanocages in the gas and the solvent phases, are listed in Table III.

For all the other studied nanocages, large negative ΔG values (ΔG bendamustine–$B_{12}N_{12}$ = –70.50 and –83.05 kJ mol^{-1}, ΔG bendamustine–$B_{12}P_{12}$ = = –45.77 and –48.78 kJ mol^{-1}, ΔG bendamustine–$Al_{12}N_{12}$ = –117.57 and –126.18 kJ mol^{-1} and ΔG bendamustine–$Al_{12}P_{12}$ = –98.95 and –109.53 kJ mol^{-1}) in the gas and solvent phases are obtained and could be represented as covalent interactions. These interactions are exothermic thermodynamically and have shown chemisorption adsorption. Therefore, studied nanocages adsorb bendamustine efficiently. Compared to the results of the adsorption of alprazolam drug

(CC) 2022 SCS.

on the $B_{12}N_{12}$ and $Al_{12}N_{12}$ nanocages,[37] ΔG value of $Al_{12}N_{12}$–B is similar to $Al_{12}N_{12}$–alprazolam, but ΔG value of $B_{12}N_{12}$–B is less than $B_{12}N_{12}$–alprazolam and the complex formation process is spontaneous in all complexes.

The recovery time and sensibility of a sensor are essential parameters. The recovery time of a pharmaceutical molecule in drug delivery is fundamental characteristic in the drug adsorption. The desorption and release of the drug molecule are also momentous for a suitable sensor. Experimentally, the recovery process has been evaluated using UV light and high temperatures.[38]

Table III illustrates the recovery time for desorption of bendamustine drug from the surface of the studied nanocages in both the gas and the solvent phases. Recovery time is calculated from the transition state theory (TST):

$$\tau = \nu_0^{-1} \exp(\frac{-\Delta G_{ads}}{kT}) \quad (6)$$

where ν_0 is the frequency of attempt, k is the Boltzmann constant (8.3262 kJ mol^{-1} K^{-1}) and T is temperature. An attempt frequency, $\nu = 10^{12}$ s^{-1}, has been applied to the recovery time for separating NO_2 molecules from carbon nanotubes at room temperature.[39]

The trend of the recovery time, for desorption bendamustine drug from the surface of nanocages, are AlN>AlP>BN>BP in both phases which are in settlement with the trend of the Gibbs energy changes. Based on Eq. (6), more changes in Gibbs energy of adsorption causes a more extensive recovery time. According to obtained recovery times, $Al_{12}N_{12}$ and $Al_{12}P_{12}$ with a noticeable recovery time may not be a suitable sensor for bendamustine since bendamustine cannot desorb itself properly after adsorbing to $Al_{12}N_{12}$ and $Al_{12}P_{12}$ and could not be used as nano vehicle.

On the other hand, the recovery times for desorbing of bendamustine from BN and BP surfaces are low. These conclusions represented that the bendamustine drug can desorb from the $B_{12}N_{12}$ and BP nanocages at a suitable time. As a result, the $B_{12}N_{12}$ and BP nanocages can act as acceptable sensors for bendamustine.

In Fig. 4, DOS plots illustrated the number of states for both valence and conduction level of bendamustine were a little shifted with adsorbing on studied nanocages. Interaction bendamustine drug with nanocages is an electronically harmless interaction and would not change the properties of the drug. Because of their negative LUMO levels, the studied nanocages have a more considerable electron affinity also, due to a negative LUMO level, tend to capture electrons. In the formed complexes, the highest state occupied level, and the lowest state unoccupied level, the electronic contribution is related to the bendamustine drug, and no remarkable changes appeared.

(CC) 2022 SCS.

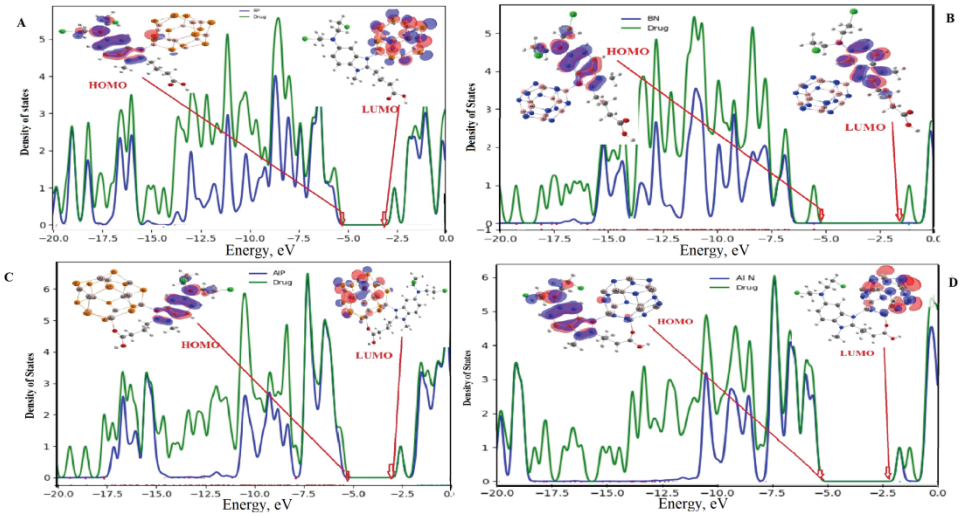

Fig. 4. Density of states for the complexation of: $B_{12}P_{12}$ (A), $B_{12}N_{12}$ (B), $Al_{12}P_{12}$ (C) and $Al_{12}N_{12}$ (D) with bendamustine drug at the B3LYP/6-31g (d,p) level of theory (PCM).

One of quantum chemistry methods for investigating the nature of bonds at interaction regions is the atoms in molecules (AIM) theory. This method uses concepts such as the Laplacian of the electron density, $\nabla^2\rho(r)$ at the critical bond point (BCP), potential energy (V), kinetic energy density (K), electron density $\rho(r)$ and, the total electronic energy density, $H(r) = V(r) + K(r)$, in terms of which the bond degree, $H(r)/\rho(r)$. As well, Eq. (6) represents a valuable relationship between them:[40]

$$¼\nabla^2\rho(r) = V(r) + 2K(r) = H(r) + K(r) \quad (6)$$

If $\nabla^2\rho(r) > 0$, it displays electrostatic interactions, but in case $\nabla^2\rho(r) < 0$ indicates the covalent bond.

Ionic interactions display positive Laplacian and $H(r)$, $\rho(r) < 0.1$, $K(r)/\rho(r)$ and $K(r)/V(r) >1$. The type of chemical bonds could be identified by the kinetic energy and potential energy values. The specifications of chemical bonds can be displayed by the values of the kinetic energy and potential energy. The type of chemical bonds is covalent if Laplacian and $H(r)$ are negative, $\rho(r) > 0.02$, $K(r)/\rho(r)$ and $K(r)/V(r) < 1$. Parameters of AIM analysis at the bond critical points for the main chemical bonds of bendamustine drug nanocages are shown in Table IV.

$E(r)$ of bonds is negative in the gas and the water phases. Furthermore, the electron density values are higher than 0.02. The values of $–K(r)/V(r)$, $E(r)$ and $\rho(r)$ descriptors indicated which of the formed bond between the bendamustine drug and studied nanocages are covalent.

(CC) 2022 SCS.

TABLE IV. Topological parameters (all in atomic units) and ellipticity, at the B3LYP/6-31g (d,p) level of theory (PCM)

Complex	Bond	$\rho(r)$	$\nabla^2\rho(r)$	Ellipticity	$-K(r)/V(r)$	$K(r)/\rho(r)$	$E(r)$
$B_{12}N_{12}$	B3–N39	0.1384	0.2952	0.0504	0.6290	1.2998	–0.1061
$B_{12}P_{12}$	B12–N39	0.1384	0.3536	0.0430	0.6503	1.3808	–0.1028
$Al_{12}N_{12}$	N15–Al58	0.0453	0.3260	0.0386	0.9962	1.5839	–0.0002
$Al_{12}N_{12}$	O21–Al59	0.0453	0.3260	0.0386	1.1370	1.6040	0.0087
$Al_{12}P_{12}$	Al8–N39	0.0561	0.2898	0.0874	0.9783	1.3193	–0.0016
$Al_{12}P_{12}$	Al9–O45	0.0498	0.3218	0.0462	1.0735	1.5107	0.0051

CONCLUSION

DFT calculations with the B3LYP/6–31G (d,p) method are used to study the interaction mechanism of the bendamustine drug with Al/B–N/P nanocages in both the gas and solvent phases. Relatively strong adsorptions occur between bendamustine and Al/B–N/P nanocages based on Gibbs energy changes. The negative values of the Gibbs energy change in all studied nanocages confirmed the spontaneous adsorption process. For bendamustine and Al/B–N/P nanocages complexes, the primary interaction mechanism is appropriate chemisorption. Optimized geometries and MEP indicate covalent interactions between the drug and nanocages. Despite, recovery time for desorption illustrated that the $B_{12}N_{12}$ and $B_{12}P_{12}$ nanovehicles for the bendamustine are more suitable than $Al_{12}N_{12}$ and $A_{12}P_{12}$ nanocages. HOMO–LUMO and density of states diagrams indicate that nanocages slightly change the global charge distribution. The NBO analysis showed that the bendamustine drug's nitrogen atom is electron-donating, and the nanocages are the electron acceptor in all complexes. Also, the AIM results showed that the bond between studied nanocages and bendamustine is covalent. Nonetheless, all studied nanocages may be favorable candidates for detecting the bendamustine drug. However, we have deduced that pristine $B_{12}P_{12}$ and $B_{12}N_{12}$ nanocages are more suitable for drug delivery than $Al_{12}P_{12}$ and $Al_{12}N_{12}$.

Acknowledgement. The authors are grateful to the Payame Noor University for encouragements.

И З В О Д

АДСОРПЦИЈА ЛЕКА ЗА РАК БИНДАМАСТИНА НА ЗАТВОРЕНИМ НАНОСТРУКТУРАМАAl/B–N/P: УПОРЕДНО DFT ПРОУЧАВАЊЕ

NOSRAT MADADI MAHANI, REZA BEHJATMANESH-ARDEKANI и ROYA YOSEFELAHI

Department of Chemistry, Payame Noor University (PNU), 19395-4697, Tehran, Iran

Третман лековима против рака путем затворених наноструктура (енгл. nanocages) је фармацеутски значајна због смањења споредних ефеката и отпуштања лека у близини туморске ћелије. Проучавали смо интеракцију лека против рака – биндамастина, са затвореним наноструктурама Al/B–N/P коришћењем теорије функционала густине (DFT) и у гасовитој и воденој фази на B3LYP/6-31G (d,p) нивоу теорије. Резултати

(CC) 2022 SCS.

показују да се квантни параметри затворених наноструктура донекле мењају при адсорпцији лека биндамастина. Лек биндамастин делује као донор електрона и може да се адсорбује на електрон-акцепторском месту затворене наноструктуре. Промена Гибсове енергије одговара процесу хемисорпције у обе фазе. Резултати су показали да је веза између проучаваних затворених наноструктура и биндамастина ковалентна. Ипак, све проучаване затворене наноструктуре могу бити погодни кандидати за транспорт лека биндамастина. Међутим, на основу њихових времена опоравка закључујемо да су се чисте $B_{12}P_{12}$ и $B_{12}N_{12}$ затворене наноструктуре показале погоднијим за испоруку лека него $Al_{12}P_{12}$ и $Al_{12}N_{12}$.

(Примљено 12. марта, ревидирано 25. маја, прихваћено 26. маја 2022)

REFERENCES

1. D. Nowak, S. Boehrer, A. Brieger, S. Z. Kim, S. Schaaf, D. Hoelzer, P. S Mitrou, E. Weidmann, K. U. Chow, *Leuk. Lymphoma* **45** (2004) 1429 (https://doi.org/10.1080/1042819042000198858)
2. J. W. Friedberg, P. Cohen, L. Chen, K. S. Robinson, A. Forero-Torres, A. S. La Casce, L. E. Fayad, A. Bessudo, E. S. Camacho, M. E. Williams, R. H. van der Jagt, J. W. Oliver, B. D. Cheson, *J. Clin. Oncol.* **26** (2008) 204 (https://doi.org/10.1200/JCO.2007.12. 5070)
3. R. Kath, K. Blumenstengel, H. J. Fricke, K. Hoffken, J. *Cancer Res. Clin. Oncol.* **127** (2001) 48 (https://doi.org/10.1007/s004320000180)
4. Q. Weng, X. Wang, X. Wang, Y. Bando, D. Goldberg, *Chem. Soc. Rev.* **45** (2016) 3989 (https://doi.org/10.1039/C5CS00869G)
5. Q. Wang, Q. Sun, P. Jena, Y. Kawazoe, *ACS Nano* **3** (2009) 621 (https://doi.org/10.1021/nn800815e)
6. G. Ciofani, V. Raffa, A. J. Yu, Y. Chen, Y. Obata, S. Takeoka, A. Mencissi, A. Cuschieri, *Curr. Nanosci.* **5** (2009) 33 (https://doi.org/10.2174/157341309787314557)
7. P. A. Denis, F. Iribarne, *Comput. Theor. Chem.***1164** (2019) 112538 (https://doi.org/10.1016/j.comptc. 2019.112538)
8. P. A. Denis, S. Ullah, F. Iribarne, *New J. Chem.* **44** (2020) 5724 (https://doi.org/10.1039/D0NJ00414F)
9. P. A. Denis, *J. Phys. Org. Chem.* **25** (2012) 322 (https://doi.org/10.1002/poc.1918)
10. A. Soltani, A. Sousaraei, M. Bezi Javan, M. Eskandaric, H. Balakheyli, *New J. Chem.* **40** (2016) 7018 (https://doi.org/10.1039/C6NJ00146G)
11. C. A. Celaya, L. F. Hernandez-Ayala, F. B. Zamudio, J. A. Vargas, M. Reina, *J. Mol. Liq.* **329** (2021) 115528 (https://doi.org/10.1016/j.molliq.2021.115528)
12. N. Madadi Mahani, R. Yosefelahi, *Mor. J. Chem.* **6** (2018) 187 (https://doi.org/10.48317/IMIST.PRSM/morjchem-v6i1.8619)
13. J. S. Al-Otaibi, Y. Sheena Mary, Y. Shyma Mary, G. Serdaroglu, *J. Mol. Mod.* **27** (2021) 113 (https://doi.org/10.1007/s00894-021-04742-z)
14. K. A. Soliman, S. Abdel Aal, *Diam. Relat. Mater.* **117** (2021) 108458 (https://doi.org/10.1016/j.diamond.2021.108458)
15. A. Hosseinian, E. Vessally, A. Bekhradnia, K. Nejati, G. Rahimpour, *Thin Solid Films* **640** (2017) 93 (http://dx.doi.org/10.1016/j.tsf.2017.08.049)
16. V. de Paul Zoua, A. D. Tamafo Fouegue, D. B. Mama, J. N. Ghogomu, R. A. Ntieche, *Int. J. Quantum Chem.* **122** (2022) e26843 (https://doi.org/10.1002/qua.26843)

(CC) 2022 SCS.

17. A. S. Rad, K. Ayub, *J. Alloys Compd.* **672** (2016) 161 (https://doi.org/10.1016/j.jallcom.2016.02.139)
18. Y. Zhao, N. E. Schultz, D. G. Truhlar, *J. Chem. Theory Comput.* **2** (2006) 364 (https://doi.org/10.1021/ct0502763)
19. *Gaussian 09*, Revision A.02, Gaussian, Inc., Wallingford, CT, 2016 (https://gaussian.com/g09citation)
20. N. Madadi Mahani, F. Sabermahani, A. Shamsolmaali, *Pak. J .Pharm. Sci.* **32** (6) (2019) 2741 (https://doi.org/10.36721/PJPS.2019.32.6.REG.2741-2744.1)
21. E. Vessally, S. Soleimani-Amiri, A. Hosseinian, L. Edjlali, A. Bekhradnia, *Physica, E* **87** (2017) 308 (https://ui.adsabs.harvard.edu/abs/2017PhyE-87-308V)
22. H. Xu, X. Tu, G. Fan, Q. Wang, X. Wang, X. Chu, *J. Mol. Liq.* **318** (2020) 114315 (https://doi.org/10.1016/j.molliq.2020.114315)
23. A. Hosseinian, E. Vessally, S. Yahyaei, L. Edjlali, A. Bekhradnia, *J. Clust. Sci.* **28** (2017) 2681 (https://doi.org/10.1007/s10876-017-1253-6)
24. B. Bankiewicz, P. Matczak, M. Palusiak, *J. Phys. Chem., A* **116** (2011) 452 (https://doi.org/10.1021/jp210940b)
25. A. Shokuhi Rad, K. Ayub, *J. Alloys Comp.* **672** (2016) 161 (https://doi.org/10.1016/j.jallcom.2016.02.139)
26. M. Karnan, V. Balachandran, M. Murugan, M. K. Murali, *Spectrochim. Acta* **130** (2014) 143 (https://doi.org/10.1016/J.SAA.2014.03.128)
27. V. V. Menon, E. Foto, Y. S. Mary, E. Karatas, C. Y. Panicker, G. Yalcin, S. Armakovic, S. J. Armakovic, C. V. Alsenoy, I. Yildiz, *J. Mol. Struct.* **1129** (2017) 86 (https://doi.org/10.1016/J.MOLSTRUC.2016.09. 059)
28. Y. S. Mary, P. J. Jojo, C.Y. Panicker, C. Van Alsenoy, S. Ataei, I. Yildiz, *Spectrochim. Acta, A* **122** (2014) 499 (https://doi.org/10.1016/J.SAA.2013.11.025)
29. Y. S. Mary, P. J. Jojo, C. Y. Panicker, C. Van Alsenoy, S. Ataei, I. Yildiz, *Spectrochim. Acta, A* **125** (2014) 12 (https://doi.org/10.1016/J.SAA.2014.01.068)
30. P. Venkata Ramana, T. Sundius , S. Muthuc, K. Chandra Mouli, Y. Rama Krishna, K. Venkata Prasadd, R. Niranjana Devi, A. Irfanf, C. Santhamma, *J. Mol. Struct.* **1253** (2022) 132211 (https://doi.org/10.1016/j.molstruc.2021.132211)
31. Y. S. Mary, H.T. Varghese, C. Y. Panicker, M. Girisha, B. K. Sagar, H. S. Yathirajan, A. A. Al-Saadi, C. Van Alsenoy, *Spectrochim. Acta* **150** (2015) 543 (https://doi.org/10.1016/j.saa.2015.05.090)
32. B. R. Raajaraman, N. R. Sheela, S. Muthu, *Comput. Biol. Chem.* **82** (2019) 44 (https://doi.org/10.1016/j.compbiolchem.2019.05.011)
33. R. Parr, W. Yang, *J. Am. Chem. Soc.* **106** (1984) 4049 (https://doi.org/10.1021/ja00326a036)
34. C. Martinez, M. Sedano, P. Lopez, *J. Mol. Graph. Model.* **28** (2009) 196 (https://doi.org/10.1016/j.jmgm.2009.07.002)
35. C. G. Zhan, J. A. Nichols,D. A. Dixon, *J. Phys. Chem., A* **107** (2003) 4184 (https://doi.org/10.1021/jp0225774)
36. A.Shokuhi Rad, A. Ayub, *J. Alloys Cmpd.* **672** (2016) 161 (https://doi.org/10.1016/j.jallcom.2016.02.139)
37. S. Kaviani, S. Shahab, M. Sheikhi, *Phys. E: Low-Dimens. Syst. Nanostruct.* **126** (2021) 114473 (https://doi.org/10.1016/j.physe.2020.114473)

(CC) 2022 SCS.

38. G. Seifert, P. W. Fowler, D. Mitchell, D. Porezag, Th. Frauenheim, *Chem. Phys. Lett.* **268** (1997) 352 (https://doi.org/10.1016/S0009-2614(97)00214-5)
39. S. Peng, K. Cho, P. Qi, H. Dai, *Chem. Phys. Let.* **387** (2004) 271 (https://doi.org/10.1016/j.cplett.2004.02.026)
40. P. Popelier, *J. Phys. Chem., A* **102** (1998) 1873 (https://doi.org/10.1021/jp9805048).

(CC) 2022 SCS.

Journal of the Serbian Chemical Society
JSCS-info@shd.org.rs • www.shd.org.rs/JSCS
J. Serb. Chem. Soc. *87* (10) 1171–1184 (2022)
JSCS–5586
Original scientific paper
Published 26 August 2022

Comparison of different types of molar volume equations for the validity and applicability in a ternary carbamazepine + alizarin + methanol solution system and study of the corresponding molecular interactions

TAPAS MALLIK, SRABANTI GHOSH and DEEPAK EKKA*

Department of Chemistry, Cooch Behar Panchanan Barma University, Cooch Behar-736101, West Bengal, India

(Received 29 April, revised 28 June, accepted 28 July 2022)

Abstract: In this work, the molecular interaction between the carbamazepine and alizarin in methanol has been represented in terms of limiting apparent molar volumes and viscosity coefficients. Before further proceeding, the validity and applicability of the calculation of apparent molar volumes have also been checked by considering the available five types of frequently used equations, where the required modifications have proposed by the addition of hypothetical mass and concentration of the solute. After that, the limiting apparent molar volume and viscosity coefficients have been calculated using Masson equation and Jones–Dole equation respectively to predict and cross-check the interactions occurring between the molecules in ternary system. The equation marked with (1) has been found the best-fit equation, and the carbamazepine and alizarin in methanol are strongly bound (ϕ_V^o = 23104 m^3 mol^{-1} and B = = 18.10 kg mol^{-1}) to each other at the concentration 0.003 mol kg^{-1}. The results have been interpreted in favour of the solute–cosolute interactions, which is dominant over the solute–solute and cosolute–cosolute interactions. The interpretations have been discussed with the help of intermolecular forces and non-covalent interactions.

Keywords: dihydroxyanthraquinone; dibenzoazepine-based compound; limiting apparent molar volume; viscosity *B*-coefficient; solute–solvent and solute–solute interactions.

INTRODUCTION

The non-covalent interaction between two drug molecules in alcohol always acts as a driving force of molecular interaction in medicinal industry, academic and research. The information regarding the physical properties of solutions with

* Corresponding author. E-mail: ekadeepak@yahoo.in
https://doi.org/10.2298/JSC220429062M

Available on line at www.shd.org.rs/JSCS/
(CC) 2022 SCS.

different solute concentration at room temperature is very important. The interaction which occurs can be interpreted by physicochemical data. Alizarin red S (Scheme 1) is a natural compound known as an anthraquinoic fluorescent dye, having antigenotoxic activity, that can be used as orthotropic drug for the treatment of bone tumours.[1] Carbamazepine (Scheme 1) is a tricycle compound like dibenzoazepine that is carrying a carbamoyl substituent at the azepine nitrogen. Carbamazepine is used in the therapy of epilepsy and trigeminal neuralgia.[2,3] To increase the bio-availability of low solubility drug like carbamazepine, Li and co--workers studied the co-crystal (carbamazepine combine with nicotinamide) formation, and showed an alternative method for reducing the side effects, other than the formation of cyclodextrin inclusion complex.[4] Since carbamazepine is poorly soluble in water, it tends to appears at the surface of water and becomes a harmful agent for the environment.[5] Andreozzi *et.al.* have tried to overcome this situation by a biotic photo degradation at 313 K with 100 days observation in a binary system.[6]

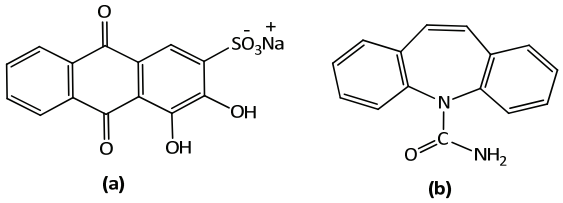

Scheme 1. 2D Molecular structure of: a) alizarin red S and b) carbamazepine.

A binary and ternary systems are common in research and industry. The solute and co-solute interactions in methanol also belongs to the ternary system. This type of molecular interactions in solutions can be determined by physicochemical properties like apparent molar volumes and viscosity coefficient. It has been seen that the molecular interaction of many important drugs like sodium salicylate, L-tryptophan, procaine HCl, ephedrine HCl, amoxicillin also been studied by apparent molar volume.[7] On the other hand, if any patient suffering from diseases above (bone tumours and trigeminal neuralgia) and if he/she is taking both medicinal compounds simultaneously, there is a possibility of interaction between these compounds.

In view of the critical survey of literature from book, journal, article, magazine, *etc*. it is clear that there is no work has done on this ternary system (carbamazepine + alizarin + methanol). The addition of carbamazepine to the solution of alizarine +methanol will perturb the structural influence, which is expected to affect the volumetric and viscometry properties to a high degree. In this work, density and viscosity of the ternary system (0.001, 0.002 and 0.003 mol kg^{-1}) have been measured, by considering carbamazepine and alizarin as a co-solute

(CC) 2022 SCS.

and solute, respectively. The result obtained from apparent molar volumes and viscosity coefficients have interpreted in terms of intermolecular forces and non--covalent interactions.

EXPERIMENTAL

Materials

Carbamazepine (molecular weight 236.26 g mol^{-1}) was obtained from medicine tegretol 200 (Novartis contain 0.0002 kg of precursor) tablet. Tegretol was first ground in mortar and dissolved in methanol, the mixture was sonicated for better solubility, then it was filtered by Whatman 41, evaporated by moderate heating, dried, and carbamazepine was obtained in powder form. The melting point of the compound is found to be ~463.15 K[8] and the UV–Vis spectral line measured by Thermo Scientific Evolution 201 UV–Vis spectrometer, which also matches the literature. Alizarin (molecular weight 364.24 kg mol^{-1}) was purchase from Sd. fine-chem Ltd., India, and use as procured. Methanol (mass fraction purity is 0.998) was purchased from Avantor Performance Materials India Ltd. Before performing the experiment all the chemicals have kept in dry and dark desiccators for minimum evaporation.

Apparatus and procedure

The solvent mixture of alizarine in methanol and the stock solutions of carbamazepine of different concentration (0.001, 0.002 and 0.003 mol kg^{-1}) in alizarine + methanol was prepared. Since some of equations the concentration is expressed in molality and some in molarity, therefore to uniform this, the conversion of molality into molarity was carried using experimental density data.[9] Required precautions were taken to trim down losses by evaporation. Density of the solutions was measured with an Ostwald-Sprengel type pycnometer. It was calibrated with doubly distilled water and acetone; equilibrated by experimental liquid in a glass-walled water bath maintained at ±0.01 K of the desired temperature. It was then taken from the bath, dried, and weight by an electronic balance with a precision of 10^{-6} kg. An average three measurements and the required precautions to avoid evaporation losses during measurements were taken. The density values were reproducible to ±0.3 g cm^{-3}. The viscosity was measured by a suspended Ubbelohde-type viscometer, calibrated with doubly distilled water and purified methanol at temperature of 298.15 K. A thoroughly cleaned and perfectly dried viscometer filled with the experimental liquid was filled; placed vertically in the glass-walled thermostat which maintained the temperature ±0.01 K. After the attainment of thermal equilibrium, times of flow were recorded with a stopwatch correct to ±0.1 s. At least three repetitions of each data measurements, reproducible to ±0.1 s, were taken to determine the average flow times. The accuracy of the viscosity measurements was ±0.003 Pa·s. The mixtures were prepared by mixing known volumes of pure liquids in air-tight stoppered bottles. The weights were measured on a Wesner electronic balance (IND/09/08/466) accurate to 10^{-6} kg.

RESULT AND DISCUSSION

Validity and acceptability of apparent molar volume equations

Apparent molar volume is very much important for the elucidation of solute––solvent and solute interactions in ternary solution system. It is usually calculated using molar mass, density and concentration of the solution and solvent. In this work, after a critical survey, only 5 different equations (Eqs. (1)–(5)) were found to appropriately calculate the apparent molar volume.[10–14] From these equations

(CC) 2022 SCS.

we have tried to justify the applicability and validity for the chosen ternary system:

$$\phi_V = \frac{m}{\rho} - \frac{(\rho - \rho_0)}{c_m \rho \rho_0} \quad (1)$$

$$\phi_V = \frac{m}{\rho} + \frac{1000(\rho_0 - \rho)}{c_n \rho_0} \quad (2)$$

$$\phi_V = \frac{m}{\rho} + \frac{1000(\rho_0 - \rho)}{\rho \rho_0} \quad (3)$$

$$\phi_V = \frac{m}{\rho} + \frac{1000(\rho_0 - \rho)}{c_m \rho \rho_0} \quad (4)$$

$$\phi_V = \frac{m}{\rho_0} - \frac{1000(\rho - \rho_0)}{c_n \rho_0} \quad (5)$$

where c_n is the molar concentration of ternary mixture in molarity, c_m is the molal concentration of ternary solutions in molality, m is molar mass of the solute, ρ is the solution density and ρ_0 is the solvent density. A confusion was noted on the use of molar mass and concentration of the solution to calculate the apparent molar volume. In some cases, some of the authors have used molar mass of a solute. But in case of ternary solution systems (solute + co-solute + solvent), it is inappropriate to use molar mass of the solute, because of the presence of the co-solute mass in the solution, the interaction with a solute is also involved. As a result, mass of the co-solute also interferes in calculating the apparent molar volume of the ternary solution system. To overcome these problems, we have tried to attempt the calculation and discussion the same using following ways.

Consideration of the molar mass of the solute

Carbamazepine was treated as a solute; therefore, molar mass has been used to calculate ϕ_V in 0.001, 0.002 and 0.003 mol kg^{-1} of alizarin + methanol solvent mixture and the results have been presented in Tables I–III, respectively.

TABLE I. Density, molar mass and apparent molar volume, with corresponding molal and molar concentration of carbamazepine in for different equation at 0.001 mol kg^{-1} alizarin + methanol; m = 236.26 g mol^{-1}

c_n / mol L^{-1}	c_m / mol kg^{-1}	ρ / g m^{-3}	ϕ_V / 10^{-3} m^3 mol^{-1}				
			Eq. (1)	Eq. (2)	Eq. (3)	Eq. (4)	Eq. (5)
0.001	0.0012	0.7905	293.25	–4147.63	293.25	4798.66	–4146.30
0.002	0.0025	0.7926	293.57	–3268.39	289.07	3897.65	–3266.26
0.003	0.0037	0.7927	295.01	–2110.47	288.93	2728.70	–2108.31
0.004	0.0050	0.7926	295.82	–1485.15	289.07	2097.86	–1483.03
0.005	0.0062	0.7928	296.12	–1184.17	288.64	1793.51	–1181.96

(CC) 2022 SCS.

TABLE I. Continued

c_n / mol L^{-1}	c_m / mol kg^{-1}	ρ / g m^{-3}	ϕ_V / 10^{-3} m^3 mol^{-1}				
			Eq. (1)	Eq. (2)	Eq. (3)	Eq. (4)	Eq. (5)
0.006	0.0075	0.7931	296.22	–1006.74	288.00	1613.69	–1004.41
0.007	0.0087	0.7887	299.13	–18.07	296.71	621.66	–17.40
0.008	0.0100	0.7898	298.55	–152.47	294.54	756.51	–151.39
0.009	0.0112	0.7893	298.91	–24.89	295.63	627.94	–24.02
0.010	0.0125	0.7900	298.54	–90.02	294.11	692.99	–88.86
0.011	0.0137	0.7904	298.42	–92.67	293.46	695.25	–91.39
0.012	0.015	0.7908	298.22	–110.40	292.53	712.58	–108.93

TABLE II. Density, molar mass and apparent molar volume, with corresponding molal and molar concentration of carbamazepine in for different equation at 0.002 mol kg^{-1} alizarin + methanol; m = 236.26 g mol^{-1}

c_n / mol L^{-1}	c_m / mol kg^{-1}	ρ / g m^{-3}	ϕ_V / 10^{-3} m^3 mol^{-1}				
			Eq. (1)	Eq. (2)	Eq. (3)	Eq. (4)	Eq. (5)
0.001	0.0012	0.7908	296.94	–1507.75	296.48	2126.28	–4146.30
0.002	0.0025	0.7913	297.29	–953.07	295.39	1563.86	–3266.26
0.003	0.0037	0.7918	297.30	–751.83	294.38	1359.35	–2108.31
0.004	0.0050	0.7913	297.93	–324.40	295.41	928.34	–1483.03
0.005	0.0062	0.7920	297.61	–378.18	294.02	981.57	–1181.96
0.006	0.0075	0.7915	298.05	–149.32	295.11	751.13	–1004.41
0.007	0.0087	0.7918	297.91	–151.71	294.38	753.07	–17.40
0.008	0.0100	0.7922	297.77	–153.55	293.66	754.44	–151.39
0.009	0.0112	0.8004	293.62	–1260.03	277.69	1849.55	–24.02
0.010	0.0125	0.8054	291.32	–1739.51	268.10	2312.49	–88.86
0.011	0.0137	0.8096	289.53	–2036.45	260.19	2592.51	–91.39
0.012	0.0150	0.8096	289.72	–1842.74	260.19	2401.09	–108.93

TABLE III. Density, molar mass and apparent molar volume, with corresponding molal and molar concentration of carbamazepine in for different equation at 0.003 mol kg^{-1} alizarin + methanol; m = 236.26 g mol^{-1}

c_n / mol L^{-1}	c_m / mol kg^{-1}	ρ / g m^{-3}	ϕ_V / 10^{-3} m^3 mol^{-1}				
			Eq. (1)	Eq. (2)	Eq. (3)	Eq. (4)	Eq. (5)
0.001	0.0012	0.7879	299.53	598.15	299.45	602.70	1.61
0.002	0.0025	0.7877	299.98	265.03	300.03	264.49	334.83
0.003	0.0037	0.7879	299.77	376.86	299.56	378.04	222.91
0.004	0.0050	0.7872	300.28	136.68	300.95	134.03	463.36
0.005	0.0062	0.7881	299.70	387.38	299.24	388.70	212.33
0.006	0.0075	0.7887	299.36	499.50	298.04	502.36	99.99
0.007	0.0087	0.7902	298.51	753.25	294.95	758.84	–154.34
0.008	0.0100	0.7917	297.77	932.33	292.00	938.94	–333.99
0.009	0.0112	0.7895	299.01	545.39	296.45	548.66	53.79
0.010	0.0125	0.7890	299.26	465.09	297.33	467.38	134.26
0.011	0.0137	0.7899	298.82	554.70	295.52	557.94	44.30
0.012	0.0150	0.7901	298.76	552.37	295.17	555.53	46.56

(CC) 2022 SCS.

The inspection of the Tables I–III for Eqs. (2), (4) and (5) gives negative ϕ_V values and abnormal trends. Furthermore, it shows 100 to 1000 times higher molar mass, and these vast differences are unusual and not acceptable. They may be explained by the fact that there must be some interaction that occurs between two drugs, and both of drugs with the combination of mass contribute in the calculation. From this result, it is concluded that in this case Eqs. (1) and (3) are the acceptable equations, which are relatively comparable with the molar mass in question.

Consideration of the reduced mass

As usual, here also the reduced mass defined as the product of the two masses divided by their sum of two masses. Since abnormal ϕ_V value have been obtained in case of Eqs. (2), (4) and (5), so the reduced mass (μ) has been used to modify the equation instead of the molar mass of solute. After that, the apparent molar volumes have been calculated and presented in Tables IV–VI. By the observation of the results, it has been inferred the same trend of results as for the molar mass calculation.

TABLE IV. Density, reduced mass, and apparent molar volume, with corresponding molal and molar concentration of carbamazepine for different equation at 0.001 mol kg^{-1} alizarin + methanol; μ = 143.30 g mol^{-1}

c_n /mol L^{-1}	c_m /mol kg^{-1}	ρ / g m^{-3}	ϕ_V / 10^{-3} m^3 mol^{-1}				
			Eq. (1)	Eq. (2)	Eq. (3)	Eq. (4)	Eq. (5)
0.001	0.0012	0.7905	175.65	-4265.22	175.65	4681.06	-4264.41
0.002	0.0025	0.7926	176.30	-3385.66	171.80	3780.37	-3384.37
0.003	0.0037	0.7927	177.74	-2227.74	171.66	2611.44	-2226.43
0.004	0.0050	0.7926	178.55	-1602.43	171.80	1980.58	-1601.14
0.005	0.0062	0.7928	178.88	-1301.41	171.40	1676.26	-1300.07
0.006	0.0075	0.7931	179.03	-1123.94	170.80	1496.49	-1122.52
0.007	0.0087	0.7887	181.28	-135.92	178.86	503.81	-135.51
0.008	0.0100	0.7898	180.86	-270.16	176.86	638.82	-269.50
0.009	0.0112	0.7893	181.14	-142.66	177.86	510.16	-142.13
0.010	0.0125	0.7900	180.89	-207.68	176.45	575.33	-206.97
0.011	0.0137	0.7904	180.81	-210.28	175.85	577.65	-209.50
0.012	0.0150	0.7908	180.68	-227.94	174.99	595.05	-227.05

TABLE V. Density, reduced mass, and apparent molar volume, with corresponding molal and molar concentration of carbamazepine for different equation at 0.002 mol kg^{-1} alizarin + methanol; μ = 143.30 g mol^{-1}

c_n / mol L^{-1}	c_m / mol kg^{-1}	ρ /g m^{-3}	ϕ_V / 10^{-3} m^3 mol^{-1}				
			Eq. (1)	Eq. (2)	Eq. (3)	Eq. (4)	Eq. (5)
0.001	0.0012	0.7908	179.39	–1625.30	178.93	2008.73	–1624.97
0.002	0.0025	0.7913	179.82	–1070.54	177.92	1446.39	–1070.08
0.003	0.0037	0.7918	179.91	–869.22	176.99	1241.96	–868.65

(CC) 2022 SCS.

TABLE V. Continued

c_n / mol L^{-1}	c_m / mol kg^{-1}	ρ /g m^{-3}	ϕ_V / 10^{-3} m^3 mol^{-1}				
			Eq. (1)	Eq. (2)	Eq. (3)	Eq. (4)	Eq. (5)
0.004	0.0050	0.7913	180.46	–441.87	177.94	810.87	–441.42
0.005	0.0062	0.7920	180.25	–495.55	176.66	864.20	–494.94
0.006	0.0075	0.7915	180.60	–266.76	177.66	633.69	–266.28
0.007	0.0087	0.7918	180.52	–269.11	176.99	635.68	–268.54
0.008	0.0100	0.7922	180.43	–270.89	176.33	637.10	–270.23
0.009	0.0112	0.8004	177.48	–1376.17	161.55	1733.41	–1373.66
0.010	0.0125	0.8054	175.90	–1854.92	152.68	2197.08	–1851.31
0.011	0.0137	0.8096	174.71	–2151.27	145.37	2477.69	–2146.74
0.012	0.0150	0.8096	174.90	–1957.57	145.37	2286.27	–1953.03

TABLE VI. Density, reduced mass, and apparent molar volume, with corresponding molal and molar concentration of carbamazepine for different equation at 0.003 mol kg^{-1} alizarin + methanol; μ = 143.30 g mol^{-1}

c_n / mol L^{-1}	c_m / mol kg^{-1}	ρ / g m^{-3}	ϕ_V / 10^{-3} m^3 mol^{-1}				
			Eq. (1)	Eq. (2)	Eq. (3)	Eq. (4)	Eq. (5)
0.001	0.0012	0.7879	181.56	480.18	181.48	484.72	–116.39
0.002	0.0025	0.7877	181.96	147.02	182.02	146.47	216.83
0.003	0.0037	0.7879	181.80	258.89	181.58	260.07	104.90
0.004	0.0050	0.7872	182.20	18.60	182.87	15.95	345.36
0.005	0.0062	0.7881	181.75	269.43	181.28	270.75	94.33
0.006	0.0075	0.7887	181.50	381.63	180.18	384.50	–18.01
0.007	0.0087	0.7902	180.88	635.61	177.32	641.21	–272.35
0.008	0.0100	0.7917	180.36	814.92	174.59	821.53	–452.00
0.009	0.0112	0.7895	181.26	427.64	178.71	430.92	–64.207
0.010	0.0125	0.7890	181.45	347.28	179.52	349.57	16.26
0.011	0.0137	0.7899	181.15	437.02	177.85	440.27	–73.69
0.012	0.0150	0.7901	181.11	434.72	177.52	437.88	–71.43

For further clarification of the equations in order to make them applicable, we have modified them by adding two type of correction factors: *i*) hypothetical mass and *ii*) solution concentration including both the solute and cosolute. The brief discussion of these sub-units is given below.

Modification by adding hypothetical mass

This issue has been overcome using hypothetical mass, which can be calculated as:

$$m_1 = \frac{(m_2 V_2 c_2 + m_3 V_3 c_3)}{V_1 c_1} \tag{6}$$

where, m_1, m_2 and m_3 are respectively the hypothetical mass of the solution, the molar mass of solute (CBZ) and the molar mass of co-solute (alizarin). c is the concentration in molality/molarity, V is the volume of solution and the subscripts 1, 2 are 3 are standing for the ternary solution, the binary solution of carbamaz-

(CC) 2022 SCS.

epine and the binary solution of alizarin, respectively. Applying the hypothetical mass on the above five equations, the calculated M_1 values and shown in Tables VII–IX.

TABLE VII. Density, hypothetical mass and apparent molar volume; with corresponding molal and molar concentration of carbamazepine for different equation at 0.001 mol kg^{-1} alizarin + methanol

c_n	c_m	ρ	m_1	ϕ_V / 10^{-3} m^3 mol^{-1}				
mol L^{-1}	mol kg^{-1}	g m^{-3}	g mol^{-1}	Eq. (1)	Eq. (2)	Eq. (3)	Eq. (4)	Eq. (5)
0.0010	0.0012	0.7905	277.59	345.52	–4095.35	345.52	4850.93	–4093.79
0.0016	0.0025	0.7926	261.06	323.95	–3950.40	320.35	4648.84	–3948.05
0.0023	0.0037	0.7927	253.97	316.48	–2776.28	311.27	3445.52	–2773.96
0.0030	0.0050	0.7926	250.04	312.45	–2062.18	306.45	2715.17	–2059.93
0.0036	0.0062	0.7928	247.53	309.66	–1708.92	302.86	2351.54	–1706.61
0.0043	0.0075	0.7931	245.80	307.61	–1496.49	300.02	2131.79	–1494.07
0.0050	0.0087	0.7887	244.53	309.45	–134.63	307.19	760.99	–133.94
0.0056	0.0100	0.7898	243.56	307.54	–329.19	303.78	954.08	–328.08
0.0063	0.0112	0.7893	242.79	307.01	–153.14	303.90	774.56	–152.24
0.0070	0.0125	0.7900	242.17	305.80	–249.30	301.58	869.29	–248.10
0.0076	0.0137	0.7904	241.65	305.02	–256.11	300.28	874.40	–254.80
0.0083	0.0150	0.7908	241.22	304.26	–284.15	298.79	900.95	–282.65

TABLE VIII. Density, hypothetical mass and apparent molar volume; with corresponding molal and molar concentration of carbamazepine for different equation at 0.002 mol kg^{-1} alizarin + methanol

c_n	c_m	ρ	m_1	ϕ_V / 10^{-3} m^3 mol^{-1}				
mol L^{-1}	mol kg^{-1}	g m^{-3}	g mol^{-1}	Eq. (1)	Eq. (2)	Eq. (3)	Eq. (4)	Eq. (5)
0.0014	0.0012	0.7908	284.05	357.88	–931.18	356.90	1664.56	–930.53
0.002	0.0025	0.7914	277.59	349.51	–900.85	347.61	1616.08	–899.97
0.0026	0.00375	0.7919	274.11	344.93	–865.61	342.18	1570.37	–864.52
0.0032	0.0050	0.7914	271.94	342.85	–435.06	340.49	1130.86	–434.21
0.0038	0.0062	0.7921	270.45	340.55	–548.65	337.18	1240.50	–547.50
0.0044	0.0075	0.7915	269.37	339.71	–270.34	336.93	957.55	–269.42
0.005	0.0087	0.7919	268.54	338.49	–290.98	335.15	975.72	–289.92
0.0056	0.0100	0.7922	267.90	337.50	–307.24	333.59	989.89	–306.02
0.0062	0.0112	0.8004	267.38	331.79	–1923.52	316.56	2590.39	–1918.84
0.0068	0.0125	0.8054	266.95	328.47	–2658.05	306.20	3300.78	–2651.31
0.0074	0.0137	0.8096	266.59	325.87	–3131.68	297.65	3749.22	–3123.24
0.008	0.0150	0.8096	266.28	325.74	–2872.96	297.27	3492.80	–2864.53

From Tables VII–IX it can be seen that among the five equations only Eqs. (1) and (3) gives a reliable value, where other equations give negative and/or large deviation values. By the inspections of the Tables, Eqs. (1) and (3) were considered as the most correct form of equation for calculating apparent molar volume. Between these two, the equation containing molality is the more appro-

(CC) 2022 SCS.

priate equation, because molality is independent on temperature. So, the Eq. (1) is considering as an acceptable equation.

TABLE IX. Density, hypothetical mass, and apparent molar volume, with corresponding molal and molar concentration of carbamazepine for different equation at 0.003 mol kg^{-1} alizarin + methanol

c_n / mol L^{-1}	c_m / mol kg^{-1}	ρ / g m^{-3}	m_l / g mol^{-1}	ϕ_V /10^{-3} m^3 mol^{-1}				
				Eq. (1)	Eq. (2)	Eq. (3)	Eq. (4)	Eq. (5)
0.0017	0.0012	0.7908	310.65	391.73	–691.08	390.54	1489.34	–690.37
0.0023	0.0025	0.7913	289.39	364.61	–707.13	362.53	1450.24	–706.21
0.0030	0.0037	0.7918	277.59	349.49	–699.65	346.57	1411.53	–698.54
0.0037	0.005	0.7913	270.07	340.60	–338.31	338.14	1028.31	–337.46
0.0043	0.0062	0.7920	264.87	333.63	–446.14	330.14	1122.81	–445.01
0.0050	0.0075	0.7915	261.06	329.28	–207.56	326.43	872.99	–206.67
0.0057	0.0087	0.7918	258.14	325.43	–229.99	322.01	887.69	–228.96
0.0063	0.0100	0.7922	255.84	322.36	–247.73	318.37	899.20	–246.56
0.0070	0.0112	0.8004	253.97	315.30	–1682.25	299.81	2315.78	–1677.87
0.0077	0.0125	0.8054	252.43	310.78	–2338.13	288.18	2947.10	–2331.768
0.0083	0.0137	0.8096	251.14	307.17	–2763.13	278.57	3347.10	–2755.18
0.0090	0.0150	0.8096	250.04	306.03	–2537.26	277.20	3121.19	–2529.35

Now, considered the variation of ϕ_V with $\sqrt{c_m}$, there is a linearly growing trend with increase of carbamazepaine concentration. Thereafter, ϕ_V values used in Masson equation were calculated by the important parameters limiting apparent molar volume ϕ_V^o and related coefficients S_V and $S_{VV}^{\neq}$ by least square method:[15]

$$\phi_V = \phi_V^0 + S_V\sqrt{c_m} + S_{VV}^{\neq}c_m \quad (7)$$

where S_V and $S_{VV}^{\neq}$ are the apparent molar volume coefficient and calculated values are shown in Table X. It has found that ϕ_V values gradually increase with higher alizarin solution concentration given in the Table XI and Fig. 1. This indicates there is more alizarin interaction with their functional groups towards carbamazepine molecule. The coefficient S_V implies that there is a possibility of interaction between carbamazepine itself and/or alizarin itself. From Table X, it is observed that the coefficient S_V has some positive values, but they are very much lower (for 0.001 mol kg^{-1}, ϕ_V^o = 16504 m^3 mol^{-1}, S_V = –14527 m^3 mol$^{-3/2}$ kg$^{1/2}$, *i.e.*, $\phi_V^o >> S_V$). The coefficient S_V reveals that there must be some self--interaction between the drug molecules. However, it is negligible in comparison to solute and co-solute interaction.

Another coefficient S_V implies that there is a higher order interaction between solute and co-solute. From Table XI, it is observed that the coefficient S_V has negative values and $S_{VV}^{\neq}$ have positive values but the magnitude is very low. S_V values are very much lower than $S_{VV}^{\neq}$, *i.e.*, $S_{VV}^{\neq} >> S_V$, which can be interpreted as solute–solute or co-solute–co-solute self-interaction being neglig-

(CC) 2022 SCS.

ible when compared to solute and co-solute interaction. The possible solute and co-solute interaction in molecular level (2D) are presented in Scheme 2.

Table X. Apparent molar volume at room temperature and atmospheric pressure on a particular Eq. (1) with variation of carbamazepine

Alizarin concentration, mol kg^{-1}								
0.001			0.002			0.003		
c_m mol L^{-1}	ρ g m^{-3}	$\phi_V\times10^3$ m^3 mol^{-1}	c_m mol L^{-1}	ρ g m^{-3}	$\phi_V\times10^3$ m^3 mol^{-1}	c_m mol L^{-1}	ρ g m^{-3}	$\phi_V\times10^3$ m^3 mol^{-1}
0.0010	0.7905	345.52	0.0014	0.7908	357.88	0.0016	0.7908	391.73
0.0016	0.7926	323.95	0.002	0.7914	349.51	0.0023	0.7913	364.61
0.0023	0.7927	316.48	0.0026	0.7919	344.93	0.003	0.7918	349.49
0.0030	0.7926	312.45	0.0032	0.7914	342.85	0.0036	0.7913	340.60
0.0036	0.7928	309.66	0.0038	0.7921	340.55	0.0043	0.7920	333.63
0.0043	0.7931	307.61	0.0044	0.7915	339.71	0.005	0.7915	329.28
0.0050	0.7887	309.45	0.005	0.7919	338.49	0.0056	0.7918	325.43
0.0056	0.7898	307.54	0.0056	0.7922	337.50	0.0063	0.7922	322.36
0.0063	0.7893	307.01	0.0062	0.8004	331.79	0.007	0.8004	315.30
0.0070	0.7900	305.80	0.0068	0.8054	328.47	0.0076	0.8054	310.78
0.0076	0.7904	305.02	0.0074	0.8096	325.87	0.0083	0.8096	307.17
0.0083	0.7908	304.26	0.0080	0.8096	325.74	0.009	0.8096	306.03

TABLE XI. Apparent molar volume coefficient S_V and $S_{VV}^{\neq}$, limiting apparent molar volume (ϕ_V^0), Falkenhagen coefficient (A), viscosity coefficient B and D values with corresponding co-solute concentration in three different alizarin solutions at room temperature

c_m mol kg^{-1}	A kg$^{1/2}$ mol$^{-1/2}$	B kg mol^{-1}	D kg$^{3/2}$ mol$^{-3/2}$	$\phi_V^0\times10^3$ m^3 mol^{-1}	S_V m^3 mol$^{-3/2}$ kg$^{1/2}$	$S_{VV}^{\neq}$ m^3 mol^{-2} kg
0.001	–0.338	20.30	–126.47	100.00	–14527.0	349.33
0.002	0.7868	26.27	–250.61	199.57	–6230.2	362.62
0.003	–5.095	92.22	–513.74	200.00	–26112.0	420.37

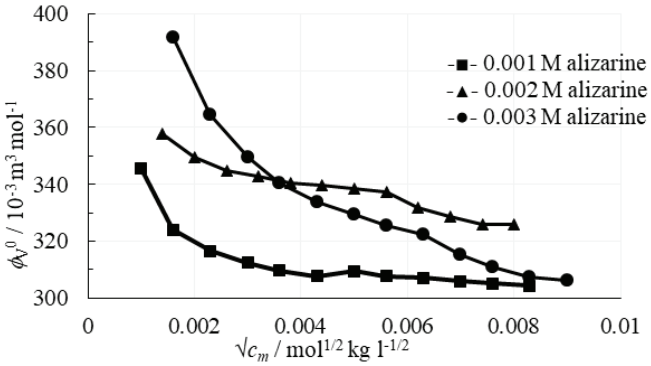

Fig. 1. Plot of apparent molar volume *vs.* different square root of concentration of carbamazepine for 0.001, 0.002, 0.003 mol kg^{-1} alizarin.

(CC) 2022 SCS.

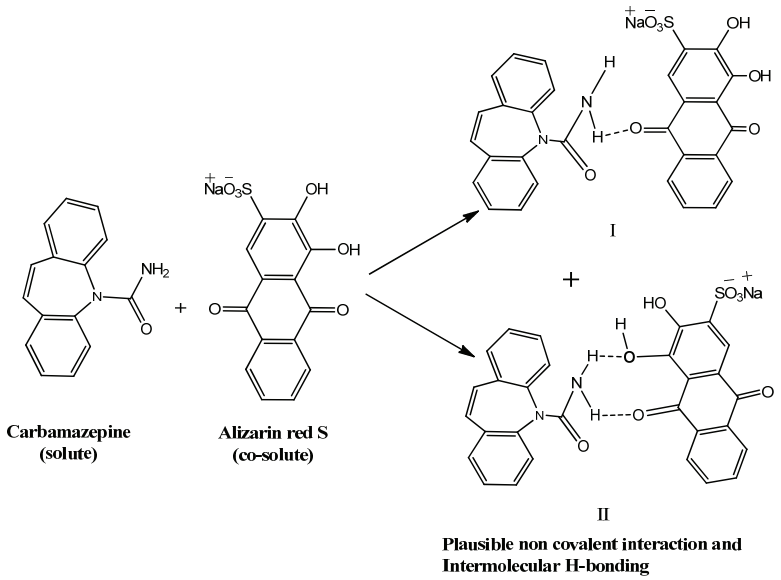

Scheme 2. Plausible non-covalent interaction between the two drug molecules.

Viscosity

Viscosity coefficient has been measured with the help of extended Jones–Dole equation for non-electrolytes:[17]

$$\frac{(\eta_r - 1)}{\sqrt{c_m}} = A + B\sqrt{c_m} + D\left(\sqrt{c_m}\right)^2 \quad (8)$$

where $\eta_r = \eta/\eta_o$ is the relative viscosity, η and η_o are the viscosities of ternary solutions (carbamazepine+alizarin+methanol) and solvent (methanol), respectively, and c_m is the molality of carbamazepine in ternary solutions. Their values are given in Table XII.

A is the Falkenhagen coefficient and it is determined by the ionic attraction theory of Falkenhagen–Vernon. Another constant, B is an empirical constant known as viscosity B-coefficient, that indicates interaction of the solute with co-solute molecules, respectively.[16] The values of $(\eta_r - 1)/\sqrt{c_m}$ and $\sqrt{c_m}$ are given in Table X. After plotting $(\eta_r - 1)/\sqrt{c_m}$ against $\sqrt{c_m}$ in Fig. 2 the coefficients A, B, and D are estimated by the least-square polynomial method. The valuable information about their effects on the structure of the co-solute (carbamazepine) in the local vicinity of the solute (alizarin) molecules, in ternary solutions, have been obtained from viscosity B coefficient. It is found from Table X the values of B coefficient are positive and higher than A coefficient.

This signifies that the solute-co-solute interaction is dominant over the solute–solute and the co-solute–co-solute interaction. It is also observed that the positive magnitude of viscosity B coefficient increases with solute concentration.

(CC) 2022 SCS.

Another co-efficient *D*, also measures the solute–co-solute interaction, presented in Table XI. The values indicate that the solute–co-solute interactions are much weaker compared to the solute–solvent interactions. The molecular interactions occurring between the drug molecules are due to the dipole–dipole interactions or van der Waals forces or non-covalent interactions.[18] These results are in good agreement with those obtained from limiting apparent molar volume ϕ_V values.

TABLE XII. $((\eta/\eta_0) - 1)/\sqrt{c_m}$ and $\sqrt{c_m}$ of carbamazepine at different concentration of alizarin (0.001, 0.002 and 0.003 mol kg^{-1}) variation with carbamazepine

Alizarin concentration, mol kg^{-1}					
0.001		0.002		0.003	
$\sqrt{c_m}$ mol$^{1/2}$ kg$^{-1/2}$	$((\eta/\eta_0) - 1)/\sqrt{c_m})$ kg$^{1/2}$ mol$^{-1/2}$	$\sqrt{c_m}$ mol$^{1/2}$ kg$^{-1/2}$	$((\eta/\eta_0) - 1)/\sqrt{c_m})$ kg$^{1/2}$ mol$^{-1/2}$	$\sqrt{c_m}$ mol$^{1/2}$ kg$^{-1/2}$	$((\eta/\eta_0) - 1)/\sqrt{c_m})$ kg$^{1/2}$ mol$^{-1/2}$
0.0316	0.3506	0.0316	0.1280	0.0316	–3.0575
0.0447	0.1338	0.0447	0.2100	0.0447	–1.8272
0.0547	0.2011	0.0548	0.1830	0.0547	–0.9566
0.0632	0.2347	0.0632	0.0730	0.0632	–1.2923
0.0707	1.0944	0.0707	0.2120	0.0707	–1.1519
0.0774	0.1545	0.0775	0.3070	0.0775	–1.1006
0.0836	0.5638	0.0837	0.1770	0.0837	–1.3279
0.0894	0.7616	0.0894	0.1700	0.0894	–1.1819
0.0948	0.1359	0.0949	0.7770	0.0949	–1.1651
0.1000	0.5967	0.1000	0.8040	0.1000	–1.0141
0.1048	0.2195	0.1049	0.8200	0.1049	–0.9227

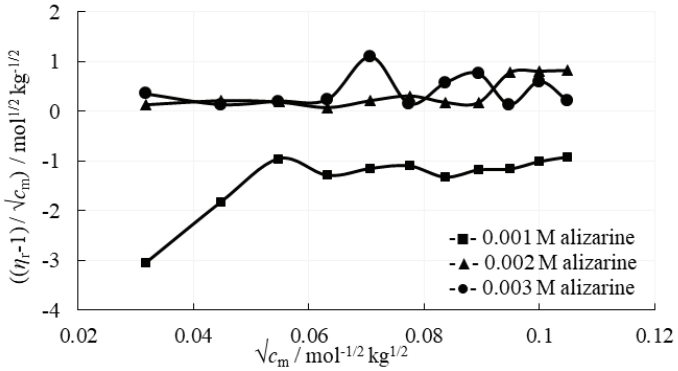

Fig. 2. Plot of $(\eta_r - 1)/\sqrt{c_m}$ against carbamazepine concentration ($\sqrt{c_m}$ at 0.001, 0.002 and 0.003 mol kg^{-1} alizarin concentration.

CONCLUSION

From the experimental results and the derived parameters of the studied ternary system *viz*. carbamazepine + alizarin + methanol, we conclude that Eq. (1), with some modification, is the most suitable equation for the calculation of apparent molar volume. We also derived the conclusion that the interaction sig-

(CC) 2022 SCS.

nifying parameters, *e.g.*, limiting apparent molar volume and viscosity *B*-coefficient are increasing with alizarin concentration. The study also proved that the solute–co-solute interaction is dominant over the solute–solute and the co-solute and co-solute.

Acknowledgment. The authors are grateful to the institution Cooch Behar Panchanan Barma University, for providing a space, and supporting the financial aids to carry out this work.

ИЗВОД

ПОРЕЂЕЊЕ РАЗЛИЧИТИХ ТИПОВА ЈЕДНАЧИНА ЗА МОЛАРНУ ЗАПРЕМИНУ ЗА ПРОВЕРУ И ПРИМЕНУ КОД ТЕРНАРНОГ КАРБАМАЗЕПИН + АЛИЗАРИН + МЕТАНОЛ СИСТЕМА И ИСПИТИВАЊЕ ОДГОВАРАЈУЋИХ МОЛЕКУЛСКИХ ИНТЕРАКЦИЈА

TAPAS MALLIK, SRABANTI GHOSH и DEEPAK EKKA

Department of Chemistry, Cooch Behar Panchanan Barma University, Cooch Behar-736101, West Bengal, India

У овом раду, молекулске интеракције карбамазепина и ализарина у метанолу су представљене ограничавајућим привидним моларним запреминама и коефицијентима вискозности. Пре даљег рада, извршена је и провера и примена прорачуна привидне моларне запремине узимајући у обзир доступних пет типова често коришћених једначина, при чему су потребне модификације извршене додатком хипотетичне масе и концентрације растворка. Након тога, ограничавајућа привидна моларна запремина и коефицијенти вискозности су израчунати применом Масон (Masson) једначине и Џонс–Долове (Jones–Dole) једначине, редом, да би предвидели и додатно проверили интеракције које се јављају између молекула у тернарном систему. Показало се да једначина означена бројем 1 представља најбољи аналитичи израз којим су фитовани резултати, а да постоје јаке интеракције између карбамазепина и ализарина у метанолу (ϕ_V^o = 23104 m^3 mol^{-1} и B = 18,10 kg mol^{-1}) при концентрацији 0,003 mol kg^{-1}. Резултати су интерпретирани у корист растворак–ко-растворак интеракција, који су доминантније у односу на растворак–растворак и ко-растворак–ко-растворак интеракције. Добијени резултати су дискутовани уз помоћ интермолекуларних сила и нековалентних интеракција.

(Примљено 29. априла, ревидирано 28. јуна, прихваћено 28. јула 2022)

REFERENCES

1. C. Fotia, S. Avnet, D. Granchi, N. Baldini, *J. Orthop. Res.* **30** (2012) 1486 (https://doi.org/10.1002/jor.22101.org/10.1002/jor.22101)
2. A. Saadia, I. Soliman, D. Louis, *Eur. J. Pharm. Biopharm*. **69** (2008) 342 (https://doi.org/10.1016/j.ejpb.2007.09.003)
3. K. Quliti, *Neurosciences (Riyadh)* **20** (2015) 107 (https://doi.org/10.17712/nsj.2015.2.20140501)
4. S. Qiu, A. Lai, M. Guo, K. Wang, X. Lai, U. Desai, N. Juma, M. Li, *Cryst. Eng. Comm*. **18** (2016) 2664 (https://doi.org/10.1039/C6CE00263C)
5. R. Andreozzi, M. Raffaele, M. Nicklas, *Chemosphere* **50** (2003) 1319 (https://doi.org/10.1016/s0045-6535(02)00769-5)
6. Q. Omar, J. Jaubert, J. Awan, *Int. J. Chem. Eng.* **1** (2018) 1 (https://doi.org/10.1155/2018/8689534)

(CC) 2022 SCS.

7. I. Mohammad, R. E. Verrall, *Canad. J. Chem.* **67** (1989) 727 (https://doi.org/10.1139/v89-111)
8. M. Xiangyu, M. Felix , H. Siyuan, L. Michael, L. Xu, S. Rebecca, R. O. Wiliams III, *Pharmaceutics* **12** (2020) 379 (https://doi.org/10.3390/pharmaceutics12040379)
9. D. P. Shoemaker, C. W. Garland, *Experiments in Physical Chemistry,* McGraw-Hill Book Comp., New York, 1962 (https://doi.org/10.1002/ange.19630751334)
10. J. Wawer, J. Krakowiak, W. Grzybkowski, *J. Chem. Thermodyn.* **40** (2008) 1193 (https://doi.org/10.1016/j.jct.2008.04.008)
11. A. Nikumbh, R. Bhujbal, *Int. J. Sci. Eng. Res.* **5** (2014) 138 (https://www.ijser.org/onlineResearchPaperViewer.aspx?Apparent-molar-volumes-and-viscosity-B-coefficients-of-sodium.pdf)
12. M. Shakeel, K. Mahmood, *J. Chin. Chem. Soc*. **67** (2020) 1552 (https://doi.org/10.1002/jccs.202000128)
13. P. Amutha, X. Rajkumar, *Asian. J. Chem*. **23** (2011) 1360 (https://asianjournalofchemistry.co.in/User/ViewFreeArticle.aspx?ArticleID=23_3_97)
14. P. Muhuri, B. Das, D. Hasra, *Ind. J. Chem.* **35** (1996) 288 (http://nopr.niscair.res.in/handle/123456789/41321)
15. D. O. Masson, *London, Edinburgh Dublin Phil. Mag. J. Sci*. **8** (1929) 218 (https://doi.org/10.1080/14786440808564880)
16. Y. Marcus, *J. Chem. Eng. Data* **57** (2012) 617 (https://doi.org/10.1021/je201209h)
17. M. N. Roy, S. Choudhury, D. Ekka, *Ind. J. Adv. Chemi. Sci*. **6** (2018) 59 (https://doi.org/10.22607/IJACS.2018.602001)
18. E. Johnson, S. Keinan, P. Mori-Sanchez, J. Cohen, W. Yang, *J. Am. Chem. Soc*. **132** (2010) 6498 (https://doi.org/10.1021/ja100936w).

(CC) 2022 SCS.

Journal of the Serbian Chemical Society
JSCS@tmf.bg.ac.rs • www.shd.org.rs/JSCS
J. Serb. Chem. Soc. *87* (10) 1185–1202 (2022)
JSCS–5587
Original scientific paper
Published 1 August 2022

Forced degradation studies and structural characterization of related substances of bisoprolol fumarate in finished drug product using LC–UV–MS/MS

ELENA LAZAREVSKA TODEVSKA[1,2], MARJAN PIPONSKI[1] and MARINA STEFOVA[2]*

[1]*Replek Farm Ltd., Quality Control Department, Skopje, North Macedonia and* [2]*Institute of Chemistry, Faculty of Natural Sciences and Mathematics, Ss. Cyril and Methodius University, Skopje, North Macedonia*

(Received 4 February, revised 20 June, accepted 21 June 2022)

Abstract: Methods for determination of bisoprolol and related substances mostly use UV detection and a phosphate buffer and are not suitable for MS detection. In this study, LC–UV–MS/MS for separation and characterization of bisoprolol related substances was developed, validated and applied for studying the degradation products of bisoprolol when exposed to hydrolytic stress, heat and light. The method uses a C18 column, formic acid in water and acetonitrile as mobile phases, gradient elution and UV and MS detection. Forced degradation revealed that acid hydrolysis produces the most intensive transformation of bisoprolol to its impurity A, along with impurities L and D. Alkaline hydrolysis produced impurities A, L, Q, G and K; oxidative and thermal degradation produced impurities A, L and K, while photodegradation produced impurities A, L, G and K, all characterized by their mass spectral data. The developed method using two detection systems was demonstrated as efficient since mass spectra allowed identification of the related substances of bisoprolol and quantification was possible using absorbance measurements at 270 nm. The obtained results will fill in the lack of data on the fragmentation patterns of bisoprolol and related substances that could be used by researchers and practitioners in research and quality control laboratories.

Keywords: bisoprolol; impurities; tablets; forced degradation study; fragmentation pathways.

INTRODUCTION

Bisoprolol fumarate is a synthetic beta-1-adrenergic blocker, which is commonly used in clinical practice for the treatment of hypertension and ventricular arrhythmias. Chemically, bisoprolol is 1-(propan-2-ylamino)-3-[4-(2-propan-2-

* Corresponding author. E-mail: marinaiv@pmf.ukim.mk
https://doi.org/10.2298/JSC220204053L

Available on line at www.shd.org.rs/JSCS/
(CC) 2022 SCS.

-yloxyethoxymethyl)phenoxy]propan-2-ol and its common form in solid pharmaceutical dosage forms is bisoprolol fumarate, which is very soluble in water.[1] Its wide use implies the need for efficient and reliable analytical methods for its quality control, including methods for characterization of its related substances.

Literature data revealed analytical methods for the determination of bisoprolol in pharmaceuticals and biological fluids, as a single active substance or in combined dosage forms that are mainly chromatographic as the most widely used. Chromatographic methods can be thin layer chromatographic,[2] and HPLC methods,[3–14] as well as ones that use HPLC with mass spectrometric detection especially for pharmacokinetic studies.[15–21]

On the other hand, published data for determination of related substances of bisoprolol are limited, especially data on the characterization of its degradation products (DPs), which have been listed in European Pharmacopoeia as impurity A, B, C, D, E, F, G, K, L, N, Q, R, S, T and U.[22,23] Several published studies have been developed for the determination of related substances by using hydrophilic interaction liquid chromatography (HILIC) coupled with UV-DAD and MS detection[24,25] and an HPLC–MS study for characterization of one unspecified impurity in a finished drug product[26] for bisoprolol or in combination with amlodipine.[27] Kasagic *et al*.[25] performed a kinetic study of the degradation of bisoprolol fumarate in order to follow its stability for 72 h in water, acid, base and oxidation environments. Pandey *et al.* also studied the degradation of bisoprolol fumarate as an active substance after severe acidic, alkaline, oxidative, thermal and light stress and monitored the results by LC–UV and identified the products by HPLC–TOF MS.[28] A very useful stability study using LC–MS/MS for characterization of the degradation products of acebutolol, an active compound from the same group, has been published giving an overview of degradation pathways as well as fragmentation patterns of the degradation products.[29] Having such data of the active substance and its related substances is a valuable tool in every quality control laboratorys. Forced degradation studies and obtaining such experimental data for bisoprolol and its degradation products was the rationale of this study.

The International Conference of Harmonization in its guidelines suggests stress testing to confirm and elucidate the critical factors that affect stability of the active principle. It is of great importance to identify the eventually formed degradation products through different pathways because it gives important information for the stability of the final product.[30,31] Information obtained during forced degradation studies gives data for both stability of the tested product and the suitability of the analytical method.[32]

HPLC with UV detection is routinely used for quality control of finished drug products in the pharmaceutical industry,[2–21] whereas mass spectrometry is used as an additional tool for structure elucidation of degradation pro-

(CC) 2022 SCS.

ducts.[25,26,28,29] Often, the pharmacopoeial methods propose non-volatile mobile phase constituents and cannot be transferred to LC–MS.[22,23]

Therefore, the main objective of this study was to introduce the method for determination of related substances of bisoprolol fumarate described in the British Pharmacopoeia/European Pharmacopoeia and then develop an analogous method compatible with mass spectrometry by optimizing the mobile phase composition and gradient elution. The developed method was then used for characterization of the products from a forced degradation study of the finished drug products using their mass spectra and also the corresponding mass spectra of these ions that have been selectively fragmented and analyzed by a second stage of mass spectrometry to generate MS^2 spectra consisting of their ion fragments (designated also as MS/MS). The mass spectrometer was used as an additional detection tool to the HPLC–UV method. In that way, a systematic overview of the degradation pathways and fragmentation patterns of the degradation products of bisoprolol is provided that can assist in their identification for regular quality control in laboratories in the pharmaceutical industry.

EXPERIMENTAL

Chemicals, reagents, materials

Bisoprolol fumarate working standard (WS) used for quantification was standardized *versus* a valid batch of bisoprolol fumarate certified reference substance according to EP (EPCRS), supplied from the European Directorate for the Quality of Medicines (EDQM). Bisoprolol for system suitability EPCRS and bisoprolol for peak identification EPCRS were from EDQM.

Bisoprolol film-coated tablets 2.5 mg were a product of ReplekFarm, Skopje, North Macedonia.

Acetonitrile (HPLC grade), phosphoric acid, formic acid, hydrochloric acid (analytical reagents), and hydrogen peroxide solution 30 % were from Carlo Erba Reagents, sodium hydroxide was from Honeywell, Riedel-de Haën™.

Instrumentation

An Agilent 1100 HPLC/MS system coupled with a diode array and a mass detector was used with an Agilent G2449A ion-trap mass spectrometer with an electrospray ionization interface. Nitrogen was used as a nebulizing gas at 50 psi and 12 L min^{-1}. Capillary temperature was 325 °C and the voltage was 3500 V. MS data were collected in the positive mode of ionization. The full scan covered the *m*/*z* range from 70–800. The detection wavelength when using the diode array detector was 270 nm.

The pharmacopoeial analytical method was transferred to using a volatile mobile phase instead of the nonvolatile phosphate containing one. For that purpose, formic acid was added to both mobile phases and mobile phase A was 1 vol. % formic acid in water, and mobile phase B was 1 vol. % formic acid in acetonitrile. The stationary phase was Zorbax C18 SB 250 mm×4.6 mm (5 μm particle diameter), the flow rate was 1.0 mL/min, the injection volume was 20 μL, and the operating temperature was 25 °C. The gradient elution program was the same as in the pharmacopoeial method that uses *o*-phosphoric acid.

(CC) 2022 SCS.

Preparation of standard solutions and test solutions

Bisoprolol for peak identification (containing fumaric acid, impurity A, bisoprolol and impurity E) was prepared by dissolving the content of the vial bisoprolol for peak identification CRS in 1 mL solvent. Bisoprolol for system suitability (containing fumaric acid, bisoprolol and impurity G) was prepared by dissolving the content of the vial bisoprolol for system suitability CRS 1 mL solvent.

Test solution was prepared by transferring weighed powdered tablet mass containing 25 mg of bisoprolol (as fumarate) into a 25 mL volumetric flask, then solvent composed of 20 vol. % acetonitrile in water was added, the sample was mechanically shaken for 15 min and filled to volume. Reference solution A was prepared by dilution of 1 mL of the test solution to 100 mL with the solvent, and additional dilution of 2 mL of this solution to 10 mL with the same solvent.

Samples for linearity testing were prepared by dilution of test solution prepared as described above, to cover the range 0.52–3.10 μg mL^{-1}. For recovery testing, 1325 mg placebos were weighed and spiked with known concentrations of bisoprolol covering the range from 1 to 3 μg mL^{-1} and prepared as test sample. A sample for system repeatability was prepared as Reference solution A. Samples for method repeatability were prepared as five separate test solutions described above from the same homogenized tablet mass.

Validation of the HPLC–UV method

The developed HPLC method with UV diode array detection at 270 nm was validated according to ICH guideline Q2(R1) recommendations. The tested validation parameters were linearity, accuracy, system repeatability, method repeatability, and selectivity/specificity. The mass spectrometer was included as an additional detection system to confirm the selectivity/specificity of the HPLC–UV diode array analytical method for determination of related substances of bisoprolol in the finished drug product.

Linearity of the method was established in the range from 0.52–3.10 mg/mL. Accuracy of the method was tested by a recovery study in three concentration levels. Specificity and selectivity were demonstrated by injecting system suitability solution, peak identification solution, placebo solution, standard solution, and test solution, as well as by conducting forced degradation studies. System repeatability was investigated by multiple injections of the reference solution and method repeatability was tested by repetition of analysis on 5 test solutions, prepared according to the previously described analytical procedure.

MS/MS studies

MS/MS studies were conducted on samples that had been stressed under different conditions as described above. The samples were analysed using an MS spectrometer with ESI in the positive ionisation mode. Separation was achieved using the HPLC method with a MS compatible mobile phase. Structure elucidation was performed using the obtained MS/MS data.

Forced degradation studies

Forced degradation studies were performed in solution with the application of heat, as well as exposure to UV radiation, temperature and humidity. Test solutions and placebo solutions prepared under normal conditions were used as control. Forced degradation studies in this research were performed in order to demonstrate that the method is stable as indicated during the development and validation.

All samples including controls, samples for hydrolytic stress studies, oxidative degradation studies, as well as samples for thermal degradation and photodegradation were prepared by weighting 1350 mg powdered tablet mass and 1325 mg placebo powder that were trans-

(CC) 2022 SCS.

ferred to 25 ml volumetric flasks. All samples were prepared as described before in *Preparation of standard solutions and test solutions*.

Hydrolytic forced degradation studies were performed on weighed powdered tablet mass and placebo powder that were treated with 2 mL 1 M hydrochloric acid at 60 °C for 1 h, and with 2 mL 1 M sodium hydroxide at 60 °C for 3 h. After the specified time intervals, samples for acid and alkaline forced degradation study were cooled and neutralised with 2 mL 1 M sodium hydroxide and 1 M hydrochloric acid, as required. Thereafter, samples were prepared as described in *Preparation of standard solutions and test solutions*.

Oxidative degradation was performed on weighed powdered tablet mass and placebo powder with the addition of 2 mL of 3 vol. % hydrogen peroxide at 60 °C for 3 h. After the specified period and treatment, sample was cooled and prepared as in *Preparation of standard solutions and test solutions*.

Thermal degradation studies were performed in a temperature-controlled oven, by placing the powdered tablet mass and placebo powder on an open quartz dish and kept at 105 °C for 5 h. Thereafter, samples were prepared and analysed according to the described method.

Photodegradation studies require exposure of the sample to UV radiation and temperature in a special chamber with an overall illumination of not less than 1.2 million lux h (UV energy not less than 200 W h m^{-2}). Samples of powdered tablet mass and placebo powder were put on an open quartz dish and kept for a period of 10 days in the chamber. Thereafter, the samples were analysed according to the described analytical procedure.

For both thermal degradation and photodegradation, after the exposure period, samples were prepared and analysed according to the described method under in *Preparation of standard solutions and test solutions*.

RESULTS AND DISCUSSION

Method transfer and optimization

Both European and British Pharmacopoeia have issued monographs for bisoprolol fumarate that include determination of related substances using a mobile phase with phosphoric acid and UV detection at 225 nm. To enable mass spectrometric detection and characterization of the related substances of bisoprolol, the method was modified to make it MS compatible. In that way, the fragmentation patterns of bisoprolol related substances were elucidated and applied for the characterization of the products of the forced degradation studies.

Zorbax C18 SB 250 mm×4.6 mm, 5 μm, was used as the stationary phase with a wide pH operation range. In the monograph for bisoprolol in European/ /British Pharmacopoeia, acidifying the mobile phase was made with *o*-phosphoric acid (10 g L^{-1}), but to transfer this method to MS, 1 vol. % formic acid was used instead since it is the preferred acidic component in the mobile phase in many HPLC applications with MS detection for enhancing both separation and ionization.[33] Bisoprolol has two absorbance maxima at 220 and 270 nm with different absorption coefficients, and the second had to be used upon changing the mobile phase to one with formic acid (the first one is recommended in the EP and BP methods that use phosphoric acid in the mobile phase).[33] The gradient elution program and the flow rate were the same as the ones described in the

(CC) 2022 SCS.

official monographs. The obtained results confirm a good correlation between the relative retention times obtained with both methods, and almost the same values for the resolution between bisoprolol and bisoprolol impurity G. The chromatograms obtained with both methods are presented in Fig. 1 showing good separation between bisoprolol and bisoprolol impuirty G with resolution 2.24 and relative retention time of the peak from bisoprolol impuirty G of 1.05 in the official method, whereas the corresponding values in the alternative method are 2.24 for the resolution and 1.03 for the RRT of bisoprolol impuirty G. In the chromatograms obtained for the peak identification CRS, the RRT of bisoprolol impuirty A and bisoprolol impuirty E calculated *vs*. the retention time of bisoprolol are 0.50 and 1.13 with the official method and 0.52 and 1.13 with the alternative method. These data demonstrate the suitability of the alternative method for further studies of the related substances to bisoprolol with HPLC coupled to mass spectrometric detection.

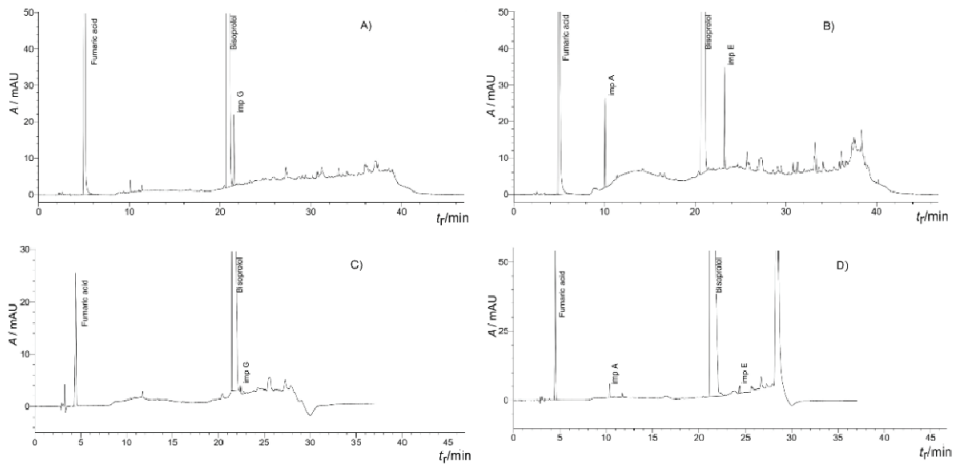

Fig. 1. UV DAD chromatograms of system suitability CRS (A and C) and of peak identification CRS (B and D) obtained with the official method (A and B) and with the alternative MS compatible method (C and D).

To confirm its performance to be used for characterization of related substances to bisoprolol in a forced degradation study, it was validated according to ICH requirements, tested for its selectivity and then applied for characterization of the samples of bisoprolol film-coated tablets subjected to forced degradation.

Validation of the HPLC–UV method for analysis of bisoprolol and related substances

To confirm its performance to be used for characterization of related substances to bisoprolol obtained in a forced degradation study, it was first validated

(CC) 2022 SCS.

according to the ICH requirements with emphasis on testing its selectivity and suitability for the identification of bisoprolol and its related substances using their mass spectra and their quantification by UV detection at 270 nm. For this purpose, standards for system suitability and for peak identification were used, and then samples from the forced degradation studies were characterized in order to evaluate the suitability of the HPLC–UV method for its purpose: characterization of substances related to bisoprolol.

Selectivity: bisoprolol and impurities G, A and E

Specificity and selectivity were confirmed by injecting the system suitability solution, peak identification solution, placebo solution, standard solution, and test solution, as well as by conducting forced degradation studies, and additional confirmation of the specified impurities and bisoprolol with MS data. The chromatograms of the placebo, test solution and standard solution confirmed that there was no interference from the excipients with the main peak of bisoprolol and the specified impurities (the chromatograms are given in the Supplementary material to this paper, Fig. S-1).

The selectivity of the method was tested with a solution for system suitability and a solution for peak identification. In the obtained chromatograms and mass spectra, peaks of bisoprolol and bisoprolol impurity G were detected at about 23.7 and 24.3 min, respectively, *i.e.*, the relative retention time for impurity G was about 1.03 min.

Mass spectral data showed two peaks with high abundance for positively charged ions at *m*/*z* 326 and 356, confirming the presence of bisoprolol (M_r = = 325) and bisoprolol impurity G (M_r = 355). Fragmentation pathways of these two compounds are given in Fig. 2 and their MS and MS^2 spectra in the Supplementary material, Fig. S-2.

As suggested by Steckel and Schlosser,[34] the initial site of protonation was the basic sp^3-hybridized nitrogen atom, and after collision-induced activation, the resulting product ions that were detected for both compounds at *m*/*z* 222 and 116 are the result of inductive cleavages: the one at *m*/*z* 222 by cleavage of the [2-(1--methylethoxy)ethoxy]-side chain and the one at *m*/*z* 116 by cleavage of the side chain containing the amino group moiety. Since the first product ion was obtained by a loss of the side chain that is different for both compounds, and the second ion is the product obtained by cleavage of the side chain that is identical for both compounds, they give the same main peaks in MS^2. However they differ in their molecular ions and retention and the method is selective so that bisoprolol and its impurity G can be distinguished.

In the chromatogram and mass spectra obtained from the standard for peak identification, peaks that confirm the presence of bisoprolol impurity A, bisoprolol and bisoprolol impurity E were detected at about 12.1, 23.3 and 26.3 min, res-

(CC) 2022 SCS.

pectively, *i.e.*, the relative retention time for bisoprolol impurity A is about 0.52 min and impurity E at about 1.13 min. The identity of these peaks were also confirmed by their mass spectra, as well (Supplementary material, Fig S-3).

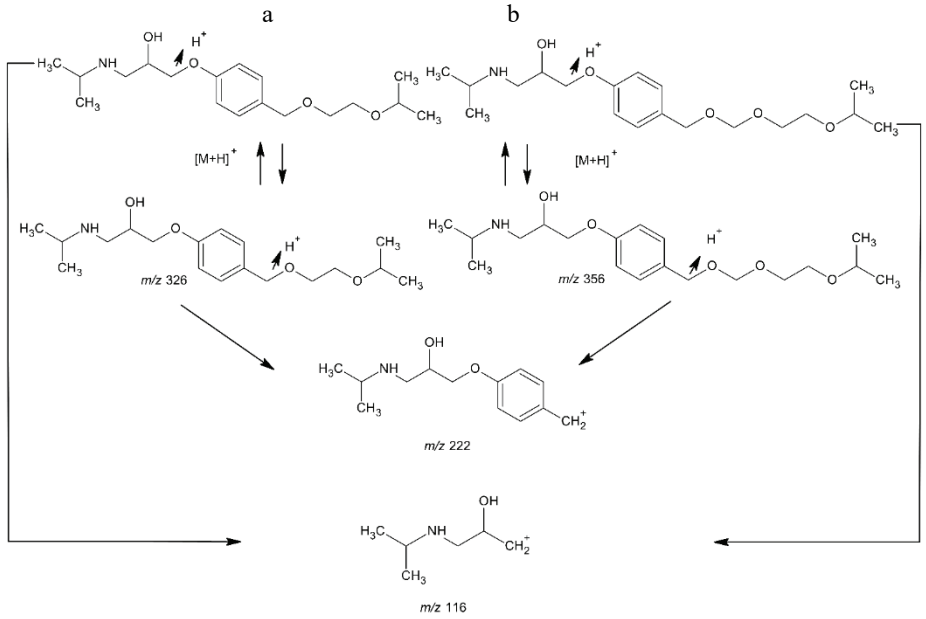

Fig. 2. Fragmentation pathways of a – bisoprolol ($C_{18}H_{31}NO_4$), and b – bisoprolol impurity G ($C_{19}H_{33}NO_5$).

The protonated molecular ion of bisoprolol impurity A (M_r = 239) was detected at *m*/*z* 240 with specific fragment ions at *m*/*z* 222, 198, 163, 133, 116, 98 and 74 in MS^2 and the fragmentation pathways are shown in Fig. 3.

The ion at *m*/*z* 222 is obtained by a loss of a water moiety in the longer side chain. The product ion is then prone to further fragmentation with a loss of 59 Da that could be attributed to cleavage of the C-N bond, resulting in a product ion with *m*/*z* 163, which is the most intensive peak in the MS^2. This ion may further lose the short side chain and give a product ion with *m*/*z* 133. The observed product ion at *m*/*z* 116 is due to cleavage of the side chain that contains nitrogen (as for impurities A and G) and may undergo further cleavage of the propyl moiety producing a fragment with *m*/*z* 74, but can also lose water, thus producing the ion at *m*/*z* 98. Another fragmentation pathway that was encountered was by a cleavage of the isopropyl group in the side chain producing the ion at *m*/*z* 198 after a neutral loss of 42 Da.

On the other hand, the protonated molecular ion of bisoprolol impurity E (M_r = 307) was detected at *m*/*z* 308. This impurity is a dehydration product of bisoprolol obtained by loss of water in the side chain. The molecular ion $[M+H]^+$

(CC) 2022 SCS.

at *m*/*z* 308 showed a fragmentation pattern with two main product ions in MS^2 at: *m*/*z* 249 obtained by loss of 59 Da (isopropylamine from the side chain), and at *m*/*z* 145 by further loss in the other side chain due to cleavage of the ether bond, as shown in Fig. 4.

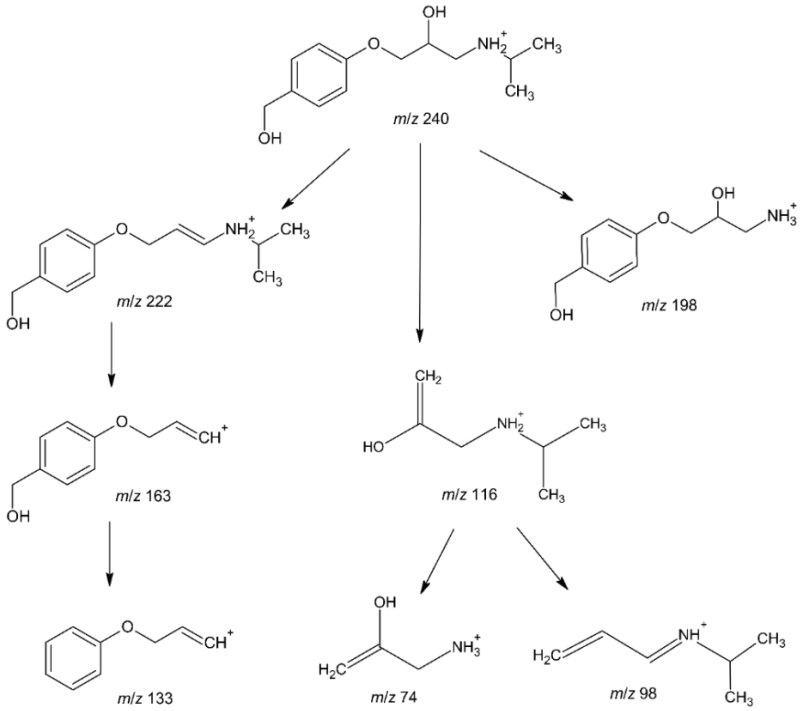

Fig. 3. Fragmentation pathways of bisoprolol impurity A ($C_{13}H_{21}NO_3$).

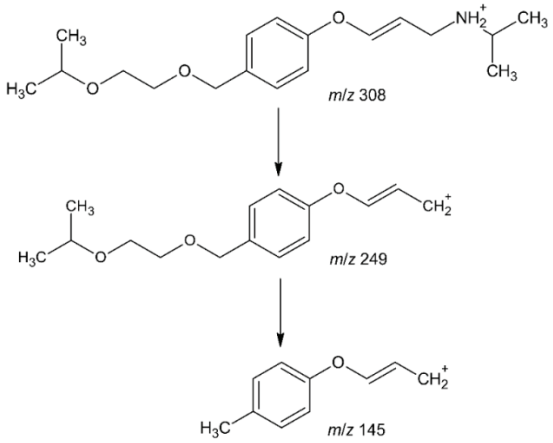

Fig. 4. Fragmentation pathway of bisoprolol impurity E ($C_{18}H_{29}NO_3$).

(CC) 2022 SCS.

Linearity, accuracy, repeatability

Acceptability of the linearity data are defined by the coefficient of determination, *y*-intercept (%) (ratio between intercept and calculated *y*-value at a certain concentration level, more precisely target level), as well as residual standard deviation of the response factors.[35]

Linearity of the method was tested in the range from 0.52–3.10 μg mL^{-1}, with a target level of about 2 μg mL^{-1} that corresponds to 0.2 % of the possibly present impurity. The calibration equation was $y = 3202x - 54.488$ with satisfactory value for the coefficient of determination R^2 of 0.9998 and an *RSD* of the response factor of 1.52 %. A coefficient of determination better than 0.998 is considered acceptable, since it represents the fit of the data with the regression line. The acceptable value for the *y*-intercept is less or equal to 5.0 % when compared to the *y*-value at a concentration level of 0.2 %,[34] which in the present case was 0.667 %. Nevertheless, the regression line is not ideal, and the intercept stands for the signal of zero concentration of active substance, which is here a peak area of 54.448 as absolute value, and if it was ideal, it should be zero. By determining the *p*-value of the intercept, the statistical significance of the obtained value of 54.448 was evaluated. To confirm that it is statistically not significant, the *p*-value should be much less than 0.05, which was found in the present case since the *p*-value was 9.93×10^{-7}.

The accuracy of the method was confirmed by a recovery study at three concentration levels (1.00, 2.00 and 3.00 μg mL^{-1}) with obtained values for analytical recovery that were within the limits of 90 and 110 %.

System repeatability tested by multiple injections of the reference solution confirmed good reproducibility with an *RSD* < 10 % and method repeatability tested by 5 test solutions prepared from powdered film-coated tablets gave *RSD* <20 %,[34] confirming its adequacy.

Application of the HPLC–UV–MS/MS method for analysis of bisoprolol and related substances obtained in forced degradation experiments

Acid degradation. During the acid degradation experiment (chromatogram on Fig. S-4 of the Supplementary material) degradation products (DPs) were generated demonstrating the sensitivity of bisoprolol to acid treatment and almost complete degradation. High amounts of impurity A and other DPs were identified using MS data demonstrating that the method could be used for their tentative identification even when the standards for all the 15 specified impurities of bisoprolol are not available. After the acid treatment, the DPs were identified as follows:

– The peak with relative retention time 0.49 (to bisoprolol) exhibited a protonated molecular ion $[M+H]^+$ at *m*/*z* 240 further fragmented into product ions at

(CC) 2022 SCS.

m/*z* 222, 198, 163, 133, 116, 98 and 74, which is consistent with its identification as bisoprolol impurity A (Fig. S-9a of the Supplementary material).

– The peak with a RRT 0.55 gave a protonated molecular ion $[M+H^+]^+$ at *m*/*z* 238 with the corresponding product ions in MS^2 and *m*/*z* 220, 196, 178, 161, 149, 133, 116, 98 and 74 (Fig. S-9b). The ion at *m*/*z* 220 is due to water loss in the side chain that may further undergo a loss of the isopropylamine moiety giving a product ion at *m*/*z* 161, and a further loss of the aldehyde group in the other side chain giving a product ion at *m*/*z* 131 (Fig. 5). The other fragmentation pathway could be explained by a loss of the isopropyl moiety giving a product ion at *m*/*z* 196 (most abundant in MS^2), and further loss of water leading to an ion at *m*/*z* 178 (Fig. 5). These data suggest that it could be attributed to the bisoprolol impurity L.

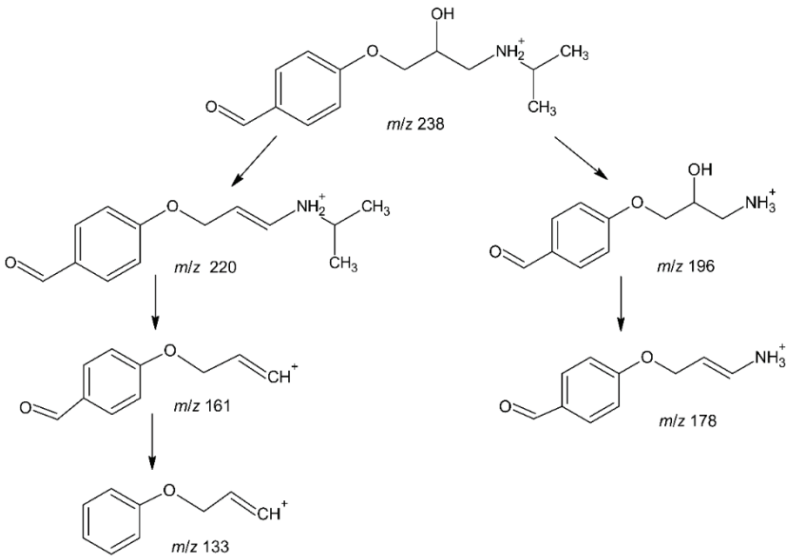

Fig. 5. Fragmentation pathway of bisoprolol impurity L ($C_{13}H_{20}NO_3$).

– The peak with relative retention time 0.56, with $[M+H]^+$ at *m*/*z* 461 was detected together with a more intensive peak at *m*/*z* 231, which is due to the same molecule (M_r = 460) that when monoprotonated gives the $[M+H^+]^+$ ion at 461, and when diprotonated gives the $[M+2H^+]^{2+}$ ion at *m*/*z* 231 (Fig. S-9c). The protonated molecular ion gave product ions in MS2 at *m*/*z* 443, 385 and 328. The first ion at *m*/*z* 443 is due to water loss, and a further loss of isopropylamine from the side chain gave the product at *m*/*z* 385. The loss of the second isopropylamine resulted in the product ion detected at *m*/*z* 328 (Fig. 6). All these arguments led to the conclusion that this peak could be attributed to bisoprolol impurity D.

(CC) 2022 SCS.

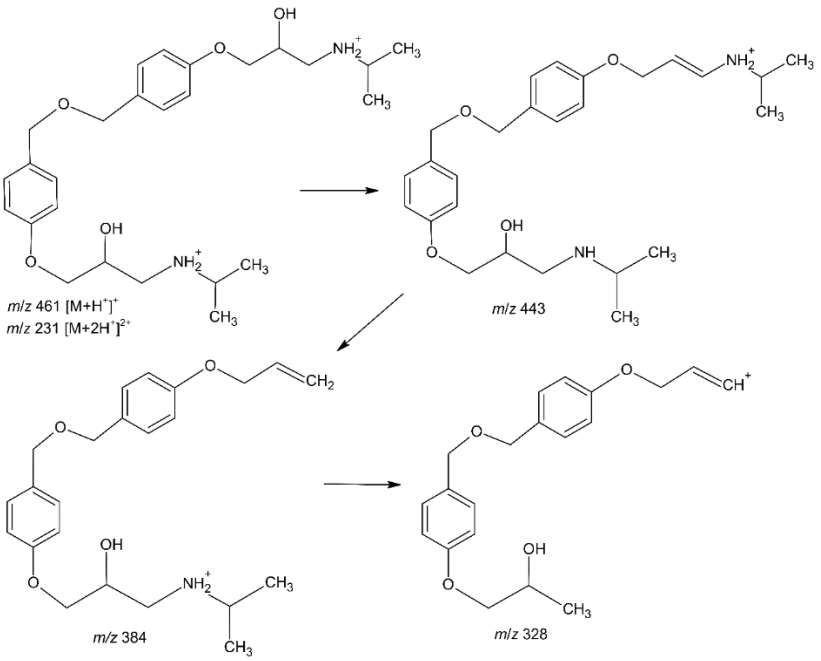

Fig. 6. Fragmentation pathway of bisoprolol impurity D ($C_{26}H_{40}N_2O_5$).

Alkaline degradation

Upon alkaline treatment, these degradation products were detected (Supplementary material, Fig. S-5 of the Supplementary material):

– The peak with relative retention time 0.51 was characterized with the protonated molecular ion at *m*/*z* 240 that gave the product ions in MS^2 at *m*/*z* 222, 198, 163, 133, 116, 98 and 74, which is consistent with its identification as bisoprolol impurity A (Fig. S-10a of the Supplementary material).

– The peak with relative retention time 0.58, with $[M+H]^+$ at *m*/*z* 238 and product ions at *m*/*z* 220, 196, 178, 161 and 133 was characterized as bisoprolol impurity L (Fig. S-10b).

– The peak with RRT 0.84, exhibited the protonated molecular ion at *m*/*z* 298 and product ions in MS^2 at *m*/*z* 280, 222 and 116 (Fig. S-10c). The fragmentation pathway is described in Fig. 7 with the product ion at *m*/*z* 280 due to a loss of water, and the ions at *m*/*z* 222 and 116 are typical product ions for bisoprolol. Following these experimental data, it could be concluded that this peak was due to bisoprolol impurity Q.

– The peak with RRT 1.03, with a protonated molecular ion at *m*/*z* 356 was observed with product ions at *m*/*z* 222 and 116 (MS/MS^2 of impurity G is given in Fig. S-10d) that suggested it is due to bisoprolol impurity G (fragmentation pattern described in Fig. 2b).

(CC) 2022 SCS.

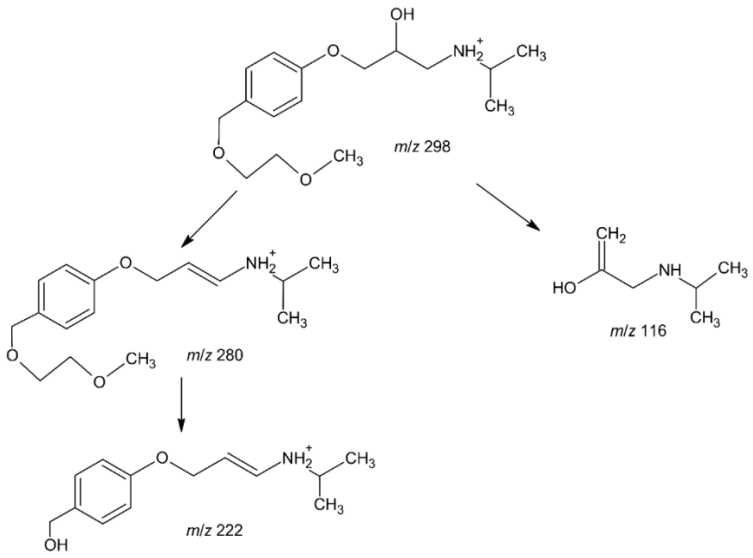

Fig. 7. Fragmentation pathway of bisoprolol impurity Q ($C_{26}H_{40}N_2O_5$).

– The peak at RRT 1.04, had a $[M+H^+]^+$ at *m*/*z* 340 with its product ions in MS^2 at *m*/*z* 322, 298, 263, 218, 205, 194, 176, 161, 121, 116 with different intensities (Fig. S-10e). The ion at *m*/*z* 322 is due to the loss of water molecule and is further fragmented by loss of the radical next to the carbonyl C-atom leading to a stable product ion at *m*/*z* 218. Another product ion is obtained by loss of the isopropylamine moiety leading to a product ion 263 that was subjected to further cleavage of the side chain giving the product ion with the most intensive peak in MS^2 at *m*/*z* 205. A signal at *m*/*z* 116, characteristic for the bisoprolol side chain, was also detected in MS^2, suggesting this compound has the same side chain in the structure (Fig. S-11 of the Supplementary material). According to all the discussed data for this detected compound, it may be concluded that the peak at RRT 1.04 is due to the presence of bisoprolol impurity K.

Oxidative degradation

After oxidative treatment (chromatogram in the Supplementary material, Fig. S-6), three DPs were detected (Fig. S-12a, b and c), two of them, impurity A and impurity L, already detected after acid and alkaline degradation. The third was detected as a peak at RRT 1.04 and exhibited a protonated molecular ion at *m*/*z* 340 due to presence of bisoprolol impurity K, and it was also observed after alkaline degradation.

Thermal degradation

The analysis of the sample following thermal degradation showed three degradation products (chromatogram in the Supplementary material, Fig. S-7): with

(CC) 2022 SCS.

relative retention time 0.50, $[M+H]^+$ at *m*/*z* 240 that was identified as impurity A (Fig. S-13a), another with RRT 0.55, $[M+H]^+$ at *m*/*z* 238, analogous to the one found in the acid, alkaline as well as in oxidative and was attributed to bisoprolol impurity L (Fig. S-13b), and with RRT 1.04, $[M+H]^+$ at *m*/*z* 340, that followed the same fragmentation pattern as described for bisoprolol impurity K (Fig. S-13c).

Photodegradation

The analysis of the sample after photodegradation gave degradation products as found in thermal degradation (chromatogram in the Supplementary material, Fig. S-8, MS/MS^2 in Fig. S-14a, b, c and d), and also impurity G. Four peaks were detected and identified as the specified impurities: with RRT 0.50 for impurity A ($[M+H]^+$ at *m*/*z* 240), with RRT 0.57 for impurity L ($[M+H]^+$ at *m*/*z* 238), with RRT 1.04 for impurity G ($[M+H]^+$ at *m*/*z* 356), and with RRT 1.05 for impurity K ($[M+H]^+$ at *m*/*z* 340).

Summary of forced degradation study

A summary of the results obtained for all detected compounds in the forced degradation study that were characterized by their mass spectral data are given in Table I.

TABLE I. Overview of the results from forced degradation studies with relative retention times (RRT) and mass spectral data (MS and MS^2 spectra) for the detected related substances of bisoprolol

Imp.	Normal condition/Control		Acid degradation		Alkaline degradation	
	RRT	*m*/*z*	RRT	*m*/*z*	RRT	*m*/*z*
A	0.50	MS: 240 MS^2: 222, 198, 163, 145, 116, 98, 74	0.49	MS: 240 MS^2: 222, 198, 163, 145, 116, 98, 74	0.51	MS: 240 MS^2: 222, 198, 163, 145, 116, 98, 74
L	0.60	MS: 238 MS^2: 220, 196, 178, 161, 133, 98, 74	0.55	MS: 238 MS^2: 220, 196, 178, 161, 133, 98, 74	0.58	MS: 238 MS^2: 220, 196, 178, 161, 133, 98, 74
D	–	–	0.56	MS: 461 MS^2: 443, 385, 328	–	–
Q	–	–	–	–	0.84	MS: 298 MS^2: 280, 204, 116
G	1.02	MS: 356 MS^2: 222, 116	–	–	1.03	MS: 356 MS^2: 222, 116
K	1.03	MS: 340 MS^2: 322, 298, 263, 218, 205, 194, 176, 161, 121, 116	–	–	1.04	MS: 340 MS^2: 322, 298, 263, 218, 205, 194, 176, 161, 121, 116

(CC) 2022 SCS.

TABLE I. Continued

Imp.	Oxidative degradation		Thermal degradation		Photodegradation	
	RRT	*m/z*	RRT	*m/z*	RRT	*m/z*
A	0.50	MS: 240 MS^2: 222, 198, 163, 145, 116, 98, 74	0.50	MS: 240 MS^2: 222, 198, 163, 145, 116, 98, 74	0.51	MS: 240 MS2: 222, 198, 163, 145, 116, 98, 74
L	0.56	MS: 238 MS^2: 220, 196, 178, 161, 133, 116	0.55	MS: 238 MS^2: 220, 196, 178, 161, 133, 116	0.57	MS: 238 MS^2: 222, 196, 178, 161, 133, 116
G	–	–	–	–	1.04	MS: 356 MS^2: 222, 116
K	1.04	MS: 340 MS^2: 322, 298, 263, 218, 205, 194, 176, 161, 121, 116	1.04	MS: 340 MS^2: 322, 298, 263, 218, 205, 194, 176, 161, 121, 116	1.05	MS: 340 MS^2: 322, 298, 263, 218, 205, 194, 176, 161, 121, 116

As could be seen, acid hydrolysis caused the most intensive transformation of bisoprolol to its related substance impurity A, along with other degradation products, impurities L and D. Alkaline hydrolysis also gave products characterized by MS as impurities A, L, Q, G and K, whereas oxidative and thermal stress produced impurities A, L and K, and photodegradation gave rise to four impurities characterized by MS as impurities A, L, G and K.

According to its structure and functional groups, bisoprolol is likely to produce degradation products when oxidative stress is applied.[25] Literature data showed forced degradation studies that confirmed that the percentage of degradation products were highest when oxidative treatment was applied, and also they revealed the fact that when acid hydrolysis was applied, bisoprolol impurity A was obtained at the highest level.[25] Pandey *et al.* performed force degradation studies of bisoprolol fumarate as an active substance and detected only three peaks: fumaric acid, bisoprolol and an unknown impurity at *m/z* 749 after thermal degradation, for which they suggested a structure and formation pathway. This degradation product was not detected in the present experiments. This study revealed the presence of six known impurities of bisoprolol and demonstrated the suitability of the method to characterize them by their mass spectra and quantified them by the HPLC–UV method.

CONCLUSIONS

The developed method that combines the two detection systems was demonstrated as very efficient since the mass spectra allowed identification of the related substances of bisoprolol by studying the protonated molecular ions and their corresponding product ions, even when not all reference standards were avail-

(CC) 2022 SCS.

able, and quantification was then possible by using UV absorbance measurements at 270 nm.

The mass spectral data obtained in this study of bisoprolol and its degradation products that are also its specified impurities, will be of great value and will contribute to fill in the lack of data on the fragmentation patterns of bisoprolol and its related substances that could be applied in quality control laboratories for their identification.

SUPPLEMENTARY MATERIAL

Additional data and information are available electronically at the pages of journal website: https://www.shd-pub.org.rs/index.php/JSCS/article/view/11609, or from the corresponding author on request.

ИЗВОД

СТУДИЈА ФОРСИРАНЕ ДЕГРАДАЦИЈЕ И СТРУКТУРНЕ КАРАКТЕРИЗАЦИЈЕ СУПСТАНЦИ СРОДНИХ БИСОПРОЛОЛ-ФУМАРАТУ У ФИНАЛНИМ ЛЕКОВИТИМ ПРОИЗВОДИМА ПРИМЕНОМ LC–UV–MS/MS

ELENA LAZAREVSKA TODEVSKA[1,2], MARJAN PIPONSKI[1] и MARINA STEFOVA[2]

[1]*Replek Farm Ltd, Quality Control Department, Skopje, North Macedonia и* [2]*Institute of Chemistry, Faculty of Natural Sciences and Mathematics, Ss. Cyril and Methodius University, Skopje, North Macedonia*

Методе за одређивање бисопролола и сродних супстанци применом UV детекције и фосфатног пуфера нису погодне за MC детекцију. У овој студији је развијена и валидирана LC–UV–MS/MS метода за раздвајање и карактеризацију супстанци сродних бисопрололу и примењена за испитивање деградационих производа бисопролола, при излагању хидролитичком стресу, топлоти и светлости. У методи се користи C18 колона, мравља киселина у води и ацетонитрил као мобилна фаза, градијентна елуција, UV и MS детекција. Форсирана деградација киселом хидролизом изазива најинтензивније трансформације бисопролола до његових нечистоћа A, L и D. Алкална хидролиза генерише нечистоће A, L, Q, G и K; оксидативна и термална деградација генерише нечистоће A, L и K, а фотодеградација A, L, G и K. Све су нечистоће окарактерисане масеном спектралном анализом. Развијена метода, која користи два детекциона система, показала се ефикасном с обзиром да масени спектри омогућују идентификацију супстанци сродних бисопрололу, а квантификација је могућа мерењем апсорбанције на 270 nm. Добијени подаци ће допунити недостатак података о фрагментацији бисоролола и сродних супстанци, који ће истраживачи и практичари моћи користити у истраживањима и лабораторијама контроле квалитета.

(Примљено 4. фебруара, ревидирано 20. јуна, прихваћено 21. јуна 2022)

REFERENCES

1. H. Bakheit, R. Ali, A. D. Alshahrani, A. S. El-Azab, *Profiles Drug Subst. Excip. Relat. Methodol.* **46** (2021) 51 (https://doi.org/10.1016/bs.podrm.2020.07.006)
2. Witek, H. Hopkala, G. Matysik, *Chromatographia* **50** (1999) 41 (https://doi.org/10.1007/BF02493615)
3. L. Logoyda, S. Kovalenko, A. M. Abdel-Megied, I. Zhulkevych, I. Drapak, I. Demchuk, O. Netsyuk, *Int. J. Appl. Pharm.* **11** (2019) 186 (https://doi.org/10.22159/ijap.2019v11i3.32391)

(CC) 2022 SCS.

4. D. Panainte, L. Agoroaei, N. Bibire, G. Tantaru, M. Apostu, M. Vieriu, F. A. Spac, F. A. *Rev. Chim.* **66** (2015) 1791 (https://www.researchgate.net/publication/299723693_A_HPLC_Method_for_the_Determination_of_Bisoprolol_in_Tablets_and_its_Application_to_a_Bioequivalence_Study)
5. E. Caudron, S. Laurent, E. M. Billaud, P. Prognon, *J. Chromatogr., B* **801** (2004) 339 (https://doi.org/10.1016/j.jchromb.2003.11.009)
6. S. Shaikh, O. A. Thusleem, M. S. Muneera, J. Akmal, A. V. Kondaguli, K. Ruckmani, *J. Pharm. Biomed. Anal*. **48** (2008) 1055 (https://doi.org/10.1016/j.jpba.2008.08.009)
7. R. J. Eastwood, J. C. Jerman, R. K. Bhamra, D. W. Holt, *Biomed. Chromatogr.* **4** (1990) 178 (https://doi.org/10.1002/bmc.1130040415)
8. L. Patel, B. Suhagia, P. Shah, R. Shah, *Ind. J. Pharm. Sci.* **68** (2006) 635 (https://doi.org/10.4103/0250-474X.29633)
9. S. J. Joshi, P. A. Karbhari, S. I. Bhoir, K. S. Bindu, C. Das, *J. Pharm. Biomed*. *Anal*. **52** (2010) 362 (https://doi.org/10.1016/j.jpba.2009.10.021)
10. S. Mahu, F. A. Spac, C. Ciobanu, M. Hancianu, L. Agroroaei, E. Butnaru, *Rev. Chim.* **67** (2016) 414 (https://www.researchgate.net/publication/299537958_Quantitative_Determination_of_Bisoprolol_Fumarate_by_HPLC_I_Method_validation)
11. G. Arjun, S. Dinakaran, B. Madhavi, M. M. Naga, R. Ramalingam, R. N. Anisetti, *Ind. Drugs* **46** (2009) 39 (https://www.researchgate.net/publication/306218289_A_simple_HPLC_method_for_quantitation_of_bisoprolol_fumarate_in_tablet_dosage_form#fullTextFileContent)
12. W. Wang, L. Gao, T. Shi, *Chin. J. Pharm. Anal.* **19** (1999) 308 (https://www.ingentaconnect.com/content/jpa/cjpa/1999/00000019/00000005/art00006)
13. Vora, A. Kadav, *Ind. J. Pharm. Sci*. 70 (2008) 542 (https://doi.org/10.4103/0250-474X.44616)
14. T. Lazarevska, M. Piponski, M. Stefova, *Maced. J. Chem. Chem. Eng.* **40** (2021) 263 (https://doi.org/10.20450/mjcce.2021.2430)
15. L. Logoyda, S. Kovalenko, M. Gaafar, A. M. Abdel-Megied, F. A. Elbarbry, *Microchem. J*. **155** (2020) 104700 (https://doi.org/10.1016/j.microc.2020.104700)
16. R. M. Turner, V. Fontana, M. Bayliss, S. Whalley, A. Santoyo Castelazo, M. Pirmohamed, *J. Pharm. Biomed. Anal.* **159** (2018) 272 (https://doi.org/10.1016/j.jpba.2018.06.062)
17. M. Liu, D. Zhang, Y. Sun, Y. Wang, Z. Liu, J. Gu, *Biomed. Chromatogr.* **21** (2007) 508 (https://doi.org/10.1002/bmc.785)
18. S. Li, G. Liu, J. Jia, Y. Liu, C. Pan, C. Yu, Y. Cai, J. Ren, *J. Chromatogr., B* **847** (2007) 174 (https://doi.org/10.1016/j.jchromb.2006.10.013)
19. G. Peste, C. Oniscu, A. Vlase, *Rom. Biotechnol. Lett.* **15** (2010) 5140 (https://www.rombio.eu/rbl2vol15/11%20%20PESTE.pdf)
20. G. Hemavathi, S. M. Hipparagi, *Asian J. Pharm. Clin. Res.* **10** (2017) 477 (https://doi.org/10.22159/ajpcr.2017.v10i4.16829)
21. L. Ding, X. Zhou, X. Guo, Q. Song, J. He, G. Xu, *J. Pharm. Biomed. Anal.* **44** (2007) 520 (https://doi.org/10.1016/j.jpba.2007.03.001)
22. *British Pharmacopoeia*, *Monograph for Bisoprolol fumarate in British Pharmacopoeia*, Stationary Office on Behalf of the Medicines and Healthcare Products Regulatory Agency (MHRA), London, 2018
23. *European Pharmacopoeia, Monograph for Bisoprolol fumarate 01/2012:171*, European Directorate for the Quality of Medicines and Healthcare, Council of Europe, Strasbourg, 2014

(CC) 2022 SCS.

24. I. Kasagic-Vujanovic, B. Jancic-Stojanovic, D. Ivanovic, *Arh. Farm.* **64** (2014) 230 (https://doi.org/10.5937/arhfarm1403230K)
25. I. Kasagić-Vujanović, B. J. Stojanović, D. Ivanović, in *CMBEBIH 2017. IFMBE Proceedings*, Vol. 62, A. Badnjevic, Ed., Springer, Singapore, 2017, p. 415 (https://doi.org/10.1007/978-981-10-4166-2_64)
26. I. Mitrevska, E. Kikovska-Stojanovska, G. Petrusevski, M. Chachorovska, S. Memed-Sejfulah, S. Ugarkovic, *Adv. Chem.* **2017** (2017) 3047517 (https://doi.org/10.1155/2017/3047517).
27. T. Rakic, M. Jovanovic, A. Tumpa, B. Jancic-Stojanovic, M. Medenica, *Arh. Farm.* **64** (2014) 95 (https://doi.org/10.5937/arhfarm1402095R)
28. S. Pandey, R. Pandey, S.S. Shukla, *Ind. J. Pharm. Educ. Res.* **56** (2022) 272 (https://doi.org/10.5530/ijper.56.1.32)
29. U. Rakibe, R. Tiwari, A. Mahajan, V. Rane, P. Wakte, *J. Pharm. Anal.* **8** (2018) 357 (https://doi.org/10.1016/j.jpha.2018.03.001)
30. *ICH Topic Q1B*, *Photostability Testing of New Active Substances and Medicinal Products Step 5 Note for guidance on the photostability testing of new active substances and medicinal products*, 1998 (http://www.emea.eu.int)
31. *ICH Topic Q 1A (R2)*, *Stability Testing of new Drug Substances and Products Step 5 Note for guidance on stability testing: stability testing of new drug substances and products*, 2003 (http://www.emea.eu.int)
32. D. W. Reynolds, K. L. Facchine, J. F. Mullaney, K. M. Alsante, T. D. Hatajik, M. G. Motto, *Pharm. Technol.* **26** (2002) 48 (https://cdn.sanity.io/files/0vv8moc6/pharmtech/cef968de93fced22f668d7a89ec492e8dc542e12.pdf/article-9668.pdf)
33. J. A. Dolan, *Guide to HPLC and LC-MS Buffer Selection*, ACE HPLC Columns, Aberdeen, 2006 (https://www.hplc.eu/Downloads/ACE_Guide_BufferSelection.pdf)
34. A. Steckel, G. Schlosser, *Molecules* **24** (2019) 611 (https://doi.org/10.3390/molecules24030611)
35. Y. Kazakevich, R. LoBrutto, Eds, *HPLC for pharmaceutical scientists*, John Wiley & Sons, Inc., Hoboken, NJ, 2007, p.462 (https://doi.org/10.1002/0470087951).

(CC) 2022 SCS.

Journal of the Serbian Chemical Society
JSCS@tmf.bg.ac.rs • www.shd.org.rs/JSCS
J. Serb. Chem. Soc. 87 (10) S380–S387 (2022) *Supplementary material*

SUPPLEMENTARY MATERIAL TO

Forced degradation studies and structural characterization of related substances of bisoprolol fumarate in finished drug product using LC–UV–MS/MS

ELENA LAZAREVSKA TODEVSKA[1,2], MARJAN PIPONSKI[1] and MARINA STEFOVA[2]*

[1]*Replek Farm Ltd., Quality Control Department, Skopje, North Macedonia and* [2]*Institute of Chemistry, Faculty of Natural Sciences and Mathematics, Ss. Cyril and Methodius University, Skopje, North Macedonia*

J. Serb. Chem. Soc. 87 (10) (2022) 1185–1202

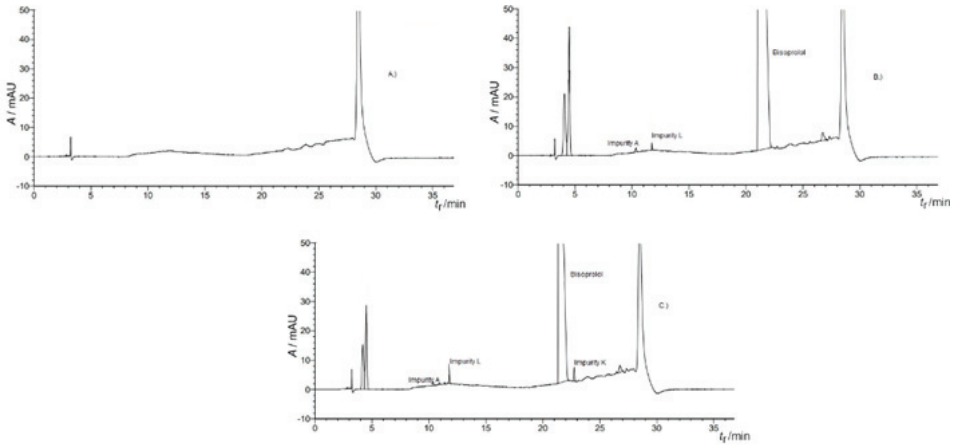

Fig. S-1. Chromatograms of: A) placebo solution, B) test solution, and C) standard solution obtained with the developed alternative method.

* Corresponding author. E-mail: marinaiv@pmf.ukim.mk

Available on line at www.shd.org.rs/JSCS/

(CC) 2022 SCS.

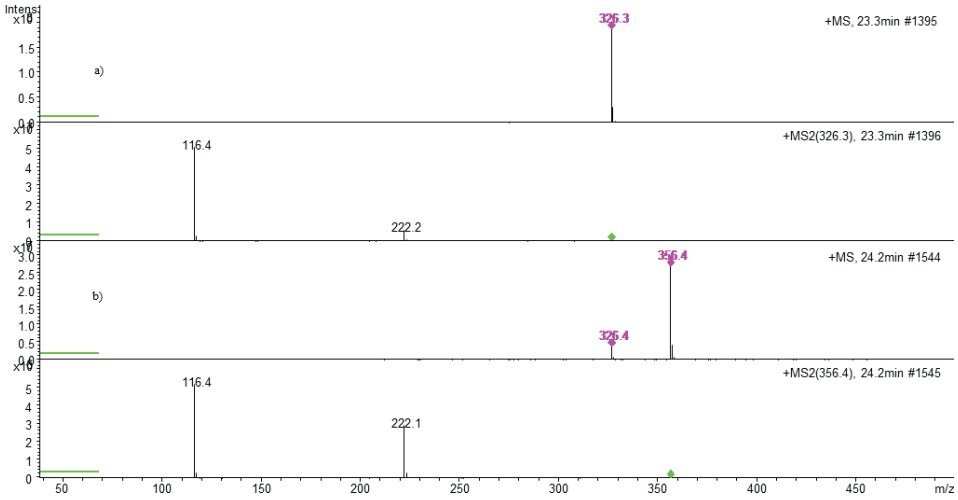

Fig. S-2. MS/MS^2 of a) bisoprolol, b) bisoprolol impurity G.

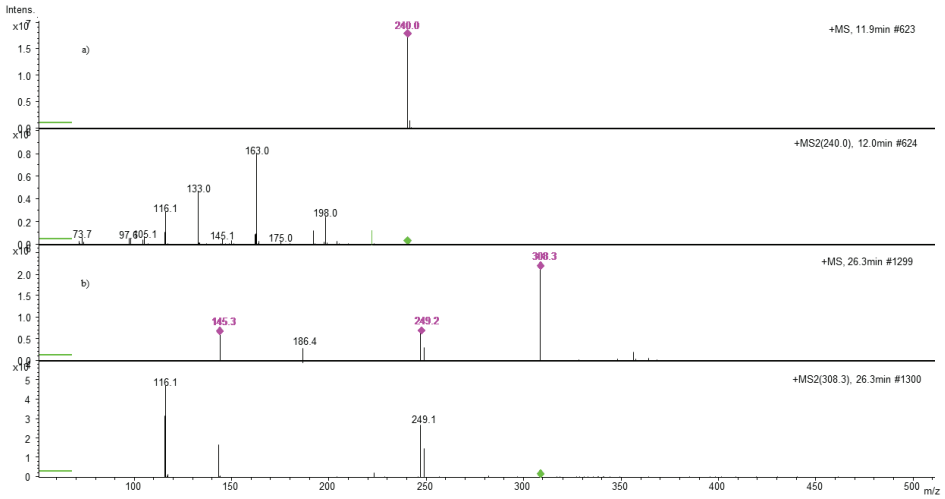

Fig. S-3. MS/MS^2 of a) bisoprolol impurity A, b) bisoprolol impurity E.

(CC) 2022 SCS.

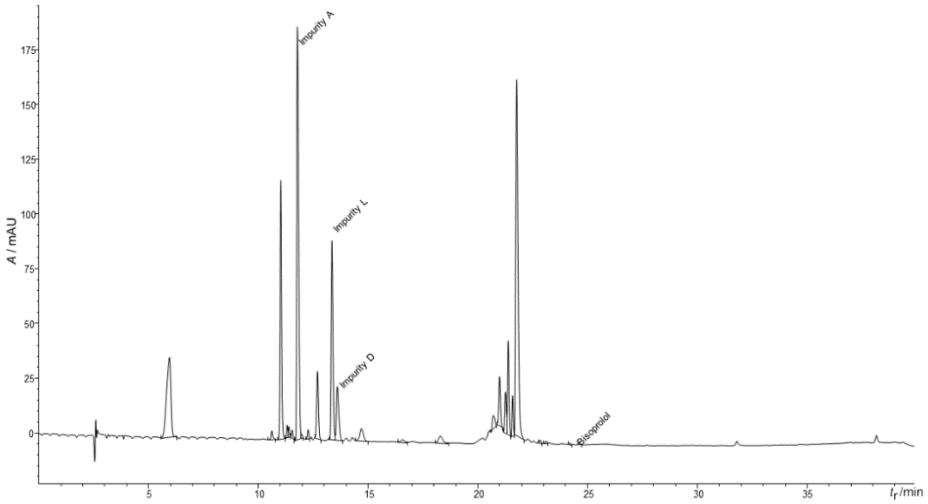

Fig. S-4. Chromatogram of test solution – acid degradation.

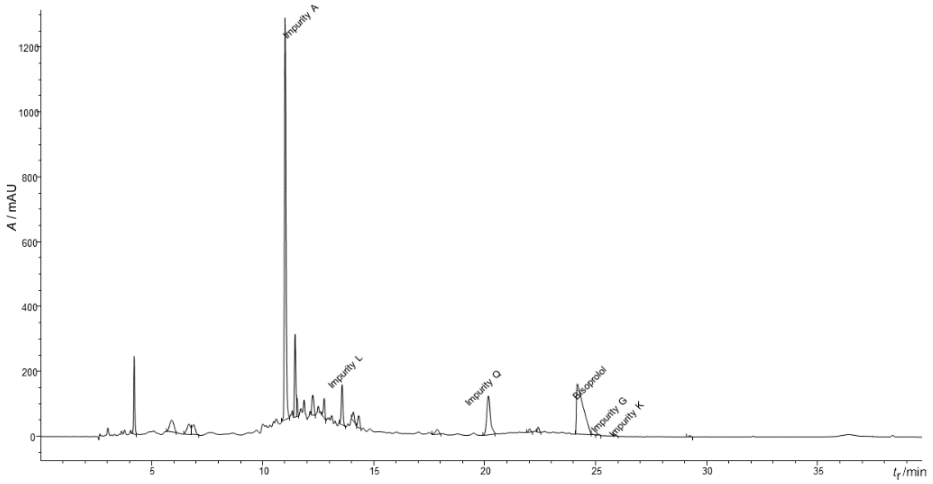

Fig. S-5. Chromatogram of test solution – alkaline degradation.

(CC) 2022 SCS.

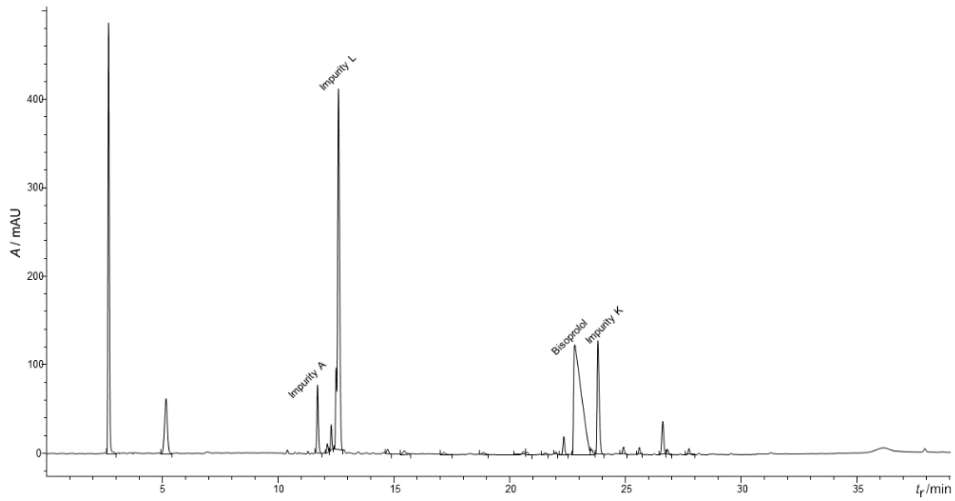

Fig. S-6. Chromatogram of test solution – oxidative degradation.

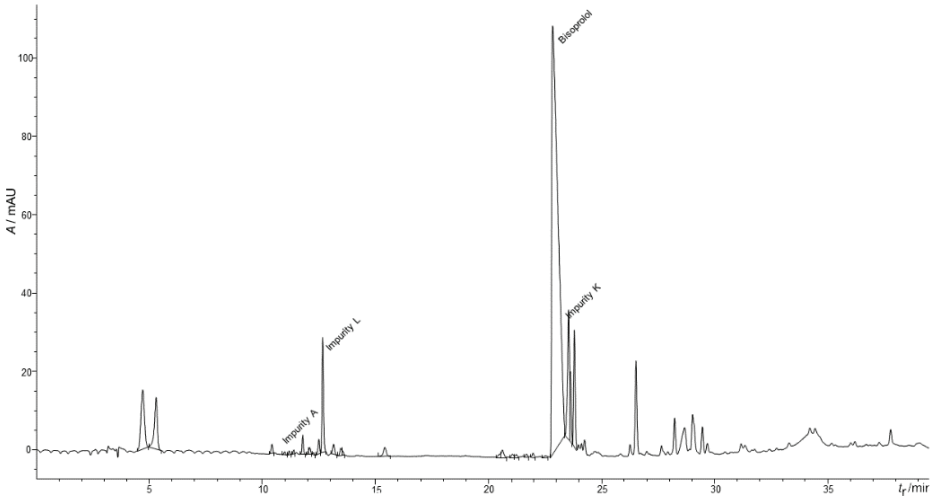

Fig. S-7. Chromatogram of test solution – thermal degradation.

(CC) 2022 SCS.

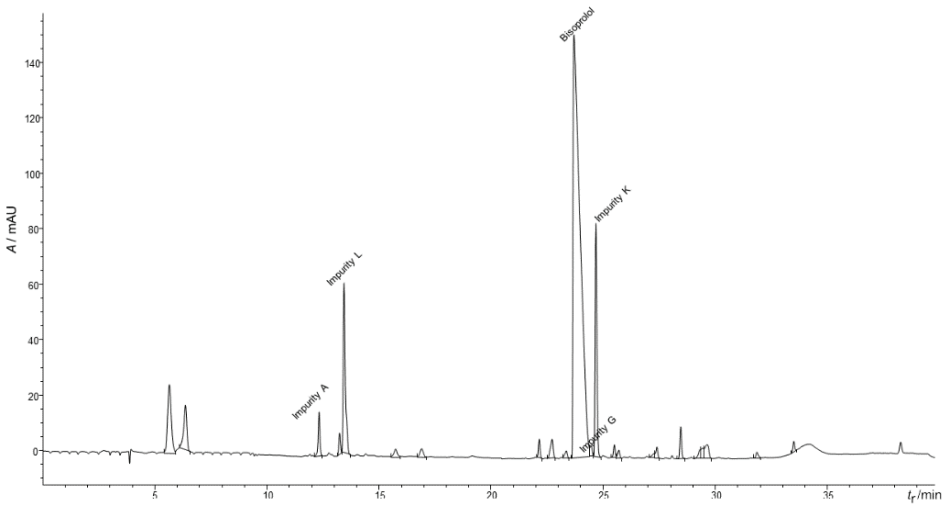

Fig. S-8. Chromatogram of test solution – photodegradation.

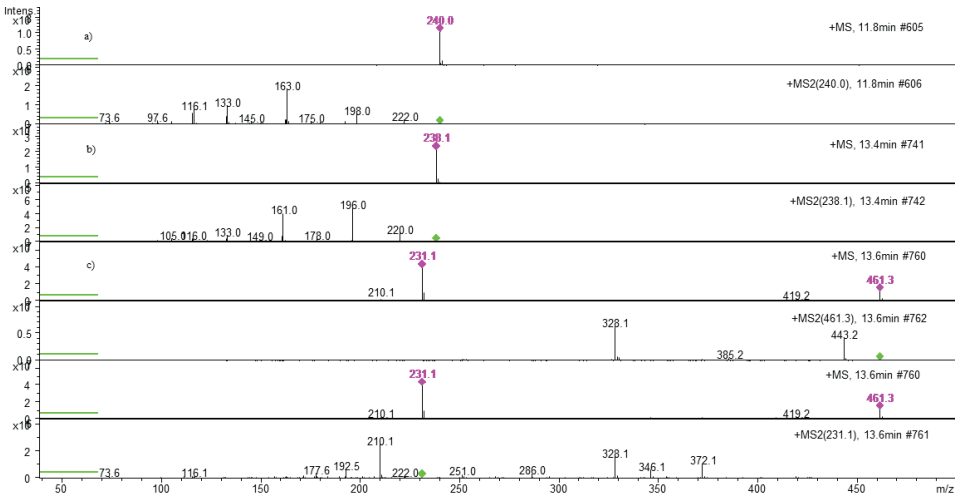

Fig. S-9. MS/MS^2 of a) bisoprolol impurity A, b) bisoprolol impurity L, and c) bisoprolol impurity D detected after acid degradation.

(CC) 2022 SCS.

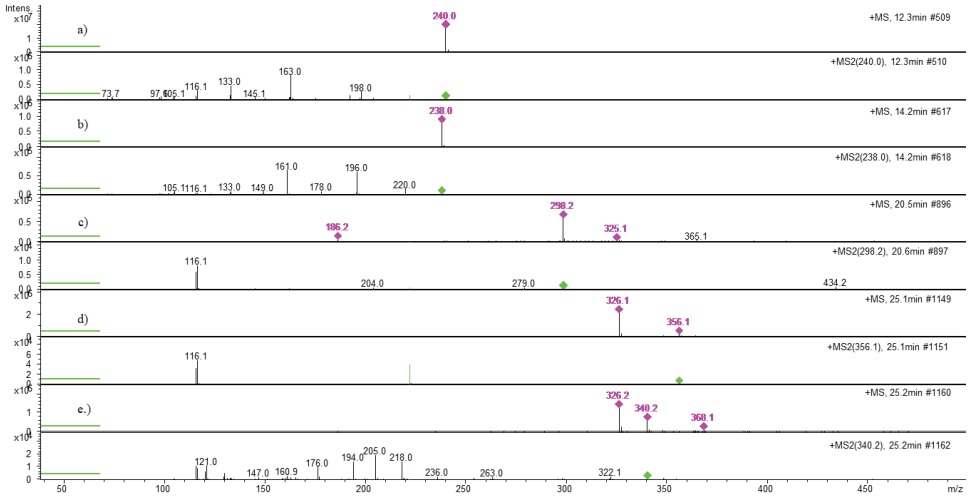

Fig. S-10. MS/MS^2 of a) bisoprolol impurity A, b) bisoprolol impurity L, c) bisoprolol impurity Q, d) bisoprolol impurity G, and e) bisoprolol impurity K detected after alkaline degradation.

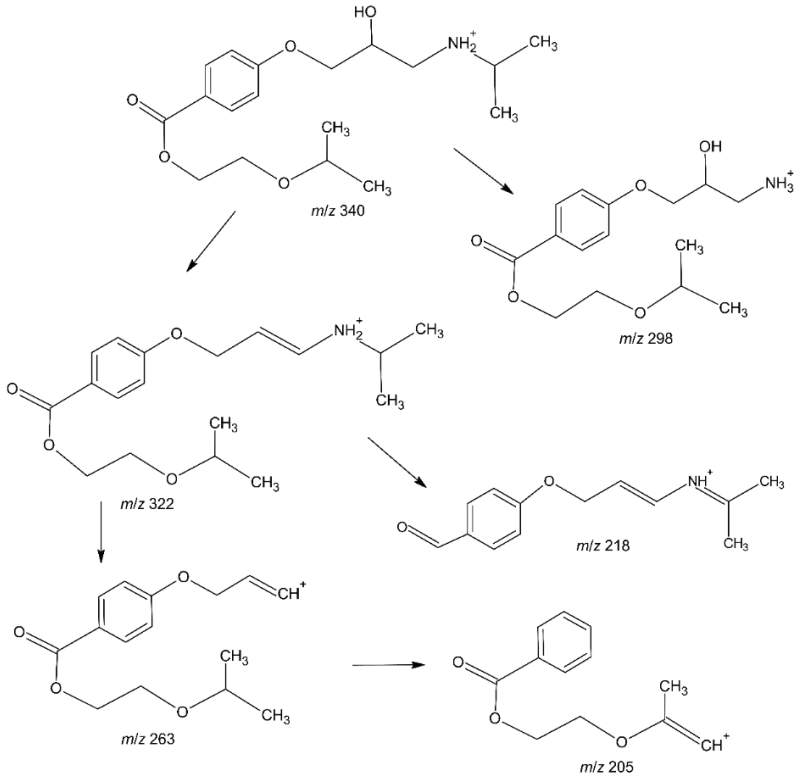

Fig. S-11. Fragmentation pathway of bisoprolol impurity K ($C_{18}H_{30}NO_5$).

(CC) 2022 SCS.

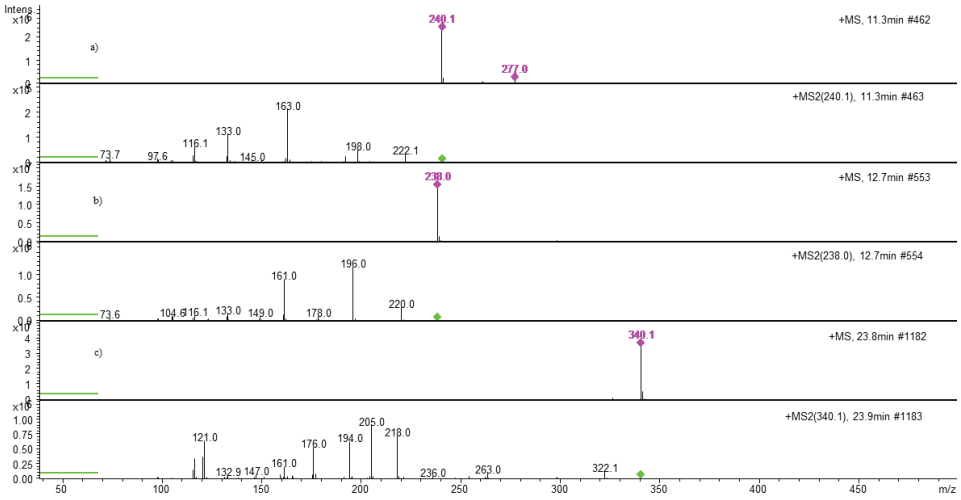

Fig. S-12. MS/MS^2 of a) bisoprolol impurity A, b) bisoprolol impurity L, c) bisoprolol impurity K detected after oxidative degradation.

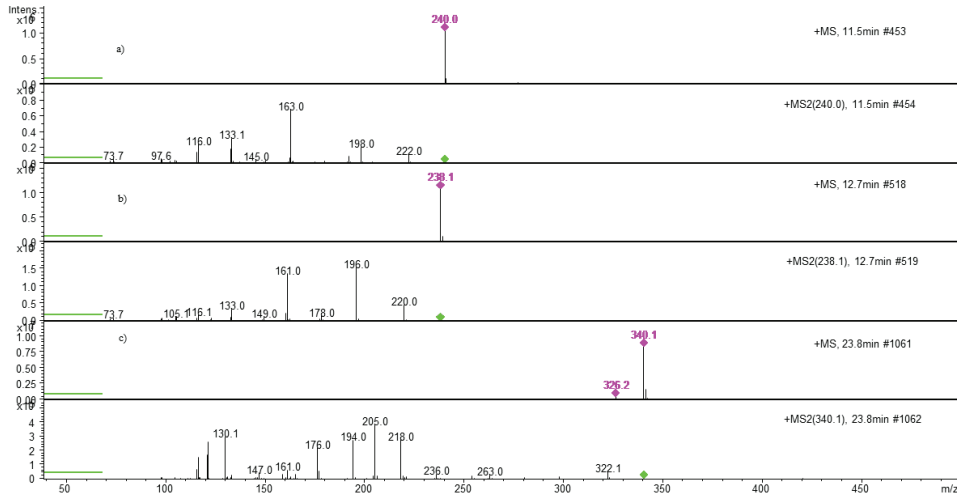

Fig. S-13. MS/MS^2 of a) bisoprolol impurity A, b) bisoprolol impurity L, c) bisoprolol impurity K detected after thermal degradation.

(CC) 2022 SCS.

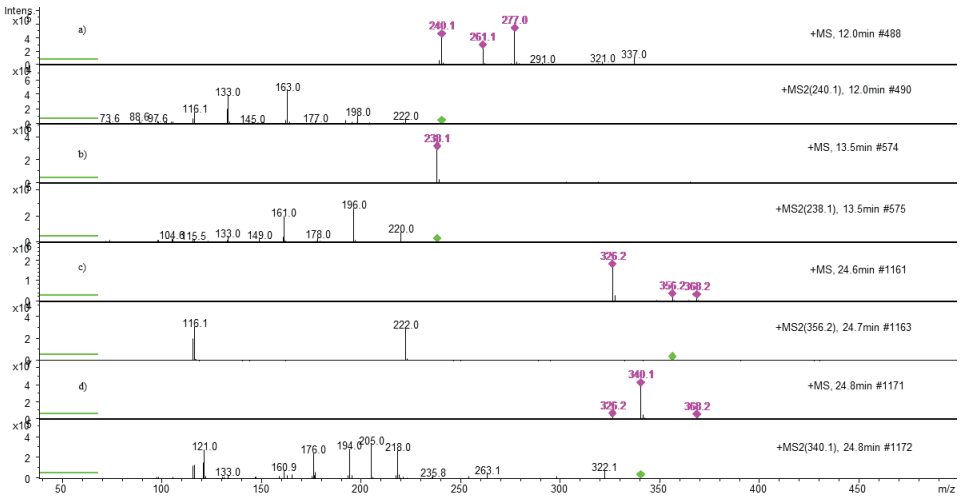

Fig. S-14. MS/MS^2 of a) bisoprolol impurity A, b) bisoprolol impurity L, c) bisoprolol impurity G, and d) bisoprolol impurity K detected after photodegradation.

(CC) 2022 SCS.

Journal of the Serbian Chemical Society
JSCS@tmf.bg.ac.rs • www.shd.org.rs/JSCS
J. Serb. Chem. Soc. *87* (10) 1203–1218 (2022)
JSCS–5588
Original scientific paper
Published 22 July 2022

Nanocomposites made from thermoplastic linear poly(urethane-siloxane) and organoclay: Composition impact on the properties

MARIJA V. PERGAL[1]*, SANJA OSTOJIĆ[2], MILOŠ STEINHART[3], IVAN S. STEFANOVIĆ[1], LATO PEZO[2] and MILENA ŠPÍRKOVÁ[3]

[1]*University of Belgrade, Institute of Chemistry, Technology and Metallurgy, National Institute of the Republic of Serbia, Njegoševa 12, 11000 Belgrade, Serbia,* [2]*Institute of General and Physical Chemistry, University of Belgrade, Studentski trg 12–16, 11000 Belgrade, Serbia and* [3]*Institute of Macromolecular Chemistry CAS (IMC), Heyrovsky Sq. 2, 16206 Prague 6, Czech Republic*

(Received 23 February, revised 10 April, accepted 19 April 2022)

Abstract: Thermoplastic poly(urethane-siloxane)/organoclay nanocomposites (TPU NCs) with different hard segment content (20–55 wt. %) were prepared by *in situ* polymerization in the presence of organically modified montmorillonite as a nanofiller (Cloisite 30B; 1 wt. %). Hydroxyl-terminated ethoxypropyl-poly(dimethylsiloxane) was used as soft segment, while 4,4'-methylenediphenyl diisocyanate and 1,4-butanediol were the hard segment components. The study of the influence of the hard segment content on the functional properties of TPU NCs was performed by Fourier transform infrared (FTIR) spectroscopy, X-ray diffractometry (XRD), atomic force microscopy (AFM), scanning electron microscopy (SEM), dynamic mechanical thermal analyses (DMTA), differential scanning calorimetry (DSC), thermogravimetric analysis (TGA), water contact angle and water absorption tests. The results revealed that TPU NCs with the increasing hard segment content exhibit higher values of degree of microphase separation, melting temperature of the hard segments, degree of crystallinity, storage modulus (except for TPU NC-55), but lower thermal stability and hydrophobicity. TPU NC films were hydrophobic and their free surface energy was in the range from 17.7 to 24.9 mJ m^{-2}. This work highlights how the composition of TPU NCs would affect their functional properties and provide an additional composition intended for designing advanced TPU NC materials for special biomedical applications.

Keywords: polyurethane; clay nanofiller; composition-dependent properties; degree of microphase separation; surface properties; thermal performance.

* Corresponding author. E-mail: marijav@chem.bg.ac.rs
https://doi.org/10.2298/JSC220223036P

Available on line at www.shd.org.rs/JSCS/
(CC) 2022 SCS.

INTRODUCTION

Thermoplastic polyurethanes (TPUs) are a class of block-copolymers which are segmented with short, glassy or crystalline chains segments known as hard segments (HS), acting as physical crosslink bonds and imparting stiffness and strength, and long amorphous rubber-segments known as soft segments (SS), conferring its elastic character.[1] Because the HS and SS are incompatible, the TPU exhibits two phase microdomain morphology: a HS rich phase and a SS rich phase.[1] TPU with poly(dimethylsiloxane) (PDMS) as a SS are very important for biomedical applications because of the many unique properties of PDMS, including low glass transition temperature, low surface energy, good biocompatibility, excellent thermal stability, ultraviolet resistance and high permeability to many gases.[2]

In recent years, TPU nanocomposites (NCs) reinforced with layered silicates, *i.e.*, clays, have earned increased interest because they show improved properties when compared to pure TPU, as a result of the high surface area and aspect ratios of the nanofillers.[3,4] The use of a very low percentage (≤5 wt. %) of layered silicates in the TPU matrix has been motivated by the silicates' potential to improve properties like thermal stability, anti-flammability, mechanical properties, improved permeation barrier, shape memory behaviour, and drugs delivery property.[4–7] It was established that for good dispersion of clay platelets into polymer matrix, clays have to be modified with some hydrophobic surfactants, since clay platelets are hydrophilic and incompatible with a relatively hydrophobic polymer matrix.[8] Clay is usually modified by exchanging the interlayer inorganic cations with organic long-chain cations like alkylammonium ions, which enables more favourable interactions with the desired, usually hydrophobic, matrix.[9] According to the literature,[10–12] intercalated or exfoliated structure, partially exfoliated or mixed exfoliated-intercalated structure, could be achieved depending on the preparation method and in correlation to strength of interfacial interactions between the polymer matrix and organoclays.

Pattanayaka and Jana[12] prepared TPU-based NCs by *in situ* polymerization. It was shown that the addition of clay before the chain extension reaction led to poor dispersion of clay platelets, while when the chain extension reaction was carried out before the addition of clay, the clay platelets were well exfoliated to the scale of individual clay layers, and the best improvement in mechanical properties was observed. Jeong *et al.*[13] and Meng *et al.*[14] showed that the microphase separation and the degree of improvement to the thermal and mechanical properties mainly depend on the degree of dispersion of clay platelets within the polyurethane matrix. Nanoclays which provide a range of aforementioned improvements to the final materials seem to be a particularly promising filler for materials based on PDMS-based TPU matrix. In our previous study,[10] it was found that TPU/clay NCs with 1–10 wt.% of Cloisite 30B could be efficiently

(CC) 2022 SCS.

prepared by *in situ* intercalation polymerization in solution. An intercalated structure of TPU/clay NCs was found, and for TPU NCs with low nanoclay contents (1 and 3 wt. %), a high extent of organoclay dispersion in the TPU matrix was achieved. Namely, TPU NC with 1 wt. % of organoclay represents the best balance between the clay concentration and the functional properties.[10]

The present article is the second part of an ongoing study in which the effects of HS content (20–55 wt. %) on the microstructure and properties of TPUs were investigated. Also, the objective of this study was to prepare a series of TPU/organoclay NCs (with different HS contents and a constant organoclay content (1 wt. %)) by *in situ* polymerization. It is of essential importance to analyse the composition-property relationships of TPU/organoclay NCs and provide guiding principles for finding the optimal thermal, thermomechanical, and surface characteristics of these materials. The use of organoclay particles indicates new possibilities for modifying TPU films with potential biomedical applications. In the present study, the influence of the HS content on the functional properties was studied by the microscopic, thermal, thermomechanical and surface analysis techniques.

EXPERIMENTAL

Materials

α,*ω*-Dihydroxyethoxy-propyl-poly(dimethylsiloxane) (PDMS, 99 %; *Mn* = 1000 g mol^{-1}) was supplied from ABCR GmbH, Germany. 4,4′-Methylenediphenyl diisocyanate (MDI, >98 %; Aldrich) was used as received. 1,4-Butanediol (BD, 99 %) was supplied from Aldrich and was purified by vacuum distillation. The clay was natural montmorillonite modified with methyl-tallow-bis-2-hydroxyethyl quaternary ammonium salt, Cloisite 30B (hereafter denoted as C30B), purchased from Southern Clay Products Inc, United States. The solvents, such as *N*,*N*-dimethylacetamide (DMAc, from Acros Organics, Belgium, 99 %) and tetrahydrofuran (THF, 98 %, from Avantor Inc., United States), were distilled before use.

Preparation of TPU NCs

A series of TPU NCs was prepared by *in situ* polymerization through the prepolymer method, including two-step reaction process as previously described[10] and as presented in Supplementary material to this paper.

Characterization

Fourier transform infrared (FTIR) spectra were acquired on a Nicolet 6700 FTIR spectrometer in attenuated total reflectance (ATR) mode as previously described.[10] The CO and NH regions in FTIR spectra were fitted by a Gaussian deconvolution technique, resulting in the locations and areas of all of these individual peaks (Table S-I of the Supplementary material).

X-ray diffraction (XRD) was conducted with the use of the HZG/4A powder diffractometer (Seifert GmbH, Germany) in the Bragg–Bretano geometry. The region of 2θ span from 4 to 40°. The wavelength X-rays used was 0.154 nm.

Morphological studies were carried out using a JEOL JSM-6460LV scanning electron microscope (SEM) at an acceleration voltage of 30 kV. The samples were cryo-fractured in liquid nitrogen and coated with a thin layer of gold prior to the measurements.

(CC) 2022 SCS.

Atomic force microscopy (AFM) characterizations were performed on an atomic force microscope (Dimension Icon, Bruker), equipped with the SSS-NCL probe, a Super Sharp Silicon^{TM}-SPM-Sensor (NanoSensors^{TM}). The AFM images of the fracture surfaces of films after previous freeze-fracturing at the temperature of liquid nitrogen were measured.

Thermogravimetric analysis (TGA) was carried out on a TA Instruments TGA Q500 thermogravimetric analyzer under nitrogen flow of 60 mL min^{-1} and from 25 to 700 °C at a rate of 5 °C min^{-1}.

Dynamic mechanical thermal properties (DMTA) were performed on an ARES G2 rheometer (TA Instruments) at a frequency of 1 Hz, strain 0.1 %, with a heating rate of 3 °C min^{-1} and in the temperature range from –135 to 250 °C. The measurements were carried out under torsion mode, using torsion fixture (rectangle) geometry.

Differential scanning calorimetry (DSC) tests were performed on an DSC, Q1000 (TA Instruments) calorimeter with a TA Instruments RCS cooling unit and from –90 to 200 °C, at a heating and cooling rate of 10 and 5 °C min^{-1}, respectively.

Static contact angle (*WCA*) was measured by a sessile drop method at 26 °C using a contact angle analyser (Krüss GmbH, Germany DSA100). Surface energy data were calculated from the contact angle values obtained using distilled water, formamide and diiodomethane and the acid–base theory for solids according to the van Oss–Chaudhury–Good approach (Supplementary material).[15]

Water absorption was investigated at room temperature by sample immersion in phosphate buffered saline (PBS, pH 7.4), for 24 h (Supplementary material). The average value of three measurements for each sample was used.

RESULTS AND DISCUSSION

The present work focused on the preparation of series of TPU NCs with different HS contents (from 20 to 55 wt. %) by *in situ* polymerization using 1 wt. % of organoclay modified by quaternary alkyl ammonium ions bearing hydroxyl groups (C30B; Fig. S-1 of the Supplementary material). The chemical structures of reactants and organoclay, as well as a simplified schematic presentation of the polymerization reaction for synthesis of TPUs, and photographs of the prepared TPU NCs are presented in Fig. S-1. The effects of HS content on structural, thermal, thermomechanical and surface properties of the TPU NCs were examined.

FTIR analysis

FTIR spectra of TPU NCs containing 1 wt. % C30B with different HS contents are shown in Fig. 1, while the band assignments are given in Table S-I of the Supplementary material. The disappearance of the –NCO stretching band at 2270 cm^{-1} confirms that all the isocyanate groups are completely consumed during the polymerization.

Namely, the NH stretching (ν(NH)) and carbonyl stretching (ν(C=O)) regions are observed at around 3330 and 1700 cm^{-1}, respectively, which are characteristic of urethane groups. In FTIR spectra, bands at 3330 cm^{-1} were due to the hydrogen-bonded N–H stretching, while free NH stretching bands at 3440 cm^{-1} were also detected in the TPU NCs' spectra. These results show the fraction of hydrogen-bonded urethane NH groups increased, but free urethane NH groups

(CC) 2022 SCS.

decreased with the increasing HS content, indicating a higher level of hydrogen bonding in TPU NCs with higher HS content (Table S-II of the Supplementary material).

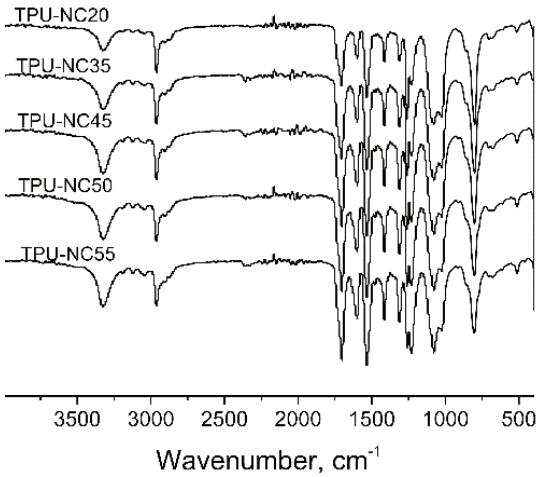

Fig. 1. FTIR spectra of TPU NCs with different hard segment content.

Carbonyl groups typically serve as proton acceptors and form hydrogen bonds with NH groups among hard segments in TPU-based NCs. Thus, the fraction of hydrogen bonded carbonyls can be used to characterize the degree of microphase separation.[16] The ordered hydrogen bonded (ν(C=O) HB-ordered), disordered hydrogen bonded (ν(C=O) HB-disordered) and free (ν(C=O) free) carbonyls in the prepared TPU NCs were observed at around 1705, 1720 and 1735 cm^{-1}, respectively.[10] In series of TPU NCs, the increase of HS content led to the rise of relative intensity of the hydrogen-bonded C=O absorption bands and reduction in the relative intensity of the free C=O absorption bands, which further showed that increasing HS content could lead to stronger HS-HS hydrogen bonding and, thus, to a more segregated structure of TPUs. In the TPU NCs, the percentage of hydrogen bonding carbonyl groups as a fraction (more than 70 %) was higher than that of free groups, so the hydrogen bonding carbonyl groups play a major role in the final materials (Table S-II). The degree of phase separation (*DPS*) data showed that for the series of TPU NCs, increasing the content of HS enhanced the phase separation from 85.5 to 93.9 % (Table S-II, Eq. (S-3), of the Supplementary material). Comparing the FTIR spectra of TPU NCs with their pure TPU[17] counterparts with the same HS content, it was found that the clay incorporation did not significantly change the relative intensities of the free or hydrogen-bonded urethane C=O bands. The DPS data showed that for TPUs with 20 or 35 wt. % of HS, adding organoclay particles did not cause significant changes in the extent of phase separation. For TPUs containing from 45 to 60 wt.

(CC) 2022 SCS.

% of HS, the incorporation of 1 wt. % of organoclay slightly enhanced the phase separation of the prepared TPU NCs, despite numerous reports suggesting that nanofillers can give rise to phase mixing.[16,18]

Our FTIR results showed the fraction of urethane carbonyl groups participating in hydrogen bonding was also higher for the TPU NCs than for the pure TPU, previously published by Pergal *et al.*[17] In a series of prepared TPU NC materials, organoclay evidently participates in hydrogen bonding between urethane carbonyl groups and $–CH_2CH_2OH$ groups inside the clay organomodifier,[12,19] but to higher extent in the case of TPU NC with higher HS content.

XRD analysis

The XRD patterns of the prepared TPU NC films are shown in Fig. S-2 of the Supplementary material. Due to the poor scattering power of the samples the data are smeared by noise of a level so high that 1 % of C30B is completely hidden in it and any systematic behaviour is hard to be seen. However, the patterns could be decomposed by fitting using the program Fityk into three peaks the position of which didn't change, but information could be obtained from their integral intensities.

The 2θ of their relevant positions were 12.22, 17.6 and 21.9°, respectively, see Fig. S-2. Their corresponding integral intensities can be seen in the Table S--III. The behaviour of the middle peak indicates that it corresponds to the amorphous halo. We can estimate the ratio of amorphous component by dividing the integral intensity of this peak by the total integral intensity. As can be seen in the Fig. S-2, the ratio of the amorphous part decreases when the ratio of the hard component increases. This agrees with the state of starting components and products forming soft and hard segments. In the diffraction patterns of TPU NCs, the amorphous halo at 17.6° corresponds to the distribution of distances of neighbouring polymer chain segments.[20] The diffraction peak observed at $2\theta = 12°$ is assigned to the internal structure of the PDMS chains. And finally, the peak at 2θ value of 21.9° corresponds to the crystalline part of the HS; the peak intensity generally increased with the rise of HS content. XRD thus confirmed the behaviour of TPU segments being considered to the hard as well as soft regions.

SEM analysis

Microstructural characterization of the prepared TPU NC materials was performed by SEM. The SEM micrographs of the cross-section of the investigated TPU NC films, at magnification 3000×, are given in Fig. S-3 of the Supplementary material. From Fig. S-3 it can be seen that the fracture surface of the TPU NCs become rougher when the organoclay was incorporated into the pure TPU matrix, previously published by Pergal *et al.*[21] The prepared TPU NC with 20 wt. % HS had a smooth surface and more homogeneous surface morphologies, when compared to other prepared TPU NCs. Therefore, the TPU NCs

(CC) 2022 SCS.

with the HS content of 35–55 wt. % have rougher and heterogeneous surface morphology, indicating the presence of more microphase separation in materials with higher HS content. The fractured-surface structure of TPU NCs was distributed with oval formations, in the range of 0.93–1.40 μm in size, composed of hard-enriched formations in TPU NCs, but they were slightly bigger in TPU NC with lower HS content. Homogeneous clay distribution was observed on all TPU NC sample surfaces, which suggested that the clay particles were uniformly dispersed within the TPUs' matrix and did not depend on HS content.

AFM

The surface topography and heterogeneity relief of the fractured TPU NCs with different HS content were examined by AFM. The 2D height and phase AFM images of TPU NCs' fractured surfaces, at both micrometer (10×10 μm^2) and nanometer scales (1×1 μm^2), are shown in Figs. 2 and S-4. The surface roughness coefficient values for 10×10 μm^2 images are given in Table S-IV.

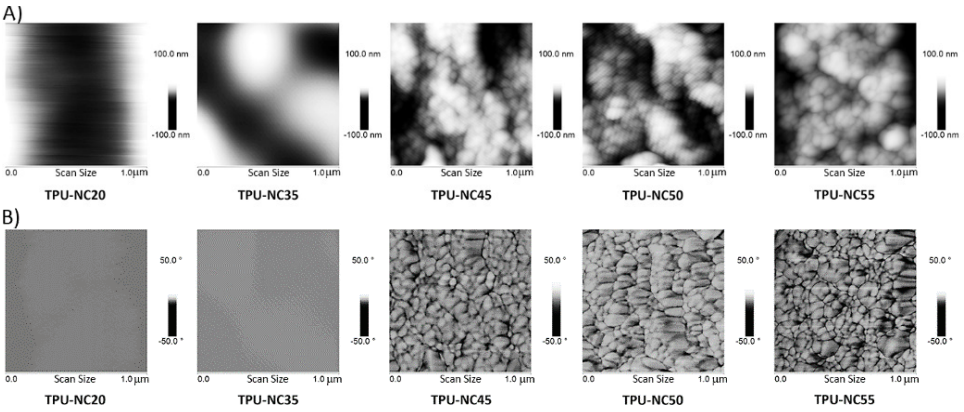

Fig. 2. A) 2D height and B) 2D phase AFM images of TPU NCs at 1×1 μm^2.

From Fig. S-4a it can be noted that the cryo-fractured reliefs of these TPU NCs show different surface morphologies dominated by the HS contents. Namely, the fractured surface of TPU NC with 20 wt. % of HS content is smoother and more homogenous than those of TPU-NC35, TPU-NC45, TPU--NC50 and TPU-NC55, where the formation of the two-phase morphology occurs. The AFM results are thus in accordance with the SEM analyses.

The roughness coefficients increased with increasing HS contents in TPU NC films (except TPU NC-55). Phase images shown in Fig. S-5b are in accordance with the μm-scale observations of height images given in Fig. S-5a, confirming the heterogeneous character of the prepared TPU NC films.

Deeper surface characterization of TPU NC surfaces was obtained based on the phase images and the phase images on the 1×1 μm^2 scale, as shown in Fig. 2.

(CC) 2022 SCS.

The phase images (Fig. 2b) give information about lighter (harder) and darker (softer) areas, originating mainly from the micro-phase separation of the soft and hard segments in TPU NCs. Both "hard-enriched formations and soft-enriched formations" were observed, and these formations appeared like clusters of soft--segment and hard-segment rich regions made from smaller building units. Rougher reliefs of TPU NCs, with the HS contents higher than 45 wt. %, were detected when compared to TPU-NC20 and TPU-NC35 films.

The materials TPU-NC20 and TPU-NC35 had a relatively homogeneous phase relief with dominating softer portions (Fig. 2b), which is in accordance with the material composition. The TPU NCs with 45, 50 or 55 wt. % of HS (TPU-NC45, TPU-NC50 and TPU-NC55) were composed of individual oval or spherical harder "nanoparticles" stuck together by the softer portion into the macroscopically compact material. These oval formations were mostly about 250 to 550 nm in TPU-NC with 45–55 wt. %, and the size of the oval formations decreased with the increasing HS content.

TGA

Thermal stability of TPU-based NCs was evaluated by TGA under a nitrogen atmosphere at a heating rate of 5 °C min^{-1}. The TGA/DTG curves of TPU NCs of different compositions are presented in Fig. 3. In Table S-V of the Supplementary material, the characteristic temperatures taken from the TGA and DTG curves are summarized: the temperatures at 5, 10 and 50 wt. % loss ($t_{5\%}$, $t_{10\%}$ and $t_{50\%}$, respectively), the maximum rate degradation temperatures (t_{max}) and the weight percent of residue. The TGA curves of TPU-based NCs indicate that the thermal degradation starts at 289–295 °C ($t_{5\%}$). The thermal stability increases with the decreasing HS content. Moreover, the thermal stability of TPU NCs was higher when compared to the pure TPU films ($t_{5\%}$, 281–286 °C),[21] suggesting some improvement in thermal stability. Temperatures at which the pure TPU films lost 10 and 50 % of weight are ranging in 293–302 °C and in 327–335 °C, respectively.[21] Thus, the TPU NCs were more thermally stable, which was expected in comparison to some previous findings[5,10,22] where an improvement in thermal stability was observed with the inclusion of clay in a polymer matrix.

The improvement in thermal stability of polymer/clay nanocomposites is attributed to the shielding effect of clay layers, which function as a barrier to the gasses and volatile degradation products.[23] The clay platelets act as heat barriers and obstacles for polymer chain motion, further stabilizing the polymer chain. The effect of mineral clay, a thermal insulator and mass transport barrier, on thermal stability can be increased by improving the dispersibility of the organoclay mineral.[8,24]

(CC) 2022 SCS.

The derivative TG analysis (DTG) was used to study the thermal degradation mechanism of TPU NCs (Fig. 3b). The DTG curves indicated that the series of TPUs NCs degraded in two (from TPU-NC35 to TPU-NC55) and three (for TPU-NC20) steps; the first step (328 to 332 °C – temperature of the first peak maximum in the corresponding DTG curve) could be attributed to the degradation of the hard segments, *i.e.*, splitting of the urethane bonds, and the second step corresponded to the decomposition of PDMS segment.[25] The DTG curve of TPU-NC20 shows t_{max} at 406 and 422 °C, as compared to other TPU NCs (only one t_{max}), due to the decomposition of PDMS block and also ethylene oxide units in the SS, a consequence of the highest SS content in this sample. For the TPU NC55, t_{max} at 506 °C is related to the decomposition of the aromatic compounds, while the second peak of degradation, corresponding to decomposition of SS, in the DTG curve for this sample did not exist due to it having the lowest SS content in the material series. In DTG curves of pure TPU films,[21] the temperatures of the first and second peaks were observed at 313–325 °C and 338–345 °C, respectively, which are lower than that in TPU NCs films (Table S-V).

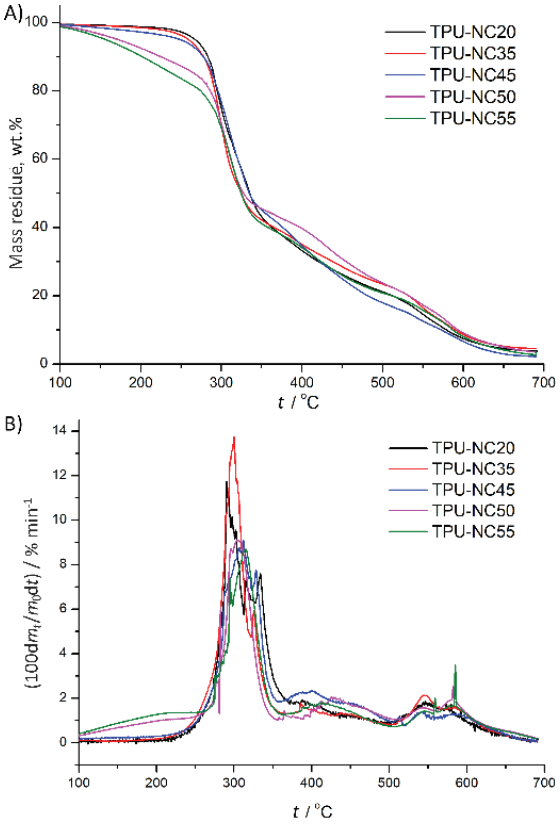

Fig. 3. A) TGA and B) DTG thermograms of TPU NCs obtained under nitrogen atmosphere.

(CC) 2022 SCS.

The results indicate an enhancement of the thermal stability of the TPU NCs upon the addition of organoclays into the polymer matrix. Based on the DTG curves, it may be concluded that the addition of clay particles with the layered structure stabilizes TPU materials and, in this case, the thermal decomposition is less influenced by the HS content. Similar stabilization effects were observed in different kinds of polyurethanes reinforced with organically modified montmorillonites.[26,27]

The residual yields of the TPU NC films at 650 °C ranged from 4.9 to 11.7 % (Table S-V) and increased with the rise of HS content. The residual yield under nitrogen originated mainly from the "organic" fraction (MDI-BD), which increased with the HS content and could be explained by the degradation mechanism of the PDMS chains under a nitrogen atmosphere that occurs after disruption of the urethane bonds. The PDMS degraded by depolymerization, giving cyclosiloxanes as the degradation products.[21]

DSC and DMTA analyses

The phase transitions in TPU NCs were examined by DMTA and DSC analyses. DMTA was performed in order to study the influence of the HS content on the viscoelastic properties of selected TPU NCs, with the HS content from 20 to 50 wt. %. Two main viscoelastic parameters were analysed: the storage modulus (G') and the damping factor (tan δ). The temperature dependences of the storage modulus and the loss factor tan δ determined by DMTA are shown in Fig. 4. Typical DMTA curves as for thermoplastic polyurethanes were found, with a t_g, rubbery plateau, melting temperature t_m, and subsequently, the flow of melted polymer.

G' and tan δ *vs.* temperature curves displayed the glass transitions which were in the range from –102 to –112 °C for TPU NCs associated with the segmental motion in the PDMS SS (t_{gPDMS}, Table S-VI). The second relaxation observed at temperatures from –5 to 5 °C (Table S-VI) is associated with the segmental relaxation of a mixed soft phase consisting of the PDMS end group segments and some dissolved hard segments.[28] Therefore, this peak might be in this case related to some relaxation at the hard-soft segment interface.

From storage modulus curves, it was observed that G' increases accordingly with the HS content, which is a typical behaviour found in semi-crystalline TPUs. The storage modulus for TPU NCs increased with the HS content as a consequence of the higher degree of physical crosslinking and better microphase separation (Table S-VI). Such increase is also accompanied by the tan δ maximum shift to higher temperatures, which took place in our case as well. In the paper published by Poręba *et al.*,[4] on polycarbonate-based PUs with hexamethylene diisocyanate-1,4-butanediol hard segments, they observed the same trend. However, they could not detect or distinguish any peaks corresponding to the

(CC) 2022 SCS.

hard segment t_g, even if the degree of crystallinity was lower than that of the HS content. In our case, it seems that this transition, also in our present study, was rather related to the hydrogen-bond disruption (t_{HBD}), or some other short-range interactions (dipol–dipol or van der Waals forces), than to the t_g of the hard MDI--BD segments (Table S-VI).[4] Another thing is that if the polymer is in the glassy state due to hard segments below 75–125 °C, the storage modulus should be of similar value for all the samples, irrespective of the composition.[4]

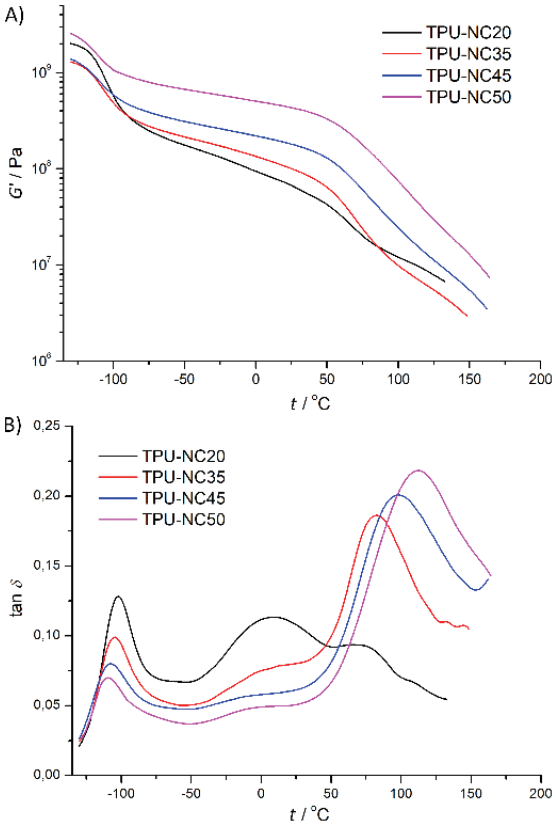

Fig. 4. A) Storage modulus and B) tan δ of TPU NCs *versus* temperature.

The DSC thermograms obtained during the second heating and cooling run are shown in Fig. S-5, and the values of the interfacial relaxation (t_{rel}), the melting temperature (t_{mHS}), the enthalpy of melting (ΔH_{mHS}), the crystallization temperature (t_{cHS}), the enthalpy of crystallization (ΔH_{cHS}) and the degree of crystallinity (X_c) are presented in Table S-V. The minimum of the first endothermic event (Fig. S-5a)) (t_{rel}) assigned to the relaxation of the soft chain segments in the diffused interfacial region,[4] was located between 60 and 112 °C for all samples, and the values for the NCs were higher by a magnitude of 28–64 °C as compared to pure TPUs.[17] The relaxation enthalpy change (ΔH_{rel}) decreased

(CC) 2022 SCS.

from 1.79 to 0.98 J g^{-1} with the increasing HS content. Various endotherms in this region have been found in similar TPU-based materials and they have been attributed to different processes.[4] A small endothermic event in this region detected on DSC curves (Fig. S-5a) was noticeable for all materials. The existence of a diffused interfacial phase between SS and HS resulted from the order–disorder relaxation of the TPU chain segments in the interface, or it suggests melting of noncrystalline HS domains in this region.[4]

The transition was in the temperature region from 153 to 206 °C detected by DSC, and it is connected with the melting temperature of HS (t_{mHS}). The multiple melting peaks which occurred in the DSC thermogram of the material with the highest HS content in our series of TPU NCs (*i.e.*, TPU-NC55) indicate the presence of crystallites of different size and perfection, due to the irregularity of the length of the hard MDI-BD segment, or to the effect of crystal reorganization during heating.[25]

A similar trend was observed for thermal transitions determined by DSC and DMTA. It was observed that values of t_{gPDMS} decrease, while t_{mHS} values increase with the HS content. The obtained results showed that organoclay nanoparticles interact with hard and soft segments. The degree of crystallinity (X_c) was calculated from the values of enthalpies of melting and comparing to the heat of melting of 100 % crystalline MDI-BD homopolymer (91.2 J g^{-1}).[25] The degree of crystallinity of TPU NCs (from 4.6 to 9.4 %; Table S-V) is lower in comparison with series of pure TPUs.[21] The values of X_c ranged from 4.3 to 28.5 % for the pure TPU films.[21] The decrease in degree of crystallinity of TPU NCs could relate to the interaction of the organoclay particles with the hard segments, which makes the packing of these domains difficult.[10]

Water contact angle and surface free energy determination

The results of surface free energy (γ), which is important for coating applications, are presented in Table I. Surface free energy and its components were calculated using the van Oss–Chaudhury–Good approach.[15] The obtained results showed that with increasing HS content, the surface free energy of TPU NCs became higher. Increasing of γ values is caused mainly by the long distance interactions between hard and soft segments γ_S^{LW}, which result from dispersion interactions of polymer chains, and also slightly from the polar interactions between functional groups of polyurethane γ_S^{AB}. The contributions from the electron-acceptor interaction slightly increased for the series of TPU NCs, while the contributions of electron-donor interaction did not change for the TPU NCs with the increasing HS content.

The water contact angles of the TPU NCs were in the range from 91.3 to 103.7°, and these values were higher than 90°, indicating the presence of hydrophobic surfaces on all prepared TPU NCs. The hydrophobicity of the TPU NC

(CC) 2022 SCS.

films increased with the decreasing HS content, which is a consequence of the hydrophobic character of soft PDMS segments. Depending on the HS content, γ varied in a wide range of 17.7–24.9 mJ m^{-2}. The obtained results showed that the obtained TPU NCs have low values of surface free energy when compared to similar polyurethane materials presented in the literature,[29] suggesting good hydrophobicity characteristics of the prepared TPU NC films.

TABLE I. Static water contact angle (θ_1 / °), formamide contact angle (θ_2 / °), diiodomethane contact angle (θ_3 / °), surface free energy (γ / mJ m^{-2}) and its components of the prepared TPU NCs; mean values in the same column with different superscript are statistically different at $p \leq 0.05$ level, according to post hoc Tukey's HSD test; values are given with their standard deviations

Material	θ_1	θ_2	θ_3	γ_S^{LW}	γ_S^{AB}	γ_S^+	γ_S^-	γ
TPU-NC20	103.7±5.6^c	92.7±3.9^b	84.7±2.8^b	15.3±0.4^a	2.4±0.1^a	1.0±0.0^a	1.5±0.1^a	17.7±0.7^a
TPU-NC35	100.6±3.9^c	90.6±5.3^b	81.3±3.1^{ab}	16.8±0.6^b	2.9±0.1^c	1.2±0.0^b	1.8±0.0^b	19.7±0.3^b
TPU-NC45	97.8±2.1^b	86.4±4.3^{ab}	79.5±2.6^b	17.7±1.0^{bc}	2.7±0.0^b	1.0±0.1^a	1.9±0.1^{bc}	20.5±0.1^c
TPU-NC50	96.0±3.9^b	84.0±5.2^a	77.9±2.6^b	18.6±1.1^c	2.7±0.2^b	1.0±0.0^a	2.0±0.1^c	21.4±0.3^d
TPU-NC55	91.3±2.7^a	81.5±2.9^a	72.8±3.7^a	21.3±0.2^d	3.6±0.2^d	1.2±0.0^b	2.7±0.1^d	24.9±0.3^e

Water absorption

The results listed in Table S-IV show that the weight percent of the absorbed water for TPU NCs after 24 h was between 0.5 and 1.1. These results suggest that with the HS content decrease, the water absorption becomes lower. This may be attributed to the hydrophobic character of PDMS and its surface activity.[29] Namely, PDMS segments can migrate to the surface of TPU NCs due to their lower surface energy in comparison to the surface energy of TPU. The obtained values of water absorption for TPU NCs were slightly lower as compared to pure TPUs, indicating higher hydrophobicity. The values of water absorption of pure TPU films ranged from 0.74 to 1.61 wt. %.[21] The TPU NCs were more hydrophobic than the pure TPUs due to the incorporation of organoclay layers that act as barrier. The enhancement of water resistance for TPU NC films and good hydrophobicity were observed based on water absorption and contact angle measurements.

CONCLUSION

The TPU NCs were synthesized by *in situ* polymerization with different ratios of hard/soft segments and their functional properties mainly depended on their HS contents. FTIR spectroscopy analysis showed that there was a multiple hydrogen bonding in the polyurethane, but the –NH and carbonyl groups are mainly in a hydrogen bonded state. FTIR, AFM and SEM results suggested an enhanced microphase separation between soft and hard segments for TPU NCs with increasing HS content. Thermal stability increases with the decreasing HS

(CC) 2022 SCS.

content, as do melting temperatures and degree of crystallinity, but the glass transition of PDMS segments decrease with the increasing HS content. Organoclay interacts with both hard and soft segments. Surface free energy values of TPU NCs increased with the rise of HS content in the range of 17.7 to 24.9 mJ m^{-2}. Thus, the prepared TPU NC films were hydrophobic.

The proper composition improved the selected functional properties of the TPU NCs. The improvement of thermomechanical properties were observed up to 50 wt. % of HS (except for the material with 55 wt. % of HS, which is a brittle material). From the potential practical use, the best combination of functional (thermosmechanical, thermal, water resistance and surface) properties was seen for the TPU NC films containing 50 wt. % HS. All these findings provide practical guidance for the modulation of the composition for the synthesis of advanced TPU-based composite materials. Taking into account composition, structure and properties of the TPU NCs, they can be considered as a main target as promising coatings for biomedical applications.

SUPPLEMENTARY MATERIAL

Additional data and information are available electronically at the pages of journal website: https://www.shd-pub.org.rs/index.php/JSCS/article/view/11708, or from the corresponding author on request.

Acknowledgments. This work was financially supported by the Ministry of Education, Science and Technological Development of the Republic of Serbia (Grant No: 451-03-68/2022-14/200026) and by the Czech Science Foundation (Grant Agency of the Czech Republic, Project No. 18-03932S). The authors are grateful to Dr Rafał Poręba (Institute of Macromolecular Chemistry CAS, Prague, Czech Republic) for DMTA measurements.

ИЗВОД

НАНОКОМПОЗИТИ НА БАЗИ ТЕРМОПЛАСТИЧНОГ ЛИНЕАРНОГ ПОЛИ(УРЕТАН-СИЛОКСАН)А И ОРГАНОГЛИНЕ: УТИЦАЈ САСТАВА НА СВОЈСТВА

МАРИЈА В. ПЕРГАЛ[1], САЊА ОСТОЈИЋ[2], MILOŠ STEINHART[3], ИВАН С. СТЕФАНОВИЋ[1], ЛАТО ПЕЗО[2] и MILENA ŠPÍRKOVÁ[3]

[1]Универзитет у Београду, Институт за хемију, технологију и металургију, Институт од националног значаја за Републику Србију, Његошева 12, 11000 Београд, [2]Институт за општу и физичку хемију, Универзитет у Београду, Студентски трг 12–16, 11000 Београд и [3]Institute of Macromolecular Chemistry CAS (IMC), Heyrovsky Sq. 2, 16206 Prague 6, Czech Republic

Термопластични поли(уретан-силоксан)/органоглина нанокомпозити (TPU NCs) са различитим садржајем тврдих сегмената (20–55 теж. %) припремљени су *in situ* полимеризацијом у присуству органски модификованог монтморилонита као нанопуниоца (Cloisite 30B; 1 теж. %). Као меки сегмент коришћен је хидроксиетоксипропил терминирани поли(диметилсилоксан), а као компоненте тврдог сегмента коршћени су 4,4'-метилендифенилдиизоцијанат и 1,4-бутандиол. Проучавање утицаја садржаја тврдог сегмента на функционална својства TPU NCs је испитивано FTIR спектроскопијом, дифракцијом X-зрака (XRD), микроскопијом атомских сила (AFM), скенирајућом електронском микроскопијом (SEM), динамичко механичко термичком анализом (DMTA), диференцијално скенирајућом калориметријом (DSC), термогравиметријском анализом

(CC) 2022 SCS.

(TGA), тестовима одређивања контактног угла са водом и апсорпције воде. Резултати су показали да TPU NCs са већим садржајем тврдих сегмената показују веће вредности степена микрофазне сепарације, температуре топљења тврдих сегмената, степена кристалиничности, модула сачуване енергије (осим за TPU NC-55), али нижу термичку стабилност и хидрофобност. TPU NC филмови су били хидрофобни и њихова површинска енергија је била у опсегу од 17,7 до 24,9 mJ m^{-2}. Овај рад истиче како би се променом састава у TPU NCs подешавала функционална својства и обезбедило додатно подешавање састава за дизајнирање напредних TPU NC материјала за специјалне биомедицинске примене.

(Примљено 23. фебруара, ревидирано 10. априла, прихваћено 19. априла 2022)

REFERENCES

1. Z. Petrović, J. Ferguson, *Prog. Polym. Sci.* **16** (1991) 695 (https://doi.org/10.1016/0079-6700(91)90011-9)
2. I. Yilgör, J. E. McGrath, *Adv. Polym. Sci.* **86** (1988) 1 (https://doi.org/10.1007/BFb0025274)
3. Y. Andriani, I. C. Morrow, E. Taran, G. A. Edwards, T. L. Schiller, A. F. Osman, D. J. Martin, *Acta Biomater.* **9** (2013) 8308 (https://doi.org/10.1016/j.actbio.2013.05.021)
4. R. Poręba, M. Špírkova, L. Brožová, N. Lazić, J. Pavlićević, A. Strachota, *J. Appl. Polym. Sci.* **127** (2013) 329 (https://doi.org/10.1002/app.37895)
5. M. Alexandre, P. Dubois, *Mater. Sci. Eng. Rep.* **28** (2000) 1 (http://dx.doi.org/10.1016/S0927-796X(00)00012-7)
6. S. Taheri, G. M. M. Sadeghi, *Appl. Clay Sci.* **114** (2015) 430 (https://doi.org/10.1016/j.clay.2015.06.036)
7. J. Pavličević, M. Špírková, O. Bera, M. Jovičić, B. Pilić, S. Baloš, J. Budinski-Simendić, *Compos., B* 45 (2013) 232 (https://doi.org/10.1016/j.compositesb.2012.09.018)
8. C. B. Godiya, E. Marcantoni, B. Dunjić, M. Tomić, M. S. Nikolić, J. Maletaškić, J. Djonlagić, *Polym. Bull.* **78** (2021) 2911 (https://doi.org/10.1007/s00289-020-03248-7)
9. Y. W. Chen-Yang, Y. K. Lee, Y. T. Chen, J. C. Wu, *Polymer* **48** (2007) 2969 (https://doi.org/10.1016/j.polymer.2007.03.024)
10. M. V. Pergal, I. S. Stefanović, R. Poręba, M. Steinhart, P. Jovančić, S. Ostojić, M. Špírková, *Ind. Eng. Chem. Res.* **56** (2017) 4970 (https://doi.org/10.1021/acs.iecr.6b04913)
11. I. S. Stefanović, M. Špírková, S. Ostojić, P. Stefanov, V. B. Pavlović, M. V. Pergal, *Appl. Clay Sci.* **149** (2017) 136 (https://doi.org/10.1016/j.clay.2017.08.021)
12. A. Pattanayak, S. C. Jana, *Polymer* **46** (2005) 3275 (https://doi.org/10.1016/j.polymer.2005.02.081)
13. E. H. Jeong, J. Yang, J. H. Hong, T. G. Kim, J. H. Kim, J. H. Youk, *Eur. Polym. J.* **43** (2007) 2286 (https://doi.org/10.1016/j.eurpolymj.2007.03.015)
14. X. Meng, Z. Wang, H. Yu, X. Du, S. Li, Y. Wang, Z. Jiang, Q. Wang, T. A. Tang, *Polymer* **50** (2009) 3997 (https://doi.org/10.1016/j.polymer.2009.06.042)
15. C. J. Van Oss, R. J. Good, M. K. Chaudhury, *Langmuir* **4** (1988) 884 (https://doi.org/10.1021/la00082a018)
16. J. Pavličević, M. Špírková, O. Bera, M. Jovičić, B. Pilić, S. Baloš, J. Budinski-Simendić, *Compos., B* **60** (2014) 673 (https://doi.org/10.1016/j.compositesb.2014.01.016)
17. M. V. Pergal, J. Nestorov, G. Tovilović, S. Ostojić, D. Gođevac, D. Vasiljević-Radović, J. Djonlagić, *J. Biomed. Mater. Res., A* **102** (2014) 3951 (https://doi.org/10.1002/jbm.a.35071)

(CC) 2022 SCS.

18. S. Shi, D. Shen, T. Xu, Y. Zhang, *Comp. Sci. Techol.* **164** (2018) 17 (https://doi.org/10.1016/j.compscitech.2018.05.022)
19. C.-H. Wang, Y.-T. Shieh, S. Nutt, *J. Appl. Polym. Sci.* **114** (2009) 1025 (https://doi.org/10.1002/app.30560)
20. M. Špírková, R. Poręba, J. Pavličević, L. Kobera, J. Baldrian, M. Pekárek, *J. Appl. Polym. Sci.* **126** (2012) 1016 (https://doi.org/10.1002/app.36993)
21. M. V. Pergal, I. S. Stefanović, D. Gođevac, V. V. Antić, V. Milačić, S. Ostojić, J. Rogan, J. Djonlagić, *J. Serb. Chem. Soc.* **79** (2014) 843 (http://doi.org/10.2298/JSC130819149P)
22. S. Sinha Ray, M. Okamoto, *Prog. Polym. Sci.* **28** (2003) 1539 (https://doi.org/10.1016/j.progpolymsci.2003.08.002)
23. A. Leszczyńska, J. Njuguna, K. Pielichowski, J. R. Banerjee, *Thermochim. Acta* **453** (2007) 75 (https://doi.org/10.1016/j.tca.2006.11.002)
24. C. M. L. Preston, G. Amarasinghe, J. L. Hopewell, R. A. Shanks, Z. Mathys, *Polym. Degrad. Stab.* **84** (2004) 533 (https://doi.org/10.1016/j.polymdegradstab.2004.02.004)
25. M. V. Pergal, V. V. Antić, G. Tovilović, J. Nestorov, D. Vasiljević-Radović, J. Djonlagić, *J. Biomater. Sci. Polym., E* **23** (2012) 1629 (https://doi.org/10.1163/092050611X589338)
26. A. K. Barick, D. K. Tripathy, *Mater. Sci. Eng., A* **527** (2010) 812 (https://doi.org/10.1016/j.msea.2009.10.063)
27. R. Poręba, M. Špirková, J. Pavličević, J. Budimski-Simendić, K. M. Szécsényi, B. Helló, *Compos., B* **58** (2014) 496 (https://doi.org/10.1016/j.compositesb.2013.11.006)
28. T. Choi, J. Weksler, A. Padsalgikar, J. Runt, *Polymer* **51** (2010) 4375 (https://doi.org/10.1016/j.polymer.2010.07.030)
29. P. Majumdar, D. C. Webster, *Macromolecules* **38** (2005) 5857 (https://doi.org/10.1021/ma050967t).

(CC) 2022 SCS.

Journal of the Serbian Chemical Society
JSCS@tmf.bg.ac.rs • www.shd.org.rs/JSCS
J. Serb. Chem. Soc. *87* (10) S388–S394 (2022) *Supplementary material*

SUPPLEMENTARY MATERIAL TO

Nanocomposites made from thermoplastic linear poly(urethane-siloxane) and organoclay: Composition impact on the properties

MARIJA V. PERGAL[1]*, SANJA OSTOJIĆ[2], MILOŠ STEINHART[3], IVAN S. STEFANOVIĆ[1], LATO PEZO[2] and MILENA ŠPÍRKOVÁ[3]

[1]*University of Belgrade, Institute of Chemistry, Technology and Metallurgy, National Institute of the Republic of Serbia, Njegoševa 12, 11000 Belgrade, Serbia,* [2]*Institute of General and Physical Chemistry, University of Belgrade, Studentski trg 12–16, 11000 Belgrade, Serbia and* [3]*Institute of Macromolecular Chemistry CAS (IMC), Heyrovsky Sq. 2, 16206 Prague 6, Czech Republic*

J. Serb. Chem. Soc. *87* (10) (2022) 1203–1218

Preparation of TPU NCs

The TPU NCs were synthesized under the following polymerization conditions:[10] the molar ratio of NCO/OH groups was 1.05/1.0, the amount of the catalyst was 0.15 mol.% $Sn(Oct)_2$/PDMS macrodiol, and a mixture of 1/1, *V*/*V* DMAc/THF was used. For the clay dispersion in DMAc/THF, intensive mixing with a magnetic stirrer (1000 rpm) for 10 h at room temperature and for 2 h at 50 °C, followed by sonication at 25 ºC for 1 h were applied. During the first step, a predetermined amount of clay dispersion was added dropwise into the PDMS macrodiol solution of DMA_C/THF in a 100 mL flask equipped with a mechanical stirrer, an argon inlet, a dropping funnel and a reflux condenser. This reaction mixture was stirred for 1 h at room temperature under an argon atmosphere. Then MDI was added to the flask and catalyst $Sn(Oct)_2$ solution and the mixture reacted at 40 °C for 30 minutes under continuous stirring to give NCO-terminated prepolymer. During the second step, a solution of BD in DMAc/THF (1/1, *V*/*V*) was charged into the prepolymer and the reaction mixture was stirred and kept at 50 °C for 10 h. Then, sonication (30 minutes, at 25 ºC) was performed to get better dispersion of organoclay in final TPU NCs. Finally, the resultant dispersion was cast into Teflon moulds and then heated in an oven at 40 °C for 24 h. Solvent residue was evaporated by drying in a vacuum oven (66.7 Pa) at 60 °C for 24 h to constant mass. All TPU NC films were allowed to age at room temperature in desiccators for at least 2 weeks prior the characterization.

* Corresponding author. E-mail: marijav@chem.bg.ac.rs

Available on line at www.shd.org.rs/JSCS/
(CC) 2022 SCS.

Surface energy calculation

The surface free energy of TPU and TPU-NCs was calculated by:[15]

$$\gamma_{LV}(1+\cos\theta) = 2\sqrt{\gamma_S^{LW}\gamma_{LV}^{LW}} + \sqrt{\gamma_S^{+}\gamma_{LV}^{-}} + \sqrt{\gamma_S^{-}\gamma_{LV}^{+}} \quad \text{(S-1)}$$

where θ is the contact angles of distilled water, formamide and diiodomethane on the surface of TPU NCs; γ_S, γ^{LW}, γ^{AB} represent the surface free energy, dispersion component and polar component, respectively; γ^{+} and γ^{-} represent the Lewis acid parameter and the Lewis base parameter of the surface free energy, respectively; γ_{LV} is the surface tension of the test liquid. Values of surface tension for distilled water, formamide and diiodomethane needed to solve these equations are listed in previously published papers.[1-3] The total surface free energy, as well as its dispersive and polar components, could be determined by solving eq. S-1, because $\gamma_{LV}{}^{LW}$, $\gamma_{LV}{}^{+}$ and $\gamma_{LV}{}^{-}$ are all available.

Water absorption calculation

The weight percent of the water absorption was calculated by:

$$\text{Water absorption} = \frac{w_W - w_{W_0}}{w_{W_0}} 100 \quad \text{(S-2)}$$

where, w_w is the weight of the fully hydrated sample and w_{W0} is the weight of the dried sample.

Degree of phase separation calculation

The degree of phase separation (DPS) in TPU NCs can be calculated by using:[10,16]

$$\text{DPS} = \frac{A_{\text{bonded.tot}}}{A_{\text{tot}}} = \frac{A_{1703} + A_{1715}}{A_{1703} + A_{1715} + A_{1733}} \quad \text{(S-3)}$$

(CC) 2022 SCS.

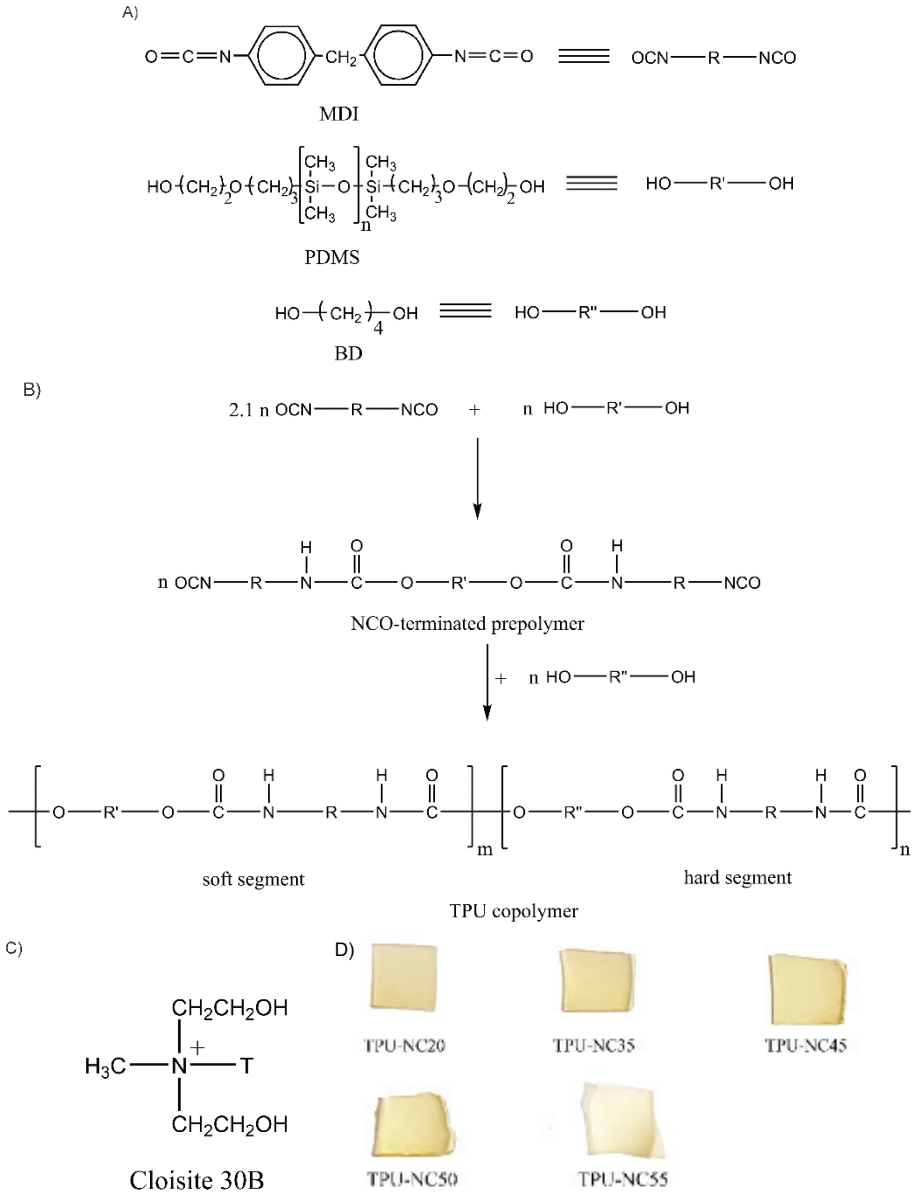

Fig. S-1. A) Chemical structures of starting reactants; B) schematic representation of synthesis of TPU based on PDMS as soft segment and MDI-BD as hard segment; C) Cloisite 30B clay modifier (methyl-tallow-bis-2-hydroxyethyl quaternary ammonium salt) attached on negatively charged clay nanolayers, T is tallow (~65 % C18, ~30 % C16, ~5 % C14) and D) photographs of the prepared TPU NC films.

(CC) 2022 SCS.

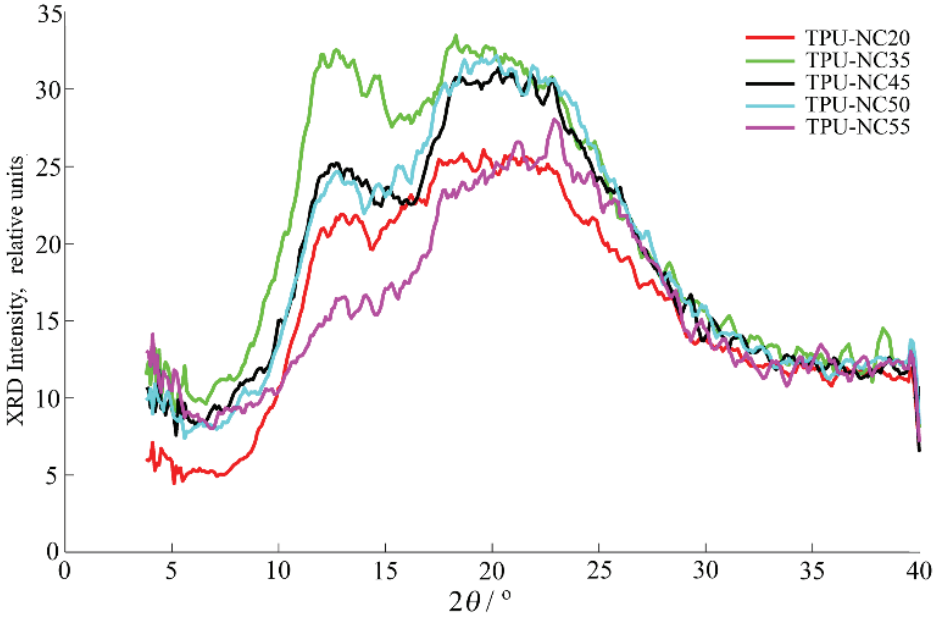

Fig. S-2. WAXS patterns of TPU NCs

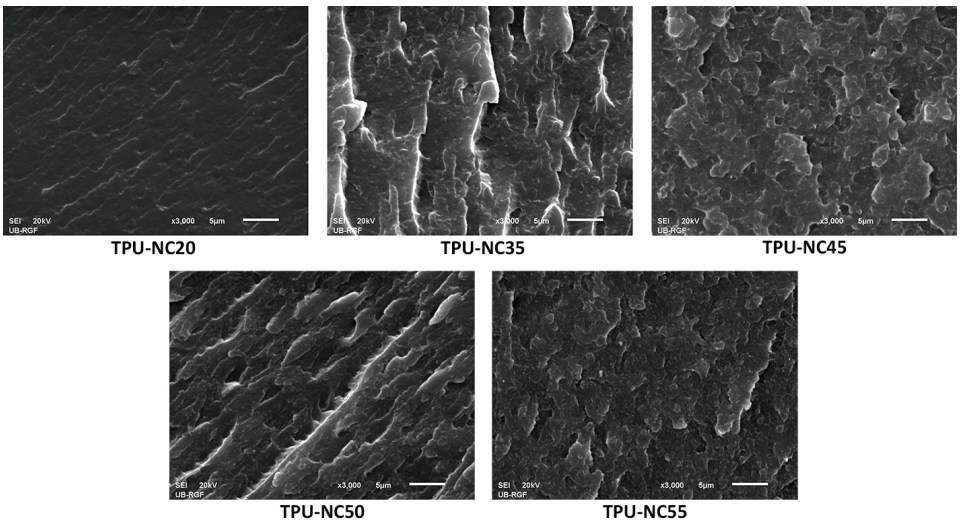

Fig. S-3. SEM images of fractured surfaces of TPU NC films at magnification ×3000.

(CC) 2022 SCS.

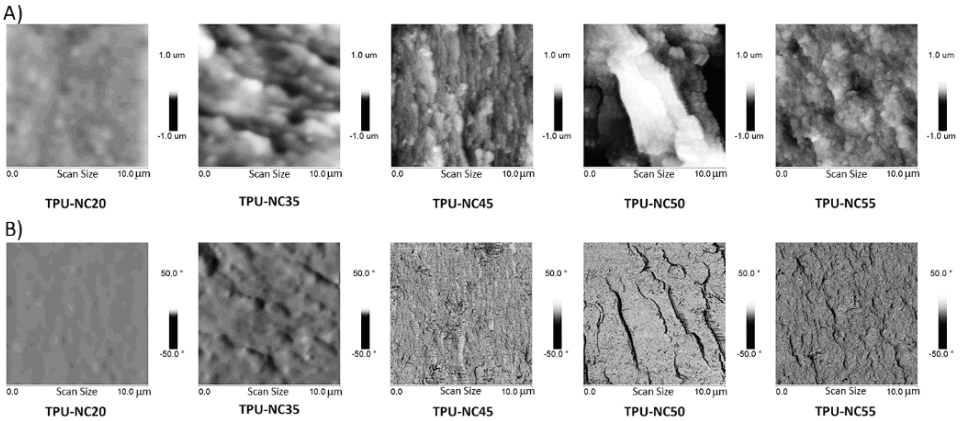

Fig. S-4. (a) 2D height and (b) 2D phase AFM images of TPU NCs at 10 × 10 μm^2.

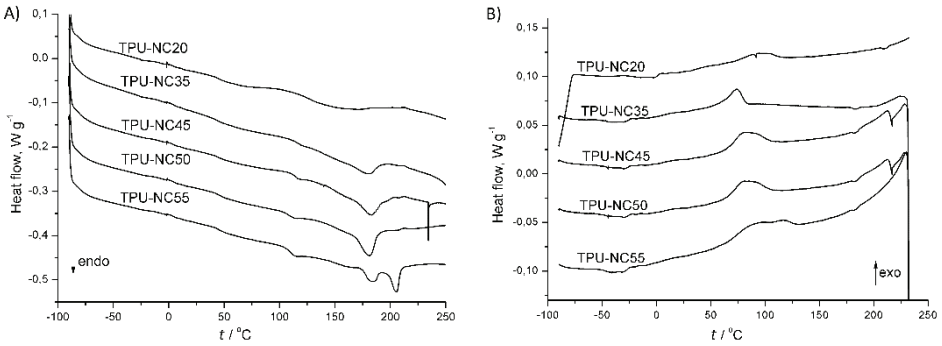

Fig. S-5. DSC curves of TPU NCs obtained during the second heating (a) and cooling (b) run.

Table S-I. Band assignments in the FTIR spectra of TPU NCs

ν / cm^{-1}	Band assignments
3310	stretching vibrations of hydrogen-bonded urethane N-H groups
2960	asymmetric stretching vibrations of CH_2 groups
2900	symmetric stretching vibrations of CH_2 groups
1735	stretching vibrations of free urethane C=O groups
1720	stretching vibrations of disordered urethane C=O groups
1705	stretching vibrations of hydrogen-bonded urethane C=O groups in hard domains
1590	C=C stretching vibrations in the aromatic rings
1530	amide II vibrations
1230	amide III vibrations
1105	stretching vibrations of C-O-C and Si-O-Si bands
1010	stretching vibrations of C-O-C and Si-O-Si bands
800	rocking vibration of C-H in $SiCH_3$
523	bending vibration of Si–O–Al
461	rocking vibration of Si–O–Si

(CC) 2022 SCS.

Table S-II. Deconvolution results of TPU NCs, determined from FTIR spectra

Material	Fraction, %					DPS, %
	$(C=O)_{free}$	$(C=O)_{HB\text{-}disordered}$	$(C=O)_{HB\text{-}ordered}$	NH_{HB}	NH_{free}	
TPU-NC20	14.5	15.1	70.4	84.3	15.7	85.5
TPU-NC35	13.2	10.6	76.2	88.9	11.1	86.8
TPU-NC45	8.1	9.4	82.5	92.4	7.6	91.9
TPU-NC50	6.9	9.1	84.0	94.5	5.5	93.1
TPU-NC55	6.1	7.2	86.7	94.9	5.1	93.9

Table S-III. Integral intensities of the three peaks into which the XRD data could be decomposed

Material	Integral intensity, arbitrary units			Amorphous ratio, %
	Peak 1-12.22°	Peak 2-17.6°	Peak 3-21.9°	
TPU-NC20	44.0	107.9	521.0	16
TPU-NC35	54.6	192.5	269.8	37
TPU-NC45	51.8	88.4	395.7	17
TPU-NC50	48.2	113.7	493.4	17
TPU-NC55	10.5	3.46	192.6	2

Table S-IV. Surface roughness determined by AFM and water absorption values of TPU NCs

Material	Surface area, μm^2	R_q^* / nm	R_a^{**} / nm	R_{max}^{***} / nm	Water absorption, wt.%
TPU-NC20	100	14.4	10.8	105	0.52±0.02
TPU-NC35	101	47.1	35.8	340	0.69±0.03
TPU-NC45	106	56.6	42.8	505	0.70±0.02
TPU-NC50	113	255	210	1629	0.97±0.02
TPU-NC55	107	59.9	46.2	558	1.11±0.03

Surface area: the total area of examined sample surface (the three-dimensioned area of a given region expressed as the sum of the area of all the triangles formed by three adjacent data points); R_q^*(rms): the standard deviation of the Z values for height images are nm and degrees for phase images within the given area; R_a^{**} (mean roughness): the mean value of the surface relative to the center place; R_{max}^{***} (max height): the difference in height between the highest and lowest points on the surface relative to the mean plane; mean: the average of all Z values within the enclosed area; Water absorption values are given with their standard deviations.

Table S-V. TGA and DSC results of the prepared TPU NCs

Material	t / °C				Residue yield at 650 °C, %	t / °C		ΔH_m / J g^{-1}	t_{cHS} / °C	ΔH_c / J g^{-1}	X_c / %
	$t_{5\%}$	$t_{10\%}$	$t_{50\%}$	t_{max}		t_{rel}	t_{mHS}				
TPU-NC20	295	305	344	328/406/422	4.9	60	153	4.2	94	3.0	4.6
TPU-NC35	295	306	341	329/460	5.5	109	180	6.2	101	3.4	6.8
TPU-NC45	293	306	339	330/435	8.5	110	183	8.3	107	5.8	9.1
TPU-NC50	289	306	341	332/463	9.0	110	182	8.6	115	6.7	9.4
TPU-NC55	288	304	339	330/506	11.7	112	184/206	8.4	119	7.5	9.2

(CC) 2022 SCS.

Table S-VI. Storage modulus and phase transitions of TPU NCs

Material	G' at 25 °C / MPa	$t_{gPDMS}^{\tan\delta}$ / °C	$t_2^{\tan\delta}$ / °C	$t_{HBD}^{\tan\delta}$ / °C
TPU-NC20	67	-102	5	75
TPU-NC35	100	-104	1	82
TPU-NC45	180	-109	-3	97
TPU-NC50	340	-112	-5	112

(CC) 2022 SCS.

Journal of the Serbian Chemical Society
JSCS@tmf.bg.ac.rs • www.shd.org.rs/JSCS
J. Serb. Chem. Soc. *87* (10) 1219–1235 (2022)
JSCS–5589
Original scientific paper
Published 26 August 2022

The improved diesel-like fuel from upgraded tire pyrolytic oil

UFUK SANCAR VURAL[1]*, SABAN UYSAL[2] and ABDULLAH YINANC[3]

[1]Pasabayır Mh. Mehmetcik Cd. 77/16, Bandirma, Balikesir, Turkey, [2]Karabuk University, Faculty of Science, Department of Chemistry, Karabuk, Turkey and [3]Tekirdag Namık Kemal University, Corlu Vocational School of Technical Sciences, Corlu, Tekirdag, Turkey

(Received 1 November 2021, revised 7 June, accepted 11 June 2022)

Abstract: Tire pyrolytic oil (TPO) obtained from thermal pyrolysis of scrap tires is not a diesel equivalent fuel which can be used directly in vehicles due to its high density, viscosity, sulfur content, low flash point and low cetane index. It can only be used in a limited way by mixing with diesel fuel (DF) in amounts less than 30 %. In this study, the pyrolysis of scrap tires was carried out at a heating rates of 5 and 10 °C min^{-1} in the range of 450–600 °C, using a mixture of hierarchical zeolite (HZSM-5), mesoporous silica (MCM-41) and quicklime (CaO) as the catalyst. The obtained TPO and catalytic pyrolytic oil (CPO) were upgraded by pre-treatment, and distillation consisting of a mixture of Cu(I)--loaded mesoporous aluminosilicate (Cu(I)–MAS) and MCM-41, desulfurization and decolourization steps, respectively. To obtain diesel-like fuel, the upgraded catalytic pyrolytic oil (UCPO) and biodiesel (PBD) obtained from palm oil were blended in certain proportions. Density, viscosity, flash point and cetane index of the obtained diesel-like fuels were found within the limit values of diesel fuel.

Keywords: desulfurization; mesoporous zeolite; microporous zeolite; catalytic pyrolysis; thermal pyrolysis.

INTRODUCTION

The amount of tires produced worldwide is over 1.5 billion tons, expired tires are replaced with new ones and stored as scrap or waste.[1,2] The rain water, which accumulates on the surfaces and interiors of scrap tires which are left indiscriminately in the environment becomes canter of biological life for pests such as bacteria and harmful insects. Scrap tires released into the environment are dangerous for human life and cause the spreading of infectious diseases. Tire management systems have been established and action plans have been prepared to combat scrap tires in developed countries.[3,4] Today, five different methods in waste management draw attention to prevent waste tires from accumulating in

* Corresponding author. E-mail: usvural@gmail.com
https://doi.org/10.2298/JSC211108048V

Available on line at www.shd.org.rs/JSCS/
(CC) 2022 SCS.

the environment. These encompass: *i*) reduction, improving the physicochemical methods used in tire manufacture to increase tire life;[5,6] *ii*) reuse of tires by coating or production of raw materials from tires by chemical or thermochemical methods;[7–9] *iii*) recovery, direct burning of tires as an energy source;[10,11] *iv*) recycling, mechanical recovery to produce industrial material (ground rubber), or thermal recovery to obtain fuel;[12,13] *v*) regulation, landfill of tires.[14,15]

All these solution methods still have not reached the capacity to reduce the amount of scrap tire accumulation. The most striking of these methods is the pyrolysis method of scrap tires, which is among the recycling methods. High market demand fuel and pyrolytic carbon black are produced in the pyrolysis method. However, low quality pyrolytic oils and pyrolytic carbon black obtained by pyrolysis of scrap tires are not yet suitable for market demand.[16] Therefore, improving the quality of the products obtained from pyrolysis in a way that will respond to the market demand will pave the way for recycling methods, reduce the amount of scrap tire accumulation and will be a prominent action plan in tire management systems.

The endothermic thermal decomposition process in which rubber, plastic, coal, heavy oils and similar hydrocarbons transform into solid residue (pyrolytic carbon black), liquid oil (pyrolytic oil) and combustible gases (pyrolytic gas) in an oxygen-free environment at high temperatures is called pyrolysis.[17] In general, 40–55 % pyrolytic oil (TPO), 30–40 % pyrolytic carbon black (pCb) and 10–20 % pyrolytic gases are obtained from the pyrolysis of scrap tires. In the pyrolysis process, variables such as reactor type, temperature, heating rate, catalyst, retention time, feed size of the raw material and flow rate of the carrier inert gas are the most important factors that determine the yield, physical and chemical structure of pyrolytic products.

Pyrolysis process of waste tire

Al-Saleh[18] and Aylon[19] comparatively explained that fixed bed reactors (FBR), rotary kiln reactors and fluidized bed reactors are the most commonly used reactor models for the pyrolysis of scrap tires. Fixed bed reactors are slow pyrolysis model with long residence time (minutes to hours) and low heating rate. Since there is no mixing, homogeneous heat distribution and homogeneous catalyst distribution cannot be achieved in the reactor. Tire processing capacity is low due to the problem of heat transfer to the inner parts of the reactor. Since mechanical problems are experienced due to rubber wires in stirred FBR reactors, it is not preferred in applications. Although the heat and catalyst mix homogeneously in the rotary kiln reactors, the rubber processing capacity is limited due to the high bulk volume of the tires. In continuous rotary reactors, additional processing costs are incurred due to the small tire size loading requirement. Fluidized bed reactors are known as flash pyrolysis and the retention time is in the

(CC) 2022 SCS.

order of seconds. However, since it requires tires in the form of granules with a high surface area and the rubber feed rate to the reactor is lower than the heating fluid. In order to achieve high tire processing capacity, it is necessary to set up very large volume processes. Therefore, fluidized bed reactors are generally in the form of pilot plants with a tire feeding capacity of 200 kg h^{-1}. Thermal conversion rates of tires are close to each other in fluidized bed reactors and fixed--bed reactors. The only difference in reactor types is that the retention and pyrolysis times are longer in the fixed bed reactor.

The effects of temperature,[18–22] heating rate,[23–26] catalyst[27–34] and fuel blends[35,36] on pyrolysis process are discussed in details in the Supplementary material to this paper.

In this study, pyrolytic oils were obtained from thermal and catalytic pyrolysis of tires in a fixed bed reactor at atmospheric pressure, in the range of 450 to 600 °C. Density, viscosity, flash point and cetane index of the obtained pyrolytic oil were upgraded by catalytic distillation and desulfurization methods. By blending the upgraded pyrolytic oil and biodiesel with high flash point and cetane indices obtained from palm oil in a wide range, a fuel with physical properties very similar to diesel was obtained.

EXPERIMENTAL

Cetyltrimethylammonium bromide (CTMAB, 98 %) and sodium aluminate ($NaAlO_2$) obtained from Sigma–Aldrich, nanocluster zeolite Y (NaY) and HZSM-5 obtained from Julong Chemical Co., China, sodium silicate solution (8 % Na_2O, 27 % SiO_2), CaO obtained from the local market, polyacrylamide (av. *MW* 150.000), H_2SO_4 (97 %), NaOH, $Cu(NO_3)_2$ and silica gel (particle size 63–200 μm, pore size 6 nm (0.7–0.85 cm^3 g^{-1} pore volume, surface area ≥ 480 m^2 g^{-1}) was obtained from Merck company. Waste tires obtained from local recycling firms as 5–10 mm sizes. Leco, CHNS-932 elemental analyzer was used for C, H, N, S analysis in fuel. Viscosity measurements were made according to the ASTM D445 method. The Ostwald viscometer was filled with the pyrolytic oil sample and kept in a water bath at a constant temperature of 40 °C for 30 min. Then, the flow time between the two marked lines was measured with a stopwatch. The kinematic viscosity of the oil was calculated by considering the flow time and the viscometer calibration constant. The calorific value of the pyrolysis oil samples was measured using a U-Therm YX-ZR model semi-automatic calorimeter according to ASTM D240-09 method. Densities of pyrolytic oils were measured with Anton Paar DMA 38N density meter according to the ASTM D7777 method. The flash point of the pyrolytic oil samples was determined using the PMA 500 model Pensky–Martens device according to the ASTM D93 method.

Mesoporous MCM-41 synthesis

MCM-41 was synthesized according to the method in the literature.[37] CTMAB (7.22 g) was dissolved in 100 cm^3 distilled water, sodium silicate (26.52 g) was added dropwise to the solution while stirring. H_2SO_4 was added dropwise to the solution until the pH was 11.0. The mixture was allowed to heat in an oven at 100 °C for 24 h. The precipitate was filtered, washed, and dried at 55 °C under vacuum, before calcination. The dried precipitate was calcined at 550 °C with a heating rate of 2 °C min^{-1} for 6 h.

(CC) 2022 SCS.

Mesoporous aluminosilicate (MAS) synthesis

MAS was synthesized by two-step method.[33] Nanocluster zeolite Y seeds (NaY) were prepared through the reaction of NaOH (0.088 mol) and $NaAlO_2$ (0.10 mol) in H_2O (8.5 mol) with silicate anions (0.9 mol) in the form of sodium silicate solution. The solution was aged overnight. Then, the seed solution was added to CTMAB (0.27 mol) solution. The pH value was lowered to 10 with sulfuric acid. The mixture was placed at 100 °C for 24 h. The as-synthesized MAS was calcined under nitrogen atmosphere at 550 °C for 1 h, and then in the air at the same temperature for 6 h.

Cu(I)–MAS synthesis

Cu(I)–MAS was synthesized according to the method in the literature.[33] Ion exchange was performed by mixing MAS with 0.5 M $Cu(NO_3)_2$ solution for 24 h. Then, the filtered adsorbent was dried at 100 °C for 24 h. Finally, Cu^{+2} was reduced to Cu^{+} by calcining in a nitrogen atmosphere at 450 °C for 3 h.

Pyrolysis experiment

Pyrolysis experiments were carried out in an apparatus consisting of a fixed-bad reactor, condenser, and desulfurization equipment of non-condensed gases. The fixed-bed reactor with a diameter of 100 mm and a height of 200 mm is made of 2 mm stainless steel and a 4 kW electric heater is mounted. The reactor was isolated by wrapping it with silica wool. Temperature and pressure in the reactor were controlled by PID. A tube bundle condenser with a length of 700 mm and a diameter of 100 mm was used to condense and separate the pyrolytic gases. The non-condensed gases were desulfurized by passing through a container with a basic solution and burned directly. The pyrolysis process was carried out at atmospheric pressure using inert N_2 carrier gas (a flow rate of 5 L min^{-1}). The scrap tire composition used is given in Table I. Shredded tire pieces and catalyst (40 wt.% HZSM-5 + 40 wt.% MCM-41 + 10 wt.% CaO) were put into the reactor and the pyrolysis was carried out at 450, 500, 550 and 600 °C with different heating rate. The pyrolytic gases were cooled by passing through the heat exchanger and the pyrolytic liquid products were collected in a collection vessel, the non-condensed gases were burned by passing through a solution containing 4 M NaOH. In the pyrolysis experiment, yields were calculated from the amount of pyrolytic liquid and the amount of carbon black remaining in the reactor. The amount of gas was calculated as the remaining balance from the sum of pyrolytic oil and carbon black:

$$\text{Content of pyrolytic oil, wt.\%} = 100(\text{Pyrolytic oil weight/Total tire weight}) \quad (1)$$

$$\text{Pyrolytic gas weight} = \text{Waste tire weight} - (\text{pyrolytic oil weight} + \text{pCB weight}) \quad (2)$$

TABLE I. Waste tire composition

Ultimate analysis	Content, wt. %
C	86
H	8
N	1
S	2
Proximate analysis	
Volatiles	62
Fixed carbon	30
Ash	7
Moistures	1

(CC) 2022 SCS.

Upgrade of pyrolytic oils (UTPO)

Refinement of pyrolytic oils consists of pretreatment, atmospheric distillation, desulfurization and decolourization, respectively.[38]

Pre-treatment and settling of sludge

The precipitation of undesirable components such as water and tar from the pyrolytic oil was carried out according to the methods in the literature.[39,40] The pyrolytic oil and a flocculant/coagulant containing 0.2 wt. % polyacrylamide and 0.5 wt. % sodium silicate was mixed with an air compressor at 60 °C for 2 h, then left for 6 h to precipitate the asphaltenes. Thus, the residue and water were separated from the pyrolytic oil.

Distillation

Some 600 cm^3 of the supernatant were placed in a packed column-mounted distillation kettle. The filled column mounted on the distillation kettle has a diameter of 32 mm and a height of 400 mm. Ceramic wool was placed at the bottom of the column and zeolite adsorbent (50 % Cu(I)–MAS + 50 % MCM-41) was filled on the column. The distillates were collected in the collection vessels between 55 and 360 °C. The non-condensed gases were burned in the burner after desulphurization by passing from a 4 M NaOH solution.

Desulfurization and decolourization process

Oxidative desulfurization experiments of pyrolytic oils were carried out according to the method in the literature.[39] Distilled pyrolytic oil (100 cm^3), 3 cm^3 of 30 % by weight H_2O_2, 5 cm^3 deionized water, 4 cm^3 formic acid and 0.7 g activated carbon were mixture in 250 cm^3 of a beaker with a mechanical stirrer (100 rpm) at 60 °C for 60 min. At the end of the reaction, the oxidized oil separated from the mixture was washed with 50 cm^3 of 5 % by weight sodium carbonate solution and dried over anhydrous sodium sulphate. The pyrolytic oil obtained after drying was mixed with 2 % silica gel at 60 °C for 1 h, the sulphur and impurities remaining in the oil were adsorbed, its colour was lightened and filtered as upgraded tire pyrolytic oil.

Synthesized palm oil biodiesel (PBD)

Biodiesel from palm oil is synthesized according to the method in the literature.[41] Palm oil was mixed with solution of 0.3 % NaOH in 6:1 ratio of methanol. The mixture was stirred at 600 rpm for 4 h by heating at 64 °C below the boiling point of methanol, 65 °C, to prevent methanol evaporation. The solution was left overnight to separate the glycerine from the synthesized biodiesel mixture. The solution was left overnight to separate the glycerine from the synthesized biodiesel mixture. The glycerine phase was separated from the biodiesel phase, the biodiesel phase was heated up to 80 °C and excess methanol was evaporated. After the solution was washed 3 times with deionized water at 45 °C, excess water was removed from the biodiesel by evaporation at 110 °C. The obtained biodiesel was mixed with 1 wt. % silica gel for 1 h at 60 °C and filtered. The obtained PBD was mixed with the UTPO in certain proportions to obtain fuel blends.

RESULTS AND DISCUSSION

Purification of pyrolytic oils consists of desulphurization and decolorization stages of distilled pyrolytic oil, after the separation of tar and heavy phases by distillation method. Even if pyrolytic fuels are upgraded by distillation and desulphurization method, combustion problems continue in diesel engines due to their low cetane index and low flash point.[42]

(CC) 2022 SCS.

In this study, the improvement of pyrolytic oil was started at the pyrolysis stage. With catalytic pyrolysis, the physical properties of crude pyrolytic oil have been improved compared to the pyrolysis method without catalyst. After the pyrolysis step, the pyrolytic oil was upgraded by catalytic distillation and desulfurization method. Finally, palm oil was blended with biodiesel to improve its physical properties such as viscosity, flash point and cetane index to obtain diesel-like fuel. Thus, pyrolytic oils have reached a more economical, sustainable alternative energy quality in diesel engines with more problem-free combustion properties, and are intended to be blended with a more environmentally friendly second fuel at high rates without the need for a limited blending with diesel fuel.

Thermal pyrolytic oil (TPO) and catalytic pyrolytic oil (CPO) were obtained from thermal and catalytic pyrolysis of scrap tires using 1 and 2 % catalysts, at 450–600 °C with heating rates of 5 and 10 °C min^{-1}. TPO and CPO were upgraded with catalytic distillation, desulfurization and decolourization methods to obtain upgraded thermal pyrolytic oil (UTPO) and upgraded catalytic pyrolytic oil (UCPO). As an exemplary study, UCPO at 600 °C with a heating rate of 5 °C min^{-1} and PBD were blended in different mixing ratios to obtain diesel-like fuel. Since the pyrolysis experiments were carried out in a fixed-bed reactor, at constant inert nitrogen gas flow, with equivalent tire sizes, other variables such as: temperature, heating rate, the effect of the catalyst, which are other factors affecting pyrolysis, are explained below. In this study, since it is aimed to obtain diesel-like fuel from pyrolytic oils, carbon black and pyrolytic gases are not emphasized.

Pyrolysis process of waste tire

In order to study the effects of temperature and catalyst on pyrolysis in laboratory-scale experiments, the fixed-bed reactor type is more suitable and more practical to set up. In this study, an industrially applicable fixed-bed pyrolysis method was used in pyrolysis experiments. In order to obtain a larger heating surface area, the pyrolysis process was carried out in a horizontal reactor, since the carbon black deposited at the bottom of the vertical reactors makes heat transfer difficult and the bottom of the reactor has a low surface area. Thus, not only is heat transfer improved, but the retention times of cracked molecules are reduced. The empty volume of pyrolysis reactor (the 10 cm diameter and 20 cm length) used in the experiments is 1.570 g cm^{-3}. The bulk volume of 5–10 mm sized tire pieces[43] is 0.546 g cm^{-3}, and theoretically 0.857 g of rubber pieces can be filled into the reactor according to the 100 % filling rate. In the experiments, 25–30 vol. % of rubber pieces was filled into the reactor. The pyrolysis experiments were carried at atmospheric pressure, using inert carrier N_2 gas at a flow rate of 5 L min^{-1}. The main variables are temperature, heating rate and amount of catalyst at pyrolysis experiments. Since the combination of microporous and mesoporous

(CC) 2022 SCS.

zeolite is used in the pyrolysis process, although the thermal decomposition rate is high, secondary reactions are minimized with mesoporous MCM-41 and carrier nitrogen gas.

Temperature

Thermocatalytic degradation of polymers is faster at high temperatures. At higher temperatures, the residence time is shorter in the polymer phase, and secondary reactions occur in the vapor phase. Therefore, as the polymer breaks down into smaller molecules and the gasification rate increases, pyrolytic oil yield and fuel quality increase. As the components decompose at high temperatures, undesirable components such as sulphur, residual carbon, moisture and ash will be reduced and the quality of pyrolytic products (carbon black and pyrolytic oil) will increase.[44,45]

As it can be seen in Fig. 1, the pyrolytic oil yield increased up to 500 °C and decreased between 500 and 600 °C. The Fig. 2 shows that the pyrolytic gas yield increases regularly from 450 to 600 °C. There is no significant deviation in the carbon black yield, the carbon black amount is within the expected values. In the pyrolysis experiments, the lowest amount of pyrolytic oil was obtained at 600 °C, at 10 °C min^{-1} heating rate, and the highest amount of pyrolytic oil was obtained at 450 °C, at 5 °C min^{-1} heating rate.

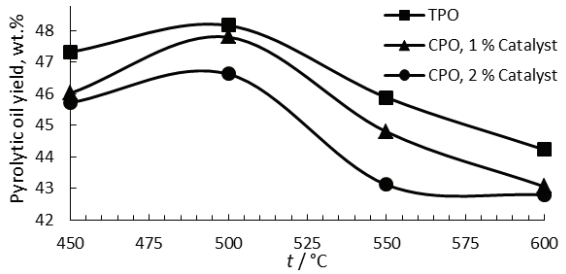

Fig. 1. The relationship of pyrolytic oil yield from catalytic pyrolysis and thermal pyrolysis with temperature, heating rate of 5 °C min^{-1}.

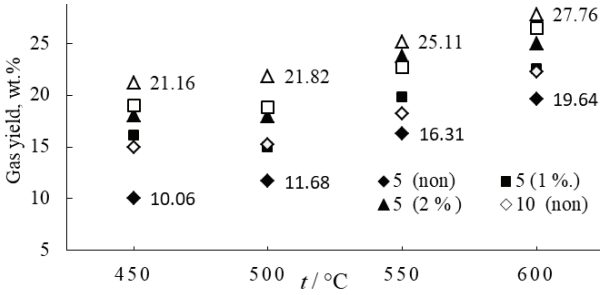

Fig. 2. The amount of pyrolytic gas obtained from pyrolysis between 450–600 °C, heating rate of 5 and 10 °C min^{-1}, with 1 and 2 % catalyst.

(CC) 2022 SCS.

The retention time in the polymer phase is longer at 450 °C. The highest pyrolytic carbon black was obtained from thermal pyrolysis at 450 °C, 42.62 % (Fig. 3). In the experiments carried out with 2 % catalyst and 10 °C min^{-1} heating rate, it is seen that carbon black decreases from 34.36 to 32.46 % levels at 500 °C. As can be understood from here, the thermal degradation of the polymer reached its maximum level up to 500 °C. While the change in the amount of carbon black decreased after 500 °C, gas formation continued to increase. As it can see in Tables II–IV, although the pyrolytic oil yield is higher at low temperatures, the physical properties of pyrolytic oil are closer to high-temperature diesel fuel. In pyrolysis processes, it is desirable to obtain higher quality pyrolytic oil instead of high efficiency. For this reason, high pyrolysis temperature should be preferred to obtain diesel-like fuel.

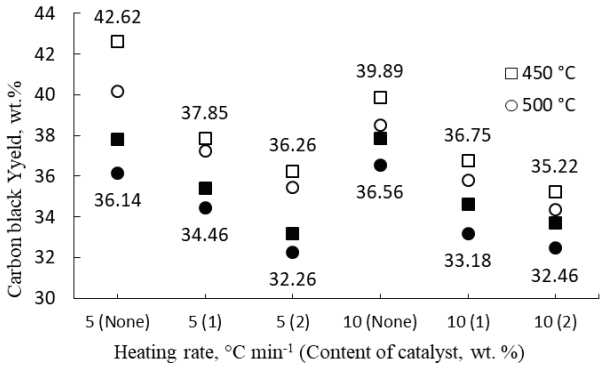

Fig. 3. The amount of pyrolytic carbon black obtained from pyrolysis between 450 and 600 °C, heating rate of 5 and 10 °C min^{-1}, with 1 and 2 % of catalyst.

TABLE II. Physicochemical properties of pyrolytic oil (TPO) and upgraded pyrolytic oil (UTPO) obtained from thermal pyrolysis at different temperatures

Pyrolytic oil properties	*t* / °C							
	450	500	550	600	450	500	550	600
	TPO				UTPO			
C content, wt. %	84.56	84.60	84.89	85.38	86.43	86.34	86.65	87.30
H content, wt. %	10.92	10.89	10.79	10.48	11.14	11.11	11.01	10.69
N content, wt. %	0.87	0.92	0.98	1.29	0.26	0.28	0.29	0.39
S content, wt. %	1.83	1.62	1.59	1.51	0.37	0.32	0.32	0.30
Ash content, wt. %	1.82	1.97	1.75	1.34	1.80	1.95	1.73	1.33
Moisture content, wt. %	5.93	5.71	4.62	4.27	0.30	0.29	0.23	0.21
Content of residue carbon, wt. %	2.47	2.11	1.89	1.82	0.25	0.21	0.19	0.18
GCV[a] / MJ kg^{-1}	40.18	40.91	41.71	42.16	42.19	42.96	43.80	44.27
Density, kg m^{-3}	920.74	915.27	905.45	895.18	874.70	869.51	860.18	850.42
ν^b / cSt at 40 °C	5.97	5.76	5.22	4.36	3.87	3.62	3.32	2.84
Flash point, °C	36.00	34.00	33.00	29.00s	37.08	35.02	33.99	29.87

[a]Gross calorific value; [b]kinematic viscosity

(CC) 2022 SCS.

TABLE III. Physicochemical properties of catalytic tire pyrolytic oil (CPO) and upgraded catalytic pyrolytic oil (UCPO) with 1 wt. % of catalyst

Pyrolytic oil properties	*t* / °C							
	450	500	550	600	450	500	550	600
	CPO with 1 % catalyst				UCPO with 1 % catalyst			
C content, wt. %	84.62	84.67	84.95	85.42	86.41	86.34	86.63	87.25
H content, wt. %	11.14	11.11	11.01	10.69	11.36	11.33	11.23	10.90
N content, wt. %	0.83	0.87	0.93	1.23	0.25	0.26	0.28	0.37
S content, wt. %	1.78	1.57	1.54	1.46	0.36	0.31	0.31	0.29
Ash content, wt. %	1.64	1.77	1.58	1.21	1.62	1.76	1.56	1.19
Moisture content, wt. %	3.56	3.43	2.77	2.56	0.18	0.17	0.14	0.13
Content of residue carbon, wt. %	1.98	1.69	1.51	1.46	0.20	0.17	0.15	0.15
GCV[a] / MJ kg^{-1}	41.39	42.14	42.96	43.42	43.45	43.40	44.25	44.73
Density, kg m^{-3}	856.29	851.20	842.07	832.52	847.73	842.69	833.65	824.19
ν^b / cSt at 40 °C	5.55	5.04	4.85	3.99	3.42	3.21	2.74	2.18
Flash point, °C	36.36	34.34	33.33	29.29	37.45	35.37	34.33	30.17

[a]Gross calorific value; [b]kinematic viscosity

TABLE IV. Physicochemical properties of catalytic tire pyrolytic oil (CPO) and upgraded catalytic pyrolytic oil (UCPO) with 2 wt. % of catalyst

Content of pyrolytic oil	*t* / °C							
	450	500	550	600	450	500	550	600
	CPO with 2 % catalyst				UCPO with 2 % catalyst			
C content, wt %	85.73	85.95	86.34	86.99	87.34	87.64	88.00	88.67
H content, wt %	10.84	10.79	10.74	10.13	10.95	10.90	10.85	10.23
N content, wt %	0.57	0.76	0.81	0.93	0.17	0.23	0.24	0.28
S content, wt %	1.64	1.57	1.49	1.41	0.33	0.31	0.30	0.28
Ash content, wt. %	1.22	0.93	0.62	0.54	1.21	0.92	0.61	0.53
Moisture content, wt. %	3.20	3.08	2.49	2.31	0.16	0.15	0.12	0.12
Content of residue carbon, wt.%	1.78	1.52	1.36	1.31	0.18	0.15	0.14	0.13
GCV[a] / MJ kg^{-1}	40.82	41.47	42.11	43.12	42.04	42.71	43.37	44.41
Density, kg m^{-3}	858.71	852.14	848.43	842.11	850.12	843.62	839.95	833.69
ν^b / cSt at 40 °C	4.92	4.62	4.32	3.76	3.57	3.46	3.22	2.57
Flash point, °C	36.54	34.51	33.50	29.44	37.64	35.55	34.50	30.32

[a]Gross calorific value; [b]kinematic viscosity

As it can be seen in Tables II–IV, in the thermal pyrolysis and catalytic pyrolysis experiments between 450 and 600 °C, a decrease was observed in parameters which decrease fuel quality such as sulphur value, ash, residual carbon, and moisture with an increase in temperature. Gross calorific value of pyrolytic oils increased, viscosity, density and flash point decreased. It can be seen that there is an improvement in the physical properties of the oil at high temperature.

Heating rate

As the heating rate increases, the density and efficiency of the pyrolytic oil decrease as a result of the increase in secondary reactions, since the retention

(CC) 2022 SCS.

time in the vapor phase is prolonged. As the retention time of cracked molecules decreases, secondary reactions such as secondary repolymerization and isomerization decrease. As the heating rate decreases, the retention time in the polymer phase increases and the density of the pyrolytic oil, tar formation, coking increases, and the pyrolytic oil yield increases.

In this study, as it can be seen in Fig. 1, the highest pyrolytic oil yield was obtained from thermal pyrolysis, similar to the results found by the researchers. As the temperature increased, maximum oil yield was obtained at 500 °C, and pyrolytic oil yield decreased after 500 °C. Figs. 1 and 2 clearly show that the optimum pyrolysis temperature is 500 °C to obtain the highest amount of pyrolytic oil, and secondary reactions (gasification) increase in the range of 450–600 °C. The lowest pyrolytic oil was obtained at 600 °C, with a heating rate of 10 °C min^{-1}. As it can be seen in Tables III and IV, although the pyrolytic oil obtained from pyrolysis without catalyst has the highest efficiency, the physical properties of the fuel obtained from the catalytic pyrolysis experiments are closer to diesel fuel.

Catalyst

Microporous HZSM-5 and mesoporous ZSM-5, whose pore diameter is smaller than MCM-41, increase the gasification rate by converting molecules into smaller molecules by vapor phase secondary reactions. Although MCM-41 has the ideal pore size to break up large molecules, it is easily deactivated due to its weak acidic structure and large pore volume. For these reasons, mesoporous and microporous catalyst combinations were preferred to obtain better fuel quality pyrolytic products such as diesel and kerosene by minimizing the gasification rate, taking into account the prolongation of the retention time in the vapor phase depending on the temperature increase in the catalytic cracking experiments.

In this study, a mixture of 40 % HZSM-5 + 40 % MCM-41 + 10 % CaO was used as a catalyst in pyrolysis experiments. The thermal cracking rate of HZSM-5 is higher than MCM-41. The use of HZSM-5 alone increases the amount of uncondensed gas. Therefore, HZSM-5 and MCM-41 were mixed in equivalent ratios to reduce the amount of non-condensable gas and increase the pyrolytic oil yield. The amount of aromatic components was reduced by adding basic CaO to the catalyst mixture.[46] It was observed that 1 and 2 % catalyst amount was sufficient for thermal cracking of the tires.

Upgrading of thermal and catalytic pyrolytic oil

Thermal and catalytic pyrolytic oils have been upgraded through pretreatment, distillation, desulphurization and decolourization steps. The results from Tables II–IV show the physical properties of pyrolytic oil and upgraded pyrolytic oil obtained from pyrolysis experiments without catalyst, using 1 % catalyst and 2 % catalyst, respectively. Ash, moisture and residual carbon content of pyrolytic oils decrease with increasing temperature. As the pyrolysis temperature inc-

(CC) 2022 SCS.

reased, the impurities were minimized, and the fuel quality was improved by distillation of the pyrolytic oil. The impurities reached the lowest value in the obtained pyrolytic oils at 600 °C. The carbon content of pyrolytic oil and upgraded pyrolytic oil increases as the temperature increases. The higher the carbon content of the fuel is, the higher is the gross calorific value. As the nitrogen value is improved in the upgraded pyrolytic fuels, lower NO_x emissions occur.

As it can be seen in Table II, the physical properties of TPO and upgraded thermal pyrolytic oil (UTPO) are incompatible with diesel fuel, since thermal pyrolytic oil has high density and viscosity, low flash point and cetane index (*CI*). In order to obtain a diesel-like fuel, the TPO must be upgraded and blended with biodiesel derived from palm oil or animal fats ($CI > 70$)[47] with a high cetane index and flash point.

UCPO obtained by catalytic pyrolysis method has better fuel properties than upgraded thermal pyrolytic oil, the results are given in Tables III and IV. Density and viscosity of UCPO were lower than CPO and closer to conventional DF values. The flash point and the cetane index are the two most important factors preventing the direct use of UCPO in vehicles. Pyrolytic oil has a low flash point and low cetane index due to its high aromatic content. Mixing pyrolytic oils directly with diesel fuel in limited proportion is insufficient to solve the problems. However, it seems that the problem is solved with UCPO and PBD mixtures at higher ratios than diesel fuel.

As it can be seen from the results of the sample study shown in Table V, the cetane index, density, viscosity, flash point and calorific values of the fuel blends of UCPO and PBD were significantly improved. The resulting blended fuel is a diesel-like fuel and can be used directly as a diesel equivalent fuel by adding engine preservatives and combustion-improving additives.[48]

TABLE V. Physicochemical properties of upgraded catalytic pyrolytic oil (UCPO), palm oil biodiesel (PBD), blends of UCPO with PBD, and comparison with diesel fuel (DF); content of catalyst is 2 wt. %, pyrolysis temperature is 600 °C. The heating rate is 5 °C min^{-1}

Properties	PBD	UCPO	UCPO 10	UCPO 20	UCPO 30	UCPO 40	UCPO 50	UCPO 60	DF
Density, kg m^{-3}	861	834	858	839	852	844	847	848	830
Flash point, °C	168	30	154	55	124	83	95	104	55
Viscosity, cSt at 40 °C	4.92	2.57	4.69	2.99	4.18	3.47	3.68	3.82	2.54
GCV / MJ kg^{-1}	39	44	40	43	41	42	42	42	44.83
Iodine number, mg I_2 g^{-1}	47	13	43	19	36	26	29	31	1.98
Cetane index	59	37	57	41	52	45	47	49	46.5
pH	7.11	5.32	6.93	5.64	6.54	6.00	6.17	6.27	5.4
Distillation									
$t_{10\ \%\ recovery}$ / °C	330	96							240
$t_{50\ \%\ recovery}$ / °C	342	220							278
$t_{90\ \%\ recovery}$ / °C	360	350							330

(CC) 2022 SCS.

It is clear from all these results that density, viscosity, flash point and cetane index must be optimized to convert pyrolytic oils into a diesel-like fuel. In the experiments performed with 1 % catalyst in Table III, it can be seen that the density and viscosity are slightly different from diesel fuel at 450 °C, and the upgraded pyrolytic oils obtained at other temperatures are more suitable for blending with palm biodiesel. In Table IV, in the experiments performed with 2 % catalyst, it was observed that the density and viscosity values of the upgraded pyrolytic oil were slightly higher than in the experiments performed with 1 % catalyst. Similar to UCPO and PBD blends obtained at 600 °C with 2 % catalyst, biodiesel blends of upgraded catalytic pyrolytic oils obtained at 450–600 °C using 1 or 2 % catalyst are also diesel-like fuels. However, mixing ratios should be determined in accordance with diesel fuels by considering density, viscosity, flash point and cetane index in blended fuels.

Pre-treatment

Before distillation, water and asphaltenes in the pyrolytic oil were precipitated and separated from the pyrolytic oil with the help of coagulators. Polyacrylamide, which is effective at 60 °C, was chosen as the coagulant.[39] Sodium silicates have been used to increase the precipitation rate and to disperse water and asphaltenes.[40] Compared to sulfuric acid, material loss is less, takes a shorter time, and the coking problems caused by metallic impurities and asphaltenes in distillation are minimized.

Distillation

The crude pyrolytic oil separated from water, metallic impurities and asphaltenes as a result of pre-treatment were distilled between 50 and 350 °C in a column-filled distillation apparatus containing the mixture of 50 % Cu-MAS + + 50 % MCM-41 as the catalyst. The molecular sieve not only separates sulphur-containing mercaptans from the fuel in the vapour phase but also removes reduced branched structures or unwanted high molecular structures. As it can be seen in Tables II–IV, a fuel with much better physical values were obtained as a result of desulfurization and decolourization after distillation.

The distillation of crude pyrolytic oil in a single fraction increases the amount of fuel suitable for the purpose due to all fractions of pyrolytic oils having a high aromatic structure, low cetane index and low flash point. In this study, pyrolytic oils were distilled at between 50 and 350 °C without fractionation to obtain a single-phase distillate. As it can be seen in Table V, although the physical properties of pyrolytic oil and distillates obtained from thermal and catalytic pyrolysis seem suitable for diesel-like fuel, it is not a suitable fuel that can be used instead of diesel due to low flash point and low cetane index. Therefore, TPO, CPO or UCPO cause noise, knocking and high emissions of particulate matter in diesel engines.[49] To obtain diesel-like fuel, it is necessary to increase the flash

(CC) 2022 SCS.

point and cetane index by reducing the amount of aromatic component in pyrolytic oil. The best method to solve these problems is to add other hydrocarbons to the pyrolytic oil, which improve the physical properties of pyrolytic oils, do not increase the cost of the fuel, and provide the physical properties of diesel fuel. The flash point of biodiesel (PBD) obtained from palm oil is 127 °C and its cetane index is 62, which makes it an environmentally friendly, economical diesel equivalent fuel. Blending pyrolytic oil and biodiesel solves the problems related to flash point and cetane index. As it can be seen in Table V, the physical properties of the fuel blends obtained from the mixture of improved pyrolytic oil and biodiesel at a ratio of 10–90 % are similar to conventional diesel fuel.

Desulfurization and decolourization mesoporous

In this study, crude pyrolytic oil was distilled using 50 wt.% Cu(I)-MAS + + 50 wt. % MCM-41 filled catalytic packed column. Then, sulphur was removed from the pyrolytic oils by the H_2O_2-formic acid desulphurization method. As a result of this combination, the sulphur values of the pyrolytic oil were significantly reduced. As it can be seen in Tables II–IV, after distillation, the sulphur value decreased from 1.49 to 0.28 % as a result of desulphurization. The sulphur content in the distilled pyrolytic oil was 81 % removed. It has been understood that the catalytic tower plays an important role in desulfurization.

The silica gel added in the last step of the desulfurization process adsorbed both the remaining sulphur and the impurities. The colour of the distillates obtained from the packed column is orange–yellow. After treating the distillate with silica gel, the colour of the upgraded oil changed to lemon yellow. Since the oxidation stability of the upgraded pyrolytic oil is high, no colour change was observed for up to 15 days.

Blending of UCPO and PBD to diesel-like fuel

As a case study, fuel blends were obtained from mixtures of different ratios of PBD and UCPO (2 % of catalyst at 600 °C). In order to use the pyrolytic oil more efficiently, it is completely distilled as a single phase. The problems caused by the low cetane index and flash point of the upgraded pyrolytic fuel were resolved by blending UCPO and PBD. Thus, the fuel obtained by blending UCPO and PBD can be used directly as diesel-like fuel without the need to add diesel fuel. In addition, a much more economical and useful blended fuel derivative has been obtained since a high percentage of UCPO can be used in the blended fuel.

Physicochemical properties of pyrolytic oil

Important parameters determining the properties of pyrolytic oils, upgraded pyrolytic oils and blended fuels[50–59]are explained separately in details in the Supplementary material.

(CC) 2022 SCS.

CONCLUSION

The resources of fossil fuels, which constitute the majority of the world's energy needs, are decreasing day by day. In this study, a new method is presented, namely the use, as diesel fuel, of the pyrolytic oils obtained from the recycling of environmentally hazardous scrap tires by pyrolysis method. While a certain fraction of pyrolytic oil was blended with diesel fuels in a limited way, alternative uses for the majority of them contained uncertainties. In this study, it has been demonstrated that distilled pyrolytic oil obtained as a result of single-phase distillation of pyrolytic oils can be mixed with palm oil biodiesel, at a ratio of 1:1 or more, in order to obtain an edible and sustainable fuel which would be an alternative to diesel fuels. In this respect, in scrape tire pyrolysis plants, a study was carried out to support the recycling of scrap tires by pyrolysis method within the waste management plans by avoiding the uncertainties regarding the usage areas of pyrolytic oils. Since the sludge remaining from the distillation of pyrolytic oils is a high-viscosity aromatic-rich phase, supporting studies can be conducted in order to use this non-distillable phase as an additive in the rubber industry or asphalt production.

SUPPLEMENTARY MATERIAL

Additional data and information are available electronically at the pages of journal website: https://www.shd-pub.org.rs/index.php/JSCS/article/view/11379, or from the corresponding author on request.

Acknowledgement. We thank Seda Chemical Company for supporting this study.

ИЗВОД

УНАПРЕЂЕНО ДИЗЕЛ ГОРИВО ОД ПОБОЉШАНОГ ПИРОЛИТИЧКОГ УЉА ДОБИЈЕНОГ ПИРОЛИЗОМ ГУМА

UFUK SANCAR VURAL[1], SABAN UYSAL[2] и ABDULLAH YINANC[3]

[1]Pasabayır Mh. Mehmetcik Cd. 77/16, Bandirma, Balikesir, Turkey, [2]Karabuk University, Faculty of Science, Department of Chemistry, Karabuk, Turkey u [3]Tekirdag Namık Kemal University, Corlu Vocational School of Technical Sciences, Corlu, Tekirdag, Turkey

Пиролитичко уље (TPO), добијено термичком пиролизом отпадних гума, није гориво еквивалентно дизелу које се може користити директно у возилима, због своје велике густине, вискозности и садржаја сумпора, ниске тачке паљења и ниског цетанског индекса. Поменуто уље се може користити само ограничено, мешањем са дизел горивом (DF), у количинама мањим од 30 %. У овој студији, пиролиза отпадних гума је спроведена при брзини загревања од 5 и 10 °C min^{-1} у опсегу од 450 до 600 °C, коришћењем мешавине хијерархијског зеолита (HZSM-5), мезопорозног силицијум-диоксида (MCM-41) и живог креча (CaO) као катализатора. Добијени TPO и каталитичко пиролитичко уље (CPO) су унапређени претходном обрадом, дестилацијом смеше напуњеног мезопорозног Cu(I) алуминосиликата (Cu(I)–MAS) и MCM-41, а затим корацима одсумпоравања и обезбојавања. Да би се добило гориво слично дизелу, побољшано каталитичко пиролитичко уље (UCPO) и биодизел (PBD) добијен од палминог уља су мешани у одре-

(CC) 2022 SCS.

ђеним размерама. Густина, вискозитет, тачка паљења и цетански индекс добијених дизел горива су били у границама граничних вредности дизел горива.

(Примљено 1. новембра 2021, ревидирано 7 јуна, прихваћено 11. јуна 2022)

REFERENCES

1. W. C. Wang, C. J. Bai, C. T. Lin, S. Prakash, *Appl. Therm. Eng.* **93** (2016) 330 (https://doi.org/10.1016/j.applthermaleng.2015.09.056)
2. W. Li, C. Huang, D. Li, P. Huo, M. Wang, L. Han, G. Chen, H. Li, X. Li, Y. Wang, M. Wang, *Chinese J. Catal.* **37** (2016) 526 (https://doi.org/10.1016/S1872-2067(15)60998-6)
3. G. C. O. Neto, L. E. C. Chaves, L. F. R. Pinto, J. C. C. Santana, M. P. C. Amorim, M. J. F. Rodrigues, *Sustainability* **11** (2019) 207b (https://doi.org/10.3390/su11072076)
4. X. Zhang, H. Li, Q. Cao, J. Li, F. Wang, *Waste Manage. Res.: J. Sust. Cir. Econ.* **36** (2018) 436 (https://doi.org/10.1177%2F0734242X18764292)
5. EPA, *Markets for scrap tires, United States Environmental Protection Agency, Office of Solid Waste*, EPAi, EPA/530-SW-90-074A, October, 199,. pp. 23–25 (https://archive.epa.gov/epawaste/conserve/materials/tyres/web/pdf/tyres.pdf)
6. A. R. Phale, *Environmental impact and waste management of used tyres in the RSA*. Magister Artium mini disseretation, University of Johannesburg, 2005 (https://core.ac.uk/download/pdf/18220959.pdf)
7. B. Lebreton, A. Tuma, *Int. J. Prod. Econ.* **104** (2006) 639 (https://doi.org/10.1016/j.ijpe.2004.11.010)
8. P. Ferrão, P. Ribeiro, P. A. Silva, *Waste Manage.* **28** (2008) 604 (https://doi.org/10.1016/j.wasman.2007.02.033)
9. P. J. Bosscher, T. B. Edil, S. Kuraoka, *J. Geotech. Geoenviron. Eng*. **123** (1997) 295 (https://doi.org/10.1061/(ASCE)1090-0241(1997)123:4(295))
10. M. Sienkiewicz, J. Kucinska-Lipka, H. Janik, A. Balas, *Waste Manage.* **32** (2012) 1742 (https://doi.org/10.1016/j.wasman.2012.05.010)
11. R. Giere, K. Smith, M. Blackford, *Fuel* **85** (2006) 2278 (https://doi.org/10.1016/j.fuel.2005.11.024)
12. A. Quek, R. Balasubramanian, *J. Air Waste Manage. Assoc.* **59** (2009) 747 (https://doi.org/10.3155/1047-3289.59.6.747)
13. N. Sunthonpagasit, M. R. Duffey, *Resour. Conserv. Recyc*. **40** (2004) 281 (https://doi.org/10.1016/S0921-3449(03)00073-9)
14. K. Bazienė, R. Vaiškūnaitė, *Sustain*. **8** (2016) 767 (https://doi.org/10.3390/su8080767)
15. T. H. Christensen, *Solid Waste Technology & Management 1 and 2*, Wiley, Chichester, 2011 (https://doi.org/10.1002/9780470666883)
16. N. Nkosi, E. Muzenda, M. Laeng, in *Proceedings of the World Congress on Engineering*, *Vol. (II)*, July 2–4, London, UK, 2014 http://www.iaeng.org/publication/WCE2014/WCE2014_pp979-985.pdf
17. D. T. Dick, O. Agboola, A. O. Ayeni, *AIMS Energy* **8** (2020) 869 (https://www.doi.org/10.3934/energy.2020.5.869)
18. A. Alsaleh, M. L. Sattler, *Curr. Sustain. Renew. Energy Rep.* **1** (2014) 129 (https://doi.org/10.1007/s40518-014-0019-0)
19. E. Aylo´n, A. Ferna´ndez-Colino, M. V. Navarro, R. Murillo, T. Garcı´a, A. M. Mastral, *Ind. Eng. Chem. Res.* **47** (2008) 4029 (https://doi.org/10.1021/ie071573o)
20. Z. Cepic, V. Mihajlović, S. Đuric, M. Milotić, M. Stošić, B. Stepanov, M. I. Micunović, *Energies* **14** (2021) 5403 (https://doi.org/10.3390/en14175403)

(CC) 2022 SCS.

21. P. T Williams, S. Besler, D. T. Taylor, *Fuel* **69** (1990)1474 (https://doi.org/10.1016/0016-2361(90)90193-T)
22. X. Dai, X. Yin, C. Wu, W. Zhang, Y. Chen, *Energy* **26** (2001) 385 (https://doi.org/10.1016/S0360-5442(01)00003-2)
23. A. Uyumaz, B. Aydogan, H. Solmaz, E. Yilmaz, D. Yesim Hopa, T. Aksoy Bahtli, O. Solamz, F. Aksoy, *J. Energy Inst.* **92** (2019) 1406 (https://doi.org/10.1016/j.joei.2018.09.001)
24. S. Chouaya, M. A. Abbassi, R. B. Younes, A. Zoulalian, *Russ. J. Appl. Chem.* **91** (2018) 1603 (https://doi.org/10.1134/S1070427218100063)
25. M. A. Aziz, M. A. Rahman, H. Molla, *J. Radiat. Res. Appl. Sci.* **11** (2018) 311 (https://doi.org/10.1016/j.jrras.2018.05.001)
26. M. Banar, V. Akyıldız, A. Ozkan, Z. Cokaygil, O. Onay, *Energy Conver. Manage.* **62** (2012) 22 (https://doi.org/10.1016/j.enconman.2012.03.019)
27. D. K. Ratnasari, M. A. Nahil, P. T. Williams, *J. Anal. Appl. Pyrolysis* **124** (2017) 631 (https://doi.org/10.1016/j.jaap.2016.12.027)
28. W. H. Chang, C. T. Tye, *Malays. J. Anal. Sci.* **17** (2013) 176 (http://mjas.analis.com.my/wp-content/uploads/2018/11/Tye.pdf)
29. D. Almeida**,** M. F. Marques, *Polímeros* **26** (2016) 44 (https://doi.org/10.1590/0104-1428.2100)
30. R. Miandad, M. A. Barakat, M. Rehan, A. S. Aburiazaiza, J. Gardy, A. S. Nizami, *Process Saf. Environ. Prot*. **116** (2018) 542 (https://doi.org/10.1016/j.psep.2018.03.024)
31. M. Olazar, R. Aguado, M. Arabiourrutia, G. Lopez, A. Barona, J. Bilbao, *Energy Fuels* **22** (2008) 2909 (https://doi.org/10.1021/ef8002153)
32. J. Zhu, X. Meng, F. Xiao, *Front. Chem. Sci. Eng.* **7** (2013) 233 (https://doi.org/10.1007/s11705-013-1329-2)
33. W. U. Eze, R. Umunakwe, H. C. Obasi, H.C., M. I. Ugbaja, C. C. Uche, I. C. Madufor, *Clean Technol. Recyc.* **1** (2021) 50 (https://doi.org/10.3934/ctr.2021003)
34. E. Santos, B. Rijo, F. Lemos, M. A. N. D. A. Lemos, *Chem. Eng. J.* **278** (2019) 122077 (https://doi.org/10.1016/j.cej.2019.122077)
35. E. R. Umeki, C. F. de Oliveira, R. B. Torres, R. G. dos Santos, *Fuel* **185** (2016) 236 (http://dx.doi.org/10.1016/j.fuel.2016.07.092)
36. M. S. Hossain, A. Abedeen, M. R. Karim, M. Moniruzzaman, M. Juwel Hosen, *Iran. J. Energy Environ.* **8** (2017) 189 (https://www.ijee.net/article_64681_b5fefefcb5742bf3931805919db680dd.pdf)
37. A. Ayanaoglu, R. Yumrutas, *Energy* **103** (2016) 456 (https://doi.org/10.1016/j.energy.2016.02.155)
38. F. Campuzano, A. G. A. Jameel, Wen. Zhang, A-H. Emwas, A. F. Agudelo, J. D. Martínez, S. M. Sarathy, *Fuel* **290** (2021) 120041 (https://doi.org/10.1016/j.fuel.2020.120041)
39. W. Li, Q. Liu, J. Xing, H. Gao, X. Xiong, Y. Li, X. Li, H. Liu, *Environ. Energy Eng.* **53** (2007) 3263 (https://doi.org/10.1002/aic.11319)
40. Q. Zhang, M. Zhu, I. Jones, Z. Zhang, D. Zhang, *Energy Fuels* **34** (2020) 6209 (https://www.doi.org/10.1021/acs.energyfuels.9b03968)
41. E. R. Umeki, C. F. de Oliveira, R. B. Torres, R. G. dos Santos, *Fuel* **185** (2016) 236 (http://dx.doi.org/10.1016/j.fuel.2016.07.092)
42. Y. Kidoguchi, C. Yang, R. Kato, K. Miwa, *JSAE Rev.* **21** (2000) 469 (https://doi.org/10.1016/S0389-4304(00)00075-8)

(CC) 2022 SCS.

43. H. M. Patel, T. M. Patel, *Int. J. Eng. Research Technol.* **1** (2012) 1 (https://www.ijert.org/performance-analysis-of-single-cylinder-diesel-engine-fuelled-with-pyrolysis-oil-diesel-and-its-blend-with-ethanol)
44. A. Sanchís, A. Veses, J. D. Martínez, J. M. López, T. García, R. Murillo, *J. Environ. Manage.* **317** (2022) 115323 (https://doi.org/10.1016/j.jenvman.2022.115323)
45. D. T. Dick, O. Agboola, A. O. Ayeni, *AIMS Energy* **8** (2020) 869 (https://doi.org/10.3934/energy.2020.5.869)
46. T. F. Parangi, R. M. Patel, U. V. Chudasama, *Bull. Mater. Sci*. **37** (2014) 609 (https://doi.org/10.1007/s12034-014-0709-7)
47. A. Khaleque, M. R. Islam, M. S. Hossain, M. Khan, M. S. Rahman, H. Haniu, *Mech. Eng. Res. J.* **10** (2016) 35 (https://www.cuet.ac.bd/merj/vol.10/MERJ-07.pdf)
48. R. Serefentse, W. Ruwona, G. Danha and E. Muzenda, *Procedia Manuf.* **35** (2019) 762 (https://www.doi.org/10.1016/j.promfg.2019.07.013)
49. U. S. Vural, *Turkish J. Eng.* **4** (2020) 62 (https://doi.org/10.31127/tuje.616960)
50. T. Yogeeswara, U. Devendra, A. Kalaisselvane, *AIP Conf. Proc.* **2225** (2020) 030003 (https://doi.org/10.1063/5.0005584)
51. Md. A. Hossain, M. Warith, J. Liu, B. Mondal, in *Proceedings of 2011 Pan-Am CGS Geotechnical Conference*, October 2–6, Toronto, Canada, 2011 (http://geoserver.ing.puc.cl/info/conferences/PanAm2011/panam2011/pdfs/GEO11Paper1073.pdf)
52. Q. Wang, X. Zhang, S. Sun, Z. Wang, D. Cui, *ACS Omega* **5** (2020) 10276 (https://doi.org/10.1021/acsomega.9b03945)
53. A. Nicolici, C. Pana, N. Negurescu, A. Cernat, C. Nutu, *IOP Conf. Ser.: Mater. Sci. Eng.* **444** (2018) 072003 (https://doi.org/10.1088/1757-899X/444/7/072003)
54. N. M. Ribeiro, A. C. Pinto, C. M. Quintella, G. O. da Rocha, L. S. G. Teixeira, L. L. N. Guarieiro, M. C. Rangel, M. C. C. Veloso, M. J. C. Rezende, R. S. Cruz, A. M. de Oliveira, E. A. Torres, J. B. de Andrade, *Energy Fuels* **21** (2007) 2433 (https://doi.org/10.1021/ef070060r)
55. M. Karagoz, U. Agbulut, S. Saridemir, *Fuel* **275** (2020) 117844 (https://doi.org/10.1016/j.fuel.2020.117844)
56. M. Z. H. Khan, M. Sultana, M. R. Al-Mamun, M. R. Hasan, *J. Environ. Public Health* **6** (2016) 7869080 (https://doi.org/10.1155/2016/7869080)
57. T. A. Tran, in *Diesel and Gasoline Engines,* R. Viskup (Ed.), IntechOpen, Rijeka, 2020 (https://doi.org/10.5772/intechopen.89400)
58. R. Cataluña, R. da Silva, Y. Ren, *J. Comb*. **2012** (2012) 738940 (https://doi.org/10.1155/2012/738940)
59. T. Yogeeswara, U. Devendra, A. Kalaisselvane, *AIP Conf. Proc.* **2225** (2020) 030003 (https://doi.org/10.1063/5.0005584).

(CC) 2022 SCS.

Journal of the Serbian Chemical Society
JSCS@tmf.bg.ac.rs • www.shd.org.rs/JSCS
J. Serb. Chem. Soc. *87* (10) S395–S404 (2022) *Supplementary material*

SUPPLEMENTARY MATERIAL TO

The improved diesel-like fuel from upgraded tire pyrolytic oil

UFUK SANCAR VURAL[1]*, SABAN UYSAL[2] and ABDULLAH YINANC[3]

[1]*Pasabayır Mh. Mehmetcik Cd. 77/16, Bandirma, Balikesir, Turkey,* [2]*Karabuk University, Faculty of Science, Department of Chemistry, Karabuk, Turkey and* [3]*Tekirdag Namık Kemal University, Corlu Vocational School of Technical Sciences, Corlu, Tekirdag, Turkey*

J. Serb. Chem. Soc. *87* (10) (2022) 1219–1235

ADDITIONAL CONSIDERATIONS OF THE PYROLYSIS PROCESS

Temperature. The effect of temperature on pyrolysis is an important factor which researchers focus on. The researchers have determined that the oil yield increased until the optimum pyrolysis temperature, then the oil yield decreased as the temperature increased, but did not change much after a maximum pyrolysis temperature. The amount of uncondensed gas during pyrolysis increases with temperature until the whole of the polymer becomes pyrolyzed. It is difficult to state a specific optimum temperature for the pyrolysis of tires, as the optimum pyrolysis temperature varies depending on the reactor type and other factors such as tire size. According to the researchers, maximum oil yield is reached in the range of 450–500 °C, the amount of oil decreases up to 600 °C, and there is not much change in the amount of oil above 600 °C. In the pyrolysis experiments carried out at temperatures below the optimum temperature, it was observed that the retention and pyrolysis times were prolonged. Coking gas and tar formation increases with repolymerization reactions, the fuel quality of the oil decreases. Although the pyrolytic oil yield at high temperature is lower, the physical properties of the obtained pyrolytic oil are closer to diesel fuel. Therefore, the pyrolysis temperature is controlled depending on whether the pyrolytic oil is to be used as a diesel-like fuel or for heating purposes.

Williams *et al.*[1] determined the maximum pyrolytic oil yield of 55 % at 450 °C between 450–600 °C in a fixed-bed reactor. They found the highest pyrolytic oil yield of 45.1 % at 500 °C in the rotary kiln between 450–600 °C. Dai *et al.*[2] found the maximum pyrolytic oil yield of 52 % at 450 °C in tire pyrolysis experiments between 360–810 °C in the fluidized bed reactor. As can be seen from the studies, the pyrolytic oil yield in the fixed-bed reactor is higher than that of

* Corresponding author. E-mail: usvural@gmail.com

Available on line at www.shd.org.rs/JSCS/
(CC) 2022 SCS.

the rotary kiln (fast pyrolysis) and fluidized bed reactor. Although pyrolysis is slow in fixed-bed reactors, secondary reactions are less due to the shorter residence time in the vapor phase. Therefore, the pyrolytic oil yield is higher. Polymer phase and vapor phase catalytic reactions, residence time, temperature control is easier in fixed-bed reactors. Consequently, more selective products can be obtained.

Cepic *et al.*[3] in the pyrolysis experiments of tires in the 400–750 °C range, showed that the oil yield increased from 27 to 43.6 % by increasing the temperature from 400 to 500 °C, and decreased to 26.6 % at >500 °C. It was observed that the amount of pyrolytic gas increased regularly from 14.3 to 33.5 % in the range of 400–720 °C. Since there is no remarkable change in the amount of carbon black after 500 °C, it is understood that the pyrolysis of the polymer is completed at 500 °C. Above this temperature, the pyrolytic oil yield first increases and then decreases, and the gas amount continues to increase, indicating that secondary reactions continue in the vapor phase. Alsaleh *et al.*[4] stated that the volatile components increase as the retention time in the gas phase is prolonged at high temperatures, therefore the pyrolytic oil yield decreases. Dai *et al*.[2] obtained the maximum oil yield of 52 % at 450 °C, in their pyrolysis experiments performed in a fixed bed reactor between 360 °C - 810 °C.

Heating rate. The heating rate is another important factor affecting the thermal degradation rate of the polymer. The heating rate also affects the residence time of thermally cracked components in the polymer phase and gas phase, which is one of the most important factors regarding the yield, chemical and physical properties of the pyrolytic oil. In high temperature pyrolysis processes, the residence time in the vapour phase is longer than in the polymer phase and secondary reactions occur in the vapour phase. In low temperature pyrolysis processes, the retention time in the polymer phase is longer than in the vapour phase and secondary reactions occur in the polymer phase. Secondary reactions in the vapour phase break molecules down into smaller molecules. Therefore, the amount of non-condensable gas at high temperature is higher and pyrolytic oil is lower. The longer retention time in the polymer phase causes the conversion of small molecules to large molecules by the repolymerization reaction, and higher is the pyrolytic oil yield at low temperature. Depending on the heating rate, pyrolysis is known as slow and fast pyrolysis. In slow pyrolysis, the pyrolysis temperature, thermal conduction, and thermal decomposition rate is low, the retention time can be up to several hours, and the feed size is relatively large. The best example of slow pyrolysis reactor is fixed-bed reactor. The main product of slow pyrolysis is carbon black. In fast pyrolysis, the thermal conduction rate is high, the residence time is short, and the thermal decomposition rate is high. Examples of fast pyrolysis reactors are rotary reactors and fluidized bed reactors. The main

(CC) 2022 SCS.

product of the fast pyrolysis process is pyrolytic oil, which is much more valuable than carbon black.

Many researchers have obtained different results in the pyrolysis experiments depending on the heating rate and pyrolysis temperature, in the amounts of pyrolytic oil and non-condensable gas. Uyumaz *et al.*[5] found the highest pyrolytic oil yield at 450 °C as 53.3 and 42 wt. %, respectively, in a nitrogen atmosphere of 1000 ml min^{-1}, at a heating rate of 10 and 20 °C min^{-1} in a fixed-bed reactor. At the same temperature, the amount of pyrolytic gas was determined as 10 and 20.4 wt. %, respectively. Chouya *et al.*[6] obtained 40 wt. % pyrolytic oil at 550 °C with the highest efficiency in the experiment performed with a heating rate of 20 °C min^{-1} in a nitrogen atmosphere between 300–600 °C. Aziz *et al.*[7] obtained 40 wt. % pyrolytic oil and 11 wt. % gas at 400 °C from the pyrolysis of bus tires at a heating rate of 20 °C min^{-1} in the range of 300–500 °C. Banar *et al.*[8] obtained 38.8 wt. % pyrolytic oil and 27.2 wt. % pyrolytic gas at 400 °C, at a heating rate of 5 °C min^{-1}, in the range of 350–600 °C, from the pyrolysis of wire-removed tires. As it can be seen in the experiments of the researchers, the amount of pyrolytic products obtained at the same heating rate or pyrolysis temperature may vary in different studies. From this, it can be understood that not only the heating rate and pyrolysis temperature are effective on pyrolysis, but also parameters such as tire size, catalyst and reactor type.

Catalyst. Catalysts play a critical role in the thermochemical processing of hydrocarbons in terms of promoting targeted reactions, reducing reaction temperature, and improving process system efficiency. Porous heterogeneous catalysts such as alumina, silica and aluminosilicate are widely used in the catalytic cracking of heavy hydrocarbons because it is more economical and easy to find. Zeolites are the most important catalysts used in petrochemical reactions such as cracking, alkylation, isomerization, oligomerisation, cyclisation, aromatisation, hydrogenation and hydrodesulfurization, dehydroaromatization, conversion of methanol to olefins and hydrocarbons. The pore size and acidity of zeolite-type catalysts are important factors in the catalytic cracking of hydrocarbons. In general, the catalytic activity of zeolites increases with increasing surface area, the number of acidic sites, and acid strength. Catalysts with large surface area and high acid strength increase the rate of degradation of polyolefins. As the acid strength and pore diameter of the catalyst increase, the isomerization rate along with the fuel quality also increases. However, the strong acidity and high pore size cause rapid deactivation of the catalyst. Therefore, slightly acidic and long-lived catalysts are preferred in the pyrolysis of polyolefins. Various studies have shown that the catalysts used during the pyrolysis process have a significant impact on the quality and quantity of pyrolytic products. Chang *et al.*[9] reported the effects of microporous zeolite (ZSM-5), hierarchical zeolite (HZSM-5) and mesoporous silica (MCM-41) catalysts on the

(CC) 2022 SCS.

cracking of palm oil. Catalytic cracking of vegetable oil over HZSM-5 was found to produce liquid fuel rich in gasoline fraction. They showed that MCM-41 is more selective for C5+ olefin products compared to the ZSM-5. The selectivity of MCM-41 towards particular liquid hydrocarbons such as gasoline, kerosene or diesel was found to be strongly dependent on the pore size and the surface area of the catalyst. Due to the higher accessibility of reactants in mesoporous MCM-41, as compared to zeolite, it is suitable for catalytic reactions dealing with large molecules. However, the cracking activity of MCM-41 is lower than that of ZSM-5 zeolite due to the lower acidity and shape selectivity of the mesoporous materials. Almeida *et al.*[10] described the pore size effect of catalytic on the cracking of polymers. Catalysts containing strong acid sites, and higher porosity, are more effective in cracking polyolefins. However, the strong acidity and high pore size cause rapid deactivation of the catalyst. They observed that the ZSM-5 catalyst allows the cracking of large molecules due to its three-dimensional pore size. Zhu *et al.*[11] stated that mass transfers of bulk molecules are insufficient in cracking reactions due to the weak hydrothermal stability and acidity of zeolites such as mesoporous MCM-41. They stated that the smaller ZSM-5 crystals increase the rate of dimeric and oligomeric cracking reactions due to their easier diffusion into the linear and branched polymer matrix, thus ZSM-5 catalysts show a good catalytic activity. Eze *et al.*[12] reported that when they used a 1:1 ratio of MCM-41 and ZSM-5 catalyst mixture, the degradation rate of plastics was the highest and a gasoline-like fuel rich in aromatic compounds was obtained. Ayanoglu *et al.*[13] distilled pyrolytic oil using lime and natural zeolite as catalysts and obtained the best results when 10 % lime was used in the experiments. They were obtained 18 % by weight light fraction (such as gasoline), 70 % by weight heavy fraction (such as diesel) and 12 % by weight precipitate phase in experiments. Li *et al.*[13] determined the desulfurization ability of mesoporous molecular sieves (MCM-41), mesoporous aluminosilicate *(*MAS) and Y-type zeolite (NaY) catalysts by using hydrotreated naphtha diesel and DPT model compounds. The pore diameter of MCM-41 (3.51×10^{-9}) and MAS 3.27×10^{-9}) is larger than NaY (7.9×10^{-10} m). The acidic character of adsorbents is NaY> MAS> MCM-41. For DPT, which is a smaller molecule than hydrotreated diesel, the desulfurization ability of amorphous microporous NaY is higher than that of MAS and MCM-41. However, the desulphurization capacity of NaY is reduced because larger molecules with higher viscosity, such as hydrotreated diesel, block the microporous NaY. In the experiment with MAS, MCM-41 and NaY catalysts, the sulfur concentration of hydrotreated diesel decreased from 207 mg L^{-1} to 93, 98 and 135 mg L^{-1}, respectively. To improve the adsorptive desulfurization properties, stability and acidity of mesoporous molecules, the adsorbent is modified with transition metals. One of the best examples of modification of mesoporous structure is MAS. Li *et al.*[13] found that Cu(I) loaded *MAS* was more

(CC) 2022 SCS.

effective than MAS, MCM-41 and NaY zeolite. In experiments with Cu(I)-MAS and MAS adsorbents, 315 mg L^{-1} sulfur value of diesel decreased to 54 mg L^{-1} and 109 mg L^{-1}, respectively. The authors stated that MAS is more effective than MCM-41 in the desulphurization process since it is more acidic than mesoporous MCM-41. Zhang *et al.*[14] reduced the sulfur value of crude pyrolytic oil and its distillates by 82 % and 84 %, respectively, by oxidative desulphurization using H_2O_2-formic acid as the oxidant and selective adsorption with Al_2O_3.

Fuel blends. The most suitable method to obtain diesel-like fuel is to blend pyrolytic oil and biodiesel obtained from animal or vegetable oils with a high cetane index and flash point. Since the commercial value of other vegetable oils and animal fats is higher than palm oil, biodiesel produced from palm oil is the most economical solution to obtaining a fuel blend. Patel *et al.*[15] determined that when 5 % ethanol is added to a mixture of 95 % pyrolytic oil and diesel (85 % pyrolytic oil), fuel consumption is reduced, it creates better brake thermal efficiency and can be used as an alternative fuel for diesel engine without any engine modification.

Quality of pyrolytic oils

Pyrolytic oils obtained from tires are not suitable for direct use as a diesel equivalent or diesel like fuel due to their low cetane index, low flash point, high density and high viscosity. The calorific value of pyrolytic oil is the diesel equivalent best feature. During the thermal or catalytic decomposition reactions of tires, physicochemical properties of pyrolytic oils change depending on parameters such as temperature, heating rate, inert carrier gas, and tire size and reactor type. Since aromatic, cyclic, mono- and dimer structures of different sizes are formed during thermal decomposition, pyrolytic oils do not have a certain standard chemical structure.

Physicochemical properties of pyrolytic oil

In the following, important parameters determining the properties of pyrolytic oils, upgraded pyrolytic oils and blended fuels are attempted to be explained separately.

Carbon residue. Carbon residue indicates the tendency of oil to deposit a carbonaceous solid residue on a hot surface, such as a burner or injection nozzle, when its vaporizable constituents evaporate. Fuel which deposits the minimum amount of carbon is preferable. As it can be seen in Tables II–IV, carbon residue was found to be between 0.13 and 0.20 % in UCPO fuels, between 1.30 and 1.98 % in CPO fuels, and 0.7 % in DF. Accordingly, more carbon residues are formed in the injection and combustion nozzles in CPO than in DF, in UCPO there is not as much residue in DF. This indicates that diesel fuels would form higher deposits. Fuels with high carbon residue content could cause increased fouling of

(CC) 2022 SCS.

the gas ways; consequently, more frequent cleaning is necessary, especially of the turbocharger and exhaust gas boiler.

pH. As it can be seen in Table V, the pH value of UCPO is almost the same as the known diesel fuel, but very slightly lower. This may be due to components with acidic functional groups formed during the thermal degradation of rubbers. The pH of palm biodiesel and UCPO blends is slightly higher than that of diesel fuels but is not corrosive.

Density. Density is an important factor which determines the combustion quality and other physicochemical properties of the fuel. Since the density of alternative fuel is lower than diesel, mechanical failures occur due to the high pressure formed in the engine as a result of feeding more fuel to the engine, and also more fuel consumption occurs. The impurities such as water, carbon residues, and asphaltenes in the pyrolytic oil are the reasons for the high density. Presumably, the catalyst reduced the conversion of large molecules to smaller molecules and the amount of water. Table II shows the density of the pyrolytic oil obtained from thermal pyrolysis to be between 895.18 and 920.74 kg mol^{-1} in the temperature range of 450–600 °C. As it can be seen in Tables III and IV, in the same temperature range, the densities of the pyrolytic oils obtained from catalytic pyrolysis with 1 and 2 % catalyst were found to be between 832.52 and 856.29 kg mol^{-1} and between 842.11 and 858.71 kg mol^{-1}, respectively. The density values of CPO were significantly reduced in catalytic pyrolysis. In the pyrolysis experiments performed with 2 % catalyst, the density values were found to be slightly higher than 1 % catalyst. From this result, it is understood that as the amount of mesoporous MCM-41 increases, cracking reactions proceed in the direction of the formation of liquid molecules, and gasification decreases. As it can be seen in Table V, the flash point and cetane index of the fuel increased despite the decrease in density in the catalytic experiments. It is understood from the decrease in the density, the cracking of large molecules into smaller molecules causes an increase in the aliphatic structure of the fuel and a decrease in the aromatic structure, and the amount of water mixed into the pyrolytic oil also decreases. At the end of the distillation of the pyrolytic fuel with the packed column, the density value of the fuels obtained as a result of the desulfurization and filtration of the distillates from the bleaching earth is close to the conventional diesel fuels. As seen in Table V, the density value of the fuel obtained by blending up to 60 % of UCPO with PBD was found to be similar to diesel fuel.

Viscosity. Viscosity is one of the most important factors affecting the combustion quality of the fuel. Low viscosity fuels do not lubricate the pistons sufficiently, causing piston wear and leaks. Since high viscosity fuels increase droplet formation during injection, they make combustion difficult, affect fuel

(CC) 2022 SCS.

economy, exhaust emissions and harm the environment. The most ideal viscosity range for the known diesel is 2–4 cSt.

The results from Table II show the viscosities of TPO and UTPO in the range of 450 to 600 °C. The viscosity values of TPO are considerably higher (4.36 to 5.97 cSt) than conventional diesel fuel, and the viscosity values decreased as the pyrolysis temperature increased. The high viscosity values of TPO show that it will cause problems even if it is blended with diesel fuels in limited proportions. The viscosity values of UTPO in the range of 450–600 °C are lower (2.84–3.87 cSt) than TPO and are equivalent to conventional diesel fuels. This shows that the upgraded thermal pyrolytic oil can be blended with other diesel--like fuels or diesel fuel in any ratio.

As it can be seen in Tables III and IV, the viscosity values of the upgraded pyrolytic oils obtained from catalytic pyrolysis were significantly improved. As can be seen in Table III, the viscosity values of UCPO obtained in range of 450 to 600 °C using 1 % catalyst were found between 2.18 and 3.42 cSt, and slightly better than the viscosity values of UTPO. These results show that the viscosity values of UCPO are equal to the conventional diesel fuels. As can be seen in Table IV, the viscosity value of the upgraded pyrolytic oils obtained from the pyrolysis experiments performed with 2 % catalyst was found to be slightly higher than the study performed with 1 % catalyst. The viscosities of the upgraded pyrolytic oils were found between 2.57 and 3.57 cSt (Table IV). As can be seen in Table V, fuel blends of UCPO with PBD in all mixing ratios can be used as diesel-like fuel.

From these results, it was understood that the viscosity of the pyrolytic oils decreased as the pyrolysis temperature increased, the viscosity of the pyrolytic oil increased slightly due to the secondary reactions triggering the formation of larger molecules as the amount of catalyst increased, and the viscosity of the pyrolytic oils obtained from the experiments without catalyst was higher. It has been observed that *UCPO* obtained from experiments with 1 % catalyst can be mixed with *PBD* or conventional diesel fuels in any ratio.

Flash point. The flash point of liquid fuel is the temperature at which the fuel reaches the necessary heat for combustion with air. There is a fire hazard in the storage and circulation of fuels with a low flash point. As it can be seen in Tables III and IV, flash points of upgraded pyrolytic oils are lower than the conventional diesel fuels. Although the flash point is expressed as a concept related to the fire hazard of the fuel during storage and transportation, volatile components are high in low flash point fuels. Volatile compounds consisting of small molecules cause a decrease in density and high-pressure during combustion. The flash point of diesel fuels is above 45 °C, both for ignition hazards during storage and transportation and for regular combustion in diesel engines.

(CC) 2022 SCS.

The amount of volatile components is high in low flash point fuels. The volatility of the fuel has a significant effect on the delay time. During injection, the fuel droplets come into contact with the heated air in the combustion chamber. During evaporation, the fuel removes energy from the droplet, cooling the environment and increasing the ignition delay time. Isoparaffins and aromatic compounds have stable molecular structures and require higher temperatures and pressures than *n*-paraffins to initiate the oxidation process by forming free radicals. As it can be seen in Tables II–V, pyrolytic oils containing high concentrations of isoparaffin and aromatic compounds have long ignition delay times (low cetane index).

Therefore, using UTPO or UCPO directly as a diesel fuel equivalent will cause problems. For this reason, it is appropriate to mix pyrolytic oils with high flash point and high cetane index fuels such as palm oil biodiesel (PBD), animal oil biodiesel (TOBD) to increase the flash point and *CI*. While mixing with normal diesel only at low ratios forces them to remain within reasonable limits, higher mixing ratios with PBD or TOBD seem possible. As seen in Table V, flash point values of UTPO fuel blended with PBD are close to diesel fuel values.

*Gross calorific value (*GCV). As it can see in Tables III–V, the calorific value of pyrolytic oils is close to the calorific value of known diesel fuels. The calorific value of the fuel mixture obtained as a result of blending with palm oil biodiesel, which has a lower calorific value, increases as the pyrolytic oil content in the mixture increases. In order to obtain a diesel-like fuel, it is considered appropriate to add at least 50 % of UTPO to PBD.

Iodine number. The iodine value gives a measure of the average degree of unsaturation of fuel: the higher the iodine value, the greater the number of C=C double bonds. The iodine value is directly proportional to the degree of unsaturation and inversely proportional to the melting point of the fuel. A lower iodine value is better for a diesel engine as it has a higher carbon content. On the other hand, the high iodine value attenuates the hydrocarbon chain. As seen from Tables II–IV, the iodine value of pyrolytic oils is considerably higher than the iodine value of conventional diesel fuels. This means that pyrolytic oils have high unsaturated bonds, a lower cetane index than diesel fuel, and a lower flash point with a lower calorific value. For this reason, pyrolytic oils cannot be used alone as a diesel equivalent fuel. They may need to be upgraded, blended with other fuels, and added with special additives to improve fuel quality. Values such as moisture, nitrogen, sulphur in upgraded pyrolytic oils are within reasonable limits when compared to the conventional diesel fuel.

Cetane index. The cetane index (*CI*) is an empirical parameter related to the ignition delay time of diesel fuels. The ignition delay is the time interval between the start of fuel injection and the self-start of ignition. The ignition delay time of fuels with high *CI* value is very short. The ignition delay time of diesel cycle

(CC) 2022 SCS.

engines is an essential parameter to effectively control the combustion process. Fuels containing high concentrations of *n*-paraffin generally have lower ignition delay times than isoparaffins and aromatic compounds. High viscosity fuels form larger droplet diameters, prevent evaporation and thus cause incomplete combustion, prevent the engine from starting in cold temperatures, and increase the emission of unburned hydrocarbons and particulate matter.. Distillation curves provide information about fuel quality to be correlated with engine performance. The temperature of 10 % of the distillation fractions reflects the ease of evaporation, while the temperature of 90 % of these fractions indicates the presence of high molecular weight compounds that will be difficult to evaporate completely. Therefore, distillation curves provide important information about particulate matter and unburned hydrocarbon emissions and residues in the engine. Fuels with low *CI* can also increase particulate matter emissions. Because combustion, in the last stage of the expansion cycle, causes a temperature drop in the combustion chamber, and the combustion rate decreases. This increases the concentration of unburned hydrocarbons condensed on the surface cause an increase in particulate matter mass. The density at 15 °C and the temperatures at which 10, 50 and 90 vol. % are recovered (distillation recovery temperatures) are determined by standard test methods and the cetane index is calculated from these test data using known correlations. *CI* was calculated empirically according to ISO 4264:2018 method, by substituting the experimental data in:

$$CI = 45.2 + 0.089x \times 2t_{10N} + (0.131 + 0.901B)t_{50N} + \\ + (0.0523 - 0.42B)t_{90N} + 0.00049(t_{10N}^2 - t_{90N}^2) + 107B + 60B^2 \quad \text{(S-1)}$$

where $t_{10N} = t_{10} - 215$; $t_{50N} = t_{50} - 260$; $t_{90N} = t_{90} - 310$; t_{10} is the 10 % distillation recovery temperature, °C; t_{50} is the 50 % distillation recovery temperature, °C; t_{90} is the 90 % distillation recovery temperature, °C; $B = (e^{-0.0035D_N})-1$; $D_N = D - 850$, D is the density at 15 °C, kg m^{-3}.

Parameters for calculating *CI* according to the ISO 4264:2018 standard are given in Table S-1. As it can be seen in Table V, the cetane index of the blended fuel increased, and the problems caused by the low cetane index of the pyrolytic fuel were eliminated.

(CC) 2022 SCS.

TABLE S-1. Parameters for calculating *CI* according to the ISO 4264:2018

Sample	Density at 15 °C	t_{10} - 215	t_{50} - 260	t_{90} - 310	D_N	*B*
PBD	879	120	82	50	-800	-0.0965
UCPO	852	-114	-40	40	2	-0.0070
UCPO10	876	107	63	49	26	-0.0870
UCPO20	874	3	52	26	24	-0.0806
UCPO30	871	68	56	39	21	-0.0709
UCPO40	868	22	28	46	18	-0.0611
UCPO50	865	31	23	43	15	-0.0511
UCPO60	861	29	30	44	11	-0.0378
DF	863	30	18	20	13	-0.0445

REFERENCES

1. P. T Williams, S. Besler, D. T. Taylor, *Fuel* **69** (1990)1474 (https://doi.org/10.1016/0016-2361(90)90193-T)
2. X. Dai, X. Yin, C. Wu, W. Zhang, Y. Chen, *Energy* **26** (2001) 385 (https://doi.org/10.1016/S0360-5442(01)00003-2)
3. Z. Cepic, V. Mihajlović, S. Đuric, M. Milotić, M. Stošić, B. Stepanov, M. I. Micunović, *Energies* **14** (2021) 5403 (https://doi.org/10.3390/en14175403)
4. A. Alsaleh, M. L. Sattler, *Curr. Sustain. Renew. Energy Rep.* **1** (2014) 129 (https://doi.org/10.1007/s40518-014-0019-0)
5. A. Uyumaz, B. Aydogan, H. Solmaz, E. Yilmaz, D. Yesim Hopa, T. Aksoy Bahtli, O. Solamz, F. Aksoy, *J. Energy Inst.* **92** (2019) 1406 (https://doi.org/10.1016/j.joei.2018.09.001)
6. S. Chouaya, M. A. Abbassi, R. B. Younes, A. Zoulalian. *Russ. J. Appl. Chem.* **91** (2018) 1603 (https://doi.org/10.1134/S1070427218100063)
7. M. A. Aziz, M. A. Rahman, H. Molla, *J. Radiat. Res. Appl. Sci.* **11** (2018) 311 (https://doi.org/10.1016/j.jrras.2018.05.001)
8. M. Banar, V. Akyıldız, A. Ozkan, Z. Cokaygil, O. Onay, *Energy Conver. Manage.* **62** (2012) 22 (https://doi.org/10.1016/j.enconman.2012.03.019)
9. W. H. Chang, C. T. Tye, *Malays. J. Anal. Sci.* **17** (2013) 176 (http://mjas.analis.com.my/wp-content/uploads/2018/11/Tye.pdf)
10. D. Almeida, M. F. Marques, *Polímeros* **26** (2016) 44 (https://doi.org/10.1590/0104-1428.2100)
11. J. Zhu, X. Meng, F. Xiao, *Front. Chem. Sci. Eng.* **7** (2013) 233 (https://doi.org/10.1007/s11705-013-1329-2)
12. W. U. Eze, R. Umunakwe, H. C. Obasi, H.C., M. I. Ugbaja, C. C. Uche, I. C. Madufor, *Clean Technol. Recyc.* **1** (2021) 50 (https://doi.org/10.3934/ctr.2021003)
13. W. Li, Q. Liu, J. Xing, H. Gao, X. Xiong, Y. Li, X. Li, H. Liu, *Environ. Energy Eng.* **53** (2007) 3263 (https://doi.org/10.1002/aic.11319)
14. Q. Zhang, M. Zhu, I. Jones, Z. Zhang, D. Zhang, *Energy Fuels* **34** (2020) 6209 (https://www.doi.org/10.1021/acs.energyfuels.9b03968)
15. H. M. Patel, T. M. Patel, *Int. J. Eng. Research Technol.* **1** (2012) 1 (https://www.ijert.org/performance-analysis-of-single-cylinder-diesel-engine-fuelled-with-pyrolysis-oil-diesel-and-its-blend-with-ethanol).

(CC) 2022 SCS.